Reconstructing Cosmic Velocities with the Kinetic Sunyaev-Zeldovich Effect

by

Utkarsh Giri

A thesis
presented to the University of Waterloo
in fulfillment of the
thesis requirement for the degree of
Doctor of Philosophy
in
Physics and Astronomy

Waterloo, Ontario, Canada, 2021

Examining Committee Membership

The following served on the Examining Committee for this thesis. The decision of the Examining Committee is by majority vote.

External Examiner:	Gil Holder Professor Department of Physics, University of Illinois, Urbana-Champaign
Supervisor:	Kendrick M. Smith Faculty Perimeter Institute of Theoretical Physics
Co-Supervisor:	Niayesh Afshordi Associate Professor Department of Physics and Astronomy, University of Waterloo
Internal Members:	Matthew Johnson Associate Faculty Perimeter Institute of Theoretical Physics
	James Taylor Associate Professor Department of Physics and Astronomy, University of Waterloo
Internal-External Member:	Eduardo Martin-Martinez Professor, Department of Applied Mathematics, University of Waterloo

Author's Declaration

This thesis consists of material all of which I authored or co-authored: see Statement of Contributions included in the thesis. This is a true copy of the thesis, including any required final revisions, as accepted by my examiners.

I understand that my thesis may be made electronically available to the public.

Statement of Contribution

Chapter 2 presents work done in collaboration with Kendrick M. Smith, Mathew S. Madhavacheril, Moritz Münchmeyer, Simone Ferraro and Matthew C. Johnson [183]. For this work, I analyzed numerical N-body simulations, in order to validate the key ansatz used throughout the paper (the tree-level kSZ bispectrum in Eq. (2.22)). Using the same simulations, I showed that the impact of small-scale redshift space distortions on the kSZ bispectrum was small, an important result in section 2.5. A revised version of the code implementing the bispectrum estimator is publicly available at `https://github.com/utkarshgiri/kszBispectrum`. These results were the starting point for the longer simulation-based study in chapter 3, where I was the lead author. The work has been accepted for publication in Physical Review D.

Chapter 3 presents work done in collaboration with Kendrick Smith and is available on arxiv [84]. I was the lead author on this paper. I did all of the numerical calculations and simulations, and most of the analytic calculations, except for the halo model calculations in section 3.5 which were done by Kendrick. All the plots shown in the chapter were produced by me. The code for the work is made publicly available at `https://github.com/utkarshgiri/kineticsz`. The work has been accepted for publication in Journal of Cosmology and Astroparticle Physics.

Chapter 4 presents ongoing work done towards the development of an MCMC analysis pipeline by me for the CHIME/FRB collaboration that builds upon the work of several members in the CHIME/FRB collaboration. In particular, the work uses the likelihood model and preprocessing algorithm of the direct fitting routine FITBURST. Figure 6 and Figure 7 are produced by me while the rest are taken from elsewhere with proper citation. The pipeline uses an implementation of affine-invariant MCMC algorithm which can be accessed from `https://github.com/utkarshgiri/jaims`

Abstract

Over the last few decades, Physical Cosmology has come a long way from a primitive and data deprived field of research with several speculative theories of origin, evolution and composition of the Universe to a mature, data-driven field of research with a very well established theoretical foundation. The Standard Model of Cosmology, the 6-parameter ΛCDM model, has been immensely successful in describing most (but not all) of what we see around us in the observable Universe. Tested against various independent cosmological probes like the Cosmic Microwave Background (CMB), Large-Scale Structure (LSS), Lyman-alpha forest, supernovae datasets etc, the model has proven to be pretty concordant. However, there still remain several tantalizing open questions about our universe which have kept cosmologists occupied. Our progress in answering these questions is usually a matter of gleaning more and more information about our universe. This is done either by finding new probes, acquiring more data for existing probes or by improving statistical methodologies employed to existing probes and datasets.

The first part of this thesis develops and explores the use of kinetic Sunyaev-Zeldovich (kSZ) effect as a cosmological probe. After giving a brief overview of the field in an introductory chapter, a theoretical framework for the study of the kSZ effect is laid out in chapter 2. We propose an optimal bispectrum estimator that combines CMB maps with galaxy surveys, and show its equivalence to existing statistics. We explore the information content of the estimator, generalize it to incorporate issues arising from redshift uncertainties in photometric surveys and redshift space distortions an produce forecasts for upcoming CMB experiments and galaxy surveys. Chapter 3 explores kSZ velocity reconstruction — a quadratic estimator for mapping the largest-scale cosmological modes of the Universe. We implement kSZ velocity reconstruction in an N-body simulation pipeline and explore its properties. We find that the reconstruction noise can be larger than the analytic prediction which is usually assumed. We revisit the analytic prediction and find additional noise terms which explain the discrepancy. The new terms are obtained from a six-point halo model calculation, and are analogous to the $N^{(1)}$ and $N^{(3/2)}$ biases in CMB lensing. We implement an MCMC pipeline which estimates f_{NL} from N-body kSZ simulations, and show that it recovers unbiased estimates of f_{NL}, with statistical errors consistent with a Fisher matrix forecast. Overall, these results confirm that kSZ velocity reconstruction will be a powerful probe of cosmology in the near future, but new terms should be included in the noise power spectrum.

The second part of the thesis presents my contribution to the CHIME/FRB collaboration where we are searching for Fast Radio Bursts (FRB). FRBs are bright, millisecond pulses of extra-galactic origin which were first seen in 2007 in a radio survey, with another handful of them seen in the ensuing decade. A tracer of large-scale structure, FRBs offer a new window into the Universe and are sensitive to many astrophysically relevant quantities. The CHIME/FRB experiment which was commissioned in 2018, is currently the leading experiment cataloguing and studying these FRBs. I developed a Markov Chain Monte Carlo pipeline that fits models of varying complexity to the FRB events observed by CHIME.

Acknowledgements

Many people have contributed directly or indirectly to the work that has resulted in this dissertation. I would like to thank my supervisor Kendrick Smith for his support and guidance over the years. He is an exceptional physicist and the nicest and most humble human being I have ever known. The things I have learned from him will stay with me forever.

I would like to thank Niayesh Afshordi, Matt Johnson, James Taylor and Achim Kempf for agreeing to be on my advisory committee.

During my Ph.D., I was really fortunate to be a part of the CHIME/FRB collaboration where I got to work with a fantastic group of people. I learnt a lot while working in such a wonderful collaborative environment and I am especially thankful to Chitrang and Ziggy for their help on various occasions.

Finally, I would like to thank my family and friends. I am lucky to have them.

Table of Contents

List of Figures

Chapter 1

Introduction

Cosmology is the study of origin, evolution and composition of our Universe. In the standard picture, the Universe came into existence approximately 13.8 billion years ago and underwent a brief phase of rapid exponential expansion called inflation that brought various patches of the observable Universe into causal contact and seeded the initial condition for its evolution. This was followed by the phase of reheating which resulted in the generation of Standard Model (SM) elementary particles. The equations describing the subsequent evolution of our background Universe come from Einstein's Theory of General Relativity. These equations relate the geometry and expansion of the Universe to the average energy content and are derived under the assumption that it is isotropic and homogeneous. However, this assumption is not entirely correct. The Universe exhibits significant departure from homogeneity on small scales. These deviations, which can be seen in the relic radiation from when the Universe was only $\sim$380,000 years old, called the Cosmic Microwave Background (CMB), encode fundamental information about the cosmos — about its origin, evolution and composition. These fluctuations were sourced by quantum fluctuations in the primordial fields and have evolved over time in accordance with the laws of physics. By studying statistical patterns in the CMB and interpreting it under a consistent theoretical framework — the ΛCDM model, we have come to learn a lot about our universe. In this introductory chapter, I will give a brief overview of the basic ingredients of theoretical and observational CMB cosmology.

1.1 Background Universe

1.1.1 Metric

The *cosmological principle* posits that on large enough scales, our Universe is spatially homogeneous and isotropic. Homogeneity means that the universe looks the same at all locations in space, while isotropy means that it looks the same in all directions. Mathematically, these statements imply translational and rotational invariance. Observations show that the universe is indeed homogeneous and isotropic on sufficiently large scales ($\gtrsim$ 100 Mpc). This simple observation has far reaching consequences. It leads to a simple geometry for the background universe that can then be combined with the field equations of Einstein's theory of relativity to solve for its evolution. The model that describes a homogeneous and isotropic system, which is also expanding with time, is called the Friedmann-Lemaître-Robertson-Walker (FLRW) model. The metric $g_{\mu\nu}$ in the FLRW model is a generalization of the Minkowski metric of Special Relativity and encodes the geometry of the Universe. For a non-static, expanding universe, it is a function of time and defines a notion of coordinate invariant distance measure ds^2 between two distinct points on the space-time.

$$ds^2 = -dt^2 + a(t)^2\left(\frac{1}{1-kr^2}dr^2 + r^2d\theta^2 + r^2sin^2\theta d\phi\right) = -dt^2 + a(t)^2dl^2 \tag{1.1}$$

where we work in natural units with c=1. Our metric convention is $(-,+,+,+)$ and we use Einstein summation convention wherever needed. $a(t)$ is the time-dependent *scale factor* encoding the expansion of our Universe. The parameter k parameterizes the geometry of the Universe. $k < 0$ and $k > 0$ correspond to open and closed geometries, respectively, while $k = 0$ describes a flat Universe that follows Euclidean principles. Observations strongly support a spatially flat Universe and we will assume the same going forward.

1.1.2 Dynamical Equation

The Friedmann equations are a set of equations derived from Einstein's theory of General relativity that govern the evolution of FLRW metric. The Einstein's field equation connects the metric $g_{\mu\nu}$ of the FLRW model and its derivatives to the energy density of the Universe

$$R_{\mu\nu} - \frac{1}{2}g_{\mu\nu}R = 8\pi GT_{\mu\nu} \tag{1.2}$$

where $R_{\mu\nu}$ is called the Ricci tensor given by

$$R_{\mu\nu} = \Gamma^{\alpha}_{\mu\nu,\alpha} - \Gamma^{\alpha}_{\mu\alpha,\nu} + \Gamma^{\alpha}_{\beta\alpha}\Gamma^{\beta}_{\mu\nu} - \Gamma^{\alpha}_{\beta\nu}\Gamma^{\beta}_{\mu\alpha} \tag{1.3}$$

where $,\alpha$ denotes derivative with respect to 4-position x^{α}. Γ is called Christoffel's symbol and is given in terms of the metric $g_{\mu\nu}$ and its derivative by

$$\Gamma^{\mu}_{\alpha\beta} = \frac{g^{\mu\nu}}{2}(g_{\alpha\nu,\beta} + g_{\beta\nu,\alpha} - g_{\alpha\beta,\nu}) \tag{1.4}$$

and $T_{\mu\nu}$ is the stress-energy tensor that contains information about pressure and energy in the Universe. For a perfect fluid, which is a valid description of constituents in the homogeneous and isotropic Universe at large scales

$$T_{\mu\nu} = diag(\rho, P, P, P) \tag{1.5}$$

The Friedmann equations are obtained by solving the time-time and one of the space-space components of the above equation for FLRW metric:

$$H^2(t) = \left(\frac{\dot{a}}{a}\right)^2 = \frac{8\pi G\rho(t)}{3}\, \frac{\ddot{a}}{a} = -\frac{4\pi G}{3}(\rho + 3P) \tag{1.6}$$

where ρ and P are energy density and pressure. They are all functions of time. The first of these equations relates the rate of expansion $a(t)$ of a *flat* Universe to its energy density $\rho(t)$.

1.1.3 Perturbed metric

To go beyond the zeroth order background Universe, one can parameterize the departures of the true metric $g_{\mu\nu}$ from the FLRW metric using linear perturbation. This is a valid approach for most of the cosmologically relevant scales and times. The general metric $g_{\mu\nu}(t, x)$ is a symmetric matrix with 10 independent degrees of freedom. They can be decomposed into scalar, vector and tensor components depending upon how they behave under spatial rotation [101]. For understanding the evolution of perturbations in radiation and matter at linear order, we only need the scalar components since only they couple to density perturbations. Under the intuitive and convenient Newtonian gauge, the metric with scalar perturbations can be parameterized as

$$ds^2 = -(1 + 2\psi(t, x))dt^2 + (1 - 2\phi(x, t))a(t)^2 dl^2 \tag{1.7}$$

where ψ is the Newtonian potential while ϕ can be interpreted as spatial variation in local curvature. This metric can be fed into the Einstein equation to derive constraint relations connecting the fields ψ and ϕ to perturbations in energy density ρ. On scales much below the horizon, the time-time component of Eq. (1.2) results in

$$\nabla^2 \psi = 4\pi G \delta\rho \tag{1.8}$$

which is called the Poisson equation. Furthermore, under the assumption of negligible anisotropic stress in relativistic components of the Universe, one can use the space-space component of Eq. (1.2) to conclude that

$$\psi = \phi \tag{1.9}$$

1.2 Statistical Background

Being an inherently statistical subject, Cosmology relies heavily on probability and statistics. Here, we will review some basic ideas that are used later in the thesis.

A random, mean zero field δ on a 3D space $\mathbb{R}^3$ is a map $\delta : \mathbb{R}^3 \to \mathbb{R}$ that assigns a random value to each point in $\mathbb{R}^3$ obtained from a joint probability distribution. For a Gaussian random field, this joint distribution for an arbitrary set of points $X = [x_1, x_2, ..., x_n]$ is given by

$$P(\delta) = \frac{1}{\sqrt{(2\pi)^n Det(C)}} \exp\left(- \frac{X^T C^{-1} X}{2} \right) \tag{1.10}$$

where $C_{ij} = \langle \delta(x_i)\delta(x_j) \rangle$ is the n-by-n covariance matrix of the field values. For a Gaussian random field, the fourier transform components $\delta(\mathbf{k})$ are also Gaussian random with a diagonal covariance matrix, by translation invariance. Such a field is fully described by its 2-point function or power spectrum $P(k)$, defined as

$$\langle \delta(\mathbf{k})\delta(\mathbf{k}') \rangle = P(k)(2\pi)^3 \delta^3(\mathbf{k} + \mathbf{k}') \tag{1.11}$$

More generally, a random field can be described by a series of N-point functions. The 3-point function or the bispectrum is similarly defined by

$$\langle \delta(\mathbf{k})\delta(\mathbf{k}')\delta(\mathbf{k}'') \rangle = B(k, k', k'')(2\pi)^3 \delta^3(\mathbf{k} + \mathbf{k}' + \mathbf{k}'') \tag{1.12}$$

Wick's Theorem: For Gaussian random fields, the N-point function vanishes when N is odd. For the case when N is even, it can be expressed in terms of products of powerspectrum summed over all possible pair combinations. As an example, the four-point function for Gaussian fields can be written as

$$\begin{aligned}\langle\delta(\mathbf{k}_1)\delta(\mathbf{k}_2)\delta(\mathbf{k}_3)\delta(\mathbf{k}_4)\rangle = \langle\delta(\mathbf{k}_1)\delta(\mathbf{k}_2)\rangle\langle\delta(\mathbf{k}_3)\delta(\mathbf{k}_4)\rangle + \langle\delta(\mathbf{k}_1)\delta(\mathbf{k}_3)\rangle\langle\delta(\mathbf{k}_2)\delta(\mathbf{k}_4)\rangle \\ + \langle\delta(\mathbf{k}_1)\delta(\mathbf{k}_4)\rangle\langle\delta(\mathbf{k}_2)\delta(\mathbf{k}_3)\rangle \end{aligned} \tag{1.13}$$

Non-Gaussianity: Theoretical models as well as observational data from CMB experiments and galaxy surveys suggest that primordial fields were (nearly) Gaussian, with very strong constraints on any departure from purely Gaussian scenario. This Gaussianity is preserved under linear transformation but breaks down when the transformations are non-linear. As long as the field values (perturbations) are small ($\delta << 1$), the evolution equations are dominated by linear terms and the evolution preserves the Gaussian nature of the field. For sufficiently large-scales ($k \lesssim 0.01$ Mpc^{-1}), this is true at all times and therefore on large scales, the fields are well described by a fully Gaussian model. For scales of size $k \sim 1$ Mpc^{-1}, gravitational collapse amplifies these perturbations which consequently require a fully non-linear treatment. The late-time universe ($z < 4$) thus becomes non-gaussian at these non-linear scales. For such a non-gaussian field, he power spectrum is no longer an optimal statistic and we need to resort to higher point functions like bispectrum and trispectrum to gain further information. The trispectrum for a non-gaussian field is given by

$$\langle\delta(\mathbf{k}_1)\delta(\mathbf{k}_2)\delta(\mathbf{k}_3)\delta(\mathbf{k}_4)\rangle_c = T(k_1, k_2, k_3, k_4, |\mathbf{k}_1+\mathbf{k}_2|, |\mathbf{k}_3+\mathbf{k}_4|)(2\pi)^3\delta^3(\mathbf{k}_1+\mathbf{k}_2+\mathbf{k}_3+\mathbf{k}_4) \tag{1.14}$$

where c stands for *connected* and denotes the contribution to the 4-point function of non-gaussian fields after the unconnected contribution as defined by Eq. (1.13) is accounted for. Another complication in the modelling and analysis of galaxy survey data obtained using a spectroscopic survey is that the large-scale structure, in addition to being non-linear, is observed in redshift space. Generally, the galaxy redshift increases with radial distance, but since redshifts also get a contribution from radial velocity, the redshift to radial position mapping gets distorted. This is called redshift-space distortion.

Estimator: An estimator is an statistic to infer quantity of interest (called the estimand) from a dataset. An example of an estimator is the maximum-likelihood estimator which estimates parameters of a model by maximizing the likelihood of the observed data over the parameter space. In cosmology, estimators are used to estimate quantities like the power spectrum of cosmological fields from the data observed in an experiment. An optimal estimator is an estimator that produces unbiased estimates of the desired quantity with minimum uncertainty.

Fisher Matrix

Fisher matrix is the expectation of the Hessian or the curvature of the negative log likelihood of parameters $\Theta = (\theta_1, \theta_2, ...\theta_n)$ given a data realization $\mathcal{D} = [d_1, d_2, ...d_m]$, taken around a fiducial value Θ_0

$$F_{ij} = -\left\langle \frac{d^2 ln\mathcal{L}(\mathcal{D}|\Theta)}{d\theta_i d\theta_j} \right\rangle_{\theta_0} \tag{1.15}$$

The inverse of the Fisher matrix forecasts the covariance matrix of model parameters. The general definition of Eq. (1.15) applies to any parameter set Θ and dataset $\mathcal{D}$. In cosmology, the data could be degrees of freedom of a random field like the CMB. When interpreted under a model like the ΛCDM, the parameters are cosmological parameters of that model.

1.3 Cosmic Microwave Background

The 19^{th} century witnessed Statistical Physics and Electrodynamics develop into mature fields. Early in the 20^{th} century, Einstein developed the theory of relativity. Around the same time, Georges Lemaitre and Edwin Hubble discovered that distant galaxies in

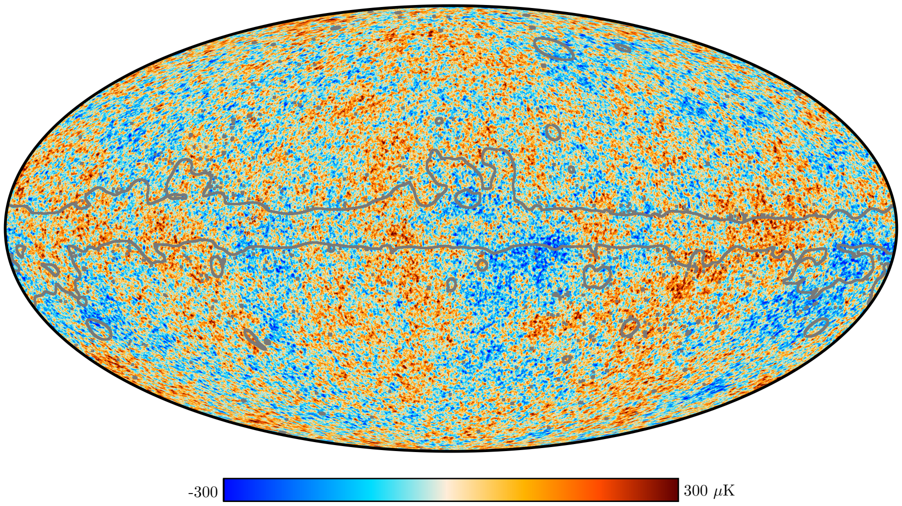

Figure 1.1: The CMB temperature anisotropies seen by Planck [6]. The grey lines delineate regions that are masked and then inpainted

the Universe were receding away from us with recessional speeds directly proportional to their distance, thus hinting at an expanding Universe. When combined in a consistent way together with the cosmological principle, these developments led to a picture of the Universe where early on it was a hot and dense soup of elementary particles. The properties of this primordial state were worked out by physicists in the following decades. One of the major predictions coming out from these calculations was the existence of a nearly isotropic black-body radiation that originated when the photons which were initially in equilibrium with the baryons, fell out of the equilibrium once the Universe cooled down to a temperature of 3000 K from an earlier hotter state. This fall in temperature was a direct outcome of cosmic expansion and allowed electrons and protons to combine together to form neutral hydrogen. Once stable neutral hydrogen started forming, the photons began streaming freely. The CMB is a relic radiation from this epoch which is observed today at micro-meter and millimeter wavelengths.

The CMB was first observed in 1964 by Arno Penzias and Robert Wilson in rather serendipitous circumstances [155]. The duo were investigating radio satellite communication using horn antennas at the Bell labs, when they encountered a constant and isotropic source of excess background power corresponding to a temperature of 3 K. They shared their findings with a group of cosmologists at Princeton who were working on detecting this very signal and had just the right interpretation of the signal [65]. Penzias and Wilson were awarded the Nobel prize in physics for their discovery in 1978. The CMB is one of the fundamental predictions of the Big Bang Model, and its observation established the model as the leading theory of our origin.

The observed CMB is a combination of contributions from different physical effects which we list here to orient the reader:

- The"primary" CMB [102] which is described by linear perturbation theory, dominates on large angular scales ($l \lesssim 2000$), and originates almost entirely at high redshift ($z \sim 1000$).
- CMB lensing [118, 90], which refers to distortions in the primary CMB due to gravitational lensing by structures in the late universe ($z \sim 2$).
- The kinetic Sunyaev-Zeldovich (kSZ) effect [200, 142], which refers to new anisotropy generated by scattering of CMB photons from free electrons, computed to first order in (v/c), where v is the electron velocity in the CMB rest frame. The kSZ effect is the main focus of this thesis.
- The thermal Sunyaev-Zeldovich (tSZ) effect [142], which refers to contributions sourced by electron-CMB scattering and proportional to $(v/c)^2$. The tSZ effect is mainly

sourced by the largest galaxy clusters, which have deep potential wells leading to large virial electron temperature T_e.

- The cosmic infrared background (CIB), which refers to thermal emission from dust in star-forming galaxies [107].
- Radio point sources – a catchall term for compact objects which emit at CMB wavelengths, such as distant quasars.
- The gravitational potential which remains static during matter domination and thus during most of post recombination era, undergoes evolution at late times when dark energy starts dominating. This introduces power at the largest scale which enter the horizon at late times and is called the integrated Sachs-Wolfe effect. The full non-linear version of this effect is known as Rees-Sciama effect.

1.3.1 Statistical Description

The CMB can be modelled as a random field on the sphere [102, 20]. The blackbody temperature $T \approx 2.726K$ of the CMB is nearly independent of which part of the sky is observed, but sensitive measurements show a small level ($\sim 200\mu K$) of anisotropy. Thus, the CMB temperature is a function $T(\boldsymbol{\theta})$ of sky location $\boldsymbol{\theta}$ (a unit vector which parameterizes a point on the sphere). In the standard cosmological model, the CMB realization $T(\boldsymbol{\theta})$ is a random field, where the underlying source of randomness is quantum mechanical randomness during inflation. The primary goal of a CMB experiment is to map out fluctuations in temperature of the CMB as a function of direction in the sky *i.e.* $T(\boldsymbol{\theta})$. The fluctuations around the mean temperature in the CMB can then be expressed as

$$\delta T(\boldsymbol{\theta}) = T(\boldsymbol{\theta}) - \langle T \rangle \tag{1.16}$$

Due to the simplicity that it offers, the CMB field is usually analyzed in its equivalent representation in harmonic space given by

$$T(\boldsymbol{\theta}) = \sum_{l=0}^{\infty} \sum_{m=-l}^{l} a_{lm} Y_{lm}(\boldsymbol{\theta}) \tag{1.17}$$

where spherical harmonics Y_{lm}'s are a set of orthonormal basis functions on 2D sphere similar to the Fourier basis in Euclidean space. A given harmonic $Y_{lm}(\boldsymbol{\theta})$ corresponds to an angular size $\theta = \pi/l$. The components a_{lm} describe the amplitude of anisotropy.

$$a_{lm} = \int d\boldsymbol{\theta}\ T(\boldsymbol{\theta}) Y^*_{lm}(\boldsymbol{\theta}) \tag{1.18}$$

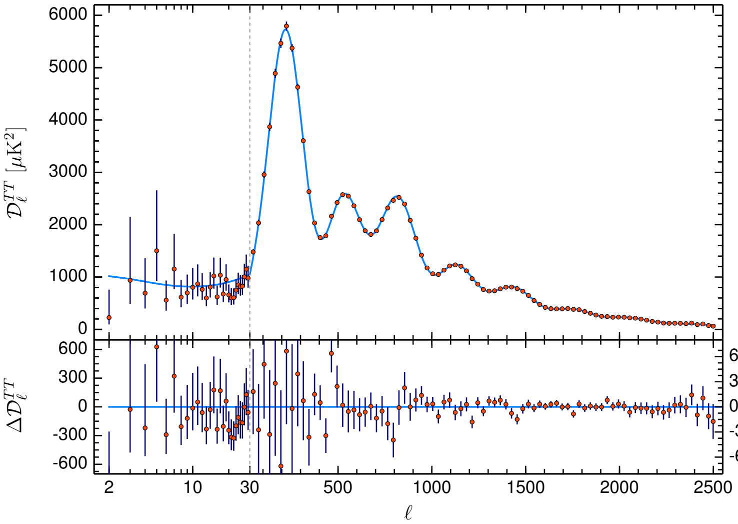

Figure 1.2: The CMB power spectrum from Planck [7]. The plotted curve corresponds to $\mathcal{D}_l^{TT} = \frac{l(l+1)C_l}{2\pi}$. The error bars show $\pm 1\,\sigma$ diagonal uncertainties.

Here, each a_{lm} is a random variable. First let's describe their two-point function *i.e.* covariance. By spherical symmetry (Wigner-Eckhart theorem), the most general two-point function invariant under rotation is:

$$\langle a_{lm} a^*_{l'm'} \rangle = C_l \delta_{ll'} \delta_{mm'} \tag{1.19}$$

This equation defines the power spectrum C_l. The CMB power spectrum is an observable extremely sensitive to the fundamental cosmological parameters.

1.3.2 Primary CMB

Primary CMB refers to the anisotropies sourced at the surface of last scattering – a 3D sphere on our past light-cone where the photons last scattered at the time of decoupling. It is what would be observed in the absence of cosmological structure (galaxies, halos etc.) between us and the surface of last scattering.

The primary CMB is a Gaussian field to an excellent approximation. This means that each a_{lm} is a Gaussian random variable, whose variance is determined by the power spectrum C_l. Therefore, the C_l's completely determines the statistics of the primary CMB.

The power spectrum C_l can be computed numerically from first principles. There are dedicated software packages for this `CAMB` [121], `CMBFAST` [171], `CLASS` [116] which solve differential equations that combine GR and Maxwell's equation (together with some crucial atomic physics during recombination) to give us theoretical prediction for C_l's as a function of fundamental cosmological parameters. The details of the computation is outside the scope of this thesis.

The primary CMB power spectrum is very sensitive to cosmological parameters, and generally speaking, the most powerful constraints on cosmological parameters come from comparing measurements of C_l to data.

1.4 Secondary Anisotropies

1.4.1 Lensing

One prominent secondary anisotropy is the gravitational lensing of CMB [118, 90]. Gravitational interaction of CMB photons with intervening structure leads to the bending of their path of propagation and maps anisotropies originating at a given spot in the sky to a slightly different location while keeping the black-body spectrum intact.

$$T_{lensed}(\boldsymbol{\theta}) = T_{unlensed}(\boldsymbol{\theta} + \boldsymbol{d}(\boldsymbol{\theta})) \tag{1.20}$$

The deflection field $\boldsymbol{d}$ is a random vector field whose power spectrum can be computed with `CAMB` or `CLASS`. Given the power spectra of $d(\boldsymbol{\theta})$ and $T_{unlensed}$, the power spectrum of T_{lensed} can be computed numerically. On large scales ($l \lesssim 1500$), lensing produces small changes to C_l. On small scales, lensing eventually dominates the primary CMB. We omit here further description of the lensed CMB and its non-Gaussian signatures, since the focus of our thesis is the kSZ effect.

1.4.2 Kinetic Sunyaev-Zeldovich effect

The Kinetic Sunyaev-Zeldovich effect [33, 200], the subject of this thesis, is another prominent secondary anisotropy in the CMB sourced by the scattering of CMB photons off free electron clouds which have bulk radial velocities. kSZ anisotropies preserve the black-body spectrum of CMB and are thus much harder to glean directly from a CMB map.

Based on its origin, the kSZ effect comes in two flavors. Patchy kSZ is sourced by moving ionized bubbles of free electrons that were formed around ionizing sources of radiation during the phase when the Universe was undergoing reionization ($6 < z < 20$). In addition to fluctuations in electron density and radial velocity field, the patchy kSZ is also sensitive to fluctuations in the ionization fraction. The focus of my work is late-time kSZ which is sourced by electrons found in post-reionization universe ($z < 6$) mainly in virialized objects like galaxies.

kSZ is a unique tool to probe electron densities in the outskirts of galaxy clusters and has been proposed as tool to resolve the 'missing baryon problem' [38, 92, 95]. The missing baryon problem refers to the discordance between high redshift estimates of baryons coming from CMB and Big Bang nucleosynthesis (BBN) to the low redshift observations of baryons in the Universe. A significant fraction of the total baryon that we expect based on CMB data and BBN has not been observed in the low-redshift Universe. Furthermore, our lack of knowledge of the baryon distribution severely limits the potential returns of future galaxy lensing surveys. A better understanding of electron (baryon) distribution provided by kSZ will help us alleviate this issue. The kSZ effect was recently used to show that the gas profile in halos is more extended than the dark matter profile [166]. Future kSZ measurements with higher signal-to-noise could provide constraints on feedback mechanism operating at galactic scales.

On the cosmological side, due to its dependence on large-scale radial velocity v_r, kSZ has also been proposed as a promising tool to constrain models of dark-energy [60, 93, 30], modified gravity [144, 32], neutrino mass [145] etc. The details of how to efficiently extract the radial velocity is presented in Chapter 2 and 3.

kSZ signal

The physical phenomenon behind the kSZ effect is the Doppler shifting of CMB photons when they scatter off electrons moving in radial direction in the CMB rest frame. Schematically, the effect can be expressed as:

$$\frac{\Delta T(\boldsymbol{\theta})}{T_{cmb}} = -\sum_i \tau_i v_{r_i} \tag{1.21}$$

where for each direction $\boldsymbol{\theta}$ we have summed up contributions coming from electron clouds with optical depth τ_i having a radial velocity v_r in the CMB rest frame. Formally, the net effect can be expressed as a line of sight integral

$$\frac{\Delta T(\boldsymbol{\theta})}{T_{cmb}} = -\int_0^{\chi_*} dr \; g(\boldsymbol{\theta}, r)\mathbf{v}(\boldsymbol{\theta}, r) \cdot \hat{r} \tag{1.22}$$

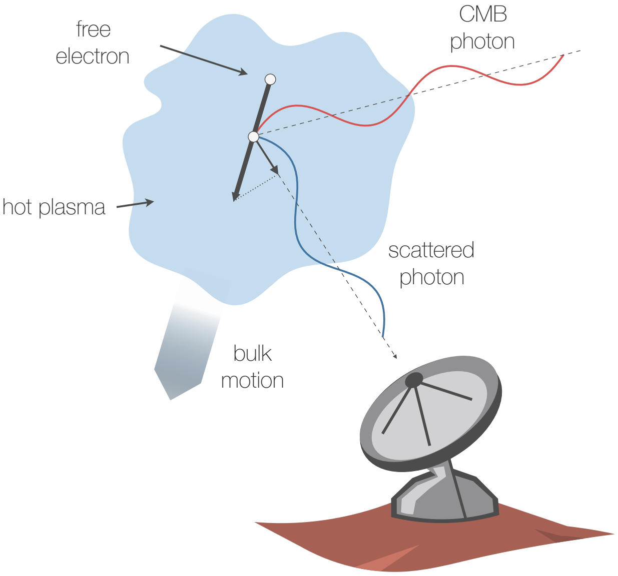

Figure 1.3: Schematic diagram for the kSZ effect. A CMB photon enters the electron cloud from an arbitrary angle, and is up-scattered to higher energy by an electron due to its bulk velocity [142].

where $\boldsymbol{\theta}$ is the 2D angular position in the sky and r is the comoving look-back distance. $g(\boldsymbol{\theta}, r)$ is called the visibility function giving us the probability of last scattering happening at distance r and $\mathbf{v}$ is the velocity field at that point in space. For late-time kSZ, the upper-limit of the integration χ_* is the comoving distance on the past light-cone corresponding to the end of re-ionization. The visibility function is given by

$$g(\boldsymbol{\theta}, r) = \dot{\tau} e^{-\tau(r)} \tag{1.23}$$

where $\tau(r)$ is the optical depth to r given by

$$\tau(\boldsymbol{\theta}, r) = \sigma_T \int_0^r \frac{dr'}{1+z}\, n_e(\boldsymbol{\theta}, r') \tag{1.24}$$

where σ_T is the Thomson cross-section. Here we work under natural units ($c = 1$) where derivative with respect to comoving time is the same as that with respect to comoving distance.

The free electron density n_e can be expressed in terms of comoving proton number density today, n_{e_0}, the baryon overdensity δ_b, free electron fraction χ_e, and redshift z. As a

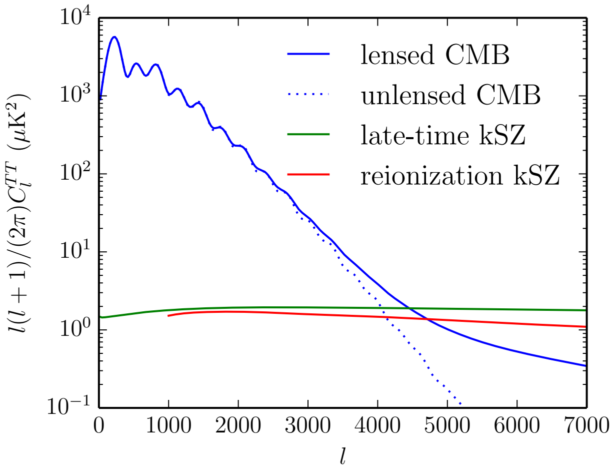

Figure 1.4: Figure showing the primary CMB power spectrum along with the power spectrum of a few prominent black-body preserving secondary anisotropies. Credit: Smith and Ferraro [182]

simplification, we assume that χ_e is a constant which is a good approximation once helium is doubly ionized in low-redshift Universe ($z < 3$).

$$n_e(\boldsymbol{\theta}, r) = n_{e_0}\chi_e(1 + \delta_b(\boldsymbol{\theta}, r))(1 + z)^3 \tag{1.25}$$

Substituting this back in Eq. (1.22), we get

$$\frac{\Delta T(\boldsymbol{\theta})}{T_{cmb}} = -n_{e_0}\chi_e\sigma_T \int dr\ e^{-\tau(r)}(1 + z)^2\mathbf{q}\cdot\hat{r} \tag{1.26}$$

where $\mathbf{q}$ is the momentum field given by $\mathbf{q} = (1 + \delta_b(\mathbf{x}))\mathbf{v}(\mathbf{x})$. It turns out that the contributions from the linear term suffers severe cancellations when projected along the line of sight so the only main contributing source is the term $\delta_b v_r$.

kSZ power spectrum

Since kSZ is the focus of the thesis, we'll next describe the calculation of the power spectrum in detail. The kSZ power spectrum, in its most general form, is a 4-point function involving velocity at linear scales and electron density on non-linear scales. Schematically, one can express it as

$$\langle\delta_b v_r \delta_b v_r\rangle = \langle v_r v_r\rangle\langle\delta_b\delta_b\rangle + 2\langle\delta_b v_r\rangle^2 + \langle\delta_b\delta_b v_r v_r\rangle_c$$

The late-time kSZ becomes a dominant effect only at scales of $\sim 2'$ and therefore small-angle limit can be used in describing it. In the linear limit where the connected term vanishes, the kSZ power spectrum can be expressed in terms of 3D power spectrum of its ingredients using the Limber approximation [124, 129] and is given by

$$C_l^{kSZ} = (n_{e_0}\sigma_T\chi_e)^2 \int \frac{dr}{r^2}(1+z)^4 e^{-2\tau(r)} P_{q_r q_r}\left(k = \frac{l+1/2}{r}, \mu = 0, z\right) \tag{1.27}$$

where $P_{q_r q_r}$ is the power spectrum of radial component of momentum field which unlike a scalar field, depends on the direction of the wave-vector encoded by the parameter $\mu = \hat{k}\cdot\hat{r}$ The power spectrum of a vector quantity like the momentum field can in general expressed as the sum of contribution from a longitudinal term and a transverse term.

$$P_{q_i q_j}(\mathbf{k}) = P^{||}_{qq}(k)\hat{\mathbf{k}}_i\hat{\mathbf{k}}_j + P^{\perp}_{qq}(\mathbf{k})\left[\delta_{ij} - \hat{\mathbf{k}}_i\hat{\mathbf{k}}_j,\right]$$

In the case of kSZ, $i = j = \hat{r}$ denoting the radial direction and $\mu = \hat{k}\cdot\hat{r} = 0$. With these considerations in place, we find that the contribution from the longitudinal component vanishes and the final expression for power spectrum becomes

$$P_{q_r q_r} = P^{\perp}_{qq}(\mathbf{k}) \tag{1.28}$$

Writing this in terms of constituent fields

$$\mathbf{q}_{\perp}(\mathbf{k}) = \int \frac{d^3\mathbf{k}'}{(2\pi)^3}(\hat{\mathbf{k}}' - \mu\hat{\mathbf{k}})\mathbf{v}(\hat{\mathbf{k}}')\delta_b(|\mathbf{k}' - \mathbf{k}|)$$

and using Wick's theorem, the $P_{q_r q_r}$ in Eq. (1.27) becomes

$$P_{q_r q_r}(k, \mu) = \frac{1}{2}\int \frac{d^3\mathbf{k}'}{2\pi^3}(1-\mu^2)P_{\delta\delta}(|\mathbf{k}' - \mathbf{k}|)P_{vv}(\mathbf{k}') - \frac{(1-\mu^2)\mathbf{k}\prime}{|\mathbf{k} - \mathbf{k}'|}P_{\delta v}(|\mathbf{k}' - \mathbf{k}|)P_{\delta v}(\mathbf{k}')$$

The kSZ power spectrum is shown in Fig. 1.4. Analogously to CMB lensing, the kSZ is non-Gaussian. Describing non-Gaussian effects in the CMB is an area of active research, and the main focus of the thesis in Chapters 2, 3.

1.4.3 Other sources of anisotropy

Thermal Sunyaev-Zeldovich

The thermal Sunyaev-Zeldovich (tSZ) effect [33] arises due to the inverse Compton scattering of CMB photons by hot electrons found near the core of massive galaxy clusters. The interaction boosts photons to a higher energy state while conserving their number, causing a slight distortion to the black-body spectrum of CMB. The resultant effect is sensitive to the electron density and temperature of the core region and probes pressure fluctuations in the Universe. Owing to its unique spectral signature, the tSZ effect can be statistically separated from other secondaries using high-resolution multi-frequency observations of the CMB.

Cosmic Infrared Background

The Cosmic Infrared Background (CIB) is sum total of radiation seen at infrared wavelengths that come from dusty star forming galaxies. The emission from stars at optical and UV wavelength are absorbed and remitted by the dust residing in these galaxies.

Chapter 2

KSZ tomography and the Bispectrum

Over the last 30 years, the CMB temperature power spectrum (Figure 2.1) has been measured with increasing precision. On large angular scales ($l \lesssim 2000$), the CMB is dominated by so-called "primary" anisotropy, i.e. anisotropy which originates on the last scattering surface at redshift $z \sim 1100$. On smaller angular scales $2000 \lesssim l \lesssim 4000$, the CMB receives large contributions from gravitational lensing: primary anisotropy which has been lensed by large-scale structure at $0 \lesssim z \lesssim 5$, shifting CMB power to smaller scales. Finally, on the smallest scales $l \gtrsim 4000$, the CMB becomes dominated by the kinetic Sunyaev-Zeldovich (kSZ) effect, i.e. Doppler shifting of CMB photons by free electrons (Fig. 2.1).

The primary and lensed CMB have been measured to high precision, and this has been a gold mine of information for cosmology. So far, the kSZ effect has been detected at a few sigma in cross-correlation with large-scale structure [88, 159, 165, 63, 94, 58], but it will be measured much more accurately in the near future. Qualitatively, it is clear that upcoming kSZ measurements will provide interesting new information in both astrophysics and cosmology. On the astrophysics side, the kSZ probes the distribution of electrons in galaxy clusters, including cluster outskirts where the gas is too cold to appear in thermal SZ, and not dense enough to appear in X-rays. This is a novel observation which can address the "missing baryon" problem [38, 92, 95]. On the cosmology side, the kSZ is a probe of velocities on large scales. Potential applications include dark energy [60, 93, 30], modified gravity [144, 32], neutrino mass [145], void models [80, 42, 48, 39, 135, 206, 202], bulk flows [203, 204], and theories predicting significant large-scale inhomogeneity [205, 193].

There are well-established statistical frameworks for analyzing the primary and lensed CMB. The primary CMB is a Gaussian field, and therefore all of the information is contained in the power spectrum. The lensed CMB is non-Gaussian, but the lens reconstruction quadratic estimator $\hat{\phi}$ provides a framework for constructing higher-point statistics [100, 103, 151].

In contrast, for the kSZ, many different statistics have been proposed [95, 88, 123, 12, 64]. It is not obvious how these statistics relate to each other, how to incorporate them into larger forecasts involving more datasets, or whether one is more informative than the others. One may wonder whether there is a unifying approach.

This work has three main purposes. First, we show that if small-scale CMB observations are combined with a galaxy survey on the same patch of sky, then the kSZ effect introduces a large three-point correlation function (or bispectrum) involving two powers of the galaxy field and one power of the CMB. Following a standard approach used in other areas of cosmology (for example estimating f_{NL} from the primary CMB), we construct the optimal bispectrum estimator for this signal. We also construct the bispectrum Fisher matrix, which can be used to forecast total signal-to-noise, or for more complex multiparameter forecasts. A crucial property of the kSZ bispectrum is that it is parity-odd under reflections in the radial direction, and therefore the estimator is not biased by other non-Gaussian signals (CIB, CMB lensing, thermal SZ), which are parity-even.

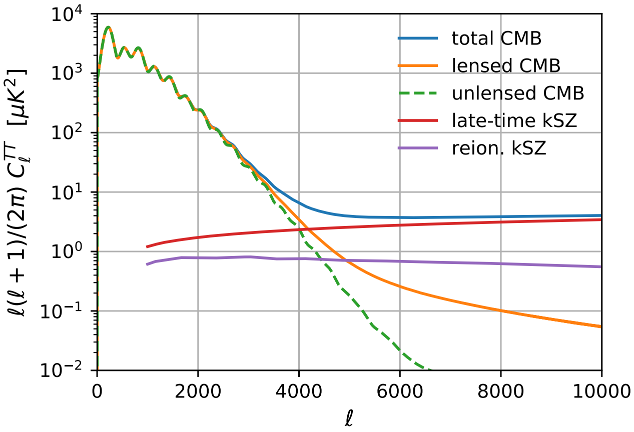

Figure 2.1: The CMB power spectrum C_l^{TT} from primary CMB, gravitational lensing, late-time kSZ ($z < 6$) and reionization kSZ. The late-time kSZ was calculated from the halo model (see App. A.3) and the reionization kSZ was taken from [154]. We have only shown contributions with blackbody frequency dependence. Non-blackbody contributions (CIB, tSZ) can be mostly removed using multifrequency analysis, but the level of residual contamination will depend on experiment-specific details.

A second purpose of the work is to show that several independently proposed statistics for analyzing the kSZ effect are mathematically equivalent, if optimally weighted. These statistics include the kSZ template method [95], the pair sum statistic [88], the velocity matched filter from [123], the velocity growth method from [12], and the velocity reconstruction introduced recently in [64]. We will use the term "kSZ tomography" as a catchall term to refer to any of these statistics.

These kSZ tomography statistics have a common property: they are all three-point estimators involving two powers of the galaxy field and one power of the CMB, as we will show explicitly in §2.3.[1] Therefore, the underlying signal is the bispectrum $\langle ggT \rangle$. In fact, we will show that all of the kSZ tomography statistics (if optimally weighted) are just different ways of algebraically representing the optimal bispectrum estimator $\hat{\mathcal{E}}$. The estimator $\hat{\mathcal{E}}$ is an integral over triples of wavenumbers $\mathbf{k} + \mathbf{k}' + \mathbf{l}/\chi = 0$, and a double sum over galaxy pairs (i, j). The ordering of these integrals and sums can be exchanged, and using different orderings, the estimator $\hat{\mathcal{E}}$ can be rewritten algebraically to take the form of any of the kSZ tomography statistics in [95, 88, 123, 12, 64].

Thus, kSZ tomography is "bispectrum estimation in disguise", and a variety of apparently different statistics are simply different ways of implementing the optimal bispectrum estimator. However, the bispectrum perspective has technical advantages. For example, it clarifies what kSZ tomography actually measures. Our calculation (§2.2) of the $\langle ggT \rangle$ bispectrum will show that it peaks in the squeezed limit where the wavenumbers k_L, k_S of the two galaxy modes satisfy $k_L \ll k_S$, and is proportional to $P_{gv}(k_L) P_{ge}(k_S)$. Here, $P_{gv}(k_L)$ is the galaxy-velocity power spectrum on large scales, and $P_{ge}(k_S)$ is the galaxy-electron power spectrum on small scales. Thus, kSZ tomography is a measurement of two power spectra $P_{gv}(k_L)$, $P_{ge}(k_S)$, within a degeneracy which allows an overall constant to be exchanged, leaving the product $P_{gv}(k_L) P_{ge}(k_S)$ invariant. This is the well-known optical depth degeneracy in the kSZ [25, 76, 128, 185].

The third purpose of this chapter is to give a simple recipe for incorporating kSZ tomography into larger analyses (either Fisher matrix forecasts or actual data analysis), using a quadratic estimator formalism. Before explaining our recipe, we pause briefly to review CMB lens reconstruction [100, 103, 151], which will turn out to be analogous.

---

[1] Not every proposed kSZ statistic is a 3-point estimator of the form $\langle ggT \rangle$. One of the first kSZ statistics proposed [67, 60] is a cross correlation between large-scale structure and the squared high-pass filtered CMB. Recently this method was used to obtain a 4σ measurement of the kSZ [94, 72]. This is a 3-point estimator of a different type, namely $\langle gTT \rangle$. As another example, a four-point estimator $\langle TTTT \rangle$ was recently proposed [182, 74] which does not use an external large-scale structure dataset and can probe reionization. In this work, we do not consider these statistics, and define "kSZ tomography" to mean any kSZ-sensitive three-point estimator of type $\langle ggT \rangle$.

In the case of the lensed CMB, the lens reconstruction quadratic estimator $\hat{\phi}(\mathbf{l})$ estimates each Fourier mode $\phi(\mathbf{l})$ of the CMB lensing potential, using a quadratic combination of CMB modes. This naturally leads to higher-point statistics. If $\hat{\phi}$ is correlated with a galaxy survey g, the result is is a three-point estimator involving two powers of the CMB and one power of the galaxies. The auto power spectrum of $\hat{\phi}$ is a four-point estimator in the underlying CMB map. Furthermore, it is straightforward to incorporate all of these higher-point statistics in larger analyses, by including ϕ as an additional field with the appropriate noise power spectrum.

Analogously, we propose that kSZ tomography can be included in larger analyses by including a large-scale *radial* velocity reconstruction $\hat{v}_r(\mathbf{k})$ with appropriate noise power spectrum. The quadratic estimator $\hat{v}_r(\mathbf{k})$ involves one power of the small-scale galaxy field and one power of the small-scale CMB. The estimator and its noise power spectrum are given explicitly in Eqs. (2.56), (2.57) below. The quadratic estimator $\hat{v}_r$ was first constructed in [64].

The auto power spectrum of $\hat{v}_r$ is a four-point estimator in the underlying galaxy and CMB maps, with schematic form $(ggTT)$. The cross spectrum of $\hat{v}_r$ with a galaxy field is a three-point estimator of schematic form (ggT). To incorporate these higher-point statistics into a larger analysis, we simply include the field v_r with appropriate noise power spectrum.

This is very similar to CMB lensing, but there are some interesting differences between the kSZ quadratic estimator $\hat{v}_r$ and the lensing estimator $\hat{\phi}$, as we now explain. The most obvious difference is that $\hat{v}_r(\mathbf{k})$ is a 3-d reconstruction, whereas $\hat{\phi}(\mathbf{l})$ is 2-d. Further differences arise by considering the noise power spectrum of $\hat{v}_r$, as we explain in the next few paragraphs.

First we note that on large scales, where linear perturbation theory is a good approximation, the radial velocity v_r is related to the density field δ_m by:

$$v_r(\mathbf{k}) = \mu \frac{faH}{k}\, \delta_m(\mathbf{k}) \tag{2.1}$$

where $f = \partial(\log D)/\partial(\log a)$ is the usual redshift-space distortion parameter, and $\mu = k_r/k$. Therefore, we can "convert" the kSZ-derived radial velocity reconstruction $\hat{v}_r$ to a reconstruction $\hat{\delta}(\mathbf{k}) = \mu^{-1}(k/faH)\hat{v}_r(\mathbf{k})$ of the large-scale density field δ_m. We will show (Eq. (2.57) below) that on large scales, the reconstruction noise $N_{v_r}(k_L)$ approaches a constant. Therefore, the kSZ reconstruction noise on the density field δ_m has the form:

$$N_{\delta\delta}^{\rm rec}(k) \propto \mu^{-2} \left(\frac{k}{faH} \right)^2 \qquad (\text{as } k \to 0) \tag{2.2}$$

From this noise power spectrum, we can deduce two qualitative features of the large-scale kSZ-derived reconstruction.

First, *the kSZ cannot reconstruct transverse modes ($\mu \approx 0$), and the kSZ reconstruction cannot be cross-correlated with a 2-d field, such as the CMB lensing potential.* This is due to the μ^{-2} prefactor in Eq. (2.2), and is easy to understand intuitively: transverse modes do not contribute to kSZ because the associated radial velocity is zero. For this reason, in this chapter we only consider 3-d large-scale structure fields, such as galaxy surveys. A galaxy survey with photometric redshifts is an interesting intermediate case between 2-d and 3-d [108]. In this case, there is a signal-to-noise penalty when cross-correlating with the kSZ reconstruction, but the SNR is still large enough to be interesting. We work out the details in §2.5.

Second, *on large scales, kSZ tomography derived from a galaxy survey constrains cosmological modes better than the galaxy survey itself.* This is because the kSZ reconstruction noise in Eq. (2.2) is proportional to k^2 on large scales, whereas the Poisson noise of the galaxy survey approaches a constant value n_g^{-1}. We find (Fig. 2.5 below) that the crossover occurs around $k \sim 0.01$ Mpc^{-1}, although the exact value depends on the details of the CMB and galaxy surveys.

Another qualitative feature of the kSZ-derived velocity reconstruction $\hat{v}_r$ is that it appears with a bias parameter $\langle \hat{v}_r \rangle = b_v v_r^{\rm true}$ which must be marginalized. This is not initially obvious, but we will show in §2.4 that this is a consequence of the kSZ optical depth degeneracy, i.e. astrophysical uncertainty in the small-scale galaxy-electron power spectrum $P_{ge}(k_S)$. Marginalizing b_v fully incorporates the optical depth degeneracy in a larger analysis.

Here is an example to illustrate the power of the velocity reconstruction approach to kSZ tomography. An interesting recent paper [188] showed that the optical depth degeneracy can be broken using an "octopolar" version of the pair sum estimator from [88]. In velocity reconstruction language, the degeneracy breaking can be described as follows. Consider two fields, the kSZ-derived velocity reconstruction $\hat{v}_r = b_v v_r = b_v \mu (faH/k)\delta_m$, and a redshift-space galaxy field field $\delta_g = (b_g + f\mu^2)\delta_m$. If we cross-correlate them, the cross power spectrum has μ dependence of schematic form $P_{\hat{v}_r \delta_g} \propto (faH\sigma_8^2/k)(b_v b_g \mu + b_v f \mu^3)$. In this form, we see that a measurement of the μ^3 term breaks the optical depth degeneracy, in the sense that it pins down the value of b_v (within uncertainty on cosmological parameters f, H, σ_8). This transparent explanation of the degeneracy breaking illustrates the power of the velocity reconstruction approach. A Fisher matrix forecast which includes redshift space distortions would automatically "discover" the degeneracy breaking, without needing to construct the octopolar pair sum explicitly (or needing to know that it exists in advance).

Earlier in this introduction, we stated that the kSZ-derived velocity reconstruction $\hat{v}_r$ is mathematically equivalent to the other kSZ tomography statistics in [95, 88, 123, 12]. This statement implicitly assumes that we cross-correlate $\hat{v}_r$ with the galaxy field g on large scales, but do not use it for anything else. However, in a larger analysis, $\hat{v}_r$ can be correlated with a variety of fields (including itself), and the μ-dependence of these correlations will lead to extra degeneracy breaking. In our view, this makes the velocity reconstruction approach more powerful than the other kSZ tomography statistics, and we advocate using it (at least for cosmology).

Summarizing the results so far, we can give a one-sentence description of how kSZ tomography fits into the larger picture of cosmological observables. KSZ tomography reconstructs the largest modes of the universe, with lower noise than galaxy surveys, up to an overall bias parameter which must be marginalized, and with the caveat that transverse modes ($\mu \approx 0$) are not reconstructed.

This picture clarifies which cosmological parameters the kSZ can constrain. The primordial non-Gaussianity parameter f_{NL} is a prime candidate. The kSZ can be used to reconstruct large-scale density fluctuations with very low noise, which improves f_{NL} constraints from galaxy surveys by using the sample variance cancellation idea from [172]. We present f_{NL} forecasts in [146].

This chapter is organized as follows. In §2.2 we compute the $\langle \delta_g \delta_g T \rangle$ bispectrum, and construct the optimal bispectrum estimator $\hat{\mathcal{E}}$ and its Fisher matrix. We then show (§2.3) that the optimal bispectrum estimator $\hat{\mathcal{E}}$ can be rewritten algebraically in several different ways, corresponding to the different kSZ tomography formalisms in [95, 88, 123, 12, 64]. Armed with this machinery, in §2.4 we analyze several aspects of kSZ tomography, including the velocity reconstruction $\hat{v}_r$ and its formal properties (§2.4.3), prospects for constraining astrophysics (§2.4.4). and the optical depth degeneracy (§2.4.5). In §2.5, we show how to incorporate photometric redshifts and redshift space distortions. We conclude in §2.6.

2.1 Definitions and notation

Throughout this chapter we use the following simplified "snapshot" geometry. We take the universe to be a periodic 3D box with comoving side length L and volume $V = L^3$, "snapshotted" at some time t_*. We denote the redshift of the snapshot by z_*, the comoving distance to redshift zero by χ_*, etc.

We take the 2D sky to be a periodic square with angular side length L/χ_*, and define line-of-sight integration by projecting onto the xy-face of the cube, with a factor $1/\chi_*$ to convert from spatial to angular coordinates. We denote the transverse coordinates of the box by (x, y), but denote the radial coordinate by r (not z, to avoid notational confusion with the redshift). We write $(\cdot)_r$ for the radial component of a three-vector, and $\hat{\mathbf{r}}$ for a unit vector in the radial direction.

With this notation, the kSZ anisotropy is given by the line-of-sight integral:

$$T_{\rm kSZ}(\boldsymbol{\theta}) = K_* \int_0^L dr\, q_r(\chi_* \boldsymbol{\theta} + r\hat{\mathbf{r}}) \tag{2.3}$$

where $q_i(\mathbf{x}) = \delta_e(\mathbf{x}) v_i(\mathbf{x})$ is the electron momentum field, $K(z)$ is the kSZ radial weight function with units μK-Mpc^{-1}:

$$K(z) = -T_{\rm CMB}\sigma_T n_{e,0} x_e(z) e^{-\tau(z)} (1+z)^2 \tag{2.4}$$

and $\tau(z)$ is the optical depth to redshift z.

This simplified geometry neglects lightcone evolution, curved-sky effects, and survey boundaries, all of which will be nontrivial complications in real data analysis. However, it is convenient to ignore these complications when asking questions such as which KSZ observables we should measure, and how we should interpret them. When forecasting galaxy surveys, we approximate the true geometry by our simplified geometry, by matching z_* to the mean redshift of the survey and matching the box volume V to the comoving volume of the survey.

Our Fourier conventions for a 3D field are:

$$f(\mathbf{x}) = \int \frac{d^3\mathbf{k}}{(2\pi)^3} f(\mathbf{k}) e^{i\mathbf{k}\cdot x} \qquad f(\mathbf{k}) = \int d^3\mathbf{x}\, f(\mathbf{x}) e^{-i\mathbf{k}\cdot x} \tag{2.5}$$

and similarly for a 2D field $T(\boldsymbol{\theta}) \leftrightarrow T(\mathbf{l})$.

We sometimes use the integral notation:

$$\int_{\mathbf{k}_1+\mathbf{k}_2+\cdots+\mathbf{k}_n=0} = \int \frac{d^3\mathbf{k}_1}{(2\pi)^3} \frac{d^3\mathbf{k}_2}{(2\pi)^3} \cdots \frac{d^3\mathbf{k}_n}{(2\pi)^3} (2\pi)^n \delta^3\left(\mathbf{k}_1 + \mathbf{k}_2 + ... + \mathbf{k}_n\right) \tag{2.6}$$

to make equations concise.

In linear theory, the velocity field has zero curl, so we can write $v_j(\mathbf{k}) = (ik_j/k) v(\mathbf{k})$, where $v(\mathbf{k})^* = v(-\mathbf{k})$. The linear density field, velocity field, and radial velocity field are related by

$$\delta(\mathbf{k}) = \frac{k}{faH} v(\mathbf{k}) \qquad v_r(\mathbf{k}) = \frac{ik_r}{k} v(\mathbf{k}) \tag{2.7}$$

where $f(z) = \partial(\log D)/\partial(\log a)$ is the usual redshift space distortion parameter. Sometimes we will also use the notation $\mu = k_r/k$.

We define the galaxy overdensity $\delta_g(\mathbf{x})$ as a sum of delta functions (or in Fourier space, a sum of complex exponentials):

$$\delta_g(\mathbf{x}) = \frac{1}{n_g}\sum_i \delta^3(\mathbf{x}-\mathbf{x}_i) \qquad \delta_g(\mathbf{k}) = \frac{1}{n_g}\sum_i e^{-i\mathbf{k}\cdot\mathbf{x}_i} \tag{2.8}$$

where the sum ranges over 3D galaxy positions $\mathbf{x}_i$, and n_g denotes the comoving number density of galaxies. We denote the galaxy bias by b_g.

The fiducial cosmological model we assume in our forecasts roughly corresponds to that determined by Planck with Hubble constant $H_0 = 67.3$ km/s/Mpc, baryon density $\Omega_b h^2 = 0.02225$, cold dark matter density $\Omega_c h^2 = 0.1198$, scalar spectral index $n_s = 0.9645$, amplitude of scalar fluctuations $A_s = 2.2 \times 10^{-9}$, optical depth to reionization $\tau = 0.06$, and minimal sum of neutrino masses $\sum m_\nu = 0.06$ eV.

For our kSZ forecasts, we will need to know the galaxy auto power spectrum $P_{gg}^{\rm tot}(k)$ and the galaxy-electron cross power spectrum $P_{ge}(k)$. We model these power spectra using the halo model. The main source of modeling uncertainty is the electron halo profile which is assumed, which affects $P_{ge}(k)$. In our fiducial model, we use the "AGN" electron profile from [25]. We calculate the kSZ power spectrum C_l from the electron power spectrum $P_{ee}(k)$, calculated self-consistently using the halo model with the same electron profile. Details of the halo model and kSZ model are in Appendix A.3.

2.2 The $\langle\delta_g\delta_g T\rangle$ bispectrum

The underlying signal for kSZ tomography is a three-point function (or the bispectrum) $\langle\delta_g(\mathbf{k})\delta_g(\mathbf{k}')T(\mathbf{l})\rangle$ involving two powers of a galaxy field, and one power of the CMB. There is a standard formalism in cosmology for constructing optimal three-point estimators, and forecasting their statistical errors (used for example to construct f_{NL} estimators for the CMB). In this section, we apply this formalism to the kSZ three-point function to construct the optimal bispectrum estimator for kSZ tomography. We also derive the bispectrum Fisher matrix, which can be used for forecasting.

The kSZ bispectrum is unusual: it involves two powers of a 3D field $\delta_g(\mathbf{k})$, and one power of a 2D field $T(\mathbf{l})$. This will change some details of the bispectrum formalism. For example, we will show that the most general bispectrum allowed by symmetry is a function of four variables $B(k, k', l, k_r)$, rather than the usual function of three variables $B(k, k', k'')$ which arises for three 3D fields (or three 2D fields).

2.2.1 Mathematical representation of the bispectrum

First we write down the most general three-point function $\langle \delta_g \delta_g T \rangle$ allowed by symmetry. In the simplified geometry used in this chapter (§2.1), the statistics of the fields $\delta_g(\mathbf{x})$, $T(\boldsymbol{\theta})$ are invariant under the following symmetries. First, we can rotate both δ_g and T in the xy-plane. Second, we can translate in the xy-plane, by applying shifts $(\Delta x, \Delta y)$ to δ_g, and angular shifts $(\theta_x, \theta_y) = ((\Delta x)/\chi_*, (\Delta y)/\chi_*)$ to T. Third, we can translate δ_g in the radial direction, leaving T unchanged.

By 3D translation invariance, the three-point function contains the delta function:

$$\langle \delta_g(\mathbf{k}) \delta_g(\mathbf{k}') T(\mathbf{l}) \rangle = B(\mathbf{k}, \mathbf{k}', \mathbf{l})\, (2\pi)^3 \delta^3 \left(\mathbf{k} + \mathbf{k}' + \frac{\mathbf{l}}{\chi_*} \right) \tag{2.9}$$

Note that the delta function implies that the radial components satisfy $k_r + k'_r = 0$. Once the radial components are specified, 2D rotation invariance implies that $B(\mathbf{k}, \mathbf{k}', \mathbf{l})$ only depends on the lengths k, k', l. Therefore we can write

$$\langle \delta_g(\mathbf{k}) \delta_g(\mathbf{k}') T(\mathbf{l}) \rangle = iB(k, k', l, k_r)(2\pi)^3 \delta^3 \left(\mathbf{k} + \mathbf{k}' + \frac{\mathbf{l}}{\chi_*} \right) \tag{2.10}$$

where the factor i has been introduced for future convenience. The permutation symmetry $\mathbf{k} \leftrightarrow \mathbf{k}'$ implies:

$$B(k, k', l, k_r) = B(k', k, l, -k_r) \tag{2.11}$$

and by taking the complex conjugate of Eq. (2.10) we get:

$$B(k, k', l, k_r)^* = -B(k, k', l, -k_r) \tag{2.12}$$

There is one more symmetry we can use: reflection symmetry in the radial direction. Under this symmetry, the kSZ temperature transforms with a minus sign, so we get:

$$B(k, k', l, -k_r) = -B(k, k', l, k_r) \tag{2.13}$$

Combining Eqs. (2.11)–(2.13), we see that $B(k, k', l, k_r)$ is real-valued, antisymmetric in k, k' and odd in k_r.

The parity-odd transformation law under radial reflections (Eq. (2.13)) has the important consequence that the kSZ bispectrum is orthogonal to bispectra produced by other secondaries (lensing, Rees-Sciama, residual tSZ, residual CIB). These secondaries all generate $\delta_g\delta_g T$-bispectra which are parity-even under radial reflections.[2] As we will show in the next section, this implies that the kSZ tomography estimator is unbiased by the non-kSZ secondaries. This property makes kSZ tomography a particularly interesting way of extracting cosmological information from future CMB experiments, where the main challenge may be disentangling different contributions, rather than obtaining high SNR.

2.2.2 Optimal bispectrum estimator and Fisher matrix

Given a predicted form of the kSZ bispectrum $B(k,k',l,k_r)$, what is the optimal bispectrum estimator $\hat{\mathcal{E}}$? To answer this question, we start with the most general three-point estimator

$$\hat{\mathcal{E}} = \int_{\mathbf{k}+\mathbf{k}'+\mathbf{l}/\chi_*=0} W(\mathbf{k},\mathbf{k}',\mathbf{l}) \Big(\delta_g(\mathbf{k})\delta_g(\mathbf{k}')T(\mathbf{l}) \Big) \tag{2.14}$$

with weight function $W(\mathbf{k},\mathbf{k}',\mathbf{l})$ to be determined by the following constrained optimization problem. We minimize the variance $\mathrm{Var}(\hat{\mathcal{E}})$, subject to the constraint that $\hat{\mathcal{E}}$ is an unbiased estimator for the bispectrum amplitude, i.e. $\langle\hat{\mathcal{E}}\rangle = 1$ if the true bispectrum is B. When computing $\mathrm{Var}(\hat{\mathcal{E}})$, we assume that the fields δ_g, T are Gaussian for simplicity.

Now a short calculation (similar to the derivation in A.1) , gives the following results. The optimal bispectrum estimator is:

$$\hat{\mathcal{E}} = \frac{1}{2F_{BB}} \int_{\mathbf{k}+\mathbf{k}'+\mathbf{l}/\chi_*=0} \frac{-iB^*(k,k',l,k_r)}{P_{gg}^{\mathrm{tot}}(k)\, P_{gg}^{\mathrm{tot}}(k')\, C_l^{TT,\mathrm{tot}}} \Big(\delta_g(\mathbf{k})\delta_g(\mathbf{k}')T(\mathbf{l}) \Big) \tag{2.15}$$

where P_{gg}^{tot} is the total power spectrum of the galaxy survey including shot noise, and $C_l^{TT,\mathrm{tot}}$ is the total power spectrum of the CMB survey including instrumental noise. The prefactor F_{BB} is the bispectrum Fisher matrix, which is defined for a pair of bispectra B, B' by:

$$F_{BB'} = \frac{V}{2} \int_{\mathbf{k}+\mathbf{k}'+\mathbf{l}/\chi_*=0} \frac{B(k,k',l,k_r)^*\, B'(k,k',l,k_r)}{P_{gg}^{\mathrm{tot}}(k)\, P_{gg}^{\mathrm{tot}}(k')\, C_l^{TT,\mathrm{tot}}} \tag{2.16}$$

---

[2] We have included CMB lensing in this list of parity-even secondaries, even though the $\delta_g\delta_g T$-bispectrum produced by lensing is probably very small. To see this, we note that if the CMB lensing potential ϕ and the *unlensed* CMB T_{unl} were statistically independent, then lensing would not produce a $\delta_g\delta_g T$-bispectrum, since the statistics of the lensed CMB would be invariant under $T \to (-T)$. However, there is a small correlation between ϕ and T_{unl} on small scales due to the Rees-Sciama effect, and this produces a small, parity-even $\delta_g\delta_g T$-bispectrum.

where V is the survey volume. The total signal-to-noise of the kSZ bispectrum is given by $\mathrm{SNR} = F_{BB}^{1/2}$. More generally, given N bispectra to be jointly estimated, their N-by-N covariance matrix is the inverse Fisher matrix. If the bispectrum estimator $\hat{\mathcal{E}}$ is constructed assuming bispectrum B, and the true bispectrum is B', then the expectation value of the estimator is $\langle \hat{\mathcal{E}} \rangle = F_{BB'}/F_{BB}$.

We can use this last property of the estimator to show that the kSZ bispectrum estimator is unbiased by parity-even secondaries (CMB lensing, Rees-Sciama, residual tSZ, residual CIB), as stated without proof in the previous section. This amounts to showing that $F_{BB'} = 0$, where B is the parity-odd kSZ bispectrum and B' is any parity-even bispectrum. Writing out the transformation laws explicitly, we have:

$$B(k,k',l,-k_r) = -B(k,k',l,k_r) \qquad B'(k,k',l,-k_r) = B'(k,k',l,k_r) \tag{2.17}$$

From the form of the Fisher matrix in Eq. (2.16), this implies $F_{BB'} = 0$. We note that this argument relies on reflections in the radial direction being an exact symmetry. This is true for the simplified snapshot geometry in this chapter (§2.1), but the symmetry is not exact in reality due to evolution along the lightcone, and therefore we expect some small leakage between kSZ tomography and parity-even secondaries in a more detailed treatment. We defer this to future work.

In Eq. (2.16), we have written the Fisher matrix $F_{BB'}$ as an integral over vector wavenumbers $\mathbf{k}, \mathbf{k}', \mathbf{l}$. While formally transparent, this is inconvenient for numerical evaluation. In Appendix A.2, we show that $F_{BB'}$ can be written as an integral over scalar wavenumbers:

$$F_{BB'} = \frac{V}{2} \int dk\, dk'\, dl\, dk_r\, I(k,k',l,k_r)\, \frac{B(k,k',l,k_r)^*\, B'(k,k',l,k_r)}{P_{gg}^{\mathrm{tot}}(k)\, P_{gg}^{\mathrm{tot}}(k')\, C_l^{TT,\mathrm{tot}}} \tag{2.18}$$

where $I(k,k',l,k_r)$ is defined in Eq. (A.22).

2.2.3 The tree-level kSZ bispectrum

In this section we calculate an explicit formula for the kSZ bispectrum $B(k,k',l,k_r)$. In real space, the kSZ anisotropy $T(\boldsymbol{\theta})$ is given by the line-of-sight integral in Eq. (2.3). Converting to Fourier space and writing $q_r = \delta_e v_r$, this becomes:

$$T(\mathbf{l}) = \frac{K_*}{\chi_*^2} \int_{\mathbf{q}+\mathbf{q}'=\mathbf{l}/\chi_*} \Big(\delta_e(\mathbf{q}) v_r(\mathbf{q}') \Big) \tag{2.19}$$

Plugging this in, we can write the $\langle \delta_g \delta_g T \rangle$ three-point function as a large-scale structure four-point function:

$$\Big\langle \delta_g(\mathbf{k})\delta_g(\mathbf{k}')T(\mathbf{l}) \Big\rangle = \frac{K_*}{\chi_*^2} \int_{\mathbf{q}+\mathbf{q}'=\mathbf{l}/\chi_*} \Big\langle \delta_g(\mathbf{k})\delta_g(\mathbf{k}')\delta_e(\mathbf{q})v_r(\mathbf{q}') \Big\rangle \tag{2.20}$$

It would be very difficult to give a complete calculation of this four-point function which extends to nonlinear scales! As a starting point, suppose we neglect the connected part of the four-point function, and compute the disconnected or tree-level part using Wick's theorem:

$$\Big\langle \delta_g(\mathbf{k})\delta_g(\mathbf{k}')T(\mathbf{l}) \Big\rangle_{\text{tree}} = \frac{K_*}{\chi_*^2} \left(P_{ge}(k) \frac{-ik'_r P_{gv}(k')}{k'} + (\mathbf{k} \leftrightarrow \mathbf{k}') \right) (2\pi)^3 \delta^3 \left(\mathbf{k} + \mathbf{k}' + \frac{\mathbf{l}}{\chi_*} \right) \tag{2.21}$$

Comparing with the definition of the bispectrum $B(k, k', l, k_r)$ in Eq. (2.10), we read off the tree-level kSZ bispectrum in the form:

$$B(k, k', l, k_r)_{\text{tree}} = \frac{K_* k_r}{\chi_*^2} \left(P_{ge}(k) \frac{P_{gv}(k')}{k'} - \frac{P_{gv}(k)}{k} P_{ge}(k') \right) \tag{2.22}$$

The tree-level kSZ bispectrum is guaranteed to be a good approximation to the true kSZ bispectrum in the limit where all wavenumbers k, k', l are small (so that loop corrections are small).

However, we are interested in the kSZ bispectrum in a different limit, namely the "squeezed" limit in which one wavenumber k is small (say $\lesssim 0.1$ Mpc^{-1}), and the other wavenumbers k', l are large (say $k' \sim l/\chi_* \sim 1$ Mpc^{-1}). To see this intuitively, consider the following argument. The kSZ is sourced by a real-space product of the form $\delta_e(\mathbf{x})v_r(\mathbf{x})$, and almost all of the power in the velocity field v_r comes from large scales. Therefore, one of the wavenumbers must correspond to a large scale, say $k \lesssim 0.1$ Mpc^{-1}. On the other hand, the CMB wavenumber must be roughly $l \sim 4000$, since smaller values of l will be dominated by the primary and lensed CMB, and larger values of l will be noise-dominated. The triangle condition $\mathbf{k} + \mathbf{k}' + (\mathbf{l}/\chi_*) = 0$ then requires the wavenumber k' to correspond to a small scale, roughly $k' \sim 1$ Mpc^{-1}.

Now we introduce an ansatz which will be of central importance throughout the chapter. We assume that in the squeezed limit ($k \lesssim 0.1$ Mpc^{-1} and $k' \sim 1$ Mpc^{-1}), the kSZ bispectrum is accurately approximated by the tree-level expression in Eq. (2.22), but using the *nonlinear* small-scale galaxy electron $P_{ge}(k')$ on the RHS. (Abusing terminology slightly, we will continue to call Eq. (2.22) the "tree-level" bispectrum, even though the P_{ge} factor now includes loop and nonperturbative contributions.)

As a direct check that our ansatz is accurate, we have estimated the bispectrum directly from N-body simulations, and compared to the tree-level approximation (2.22). We used the public DarkSky simulation [180] with box size 1600 h Mpc^{-1} and 4096^3 particles, and used dark matter particles instead of electrons, and halos instead of galaxies. Empirically, we find in the squeezed limit ($k \leq 0.04$ h Mpc^{-1} and $1 \leq k' \leq 2$ h Mpc^{-1}), the tree-level bispectrum (2.22) is accurate to a few percent or better. The details of our N-body simulation results will be presented separately [83].

As a check that our approximations are self-consistent, we can show that if we *assume* that the kSZ bispectrum is given by the tree-level expression in Eq. (2.22), then the signal-to-noise is dominated by the squeezed limit $k \ll k'$. We write the total signal-to-noise of the bispectrum as $\mathrm{SNR}^2 = F_{BB}$, where F_{BB} is the Fisher matrix defined in Eq. (2.18). We then plug in the tree-level kSZ bispectrum in Eq. (2.22), and integrate out the variables k_r, l to write the Fisher matrix as a double integral over (k, k'). After a short calculation we get:

$$\mathrm{SNR}^2 = \frac{V}{2} \int \frac{dk}{k} \frac{dk'}{k'} f(k, k') \tag{2.23}$$

where $f(k, k')$ is defined by:

$$\begin{aligned} f(k,k') \quad &= \quad \frac{K_*^2}{16\pi^3 \chi_*^3} \frac{k^2 (k')^2}{P_{gg}^{\mathrm{tot}}(k) P_{gg}^{\mathrm{tot}}(k')} \left(P_{ge}(k) \frac{P_{gv}(k')}{k'} - \frac{P_{gv}(k)}{k} P_{ge}(k') \right)^2 \\ &\qquad \times \int_{|k-k'|\chi_*}^{(k+k')\chi_*} dl \, \frac{\Gamma(k,k',l/\chi_*)^2}{C_l^{TT,\mathrm{tot}}} \end{aligned} \tag{2.24}$$

and Γ is defined in Eq. (A.21). By plotting the integrand $f(k, k')$, we can see which parts of the (k, k')-plane contribute to the integral. We find that almost all of the signal-to-noise comes from the squeezed limit (Figure 2.2).

2.2.4 Squeezed limit

Summarizing the previous section, we have argued that the kSZ bispectrum is dominated by the squeezed limit $k_L \ll k_S$, where $k_L \lesssim 0.1$ Mpc^{-1} is a linear scale, and $k_S \sim 1$ Mpc^{-1} is a nonlinear scale.

In the squeezed limit, our previous results simplify. The bispectrum becomes:

$$B(k_L, k_S, l, k_{Lr}) = -\frac{K_* k_{Lr}}{\chi_*^2} \frac{P_{gv}(k_L)}{k_L} P_{ge}(k_S) \tag{2.25}$$

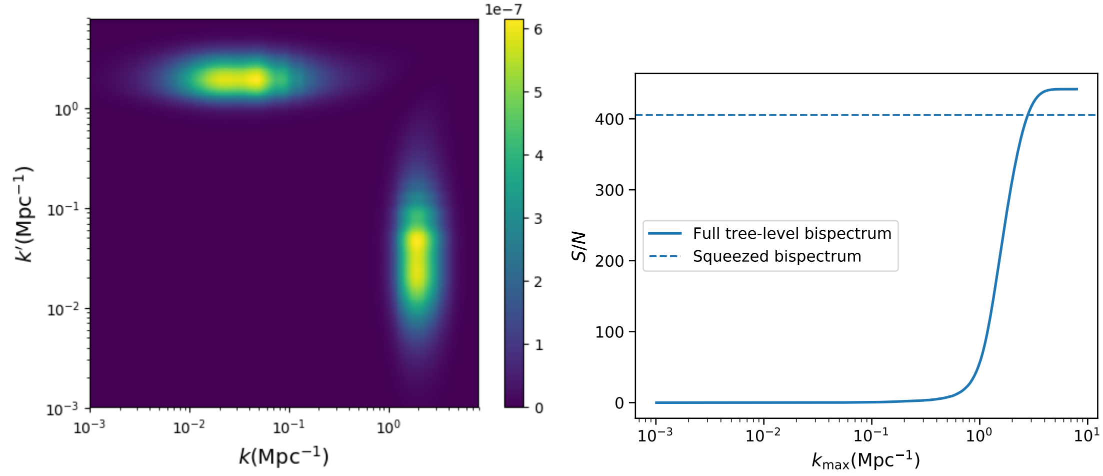

Figure 2.2: Scale dependence of the kSZ bispectrum. *Left:* SNR distribution in the (k, k')-plane, obtained by plotting the integrand $f(k, k')$ defined in Eq. (2.24). As expected, most of the SNR comes from the squeezed limits $k \ll k'$ and $k' \ll k$. *Right:* The cumulative SNR of the bispectrum as more short-wavelength modes are included in the Fisher integral. The difference between the squeezed limit SNR and the tree-level integral is 11%. In both plots, noise parameters from Simons Observatory and DESI were assumed (see Tables 2.1, 2.2 below).

since the first term in Eq. (2.22) is much smaller than the second. We have omitted the "tree" subscript on the LHS since the tree-level bispectrum is an accurate approximation in the squeezed limit, provided that the nonlinear power spectrum $P_{ge}(k_S)$ is used on the RHS. In this chapter, we model $P_{ge}(k_S)$ using the halo model (Appendix A.3). Note that the triangle condition $\mathbf{k}_L + \mathbf{k}_S + (\mathbf{l}/\chi_*) = 0$ implies $l \approx (k_S \chi_*)$ and $k_{Sr} = -k_{Lr}$.

The optimal bispectrum estimator $\hat{\mathcal{E}}$ in Eq. (2.15) can be simplified, if we restrict the integrals to the squeezed limit $k_L \ll k_S$:

$$\hat{\mathcal{E}} = \frac{K_*}{\chi_*^2 F_{BB}} \int_{\mathbf{k}+\mathbf{k}'+\mathbf{l}/\chi_*=0} \frac{ik_{Lr}}{k_L} \frac{P_{gv}(k_L) P_{ge}(k_S)}{P_{gg}^{\mathrm{tot}}(k_L) P_{gg}^{\mathrm{tot}}(k_S) C_l^{TT,\mathrm{tot}}} \Big(\delta_g(\mathbf{k}_L) \delta_g(\mathbf{k}_S) T(\mathbf{l}) \Big) \tag{2.26}$$

where the integrals on the RHS should be understood as running over wavenumbers $k_L \ll k_S$ which contribute significantly to the signal-to-noise (as shown in Figure 2.2). Note that there is a factor of two in Eq. (2.26) relative to Eq. (2.15) because the (k, k') integral in (2.15) runs over squeezed configurations twice (for $k \ll k'$ and $k' \ll k$).

The Fisher matrix in Eq. (2.16) simplifies as follows. If we make no assumptions on the bispectra other than assuming that the squeezed limit dominates, then:

$$F_{BB'} = V \int dk_L\, dk_S\, dk_{Lr}\, \frac{k_L k_S \chi_*^2}{8\pi^3} \left(\frac{B(k_L, k_S, l, k_{Lr})^*\, B'(k_L, k_S, l, k_{Lr})}{P_{gg}^{\rm tot}(k_L)\, P_{gg}^{\rm tot}(k_S)\, C_l^{TT,{\rm tot}}} \right)_{l=k_S\chi_*} \tag{2.27}$$

where the integral runs over $|k_{Lr}| \le k_L \ll k_S$, and both positive and negative k_{Lr}. This form of the Fisher matrix is nice since the algebraically messy factor $I(k, k', l, k_r)$ does not appear (as in Eq. (2.18)). Now suppose we specialize further, by considering bispectra B, B' which are of "kSZ type", meaning that the bispectra are given by the functional form in Eq. (2.25) for different choices of power spectra P_{gv}, P_{ge}:

$$B(k_L, k_S, l, k_{Lr}) = -\frac{K_* k_{Lr}}{\chi_*^2} \frac{P_{gv}(k_L)}{k_L} P_{ge}(k_S) \qquad B'(k_L, k_S, l, k_{Lr}) = -\frac{K_* k_{Lr}}{\chi_*^2} \frac{P'_{gv}(k_L)}{k_L} P'_{ge}(k_S) \tag{2.28}$$

Plugging into Eq. (2.27), the Fisher matrix between kSZ-type bispectra can be written:

$$\begin{aligned} F_{BB'} &= V \frac{K_*^2}{8\pi^3 \chi_*^2} \int dk_L\, dk_S\, dk_{Lr}\, k_{Lr}^2 \left(\frac{P_{gv}(k_L) P'_{gv}(k_L)}{k_L P_{gg}^{\rm tot}(k_L)} \right) \left(\frac{k_S P_{ge}(k_S) P'_{ge}(k_S)}{P_{gg}^{\rm tot}(k_S)} \right) \left(\frac{1}{(C_l^{\rm tot})_{l=k_S\chi_*}} \right) \\ &= V \frac{K_*^2}{12\pi^3 \chi_*^2} \left(\int dk_L\, k_L^2 \frac{P_{gv}(k_L) P'_{gv}(k_L)}{P_{gg}^{\rm tot}(k_L)} \right) \left(\int dk_S\, k_S \frac{P_{ge}(k_S) P'_{ge}(k_S)}{P_{gg}^{\rm tot}(k_S)} \frac{1}{(C_l^{\rm tot})_{l=k_S\chi_*}} \right) \end{aligned} \tag{2.29}$$

where in the second line we have integrated k_{Lr} from $-k_L$ to k_L. The Fisher matrix factorizes as the product of integrals over k_L and k_S. This factorization implies that the measurements of $P_{gv}(k_L)$ and $P_{ge}(k_S)$ obtained from kSZ tomography are independent, aside from an overall normalization which is degenerate. This degeneracy in kSZ tomography is called the "optical depth degeneracy" and will be discussed in more detail in §2.4.

2.3 Equivalence with other formalisms

Summarizing previous sections, we have now shown that the optimal estimator for kSZ tomography is:

$$\hat{\mathcal{E}} = \frac{K_*}{\chi_*^2 F_{BB}} \int_{\mathbf{k}+\mathbf{k}'+\mathbf{l}/\chi_*=0} \frac{ik_{Lr}}{k_L} \frac{P_{gv}(k_L) P_{ge}(k_S)}{P_{gg}^{\rm tot}(k_L) P_{gg}^{\rm tot}(k_S) C_l^{TT,{\rm tot}}} \Big(\delta_g(\mathbf{k}_L) \delta_g(\mathbf{k}_S) T(\mathbf{l}) \Big) \tag{2.30}$$

where the integral runs over triangles $\mathbf{k}_L + \mathbf{k}_S + \mathbf{l}/\chi_* = 0$. The integral should also be restricted to squeezed triangles, in order to ensure that Eq. (2.25) for the bispectrum is an accurate approximation. For example, the integrals could be cut off at $k_{L,\max} = 0.1$ Mpc^{-1} and $k_{S,\min} = 1$ Mpc^{-1}. We have shown (Fig. 2.2) that almost all of the signal-to-noise comes from the squeezed limit, so that the value of $\hat{\mathcal{E}}$ will not depend much on the precise choice of cutoffs.

The form of $\hat{\mathcal{E}}$ in Eq. (2.30) is convenient for many calculations, but less intuitive than the kSZ tomography formalisms proposed in [95, 88, 123, 12, 64]. One may also wonder how best to evaluate $\hat{\mathcal{E}}$ algorithmically, given a CMB map and a galaxy catalog. There is more than one way to do this, since $\hat{\mathcal{E}}$ is a triple integral, and there is also a double sum over galaxies hidden in the $\delta_g(\mathbf{k}_L)\delta_g(\mathbf{k}_S)$ factor. These integrals and sums can be evaluated using different orderings, leading to different implementations of the estimator $\hat{\mathcal{E}}$. In this section, we will show that each of the kSZ tomography formalisms in [95, 88, 123, 12, 64] corresponds to a different implementation of $\hat{\mathcal{E}}$ as follows:

- We can write both factors of $\delta_g(\mathbf{k})$ in Eq. (2.30) as sums over galaxy positions $\delta_g(\mathbf{k}) = \sum_i e^{-i\mathbf{k}\cdot x_i}$, and bring both sums to the outside, to write $\hat{\mathcal{E}}$ as a double sum over galaxy positions $\hat{\mathcal{E}} = \sum_{ij} W_{ij}$, where the pair weighting W_{ij} depends on the CMB temperatures at galaxy positions i, j. This turns out to be equivalent to the pair sum estimator proposed in [88].

- We can bring the $\mathbf{l}$-integral to the outside, and write the estimator in the schematic form $\hat{\mathcal{E}} = \int d^2\mathbf{l}\, T(\mathbf{l})^* \hat{T}(\mathbf{l})$, where $\hat{T}$ is a 2D map formed from two powers of the galaxy field. This turns out to be equivalent to the kSZ template formalism from [95].

- We can write $\delta_g(\mathbf{k}_S) = \sum_i e^{-i\mathbf{k}_S\cdot\mathbf{x}_i}$ as a sum over galaxy positions $\mathbf{x}_i$, and bring the sum to the outside, to write $\hat{\mathcal{E}}$ as a sum of schematic form $\sum_i \eta_i \tilde{T}_i$. Here, $\tilde{T}_i$ is the high-pass filtered CMB at galaxy location i, and η_i is an estimate of the radial velocity at galaxy i which is derived from the long-wavelength modes of the galaxy survey. This turns out to be equivalent to either of the kSZ tomography statistics in [123, 12].

- We can bring the $\mathbf{k}_L$-integral to the outside, and write the estimator in the schematic form $\hat{\mathcal{E}} = \int d^3\mathbf{k}_L\, \delta_g(\mathbf{k}_L)^*\, \hat{v}(\mathbf{k}_L)$, where $\hat{v}(\mathbf{k}_L)$ is a 3D map formed from one power of the small-scale CMB temperature and one power of the small-scale galaxy modes. This turns out to be equivalent to the kSZ-derived velocity reconstruction from [64].

In the following subsections we will work out the details of this equivalence, for each of the kSZ tomography statistics in turn. We will do this in more detail for the last statistic (the kSZ-derived velocity reconstruction from [64]), since some intermediate results in the derivation will be used in later sections of the chapter.

2.3.1 Equivalence between the bispectrum and pair sum

In this section we will show that the bispectrum estimator $\hat{\mathcal{E}}$ is equivalent to the pair sum estimator from [88]. We start by writing $\hat{\mathcal{E}}$ as:

$$\hat{\mathcal{E}} = \int_{\mathbf{k}+\mathbf{k}'+\mathbf{l}/\chi_*=0} \frac{ik_{Lr}}{k_L} \frac{P_{gv}(k_L) P_{ge}(l/\chi_*)}{P_{gg}^{\rm tot}(k_L) P_{gg}^{\rm tot}(l/\chi_*) C_l^{TT,{\rm tot}}} \Big(\delta_g(\mathbf{k}_L) \delta_g(\mathbf{k}_S) T(\mathbf{l}) \Big) \tag{2.31}$$

where we have replaced $P_{ge}(k_S)$ by $P_{ge}(l/\chi_*)$ in Eq. (2.30), and likewise for $P_{gg}^{\rm tot}(k_S)$. This is an accurate approximation in the squeezed limit $k_L \ll k_S$. We have also removed a constant prefactor, since the overall normalization of the estimator will not be important in this section.

In a galaxy catalog, the galaxies are specified as a sequence of 3D locations $\mathbf{x}_i$ where $i = 1, \cdots, N_{\rm gal}$, and the galaxy field $\delta_g(\mathbf{x})$ is a sum of delta functions (or in Fourier space, a sum of complex exponentials):

$$\delta_g(\mathbf{x}) = \frac{1}{n_g} \sum_i \delta^3(\mathbf{x} - \mathbf{x}_i) \qquad\qquad \delta_g(\mathbf{k}) = \frac{1}{n_g} \sum_i e^{-i\mathbf{k}\cdot\mathbf{x}_i} \tag{2.32}$$

We plug this into Eq. (2.31) and bring the sums to the outside, to write the result as a sum over galaxy pairs (i, j):

$$\begin{aligned} \hat{\mathcal{E}} &= \sum_{ij} \int_{\mathbf{k}+\mathbf{k}'+\mathbf{l}/\chi_*=0} \frac{ik_{Lr}}{k_L} \frac{P_{gv}(k_L) P_{ge}(l/\chi_*)}{P_{gg}^{\rm tot}(k_L) P_{gg}^{\rm tot}(l/\chi_*) C_l^{TT,{\rm tot}}} T(\mathbf{l}) e^{-i(\mathbf{k}_L\cdot\mathbf{x}_i + \mathbf{k}_S\cdot\mathbf{x}_j)} \\ &= \sum_{ij} \int \frac{d^3\mathbf{k}_L}{(2\pi)^3} \frac{d^2\mathbf{l}}{(2\pi)^2} \frac{ik_{Lr}}{k_L} \frac{P_{gv}(k_L) P_{ge}(l/\chi_*)}{P_{gg}^{\rm tot}(k_L) P_{gg}^{\rm tot}(l/\chi_*) C_l^{TT,{\rm tot}}} e^{-i\mathbf{k}_L\cdot(\mathbf{x}_i - \mathbf{x}_j)} e^{i\mathbf{l}\cdot(\mathbf{x}_j^\perp/\chi_*)} T(\mathbf{l}) \\ &= \sum_{ij} \Omega(\mathbf{x}_j - \mathbf{x}_i)\, \tilde{T}(\boldsymbol{\theta}_j) \qquad\qquad (\text{where } \boldsymbol{\theta}_j = \mathbf{x}_j^\perp/\chi_*) \end{aligned} \tag{2.33}$$

where we have defined a filtered CMB $\tilde{T}(\boldsymbol{\theta})$ and a weight function $\Omega(\mathbf{x})$ by:

$$\tilde{T}(\boldsymbol{\theta}) = \int \frac{d^2\mathbf{l}}{(2\pi)^2} \frac{P_{ge}(l/\chi_*)}{P_{gg}^{\rm tot}(l/\chi_*) C_l^{TT,{\rm tot}}} T(\mathbf{l}) e^{i\mathbf{l}\cdot\boldsymbol{\theta}} \tag{2.34}$$

$$\Omega(\mathbf{x}) = \int \frac{d^3\mathbf{k}_L}{(2\pi)^3} \frac{ik_{Lr}}{k_L} \frac{P_{gv}(k_L)}{P_{gg}^{\rm tot}(k_L)} e^{i\mathbf{k}_L\cdot\mathbf{x}} \tag{2.35}$$

The quantity $\boldsymbol{\theta}_j = \mathbf{x}_j/\chi_*$ defined in Eq. (2.33) is just the angular location of the j-th galaxy, in the simplified box geometry used in this work (§2.1).

To simplify the pair weighting $\Omega(\mathbf{x}_j - \mathbf{x}_i)$ in Eq. (2.33), we note that $\Omega(\mathbf{x}) = \partial_r W(|\mathbf{x}|)$, where:

$$W(|\mathbf{x}|) = \int \frac{d^3\mathbf{k}}{(2\pi)^3} \frac{P_{gv}(k)}{k P_{gg}^{\rm tot}(k)} e^{i\mathbf{k}\cdot\mathbf{x}} \tag{2.36}$$

and $\partial_r(\cdot)$ denotes the radial derivative. We evaluate the radial derivative as:

$$\Omega(\mathbf{x}) = \partial_r W(|\mathbf{x}|) = \frac{\mathbf{x}\cdot\hat{\mathbf{r}}}{|\mathbf{x}|} W'(|\mathbf{x}|) \tag{2.37}$$

where $\hat{\mathbf{r}}$ is the unit vector in the radial direction. Plugging into Eq. (2.33), we can write $\hat{\mathcal{E}}$ as:

$$\begin{aligned} \hat{\mathcal{E}} &= \sum_{ij} \frac{\mathbf{x}_{ij}\cdot\hat{\mathbf{r}}}{|\mathbf{x}_{ij}|} W'(|\mathbf{x}_{ij}|) \tilde{T}(\boldsymbol{\theta}_j) \\ &= \frac{1}{2} \sum_{ij} \frac{\mathbf{x}_{ij}\cdot\hat{\mathbf{r}}}{|\mathbf{x}_{ij}|} W'(|\mathbf{x}_{ij}|) (\tilde{T}(\boldsymbol{\theta}_j) - \tilde{T}(\boldsymbol{\theta}_i)) \qquad (\text{where } \mathbf{x}_{ij} = \mathbf{x}_j - \mathbf{x}_i) \end{aligned} \tag{2.38}$$

In the second line, we have antisymmetrized $\tilde{T}(\boldsymbol{\theta}_j) \to (\tilde{T}(\boldsymbol{\theta}_j) - \tilde{T}(\boldsymbol{\theta}_i))/2$, since the remaining factors in the double sum are antisymmetric in i, j.

Our final form for $\hat{\mathcal{E}}$ in Eq. (2.38) is a sum over galaxy pairs. The pair weighting agrees perfectly with the pair sum estimator from [88], including the overall angular dependence $(\mathbf{x}_{ij}\cdot\hat{\mathbf{r}})/|\mathbf{x}_{ij}|$. Therefore, the bispectrum estimator is equivalent to the pair sum.

This equivalence establishes some interesting properties of the pair sum estimator which are not obvious in advance. First, the optimal l-weighting of the CMB is given by Eq. (2.34). Second, the optimal weighting in the pair separation $r = |\mathbf{x}_{ij}|$ is given by $W'(r)$, where $W(r)$ is defined in Eq. (2.36). Third, the pair sum statistic is an optimal kSZ tomography estimator, if these weightings in l and r are used. Fourth, the total signal-to-noise of the pair sum can be forecasted as $\text{SNR} = F_{BB}^{1/2}$, where F_{BB} is the bispectrum Fisher matrix defined previously in Eq. (2.29).

2.3.2 Equivalence between the bispectrum and kSZ template formalisms

In this section we will show that the bispectrum estimator is equivalent to the kSZ template formalism from [95]. First we recall the details of the kSZ template formalism. We start by defining the 3D field:

$$\eta(\mathbf{k}_L) = \frac{ik_{Lr}}{k_L}\frac{P_{gv}(k_L)}{P_{gg}^{\rm tot}(k_L)}\delta_g(\mathbf{k}_L) \tag{2.39}$$

This can be interpreted as a minimum variance linear reconstruction of the radial velocity $v_r(\mathbf{k}_L)$ from the long-wavelength modes of the galaxy survey.[3] Similarly, we define the 3D field:

$$\epsilon(\mathbf{k}_S) = \frac{P_{ge}(k_S)}{P_{gg}^{\rm tot}(k_S)}\delta_g(\mathbf{k}_S) \tag{2.40}$$

which can be interpreted as a best estimate for the small-scale electron density $\delta_e(\mathbf{k}_S)$, given the galaxy map. Finally, we define a 2D "kSZ template" field $\hat{T}(\boldsymbol{\theta})$, by radially integrating the product of fields $(\eta\epsilon)$:

$$\hat{T}(\boldsymbol{\theta}) = K_* \int_0^L dr\, \eta(\chi_*\boldsymbol{\theta} + r\hat{\mathbf{r}})\, \epsilon(\chi_*\boldsymbol{\theta} + r\hat{\mathbf{r}}) \tag{2.41}$$

The kSZ template field $\hat{T}(\boldsymbol{\theta})$ is constructed purely from the galaxy survey, but we expect it to be highly correlated with the CMB temperature $T(\boldsymbol{\theta})$, since $\hat{T}$ has been defined using an integral (2.41) which mimics the line-of-sight integral (3.5) for the kSZ. Ref. [95] proposes using the cross power spectrum $C_l^{T\hat{T}}$ as a statistic for kSZ tomography.

To show that $C_l^{T\hat{T}}$ is equivalent to the bispectrum estimator $\hat{\mathcal{E}}$, we proceed as follows. First, we write $\hat{T}$ in Fourier space, by plugging the definitions of η, ϵ (Eqs. (2.39), (2.40)) into the definition of $\hat{T}$ (Eq. (2.41)):

$$\hat{T}(\mathbf{l}) = \frac{K_*}{\chi_*^2}\int_{\mathbf{k}_L+\mathbf{k}_S=\mathbf{l}/\chi_*} \frac{ik_{Lr}}{k_L}\frac{P_{gv}(k_L)}{P_{gg}^{\rm tot}(k_L)}\frac{P_{ge}(k_S)}{P_{gg}^{\rm tot}(k_S)}\Big(\delta_g(\mathbf{k}_L)\delta_g(\mathbf{k}_S)\Big) \tag{2.42}$$

---

[3] We have used the notation η (rather than say $\hat{v}_r$) in order to distinguish between two notions of "large-scale velocity reconstruction" that will be used throughout the chapter. The estimator η defined in Eq. (3.34) is a linear reconstruction of the large-scale radial velocity from the large-scale galaxy field. In the next section we will introduce a kSZ-derived quadratic estimator $\hat{v}_r$ which also reconstructs the large-scale radial velocity, using one power of the small-scale CMB and one power of the small-scale galaxy field.

Then we calculate $C_l^{T\hat{T}}$ as follows:

$$\begin{aligned}
C_l^{T\hat{T}} &= -K_* L \int \frac{d^3\mathbf{k}_L}{(2\pi)^3} \frac{d^3\mathbf{k}_S}{(2\pi)^3} \frac{k_{Lr}}{k_L} \frac{P_{gv}(k_L)}{P_{gg}^{\rm tot}(k_L)} \frac{P_{ge}(k_S)}{P_{gg}^{\rm tot}(k_S)} B(k_L, k_S, l, k_{Lr})\, (2\pi)^3 \delta^3\left(\mathbf{k}_L + \mathbf{k}_S + \frac{\mathbf{l}}{\chi_*}\right) \\
&= \frac{K_*^2 L}{\chi_*^2} \int \frac{d^3\mathbf{k}_L}{(2\pi)^3} \frac{d^3\mathbf{k}_S}{(2\pi)^3} \frac{k_{Lr}^2}{k_L^2} \frac{P_{gv}(k_L)^2}{P_{gg}^{\rm tot}(k_L)} \frac{P_{ge}(k_S)^2}{P_{gg}^{\rm tot}(k_S)} (2\pi)^3 \delta^3\left(\mathbf{k}_L + \mathbf{k}_S + \frac{\mathbf{l}}{\chi_*}\right) \\
&= \frac{K_*^2 L}{6\pi^2 \chi_*^2} \left(\int dk_L\, k_L^2 \frac{P_{gv}(k_L)^2}{P_{gg}^{\rm tot}(k_L)}\right) \left(\frac{P_{ge}(k_S)^2}{P_{gg}^{\rm tot}(k_S)}\right)_{k_S = l/\chi_*}
\end{aligned} \tag{2.43}$$

To get the first line, we have used Eq. (2.42) and the definition (2.10) of the bispectrum. To get the second line, we have plugged in the bispectrum in the form (2.25). The third line is a simplification which is valid in the squeezed limit $k_L \ll k_S$. A similar calculation, omitted for brevity, shows that the auto power spectrum of the template $\hat{T}$ is given by the same expression, i.e.

$$N_l^{\hat{T}\hat{T}} = C_l^{T\hat{T}} \tag{2.44}$$

where we have used the notation N_l since we interpret the auto spectrum of $\hat{T}$ as a noise power spectrum.

Using the results in Eqs. (2.42), (2.43), (2.44), a short calculation starting from Eq. (2.30) now shows that the optimal bispectrum estimator $\hat{\mathcal{E}}$ can be written in the form:

$$\hat{\mathcal{E}} = \frac{1}{F_{BB}} \int \frac{d^2\mathbf{l}}{(2\pi)^2} \frac{C_l^{T\hat{T}}}{C_l^{TT,\rm tot} N_l^{\hat{T}\hat{T}}} \left(T(\mathbf{l}) \hat{T}(-\mathbf{l})\right) \tag{2.45}$$

(This equation can be simplified using $N_l^{\hat{T}\hat{T}} = C_l^{T\hat{T}}$, but we have written it in a way which makes equivalence with the kSZ template formalism most transparent.)

This expression for $\hat{\mathcal{E}}$ agrees perfectly, including the l-weighting, with the minimum variance estimator for the cross-correlation of two fields $T, \hat{T}$ with auto and cross spectra given by $C_l^{TT,\rm tot}$, $C_l^{T\hat{T}}$, and $N_l^{\hat{T}\hat{T}}$. This proves that the kSZ tomography statistic $C_l^{T\hat{T}}$ from [95] is equivalent to the optimal bispectrum estimator $\hat{\mathcal{E}}$.

2.3.3 Equivalence between the bispectrum and velocity matched filter

In this section, we will show that the bispectrum estimator $\hat{\mathcal{E}}$ is equivalent to the "velocity matched filter" statistic from [123].

The idea of [123] is that at the location of each galaxy, the kSZ effect produces a small correlation between the radial velocity v_r and the high-pass filtered CMB temperature $\tilde{T}$. The correlation is small on a per-object basis, but can be detected by summing over many galaxies. In our notation, the velocity matched-filter statistic is:[4]

$$\hat{\alpha} = \sum_i \eta(\mathbf{x}_i)\tilde{T}(\boldsymbol{\theta}_i) \qquad (\text{where } \boldsymbol{\theta}_i = \mathbf{x}_i^\perp/\chi_*) \tag{2.46}$$

where $\tilde{T}(\boldsymbol{\theta})$ is the high-pass filtered CMB defined previously in Eq. (2.34), and $\eta(\mathbf{x})$ is the linear radial velocity reconstruction defined in Eq. (3.34).

To show that the kSZ tomography statistic $\hat{\alpha}$ is equivalent to the bispectrum estimator $\hat{\mathcal{E}}$, we start by writing $\hat{\mathcal{E}}$ in the form:

$$\hat{\mathcal{E}} = \int_{\mathbf{k}_L+\mathbf{k}_S+\mathbf{l}/\chi_*} \frac{ik_{Lr}}{k_L} \frac{P_{gv}(k_L)P_{ge}(l/\chi_*)}{P_{gg}^{\rm tot}(k_L)P_{gg}^{\rm tot}(l/\chi_*)C_l^{TT,{\rm tot}}} \Big(\delta_g(\mathbf{k}_L)\delta_g(\mathbf{k}_S)T(\mathbf{l})\Big) \tag{2.47}$$

where we have replaced $P_{ge}(k_S)$ by $P_{ge}(l/\chi_*)$ in Eq. (2.30), and likewise for $P_{gg}^{\rm tot}(k_S)$. These replacements are valid in the squeezed limit $k_L \ll k_S$. We then manipulate as follows:

$$\begin{aligned}
\hat{\mathcal{E}} &= \frac{1}{n_g}\sum_i \int \frac{d^3\mathbf{k}_L}{(2\pi)^3}\frac{d^2\mathbf{l}}{(2\pi)^2}\frac{ik_{Lr}}{k_L}\frac{P_{gv}(k_L)P_{ge}(l/\chi_*)}{P_{gg}^{\rm tot}(k_L)P_{gg}^{\rm tot}(l/\chi_*)C_l^{TT,{\rm tot}}}\Big(\delta_g(\mathbf{k}_L)T(\mathbf{l})\Big)e^{i(\mathbf{k}_L+\mathbf{l}/\chi_*)\cdot\mathbf{x}_i} \\
&= \frac{1}{n_g}\sum_i \left(\int \frac{d^3\mathbf{k}_L}{(2\pi)^3}\frac{ik_{Lr}}{k_L}\frac{P_{gv}(k_L)}{P_{gg}^{\rm tot}(k_L)}\delta_g(\mathbf{k}_L)e^{i\mathbf{k}_L\cdot\mathbf{x}_i}\right)\int \frac{d^2\mathbf{l}}{(2\pi)^2}\frac{P_{ge}(l/\chi_*)}{P_{gg}^{\rm tot}(l/\chi_*)C_l^{TT,{\rm tot}}}T(\mathbf{l})e^{i\mathbf{l}\cdot(\mathbf{x}_i^\perp/\chi_*)} \\
&= \frac{1}{n_g}\sum_i \eta(\mathbf{x}_i)\tilde{T}(\mathbf{x}_i^\perp/\chi_*)
\end{aligned} \tag{2.48}$$

In the first line, we have plugged in $\delta_g(\mathbf{k}_S) = n_g^{-1}\sum_i e^{-i\mathbf{k}_S\cdot\mathbf{x}_i}$, and used the delta function to do the $\mathbf{k}_S$-integral. To get from the second line to the third, we have recognized the factors in parentheses as the definitions of $\tilde{T}(\boldsymbol{\theta})$ and $\eta(\mathbf{x})$ in Eqs. (2.34), (3.34). The final result is the $\hat{\alpha}$-statistic in Eq. (2.46), completing the proof that $\hat{\alpha}$ is equivalent to the bispectrum estimator $\hat{\mathcal{E}}$.

---

[4] Ref. [123] uses different notation as follows. The linear radial velocity $\eta(\mathbf{x}_i)$ is denoted $v_{\rm rec,i}$, and the high-pass filtered CMB $\tilde{T}(\boldsymbol{\theta}_i)$ is denoted K_i. The kSZ tomography statistic is written $\hat{\alpha} = \sum_i w_i(K_i/v_{\rm rec,i})$, where $w_i \propto v_{\rm rec,i}^2$, or equivalently $\hat{\alpha} \propto \sum_i v_{\rm rec,i}K_i$.

2.3.4 Equivalence between the bispectrum and the velocity growth method

In this section, we will show that the optimal bispectrum estimator $\hat{\mathcal{E}}$ is equivalent to the "velocity growth method", a kSZ tomography statistic introduced recently in [12].

In [12], the large-scale structure catalog is assumed to be a catalog of galaxy clusters with mass estimates, and a prescription is given for the relative weighting of mass bins. Let us first consider the simpler case of a narrow mass bin. We are also implicitly assuming a narrow redshift bin, by using the "snapshot" geometry from §2.1.

The kSZ tomography statistic from [12] is defined by maximizing a likelihood function $\mathcal{L}(\alpha)$, which in our notation is given by:[5]

$$-\log \mathcal{L}(\alpha) \propto \sum_i \Big(\alpha \eta(\mathbf{x}_i) \tau_{500} - \tilde{T}(\boldsymbol{\theta}_i) \Big)^2 \tag{2.49}$$

where τ_{500} is an estimate for the cluster optical depth, $\tilde{T}(\boldsymbol{\theta})$ is the high-pass filtered CMB defined previously in Eq. (2.34), and $\eta(\mathbf{x})$ is the linear radial velocity reconstruction defined in Eq. (3.34).

Given this likelihood, the maximum-likelihood estimator $\hat{\alpha}_{\rm ML}$ is:

$$\hat{\alpha}_{\rm ML} = \frac{\sum_i \eta(x_i) \tilde{T}(\boldsymbol{\theta}_i)}{\tau_{500} \sum_i \eta(\mathbf{x}_i)^2} \tag{2.50}$$

We note that statistical fluctuations in the denominator will be small, since there will be many clusters in the catalog, and the value of $\eta(\mathbf{x}_i)^2$ will be uncorrelated from one cluster to the next, provided the cluster separation is larger than the correlation length of the velocity field. Therefore, to a good approximation, we can replace $\eta(\mathbf{x}_i)^2$ in the denominator by its expectation value $\langle \eta^2 \rangle$, and write:

$$\hat{\alpha}_{\rm ML} \approx \frac{\sum_i \eta(x_i) \tilde{T}(\boldsymbol{\theta}_i)}{N \tau_{500} \langle \eta^2 \rangle} \tag{2.51}$$

---

[5] Ref. [12] uses different notation as follows. The linear radial velocity reconstruction $\eta(\mathbf{x}_i)$ is denoted $\hat{\beta}_r^i$, and the high-pass filtered CMB $\hat{T}(\boldsymbol{\theta}_i)$ is denoted $a^i_{\rm kSZ}$. In writing the likelihood in Eq. (2.49), we have assumed that all clusters are identical, so that the estimated optical depth τ_{500} is independent of i, and so are statistical errors on the quantities τ_{500}, $\hat{T}$, η. This is a reasonable assumption because we are considering narrow mass and redshift bins.

In this form, we see that $\hat{\alpha}_{\rm ML}$ is proportional to the kSZ tomography statistic considered in the previous section (in Eq. (2.46), also denoted $\hat{\alpha}$), where we showed that it is equivalent to the optimal bispectrum estimator $\hat{\mathcal{E}}$.

In this analysis, we only considered the case of a narrow mass bin, setting aside the question of how to optimally weight different mass bins. Ref. [12] discusses this optimization in detail, in addition to the optimal choices of l and k_L-weightings which appear in the filtered CMB $\tilde{T}$ and velocity reconstruction η (Eqs. (2.34), (3.34)).

In the bispectrum approach used in this chapter, these weight optimizations are performed differently. The optimal l and k_L-weightings are part of the optimal bispectrum estimator $\hat{\mathcal{E}}$, which was derived previously in §2.2. So far, we have not discussed how to optimally weight cluster mass bins. We will defer this question to §2.4.6 as part of a more general discussion of how to incorporate kSZ tomography into larger analyses.

2.3.5 Equivalence between the bispectrum and long-wavelength velocity reconstruction

In this section, we will show that the optimal bispectrum estimator $\hat{\mathcal{E}}$ is equivalent to the long-wavelength radial velocity reconstruction from [64].

First we recall the idea from [64] (see also [193, 46] for further related details). The kSZ induces a squeezed bispectrum of schematic form $\langle v_r(\mathbf{k}_L)\delta_g(\mathbf{k}_S)T(\mathbf{l})\rangle$. Therefore, we can build a quadratic estimator for long-wavelength radial velocity modes $v_r(\mathbf{k}_L)$ by summing over pairs $(\delta_g(\mathbf{k}_S)T(\mathbf{l}))$ of short-wavelength modes in the galaxy and CMB maps. This is analogous to CMB lensing, where there is a squeezed bispectrum of the form $\langle\phi(\mathbf{l})T(\mathbf{l}')T(\mathbf{l}'')\rangle$, and consequently the long-wavelength CMB lensing potential ϕ can be reconstructed from small-scale CMB modes.

We next derive the minimum variance estimator $\hat{v}_r(\mathbf{k}_L)$ in the simplified "snapshot" geometry from §2.1, by solving a constrained optimization problem as follows. Consider a general quadratic estimator of the form:

$$\hat{v}_r(\mathbf{k}_L) = \int \frac{d^3\mathbf{k}_S}{(2\pi)^3}\frac{d^2\mathbf{l}}{(2\pi)^2}\, W(\mathbf{k}_S,\mathbf{l})\, \delta_g^*(\mathbf{k}_S)\, T^*(\mathbf{l})\, (2\pi)^3\delta^3\left(\mathbf{k}_L + \mathbf{k}_S + \frac{\mathbf{l}}{\chi_*}\right) \tag{2.52}$$

with weights $W(\mathbf{k}_S,\mathbf{l})$ to be determined. We want to find the weights $W(\mathbf{k}_S,\mathbf{l})$ which minimize the power spectrum of the reconstruction, subject to the constraint that the reconstruction is unbiased, i.e. $\langle\hat{v}_r(\mathbf{k}_L)\rangle$ is equal to the true radial velocity $v_r(\mathbf{k}_L)$. Here, the expectation value $\langle \hat{v}_r(\mathbf{k}_L) \rangle$ is an average over small-scale modes, in a fixed realization of the long-wavelength modes.

A short calculation gives the mean and noise power spectrum of the quadratic estimator in Eq. (2.52), for arbitrary weights $W(\mathbf{k}_S, \mathbf{l})$:

$$\langle \hat{v}_r(\mathbf{k}_L) \rangle = \frac{K_*}{\chi_*^2} \left[\int \frac{d^3\mathbf{k}_S}{(2\pi)^3} \frac{d^2\mathbf{l}}{(2\pi)^2} \, W(\mathbf{k}_S, \mathbf{l}) \, P_{ge}(k_S) (2\pi)^3 \delta^3\left(\mathbf{k}_L + \mathbf{k}_S + \frac{\mathbf{l}}{\chi_*} \right) \right] v_r(\mathbf{k}_L) \quad (2.53)$$

$$N_{v_r}(k_L) = \int \frac{d^3\mathbf{k}_S}{(2\pi)^3} \frac{d^2\mathbf{l}}{(2\pi)^2} \, |W(\mathbf{k}_S, \mathbf{l})|^2 P_{gg}^{\rm tot}(k_S) C_l^{TT,{\rm tot}} (2\pi)^3 \delta^3\left(\mathbf{k}_L + \mathbf{k}_S + \frac{\mathbf{l}}{\chi_*} \right) \quad (2.54)$$

To get the first line, we have used the identity $\langle \delta_g(\mathbf{k}_S) T(\mathbf{l}) \rangle = (K_*/\chi_*^2) P_{ge}(k_S) v_r(\mathbf{k}_S + \mathbf{l}/\chi_*)$, which follows from Eq. (2.19).

Now we solve for the weights $W(\mathbf{k}_S, \mathbf{l})$ which minimize $N_{v_r}(k_L)$, subject to the constraint $\langle \hat{v}_r(\mathbf{k}_L) \rangle = v_r(\mathbf{k}_L)$. A short calculation using Eqs. (2.53), (2.54) shows that $W(\mathbf{k}_S, \mathbf{l})$ and $N_{v_r}(k_L)$ are related by:

$$W(\mathbf{k}_S, \mathbf{l}) = N_{v_r}(k_L) \frac{K_*}{\chi_*^2} \frac{P_{ge}(k_S)}{P_{gg}^{\rm tot}(k_S) C_l^{TT,{\rm tot}}} \quad (2.55)$$

Plugging back into Eqs. (2.52), (2.54), our final expressions for the minimum-variance quadratic estimator $\hat{v}_r(\mathbf{k}_L)$ and its reconstruction noise power spectrum are:

$$\hat{v}_r(\mathbf{k}_L) = N_{v_r}(k_L) \frac{K_*}{\chi_*^2} \int \frac{d^3\mathbf{k}_S}{(2\pi)^3} \frac{d^2\mathbf{l}}{(2\pi)^2} \, \frac{P_{ge}(k_S)}{P_{gg}^{\rm tot}(k_S) C_l^{TT,{\rm tot}}} \Big(\delta_g^*(\mathbf{k}_S) T^*(\mathbf{l}) \Big) (2\pi)^3 \delta^3\left(\mathbf{k}_L + \mathbf{k}_S + \frac{\mathbf{l}}{\chi_*} \right) \quad (2.56)$$

$$\begin{aligned} N_{v_r}(k_L) &= \frac{\chi_*^4}{K_*^2} \left[\int \frac{d^3\mathbf{k}_S}{(2\pi)^3} \frac{d^2\mathbf{l}}{(2\pi)^2} \, \frac{P_{ge}(k_S)^2}{P_{gg}^{\rm tot}(k_S) C_l^{TT,{\rm tot}}} (2\pi)^3 \delta^3\left(\mathbf{k}_L + \mathbf{k}_S + \frac{\mathbf{l}}{\chi_*} \right) \right]^{-1} \\ &= \frac{\chi_*^2}{K_*^2} \left[\int \frac{k_S \, dk_S}{2\pi} \left(\frac{P_{ge}(k_S)^2}{P_{gg}^{\rm tot}(k_S) C_l^{TT,{\rm tot}}} \right)_{l = k_S \chi_*} \right]^{-1} \end{aligned} \quad (2.57)$$

where we have used $k_L \ll k_S$ in the last line to simplify.

This concludes our description of the quadratic estimator $\hat{v}_r$. We mention in advance that the expressions for $\hat{v}_r$ and N_{v_r} (Eqs. (2.56), (2.57)) will be used extensively throughout the rest of the chapter.

To construct a kSZ tomography statistic, i.e. a scalar quantity which is kSZ-sensitive, we can cross-correlate the radial velocity reconstruction $\hat{v}_r(\mathbf{k}_L)$ with the galaxy field on large scales, with a suitable $\mathbf{k}_L$-weighting. We next show that this procedure is equivalent to the optimal bispectrum estimator $\hat{\mathcal{E}}$. Starting from Eq. (2.30) for $\hat{\mathcal{E}}$, we plug in Eq. (2.56) for $\hat{v}_r$, to write $\hat{\mathcal{E}}$ in the form:

$$\hat{\mathcal{E}} = \frac{1}{F_{BB}} \int \frac{d^3\mathbf{k}_L}{(2\pi)^3} \frac{ik_{Lr}}{k_L} \frac{P_{gv}(k_L)}{P_{gg}^{\rm tot}(k_L) N_{v_r}(k_L)} \Big(\delta_g(\mathbf{k}_L) \hat{v}_r(\mathbf{k}_L)^* \Big) \tag{2.58}$$

Similarly, we start with the Fisher matrix element F_{BB} in the following form:

$$F_{BB} = V \frac{K_*^2}{\chi_*^4} \int \frac{d^3\mathbf{k}_L}{(2\pi)^3} \frac{d^3\mathbf{k}_S}{(2\pi)^3} \frac{d^2\mathbf{l}}{(2\pi)^2} \frac{k_{Lr}^2}{k_L^2} \frac{P_{gv}(k_L)^2}{P_{gg}^{\rm tot}(k_L)} \frac{P_{ge}(k_S)^2}{P_{gg}^{\rm tot}(k_S)} \frac{1}{C_l^{TT,\rm tot}} (2\pi)^3 \delta^3 \left(\mathbf{k}_L + \mathbf{k}_S + \frac{\mathbf{l}}{\chi_*} \right) \tag{2.59}$$

which follows from Eq. (2.16), after restricting the integral to squeezed triangles and plugging in the kSZ bispectrum from Eq. (2.25). We then plug in Eq. (2.57) for N_{v_r}, to write F_{BB} in the form:

$$F_{BB} = V \int \frac{d^3\mathbf{k}_L}{(2\pi)^3} \frac{k_{Lr}^2}{k_L^2} \frac{P_{gv}(k_L)^2}{P_{gg}^{\rm tot}(k_L) N_{v_r}(k_L)} \tag{2.60}$$

The expressions (2.58), (2.60) for $\hat{\mathcal{E}}$ and F_{BB} agree perfectly, including constant factors, with the minimum variance estimator for the cross-correlation of two fields $\delta_g(\mathbf{k}_L), \hat{v}_r(\mathbf{k}_L)$, with an anisotropic two-point function of the form $\langle \delta_g(\mathbf{k}')^* \hat{v}_r(\mathbf{k}) \rangle = (ik_r/k) P_{gv}(k) (2\pi)^3 \delta^3(\mathbf{k}-\mathbf{k}')$. This completes the proof that the optimal bispectrum estimator $\hat{\mathcal{E}}$ is equivalent to cross-correlating the kSZ-derived velocity reconstruction $\hat{v}_r$ with the galaxy field δ_g on large scales.

The reconstruction $\hat{v}_r$ can be used to build more general statistics as well. For example, we could consider the auto power spectrum of $\hat{v}_r$ (rather than the cross power spectrum with a galaxy field). Or we could introduce $\hat{v}_r$ into a larger analysis including many fields which can be cross-correlated with each other. The $\hat{v}_r$ formalism is also particularly convenient for incorporating redshift-space distortions and photometric redshift errors. For this reason, the kSZ-derived velocity reconstruction is a particularly powerful approach to kSZ tomography (at least for cosmology), and we advocate using it. Most of the rest of the chapter is devoted to exploring properties of $\hat{v}_r$ in more detail.

2.4 Forecasts and phenomenology

So far, we have built up a lot of formal machinery. We have interpreted kSZ tomography as bispectrum estimation, constructed the optimal bispectrum estimator, and its Fisher matrix (§2.2). We have shown that the formalisms [95, 88, 123, 12, 64] for kSZ tomography are equivalent to the bispectrum, and worked out the details of how to translate between them (§2.3).

In this section, we will analyze several aspects of kSZ tomography using our machinery. The ability to translate between different formalisms will be useful, since calculations which are intuitive in one formalism may not be in others.

In forecasts in this section, we consider galaxy surveys with parameters given in Table 2.1. The parameters for LSST are based on [132, 130], and those for DESI are based on [61]. We use the LSST Gold sample up to Year 1 (LSST-Y1) and up to Year 10 (LSST-Y10). The DESI sample we consider includes the BGS, LRG, ELG and QSO samples.

For the Planck and CMB-S4 CMB experiments, we model the noise power spectrum in each frequency channel as

$$N_\ell^\nu = N_0^\nu \left(1 + \left(\frac{\ell}{\ell_{\rm knee}}\right)^\alpha\right) \exp\left(\frac{\ell(\ell+1)\theta_{\rm FWHM}^2}{8\ln 2}\right). \tag{2.61}$$

with frequencies ν, beamsize $\theta_{\rm FWHM}$ and white noise sensitivity s_w given in Table 2.2. For CMB-S4, we conservatively assume atmospheric noise parameters of $\ell_{\rm knee} = 3000$ and $\alpha = -4$ in all frequency channels, and do not include the atmospheric noise term for Planck. We then construct a standard internal linear combination (ILC) noise curve from those frequencies in combination with the Planck frequency bandpasses specified in Table 2.2, with foreground noise from tSZ, clustered and point source CIB, and radio point sources [69] in addition to reionization and late-time kSZ. For Simons Observatory, we use a parametric fit to the publicly available noise curves [178] for the Goal $f_{\rm sky} = 0.4$ standard ILC cleaned case.

We assume that the CMB experiment overlaps with DESI over $f_{\rm sky} = 0.2$ and with LSST over $f_{\rm sky} = 0.3$. For all small-scale power spectra ($P_{ge}(k_S)$, $P_{gg}(k_S)$ and late-time $C_\ell^{\rm kSZ}$), we use the halo model as described in Appendix A.3, where the stellar mass threshold is chosen such that the predicted number density of galaxies is the same as in Table 2.1. For large-scale power spectra ($P_{gv}(k_L)$, $P_{gg}(k_L)$), we multiply the nonlinear matter power spectrum by the linear galaxy bias in Table 2.1.

2.4.1 Total signal-to-noise ratio

The total SNR for kSZ tomography can be computed using any of the three expressions:

$$\begin{aligned}
\mathrm{SNR}^2 &= V \frac{K_*^2}{12\pi^3\chi_*^2} \left(\int dk_L\, k_L^2 \frac{P_{gv}(k_L)^2}{P_{gg}^{\rm tot}(k_L)} \right) \left(\int dk_S\, k_S \frac{P_{ge}(k_S)^2}{P_{gg}^{\rm tot}(k_S)} \frac{1}{(C_l^{\rm tot})_{l=k_S\chi_*}} \right) && (2.62) \\
&= \Omega \int \frac{d^2\mathbf{l}}{(2\pi)^2} \frac{(C_l^{T\hat{T}})^2}{C_l^{TT,\rm tot} N_l^{\hat{T}\hat{T}}} && (2.63) \\
&= V \int \frac{d^3\mathbf{k}_L}{(2\pi)^3} \frac{k_{Lr}^2}{k_L^2} \frac{P_{gv}(k_L)^2}{P_{gg}^{\rm tot}(k_L) N_{v_r}(k_L)} && (2.64)
\end{aligned}$$

These expressions are mathematically equivalent and correspond to different formalisms introduced previously. The first expression (2.62) is the bispectrum Fisher matrix element F_{BB} from Eq. (2.29). The second expression (2.63) is the total SNR^2 for the cross-correlation between the CMB and the kSZ template $\hat{T}$ from §2.3.2. Here, Ω is the angular survey area in steradians, and the power spectra $C_l^{T\hat{T}}$, $N_l^{\hat{T}\hat{T}}$ which appear were given in Eqs. (2.43), (2.44). The third expression (2.64) is the total SNR^2 for the cross-correlation between the large-scale galaxy field and the kSZ-derived velocity reconstruction $\hat{v}_r$ from §2.3.5. The reconstruction noise power spectrum $N_{v_r}(k_L)$ was given in Eq. (2.57).

Although kSZ tomography has currently been detected at the few-sigma level, the SNR will rapidly improve in the near future. We forecast that CMB-S4 will have total $\mathrm{SNR} = (653, 333, 366)$, in combination with (DESI, LSST-Y1, LSST-Y10) respectively. On

	DESI	**LSST-Y1**	**LSST-Y10**
Mean redshift	0.75	0.9	1.1
Overlap survey volume (Gpc^3)	116	113.4	180
Overlap $f_{\rm sky}$	0.2	0.3	0.3
Number density (Mpc^{-3})	1.7×10^{-4}	6.9×10^{-3}	1.2×10^{-2}
Number density (arcmin^{-2})	0.66	18	48
Galaxy bias	1.51	1.7	1.6
Photo-z error $\sigma_z/(1+z)$	0	0.03	0.03

Table 2.1: Galaxy survey parameters used throughout §2.4. In the case of LSST, photo-z errors are incorporated into kSZ tomography forecasts using machinery which will be developed in §2.5.

Planck		
Frequency (GHz)	Beam (arcmin)	Noise RMS (μK-arcmin)
30	33	145
44	23	149
70	14	137
100	10	65
143	7	43
217	5	66
353	5	200

CMB-S4		
Frequency (GHz)	Beam (arcmin)	Noise RMS (μK-arcmin)
28	7.6	20.0
41	5.1	17.5
90	2.4	2.0
150	1.5	1.8
230	1.0	6.3

Table 2.2: CMB frequency channels, white noise levels, and beam sizes used throughout §2.4. For CMB-S4, we conservatively assume atmospheric noise parameters of $\ell_{\rm knee}$=3000 and $\alpha = -4$ in all frequency channels.

a shorter timescale, Simons Observatory will have SNR $= (405, 205, 221)$ in combination with the same galaxy surveys. To put these in context, the current best measurement is around 6σ [166]. Note that LSST has lower SNR than DESI, even though its density is higher, due to photo-z errors. In Figure 2.3, we show more SNR forecasts, for varying CMB parameters in correlation with DESI.

2.4.2 What does kSZ tomography actually measure?

In this section we will give a simple answer to the question, "what does kSZ tomography measure"? It is convenient to use the bispectrum formalism. Here, the underlying signal is the squeezed bispectrum:

$$B(k_L, k_S, l, k_{Lr}) = -\frac{K_* k_{Lr}}{\chi_*^2} \frac{P_{gv}(k_L)}{k_L} P_{ge}(k_S) \tag{2.65}$$

We see that the observables are the large-scale galaxy-velocity power spectrum $P_{gv}(k_L)$ and the small-scale galaxy-electron power spectrum $P_{ge}(k_S)$.

Because the bispectrum in Eq. (2.65) can be measured as a function of two variables (k_L, k_S), the power spectra $P_{gv}(k_L)$ and $P_{ge}(k_S)$ can be measured independently, except for one degeneracy: we have the freedom to multiply $P_{gv}(k_L)$ by a constant A, while

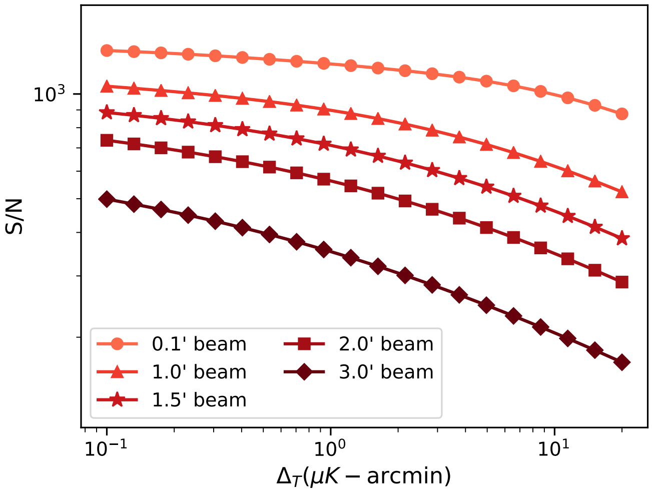

Figure 2.3: KSZ tomography signal-to-noise ratio as a function of CMB noise level and beam at 150 GHz, in cross-correlation with DESI. The fiducial CMB experiment configuration is CMB-S4 as described in Table 2.2, with white noise level and beams in all frequency channels scaled appropriately. The total noise in the CMB includes contributions from the lensed CMB, reionization and late-time kSZ, and the tSZ/CIB/radio residual after standard ILC foreground cleaning.

multiplying $P_{ge}(k_S)$ by $1/A$. This leaves all kSZ tomography observables unchanged, since the bispectrum (2.65) is invariant. This degeneracy is the well-known "kSZ optical depth degeneracy" [25, 76, 128, 185].[6]

Thus, kSZ tomography measures two power spectra $P_{gv}(k_L)$ and $P_{ge}(k_S)$. The results of a kSZ tomography analysis could be presented as a pair of power spectra with error bars, as in Figure 2.4. When interpreting these plots, the only subtlety is the optical depth degeneracy, which allows an overall normalization to be exchanged between $P_{gv}(k_L)$ and $P_{ge}(k_S)$.

---

[6] This is unrelated to another "optical depth degeneracy" in the CMB: the cosmological parameters A_s and τ are constrained with less precision than the combination $A_s e^{-2\tau}$.

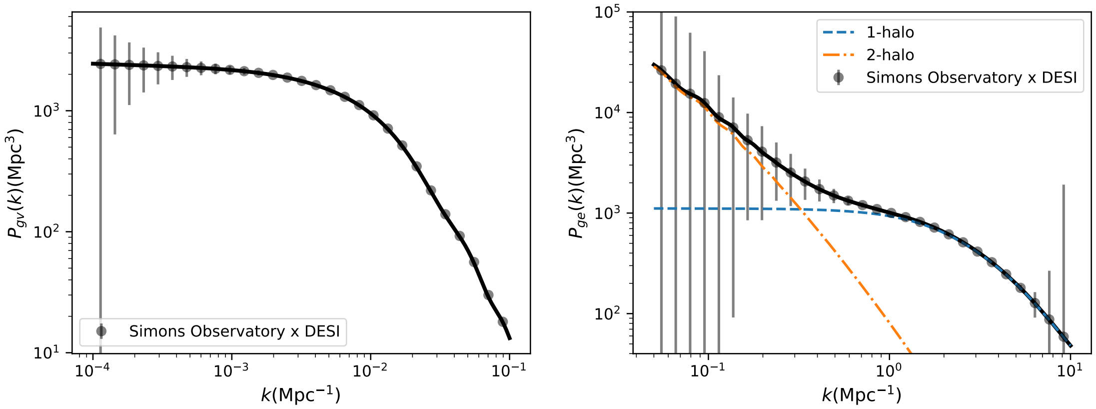

Figure 2.4: Statistical uncertainties on the galaxy-velocity (left) and galaxy-electron (right) power spectrum from kSZ tomography, for Simons Observatory and DESI. Error bars were computed using Eqs. (2.68), (2.72) below. The galaxy-electron cross-spectrum includes contributions from 1-halo (blue dashed) and 2-halo terms (orange dot-dashed). KSZ tomography measures the galaxy-electron cross-spectrum very well in a window of wavenumbers $0.3 \lesssim k \lesssim 5$ Mpc^{-1} where it is primarily 1-halo dominated.

2.4.3 Constraining cosmology: the large-scale power spectrum $P_{gv}(k_L)$

The large-scale galaxy-velocity power spectrum $P_{gv}(k_L)$ can be used to constrain cosmological parameters. For simplicity, we first assume that $P_{ge}(k_S)$ is fixed to a fiducial value.

For cosmological forecasts, we find it most convenient to use the long-wavelength velocity reconstruction formalism from §2.3.5. There we showed that a kSZ-derived quadratic estimator $\hat{v}_r(\mathbf{k})$ can reconstruct each mode of the long-wavelength radial velocity with noise power spectrum:

$$N_{v_r}(k_L) = \frac{\chi_*^2}{K_*^2} \left[\int \frac{k_S\, dk_S}{2\pi} \left(\frac{P_{ge}(k_S)^2}{P_{gg}^{\rm tot}(k_S) C_l^{TT,{\rm tot}}} \right)_{l=k_S\chi_*} \right]^{-1} \tag{2.66}$$

Equivalently, the quadratic estimator can be viewed as a reconstruction of the (non-radial) velocity $v(\mathbf{k}_L) = \mu^{-1} v_r(\mathbf{k}_L)$ or density $\delta_m(\mathbf{k}_L) = \mu^{-1}(k/faH) v_r(\mathbf{k}_L)$, with noise power spectra:

$$N_{vv}^{\rm rec}(k_L,\mu) = \mu^{-2} N_{v_r}(k_L) \qquad N_{\delta\delta}^{\rm rec}(k_L,\mu) = \mu^{-2} \left(\frac{k}{faH} \right)^2 N_{v_r}(k_L) \tag{2.67}$$

Given these noise power spectra, error bars on $P_{gv}(k_L)$ can be computed as:

$$\begin{aligned}\Delta P_{gv} &= \left(V \int_{\mathbf{k}_L \in b} \frac{d^3\mathbf{k}_L}{(2\pi)^3} \frac{1}{P_{gg}^{\rm tot}(k_L) N_{vv}^{\rm rec}(k_L,\mu)} \right)^{-1/2} \\ &= \left(V \int_{k_L^{\rm min}}^{k_L^{\rm max}} \int_{-1}^{1} \frac{k_L^2 dk_L\, d\mu}{4\pi^2} \frac{1}{P_{gg}^{\rm tot}(k_L) N_{vv}^{\rm rec}(k_L,\mu)} \right)^{-1/2} \qquad (2.68)\end{aligned}$$

where V is the survey volume, and $b = (k_L^{\rm min}, k_L^{\rm max})$ is a k_L-bin. This result was used previously to plot error bars in Figure 2.4. We note that Eq. (2.68) can also be derived in the other kSZ tomography formalisms, for example by splitting the bispectrum in k_L-bins and using the bispectrum Fisher matrix in Eq. (2.29).

The reconstruction noise power spectrum $N_{\delta\delta}^{\rm rec}(k_L)$ in Eq. (2.67) has two novel features. First, *on large scales, kSZ tomography derived from a galaxy survey constrains cosmological modes better than the galaxy survey itself.* This is because $N_{\delta\delta}^{\rm rec}$ is proportional to k^2 on large scales, whereas the Poisson noise power spectrum of the galaxy survey has a constant value $n_{\rm gal}^{-1}$. Therefore, on sufficiently large scales, the kSZ-derived noise must be lower.

To quantify this, in Figure 2.5, we compare Poisson noise to kSZ-derived noise, for several combinations of galaxy and CMB surveys. The crossover occurs around $k_L \sim 0.01$ Mpc^{-1}, but depends on the details of the surveys.

Since future galaxy surveys will generally be sample variance limited on large scales, one may wonder whether lowering the noise using kSZ tomography actually gains anything. In situations where sample variance cancellation is beneficial, the low-noise measurement from kSZ tomography can be quite helpful. A prime candidate is constraining f_{NL} using large-scale halo bias. This is explored in detail in [146].

A second novel feature of the reconstruction noise power spectrum in Eq. (2.67) is that it is anisotropic, with an overall μ^{-2} prefactor. This is easy to understand intuitively. Since the velocity is curl-free in linear theory, the velocity v_i of a mode points in a direction parallel to its Fourier wavenumber k_i. In particular, a mode with $\mu = 0$ has velocity perpendicular to the line of sight and does not produce a kSZ signal. Therefore, its reconstruction noise must be infinite, since the amplitude of the mode cannot be constrained from kSZ.

The μ^{-2} dependence has the qualitative consequence that *the kSZ-derived reconstruction of the long-wavelength modes cannot be cross-correlated with a 2D field*, for example the CMB lensing potential ϕ. Indeed, in the Limber approximation, only 3D modes with $\mu = 0$ will contribute to ϕ, and these modes have infinite noise in the kSZ reconstruction.

(Because the Limber approximation is not perfect, the cross correlation between ϕ and the kSZ reconstruction will not be exactly zero, but we expect it to be very small.) For cross-correlations with a 3D field, such as the galaxy-velocity cross correlation $\langle \delta_g v_{\rm rec} \rangle$, the μ^{-2} prefactor does not have a qualitative effect, although it does result in an order-one signal-to-noise penalty.[7]

So far in this section, we have assumed that the small-scale power spectrum $P_{ge}(k_S)$ is known in advance. Now let us consider the effect of uncertainty in $P_{ge}(k_S)$ when reconstructing long-wavelength modes. Suppose the quadratic estimator $\hat{v}(\mathbf{k}_L)$ is constructed using a fiducial power spectrum $P_{ge}^{\rm fid}(k_S)$, but the true power spectrum is $P_{ge}^{\rm true}(k_S) \neq P_{ge}^{\rm fid}(k_S)$. Then $\hat{v}_r(\mathbf{k}_L)$ will be a biased estimator of $v_r(\mathbf{k}_L)$. After a short calculation, the bias can be written in the following form:

$$\langle \hat{v}_r(\mathbf{k}_L) \rangle = b_v v_r(\mathbf{k}_L) \tag{2.69}$$

where the velocity reconstruction bias b_v is given by:

$$b_v = \frac{\int dk_S \, F(k_S) P_{ge}^{\rm true}(k_S)}{\int dk_S \, F(k_S) P_{ge}^{\rm fid}(k_S)} \qquad \text{where } F(k_S) = k_S \frac{P_{ge}^{\rm fid}(k_S)}{P_{gg}^{\rm tot}(k_S)} \left(\frac{1}{C_l^{TT,\rm tot}} \right)_{l = k_S \chi_*} \tag{2.70}$$

The details of Eq. (2.70) are unimportant, except for the crucial property that the bias b_v is independent of k_L. That is, the kSZ-derived velocity reconstruction actually reconstructs the velocity (or density) field up to an overall normalization b_v which is not known in advance, and therefore must be marginalized. This is similar to the case of a galaxy field, where the galaxy bias b_g must be marginalized. In the kSZ context, the bias parameter b_v arises because of the optical depth degeneracy.

2.4.4 Constraining astrophysics: the small-scale power spectrum $P_{ge}(k_S)$

KSZ tomography can be used to measure the small-scale galaxy-electron power spectrum $P_{ge}(k_S)$ in k_S-bins. Here, we will neglect the optical depth degeneracy, since $P_{gv}(k_L)$

---

[7] There are other examples of cosmological fields with the property that cross-correlations with 2d fields are always near-zero, but for different reasons. The 21-cm brightness temperature $T_b(\mathbf{n}, z)$ has this property, because 21-cm maps must be high-pass filtered in the radial direction in order to remove Galactic foregrounds. Similarly, when analyzing Lyman-alpha forest spectra from bright quasars, each spectrum is normalized by dividing by the quasar continuum emission, which is obtained from the data by some form of low-pass filtering. This normalization procedure is a radial high-pass filter which removes correlations with 2d fields.

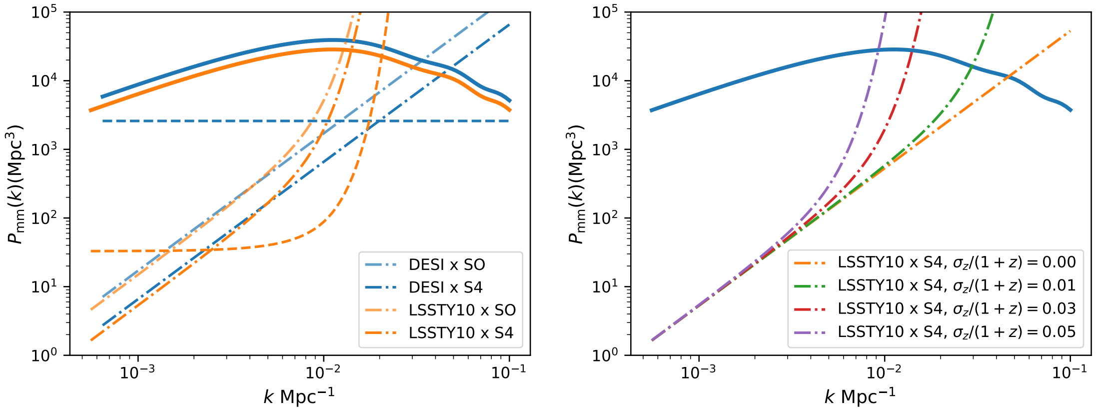

Figure 2.5: *Left:* Reconstruction noise on large-scale modes using kSZ tomography. The solid lines are the total matter power spectrum at the redshifts of DESI and LSST. The dashed lines are the shot noise levels $1/(W^2 b^2 \bar{n})$ in galaxy clustering (scaled appropriately by the galaxy bias b and photo-z error $W(k)$). The dot-dashed lines are reconstruction noise levels $N_{\delta\delta}^{\rm rec}(k_L)$ using kSZ tomography (Eq. (2.67)), for longitudinal modes ($\mu = 1$), for various combinations of galaxy and CMB surveys. *Right:* The matter power spectrum at the mean redshift of the LSST sample compared with kSZ tomography reconstruction noise, for a few choices of photo-z error σ_z.

can be predicted in advance to a few percent, by combining well-measured cosmological parameters with an external measurement of galaxy bias (say from cross-correlating with CMB lensing).

First we ask, what is the statistical error ΔP_{ge} on the power spectrum $P_{ge}(k_S)$ in a k_S-bin? This can be derived in any of our kSZ formalisms, but a quick way to read off the answer using our previous results is as follows. We start with Eq. (2.62) for the total SNR^2, which is written in a form where it can be split into k_S-bins. If we restrict to a single bin $(k_S^{\rm min}, k_S^{\rm max})$, and assume that $P_{ge}(k_S)$ has the constant value $P_{ge}^{\rm fid}$ over the bin, then the single-bin SNR is:

$$\mathrm{SNR}^2_{\rm bin} = V \frac{K_*^2}{12\pi^3 \chi_*^2} (P_{ge}^{\rm fid})^2 \left(\int dk_L \, k_L^2 \frac{P_{gv}(k_L)^2}{P_{gg}^{\rm tot}(k_L)} \right) \left(\int_{k_S^{\rm min}}^{k_S^{\rm max}} dk_S \, k_S \frac{1}{P_{gg}^{\rm tot}(k_S)} \frac{1}{(C_l^{\rm tot})_{l=k_S\chi_*}} \right) \tag{2.71}$$

The single-bin statistical error ΔP_{ge} and SNR are related by $\Delta P_{ge} = P_{ge}^{\rm fid}/\mathrm{SNR}_{\rm bin}$. Therefore:

$$\Delta P_{ge} = \left[V \frac{K_*^2}{12\pi^3 \chi_*^2} \left(\int dk_L \, k_L^2 \frac{P_{gv}(k_L)^2}{P_{gg}^{\rm tot}(k_L)} \right) \left(\int_{k_S^{\rm min}}^{k_S^{\rm max}} dk_S \, k_S \frac{1}{P_{gg}^{\rm tot}(k_S)} \frac{1}{(C_l^{\rm tot})_{l=k_S\chi_*}} \right) \right]^{-1/2} \tag{2.72}$$

This expression was used previously to show error bars on $P_{ge}(k_S)$ in Figure 2.4. One interesting property of this measurement is that the error bars blow up for both low and small k_S. The power spectrum is constrained in a window of scales (roughly $0.3 \lesssim k \lesssim 5$ Mpc^{-1}) which are mainly 1-halo dominated.

In this work, our focus is on cosmology, and we will not explore the astrophysical implications of a precision measurement of $P_{ge}(k_S)$, aside from a few brief comments as follows.

A kSZ-derived measurement of $P_{ge}(k)$ probes the distribution of electrons in halos. This is similar to galaxy-galaxy lensing, which measures the galaxy-matter power spectrum $P_{gm}(k)$, and probes the distribution of matter in halos. In galaxy-galaxy lensing, $P_{gm}(k)$ is usually modelled using the halo model, and we can do the same for $P_{ge}(k)$, writing it as the sum of 1-halo and 2-halo terms:

$$P_{ge}(k) = b_g b_e P_{mm}(k) + \frac{1}{n_g \rho_m} \int dm \, m n(M) u_g(k|m) u_e(k|m) \tag{2.73}$$

where $u_g(k|m)$ and $u_e(k|m)$ denote the galaxy and electron profiles respectively. (For more details on the halo model, see Appendix A.3.) In particular, "miscentering", or the nonzero offset between galaxies and halo centers [41], is naturally incorporated by including a galaxy profile $u_g(k|m) \neq 1$ in the model, as is already standard for galaxy-galaxy lensing.

There is a degeneracy in $P_{ge}(k_S)$ (Eq. (2.73)) between the electron profile $u_e(k|m)$ and the galaxy profile $u_g(k|m)$. One way of breaking this degeneracy is to measure the galaxy-matter power spectrum $P_{gm}(k)$ using galaxy-galaxy lensing with the same galaxy sample. The dependence on the galaxy profile largely cancels in the ratio $P_{ge}(k)/P_{gm}(k)$ (but not perfectly, since the galaxy profile can depend on halo mass). Therefore, galaxy-galaxy lensing nicely complements kSZ tomography.

KSZ tomography is also complementary to thermal SZ and X-ray observations, which also probe the distribution of electrons in halos. Relative to tSZ and X-ray, kSZ tomography is more sensitive to electrons in the outskirts of halos. This is because the kSZ profile is proportional to one power of the electron number density n_e, whereas X-ray profiles are proportional to n_e^2, and tSZ profiles are proportional to $n_e T$, where T is the gas temperature.

Normally, a measurement of a power spectrum such as $P_{ge}(k)$ can be converted (by taking a Fourier transform) to a measurement of the associated correlation function $\zeta_{ge}(r)$. This is particularly intuitive for kSZ tomography since $\zeta_{ge}(r)$ is the stacked electron profile around galaxies, which is easy to interpret. However, kSZ tomography has the unusual property that the error bars on $P_{ge}(k)$ blow up at both small and large k (Figure 2.4, right panel). In real space, this means that if we estimate $\zeta_{ge}(r)$ in r-bins, the marginalized error bars on each bin will be artificially large and highly correlated. For this reason, it seems preferable to work in Fourier space, and use the power spectrum $P_{ge}(k)$ when visualizing results or performing model fits.

2.4.5 More on the optical depth degeneracy

As previously described (§2.4.2), kSZ tomography measures the power spectra $P_{ge}(k_S)$ and $P_{gv}(k_L)$, up to an overall amplitude which can be exchanged (the "optical depth degeneracy").

If the goal of kSZ tomography is to constrain the galaxy-electron power spectrum $P_{ge}(k_S)$, then the optical depth degeneracy adds extra uncertainty to the overall amplitude, due to uncertainty in $P_{gv}(k_L)$. At back-of-the-envelope level, $P_{gv}(k_L)$ can be predicted in advance to a few percent, since cosmological parameters and galaxy bias can be measured to this accuracy. Therefore, the optical depth degeneracy should not be an issue if the kSZ tomography measurement has total SNR $\lesssim 30$, but should be taken into account above this threshold.

If the goal of kSZ tomography is to constrain cosmological modes on large scales, then the optical depth degeneracy shows up as a bias parameter $\langle \hat{v}_r \rangle = b_v v_r$ in the velocity reconstruction, which must be marginalized. For some purposes, for example the f_{NL} forecasts which we present in [146], marginalizing b_v turns out to have a minimal effect. For other purposes, for example if we want to use the overall amplitude of $P_{gv}(k_L)$ to constrain the cosmological growth rate, then the optical depth degeneracy is a serious problem, unless it can be broken somehow.

The optical depth degeneracy could be broken (for cosmological purposes) if the galaxy-electron power spectrum $P_{ge}(k_S)$ can be predicted in advance to better than a few percent. As previously noted [25, 76, 128, 185], a *necessary* condition for doing this is that the mean optical depth $\bar{\tau}$ of galaxy clusters in the sample must be determined, since $\bar{\tau}$ sets the overall amplitude of the 2-halo term in $P_{ge}(k_S)$. (This is the origin of the term "optical depth degeneracy".)

However, we would like to add the observation that predicting $\bar{\tau}$ is not sufficient for breaking the optical depth degeneracy, since kSZ tomography is mainly sensitive to $P_{ge}(k_S)$ in the 1-halo dominated regime (Figure 2.4). On these scales, $P_{ge}(k_S)$ depends not only on $\bar{\tau}$, but also on the details of the spatial profile of the free electrons, including the outskirts of the cluster where the profile is difficult to measure in X-ray or tSZ. ("Optical depth degeneracy" is not really the right term, since $\bar{\tau}$ is one of several factors which determine the small-scale power spectrum $P_{ge}(k_S)$, and we need to know the amplitude of $P_{ge}(k_S)$ on 1-halo scales to break the degeneracy.) For this reason, we suspect that breaking the kSZ optical depth degeneracy astrophysically will be very difficult.

Recently, [188] proposed breaking the kSZ optical depth degeneracy in a different way, by using an "octopolar" version of the pair sum estimator, rather than an astrophysical prior on $P_{ge}(k_S)$. We will study this proposal in the next section.

2.4.6 Including kSZ tomography in larger cosmological analyses

We have shown that the kSZ tomography statistics in [95, 88, 123, 12, 64] are "bispectrum estimation in disguise" and mathematically equivalent. In particular, bispectrum estimation can be implemented by cross-correlating the kSZ-derived velocity reconstruction $\hat{v}_r$ with the galaxy survey g on large scales.

If the kSZ-derived velocity reconstruction $\hat{v}_r$ is included in a larger analysis (either a Fisher matrix forecast or actual data analysis) with the appropriate noise power spectrum, then additional higher-point statistics will naturally arise. For example, consider a forecast with two fields: the velocity reconstruction $\hat{v}_r$ and the galaxy field δ_g. The Fisher matrix would combine contributions from the galaxy auto power spectrum $P_{gg}(k)$, the cross power spectrum $P_{g\hat{v}}(k)$ (which is really a three-point function $\langle ggT \rangle$), and the auto power spectrum $P_{\hat{v}\hat{v}}(k)$ (which is really a four-point function $\langle ggTT \rangle$). This is very similar to CMB lensing, where including the lens reconstruction $\hat{\phi}$ in a larger analysis naturally generates all "interesting" three-point and four-point statistics.

Previously, we stated that velocity reconstruction is equivalent to the other kSZ tomography statistics. This statement implicitly assumes that we cross-correlate $\hat{v}_r$ with the galaxy field g on large scales, but do not use it for anything else. However, in a scenario where $\hat{v}_r$ is included in a larger analysis involving more fields, it automatically captures multiple higher-point statistics and their covariances. For this reason, we prefer the velocity reconstruction formalism to the other approaches to kSZ tomography, at least for cosmological purposes. (For purposes of constraining astrophysics through measurements of $P_{ge}(k_S)$, the kSZ template method from [95] seems simplest.) Another technical advantage of $\hat{v}_r$ is that it makes the optical depth degeneracy easy to incorporate, by adding a nuisance parameter b_v and marginalizing it at the end.

As another example, suppose we have N tracer fields, for example corresponding to halos in different mass bins. Then we can construct N kSZ-derived velocity reconstructions $\hat{v}_r^{(i)}$, which can be cross-correlated with tracer field j, or with each other. To find the optimal weighting of all these power spectra, we need to know the N-by-N matrix $N_{v_r}^{(ij)}$ of reconstruction noise power spectra. Starting from the definition of $\hat{v}_r$ in Eq. (2.56), a short calculation gives:

$$N_{v_r}^{(ij)} = \frac{2\pi\chi_*^2}{K_*^2} \frac{A_{ij}}{A_{ii}A_{jj}} \tag{2.74}$$

where we have defined

$$A_{ij} = \int dk_S \, k_S \frac{P_{ge}^{(i)}(k_S) P_{ge}^{(j)}(k_S) P_{gg}^{(ij)}(k_S)}{P_{gg}^{(i)}(k_S) P_{gg}^{(j)}(k_S)} \left(\frac{1}{C_l^{TT,\mathrm{tot}}} \right)_{l=k_S\chi_*} \tag{2.75}$$

In principle, each velocity reconstruction has its own reconstruction bias $b_v^{(i)}$ which must be independently marginalized. The bias parameters for $i \neq j$ are different because the k_S-weighting $F(k_S)$ in Eq. (2.70) is different for each galaxy field.

As a final illustration of the power of the velocity reconstruction approach, it is straightforward to see how the optical depth degeneracy gets broken when redshift-space distortions in the galaxy field are included, as shown by [188]. Consider a Fisher matrix forecast with two 3-d fields, a galaxy field δ_g and its kSZ-derived velocity reconstruction $\hat{v}_r$. On large scales,

$$\delta_g(\mathbf{k}) = (b_g + f\mu^2)\delta_m(\mathbf{k}) + (\text{noise}) \qquad \hat{v}_r(\mathbf{k}) = \mu \frac{b_v f a H}{k} \delta_m(\mathbf{k}) + (\text{noise}) \tag{2.76}$$

where $\mu = k_r/k$ as usual. Then the cross power spectrum $P_{g\hat{v}_r}(k,\mu)$ is:

$$P_{g\hat{v}_r}(k,\mu) = \left(\mu b_g b_v + \mu^3 f b_v \right) \frac{faH}{k} P_{mm}(k) \tag{2.77}$$

The two terms have different μ dependence and their coefficients can be measured separately. In particular, the coefficient of the μ^3 term is a measurement of the parameter combination $b_v f^2 H \sigma_8^2$. Because f, H, and σ_8 are well-determined cosmological parameters, this pins down b_v and breaks the optical distance degeneracy.

Summarizing, the velocity reconstruction approach is powerful because it fully incorporates kSZ tomography into a larger analysis. It automatically "discovers" subtle effects such as the degeneracy breaking from higher-μ terms, without needing to construct the appropriate statistic (octopole pair sum) explicitly, or even needing to know in advance that it exists.

2.5 Photometric redshift errors and redshift space distortions

As previously explained, kSZ tomography requires a 3D field. If a 2D field were used, the signal-to-noise would be near-zero. A galaxy survey with photometric redshifts is an interesting intermediate case between 2D and 3D, and one may wonder whether photometric surveys are useful for kSZ tomography.

At back-of-the-envelope level, the answer can be worked out as follows. The effect of photo-z errors is to suppress power in modes of the galaxy survey whose radial wavenumber k_r is larger than $k_z = H/\sigma_z$, where σ_z is the RMS photo-z error. On the other hand, most of the SNR for kSZ tomography comes from scales $k \sim k_v$, where $k_v \sim 0.02\ h\ \mathrm{Mpc}^{-1}$ is the velocity correlation length. Therefore, photo-z errors impose a large SNR penalty in the limit $k_z \ll k_v$, and a small penalty in the limit $k_z \gg k_v$. Taking $H \sim 3 \times 10^{-4}\ h\ \mathrm{Mpc}^{-1}$ and $\sigma_z \sim 0.02$, a typical value of k_z might be $k_z \sim 0.015\ h\ \mathrm{Mpc}^{-1}$. That is, the characteristic scales k_z and k_v are usually comparable, which means that photo-z errors result in an order-one SNR penalty.

To take a concrete example, previously in §2.4.1, we found that the total SNR for kSZ tomography with CMB-S4 and LSST-Y10 was 366. This forecast includes the effect of photometric redshift errors, using machinery that will be developed in this section. If we artificially assume that LSST has no photo-z errors, then we find SNR=827. Thus, photo-z errors reduce total SNR by a factor ≈2.3 in this example.

In this section, we will also consider redshift space distortions (RSD), i.e. apparent radial displacement of galaxies due to their peculiar velocities. We will analyze the effect of photo-z errors and RSD on kSZ tomography using a common framework.

2.5.1 Modelling photo-z errors and RSD

In the next few sections, we use a bar $(\bar{\cdot})$ to denote "distorted by photo-z errors and RSD" and a tilde $(\tilde{\cdot})$ to denote "undistorted". We derive expressions for distorted power spectra such as $\bar{P}_{ge}$, in terms of their undistorted counterparts.

Considering photo-z errors first, we will assume the simplest possible model: each galaxy has an independent Gaussian redshift error with variance σ_z^2. In our halo model (Appendix A.3), this is equivalent to convolving the real-space galaxy profile $u_g(x)$ by a Gaussian radial kernel with comoving width $\Delta x = \sigma_z / H_*$. In Fourier space, this corresponds to multiplication by a Gaussian in k_r:

$$u_g(\mathbf{k}) \to W(k_r) u_g(k) \qquad \text{where } W(k_r) = \exp\left(-\frac{\sigma_z^2}{2H_*^2} k_r^2\right) \tag{2.78}$$

The profile $u_g(\mathbf{k})$ is now a function of both the length $k = |\mathbf{k}|$ and the radial component k_r of the wavenumber $\mathbf{k}$.

Note that convolving the profile $u_g(\mathbf{k}) \to W(k_r) u_g(k)$ is not the same thing as convolving the galaxy field $\delta_g(\mathbf{k}) \to W(k_r)\delta_g(\mathbf{k})$ (and the latter would be incorrect). If we write $\delta_g(\mathbf{x})$ as a sum of delta functions $n_g^{-1} \sum_i \delta^3(\mathbf{x} - \mathbf{x}_i)$, then the underlying profile u_g which determines the locations $\mathbf{x}_i$ is convolved with $W(k_r)$, but the delta functions themselves are not convolved with $W(k_r)$.

Now we analyze the effect of photo-z errors on the total galaxy power spectrum $P_{gg}^{\rm tot}$. First recall that in the undistorted case, $\widetilde{P}_{gg}^{\rm tot}$ is the sum of a 2-halo term, a 1-halo term, and a shot noise term:

$$\widetilde{P}_{gg}^{\rm tot}(k) = \widetilde{P}_{gg}^{2h}(k) + \widetilde{P}_{gg}^{1h}(k) + \frac{1}{n_g} \tag{2.79}$$

From the explicit formulas for P_{gg}^{2h} and P_{gg}^{1h} in Eqs. (A.41), (A.42), we see that if we modify the profile u_g as in Eq. (2.78), then the two-halo and one-halo terms get a factor W^2, whereas the shot noise term is unmodified:

$$\bar{P}_{gg}^{\rm tot}(k, k_r) = W(k_r)^2 \Big(\widetilde{P}_{gg}^{2h}(k) + \widetilde{P}_{gg}^{1h}(k) \Big) + \frac{1}{n_g} \qquad \text{(photo-z only)} \tag{2.80}$$

where "photo-z only" means that we have included photo-z errors but not redshift-space distortions. Note that $\bar{P}_{gg}^{\rm tot}$ is anisotropic: it is a function of both k and k_r.

We can apply a similar analysis to cross spectra of the form P_{gX}, where X could be the electron field e, the matter field m, or the velocity field v. We model these cross spectra as 1-halo and 2-halo terms (e.g. Eqs. (A.49), (A.50) for the P_{ge} case). Looking at these expressions, we see that both the 1-halo and 2-halo terms get a factor $W(k_r)$. That is, the effect of photo-z errors on cross spectra is simply:

$$\bar{P}_{gX}(k, k_r) = W(k_r) \widetilde{P}_{gX}(k) \qquad \text{(photo-z only)} \tag{2.81}$$

where $X \in \{e, m, v\}$.

In real galaxy surveys, modelling photometric errors is more complex than the simple Gaussian model considered here. We have assumed a Gaussian error distribution, whereas a real survey would have a small population of drastic outliers. We have also assumed that galaxies have independent photo-z errors, i.e. a halo with N galaxies would have redshift error $\sigma_z/\sqrt{N}$. This may be an incorrect assumption if the errors have systematic dependence, e.g. on metallicity. Exploring these issues further is outside the scope of this work.

Now we consider redshift-space distortions. On large scales, the effect of RSD is given by the Kaiser formula, which states that the galaxy profile u_g is modified as:

$$u_g(\mathbf{k}) \to \left(1 + \beta \frac{k_{Lr}^2}{k_L^2}\right) u_g(k) \tag{2.82}$$

where $\beta = f/b_g$ and $f = \partial(\log D)/\partial(\log a)$. As in the photo-z case, convolving the profile u_g is not equivalent to convolving the galaxy field δ_g. Large-scale power spectra are modified as:

$$\begin{aligned} \bar{P}_{gg}^{\rm tot}(k_L, k_{Lr}) &= \left(1 + \beta \frac{k_{Lr}^2}{k_L^2}\right)^2 \left(\widetilde{P}_{gg}^{2h}(k_L) + \widetilde{P}_{gg}^{1h}(k_L)\right) + \frac{1}{n_g} && \text{(RSD only)} \\ \bar{P}_{gX}(k_L, k_{Lr}) &= \left(1 + \beta \frac{k_{Lr}^2}{k_L^2}\right) \widetilde{P}_{gX}(k_L) && \text{(RSD only)} \end{aligned} \tag{2.83}$$

where $X \in \{e, m, v\}$ and a large scale has been assumed.

On small scales, redshift space distortions ("Fingers of God") are nonlinear and difficult to model. However, we will be interested in "near-transverse" small-scale modes where k_{Sr} is small, even though k_S is large. This is because kSZ tomography always involves a delta function of the form $\delta^3(\mathbf{k}_L + \mathbf{k}_S + \mathbf{l}/\chi_*)$ which implies $k_{Sr} = -k_{Lr}$. For near-transverse small-scale modes, we have checked with simulations that the effect of redshift space distortions is small, and we will neglect it in this work. Details of the simulations will be presented separately in [83]. Thus, on small scales we will assume:

$$\bar{P}_{gg}^{\rm tot}(k_S, k_{Sr}) = \widetilde{P}_{gg}^{\rm tot}(k_S) \qquad \bar{P}_{gX}(k_S, k_{Sr}) = \widetilde{P}_{gg}^{\rm tot}(k_S) \qquad \text{(RSD only)} \tag{2.84}$$

where $X \in \{e, m, v\}$ and a near-transverse small-scale mode has been assumed.

Summarizing this section, our model for photo-z errors and RSD's on large and small scales is defined by Eqs. (2.80), (2.81), (2.83), (2.84) above. Combining these results, our "bottom-line" model including both effects is:

$$
\begin{aligned}
\bar{P}_{gg}^{\rm tot}(k_L,k_{Lr}) &= W(k_{Lr})^2\left(1+\beta\frac{k_{Lr}^2}{k_L^2}\right)^2\Big(\widetilde{P}_{gg}^{2h}(k_L)+\widetilde{P}_{gg}^{1h}(k_L)\Big)+\frac{1}{n_g} && (2.85)\\
\bar{P}_{gg}^{\rm tot}(k_S,k_{Sr}) &= W(k_{Sr})^2\Big(\widetilde{P}_{gg}^{2h}(k_S)+\widetilde{P}_{gg}^{1h}(k_S)\Big)+\frac{1}{n_g} && (2.86)\\
\bar{P}_{gX}(k_L,k_{Lr}) &= W(k_{Lr})\left(1+\beta\frac{k_{Lr}^2}{k_L^2}\right)\widetilde{P}_{gX}(k_L) && (2.87)\\
\bar{P}_{gX}(k_S,k_{Sr}) &= W(k_{Sr})\,\widetilde{P}_{gX}(k_S) && (2.88)
\end{aligned}
$$

where $X \in \{e,m,v\}$, and $W(k_r)$ is the Fourier transformed photo-z error distribution defined in Eq. (2.78).

2.5.2 The kSZ bispectrum with photo-z's and RSD

Next we consider the combined effect of photo-z errors and RSD on previous results in the chapter. In some cases, the derivations involve repeating analysis from previous sections, which we do in streamlined form.

First we consider the kSZ bispectrum. In the squeezed limit $k_L \ll k_S$, the distorted bispectrum $\bar{B}$ can be written in any of the following forms:

$$
\begin{aligned}
\bar{B}(k_L,k_S,l,k_{Lr}) &= -\frac{K_* k_{Lr}}{\chi_*^2}\frac{\bar{P}_{gv}(k_L,k_{Lr})}{k_L}\bar{P}_{ge}(k_S,k_{Lr})\\
&= -\frac{K_* k_{Lr}}{\chi_*^2}W(k_{Lr})^2\left(1+\beta\frac{k_{Lr}^2}{k_L^2}\right)\frac{\widetilde{P}_{gv}(k_L)}{k_L}\widetilde{P}_{ge}(k_S)\\
&= W(k_{Lr})^2\left(1+\beta\frac{k_{Lr}^2}{k_L^2}\right)\widetilde{B}(k_L,k_S,l,k_{Lr}) && (2.89)
\end{aligned}
$$

generalizing Eq. (2.25) in the undistorted case.

Note that in the first line of Eq. (2.89), we have written $\bar{P}_{ge}(k_S,k_{Lr})$ on the RHS instead of $\bar{P}_{ge}(k_S,k_{Sr})$. We have used the relation $k_{Sr}=-k_{Lr}$ to eliminate k_{Sr} in favor of k_{Lr}, for notational consistency with the LHS, where only k_{Lr} appears. We will do the same elsewhere in this section without commenting on it explicitly.

The minimum-variance bispectrum estimator $\hat{\mathcal{E}}$ is given by:

$$\begin{aligned}\hat{\mathcal{E}} &= \frac{K_*}{\chi_*^2 F_{BB}} \int \frac{d^3\mathbf{k}_L}{(2\pi)^3} \frac{d^3\mathbf{k}_S}{(2\pi)^3} \frac{d^2\mathbf{l}}{(2\pi)^2} \frac{ik_{Lr}}{k_L} \frac{\bar{P}_{gv}(k_L, k_{Lr}) \bar{P}_{ge}(k_S, k_{Lr})}{\bar{P}_{gg}^{\rm tot}(k_L, k_{Lr}) \bar{P}_{gg}^{\rm tot}(k_S, k_{Lr}) C_l^{TT,\rm tot}} \\ &\quad \times \Big(\delta_g(\mathbf{k}_L) \delta_g(\mathbf{k}_S) T(\mathbf{l}) \Big) (2\pi)^3 \delta^3 \left(\mathbf{k}_L + \mathbf{k}_S + \frac{\mathbf{l}}{\chi_*} \right) \end{aligned} \tag{2.90}$$

generalizing Eq. (2.26) in the undistorted case.

As in the undistorted case, the integrals in Eq. (2.90) should be understood as running over wavenumbers $k_L \ll k_S$ which contribute significantly to the signal-to-noise (Figure 2.2). The barred power spectra on the RHS of Eq. (2.90) are given by Eqs. (2.85)–(2.88).

The Fisher matrix F_{BB} is given by any of the following forms:

$$\begin{aligned} F_{BB} &= V \int_{\mathbf{k}_L + \mathbf{k}_S + \frac{\mathbf{l}}{\chi_*} = 0} \frac{\bar{B}(k_L, k_S, l, k_{Lr})^2}{\bar{P}_{gg}^{\rm tot}(k_L, k_{Lr})\, \bar{P}_{gg}^{\rm tot}(k_S, k_{Lr})\, C_l^{TT,\rm tot}} \\ &= V \int dk_L\, dk_S\, dk_{Lr}\, \frac{k_L k_S \chi_*^2}{8\pi^3} \left(\frac{\bar{B}(k_L, k_S, l, k_{Lr})^2}{\bar{P}_{gg}^{\rm tot}(k_L, k_{Lr})\, \bar{P}_{gg}^{\rm tot}(k_S, k_{Lr})\, C_l^{TT,\rm tot}} \right)_{l = k_S \chi_*} \\ &= V \frac{K_*^2}{8\pi^3 \chi_*^2} \int dk_L\, dk_S\, dk_{Lr} \left(\frac{k_{Lr}^2}{k_L} \frac{\bar{P}_{gv}(k_L, k_{Lr})^2}{\bar{P}_{gg}^{\rm tot}(k_L, k_{Lr})} \right) \\ &\qquad \times \left(\frac{k_S \bar{P}_{ge}(k_S, k_{Lr})^2}{\bar{P}_{gg}^{\rm tot}(k_S, k_{Lr})} \right) \left(\frac{1}{(C_l^{\rm tot})_{l = k_S \chi_*}} \right) \end{aligned} \tag{2.91}$$

generalizing Eqs. (2.16), (2.27), (2.29) in the undistorted case. In the second and third lines, the integral runs over $|k_{Lr}| \le k_L \ll k_S$, with positive or negative k_{Lr}.

Recall that in the undistorted case, F_{BB} could be simplified further by doing the k_{Lr} integral, leading to the simple form of the Fisher matrix in Eq. (2.29). This does not work in the distorted case because the k_{Lr} dependence of the integrand is more complicated, due to the $\bar{P}_{gg}^{\rm tot}$ denominators.

2.5.3 Constraining astrophysics using $P_{ge}(k_S)$, with photo-z's and RSD

Previously in §2.4.4, we forecasted error bars on the galaxy-electron power spectrum $\widetilde{P}_{ge}(k_S)$ in the undistorted case. In this section we will generalize to include photo-z errors and RSD.

For simplicity, we will assume that $\bar{P}_{gv}(k_L, k_{Lr})$ is known in advance. For example, it could be given by Eq. (2.87) above, with β and $W(k_{Lr})$ assumed known. We will forecast constraints on the small-scale galaxy-electron power spectrum P_{ge} twice, with different levels of generality.

First, a general "two-variable" forecast: suppose $\bar{P}_{ge}(k_S, k_{Sr})$ is a free function of two variables (k_S, k_{Sr}), which we want to measure using kSZ tomography. We will derive an expression for the statistical error $\Delta\bar{P}_{ge}$ over a "band" β, which can be an arbitrary subset of the (k_S, k_{Sr}) plane (including positive and negative values of k_{Sr}). Following the derivation in §2.4.4, we start with Eq. (2.91) for the total SNR^2 and restrict the integrals to the band β, to obtain the SNR^2 in the band, and the bandpower error $\Delta\bar{P}_{ge} = \bar{P}_{ge}/\mathrm{SNR}_\beta$. The result is:

$$\mathrm{SNR}^2_\beta = V\frac{K_*^2}{\chi_*^2}\int_{(k_S,k_{Sr})\in\beta}\frac{k_S\,dk_S\,dk_{Sr}}{2\pi}\frac{A(k_{Sr})\bar{P}_{ge}(k_S,k_{Sr})^2}{\bar{P}^{\mathrm{tot}}_{gg}(k_S,k_{Sr})}\left(\frac{1}{C_l^{TT,\mathrm{tot}}}\right)_{l=k_S\chi_*} \tag{2.92}$$

$$\Delta\bar{P}_{ge} = \left[V\frac{K_*^2}{\chi_*^2}\int_{(k_S,k_{Sr})\in\beta}\frac{k_S\,dk_S\,dk_{Sr}}{2\pi}\frac{A(k_{Sr})}{\bar{P}^{\mathrm{tot}}_{gg}(k_S,k_{Sr})}\left(\frac{1}{C_l^{TT,\mathrm{tot}}}\right)_{l=k_S\chi_*}\right]^{-1/2} \tag{2.93}$$

where we have defined:

$$A(k_{Lr}) = \int_{|k_{Lr}|}^\infty \frac{k_L dk_L}{4\pi^2}\frac{k_{Lr}^2}{k_L^2}\frac{\bar{P}_{gv}(k_L,k_{Lr})^2}{\bar{P}^{\mathrm{tot}}_{gg}(k_L,k_{Lr})} \tag{2.94}$$

Second, we do a "one-variable" forecast, where we make the extra assumptions that $\bar{P}_{ge}(k_S, k_{Sr}) = W(k_{Sr})\widetilde{P}_{ge}(k_S)$ as in Eq. (2.88), and the photo-z error distribution $W(k_{Sr})$ is known. In the one-variable forecast, we want to measure the *undistorted* galaxy-electron power spectrum $\widetilde{P}_{ge}(k_S)$ in a k_S-bin $(k_S^{\mathrm{min}}, k_S^{\mathrm{max}})$. We specialize Eq. (2.92) by setting $\bar{P}_{ge}(k_S, k_{Sr}) = W(k_{Sr})\widetilde{P}_{ge}(k_S)$ and integrate out k_{Sr}, to obtain the SNR^2 in the k_S-bin, and the bandpower error $\Delta\widetilde{P}_{ge} = \widetilde{P}_{ge}/\mathrm{SNR}_{\mathrm{bin}}$:

$$\mathrm{SNR}^2_{\mathrm{bin}} = V\frac{K_*^2}{\chi_*^2}\int_{k_S^{\mathrm{min}}}^{k_S^{\mathrm{max}}}\frac{k_S\,dk_S}{2\pi}B(k_S)\widetilde{P}_{ge}(k_S)^2\left(\frac{1}{C_l^{TT,\mathrm{tot}}}\right)_{l=k_S\chi_*} \tag{2.95}$$

$$\Delta\widetilde{P}_{ge} = \left[V\frac{K_*^2}{\chi_*^2}\int_{k_S^{\mathrm{min}}}^{k_S^{\mathrm{max}}}\frac{k_S\,dk_S}{2\pi}B(k_S)\left(\frac{1}{C_l^{TT,\mathrm{tot}}}\right)_{l=k_S\chi_*}\right]^{-1/2} \tag{2.96}$$

Here, we have defined:

$$B(k_S) = \int_{-k_S}^{k_S} dk_{Sr}\,\frac{W(k_{Sr})^2 A(k_{Sr})}{\bar{P}^{\mathrm{tot}}_{gg}(k_S,k_{Sr})} \tag{2.97}$$

2.5.4 Constraining cosmology with photo-z's and RSD

Previously in §2.4, we argued that for cosmological applications, kSZ tomography is best formulated as a quadratic estimator $\hat{v}_r(\mathbf{k}_L)$ which reconstructs long-wavelength modes of the radial velocity field. In this section, we revisit this analysis in the presence of RSD and photo-z errors. We mention in advance that we will construct two different quadratic estimators, a "minimum variance" estimator $\hat{v}_r^{\rm mv}(\mathbf{k}_L)$ and a "robust" estimator $\hat{v}_r^{\rm rob}(\mathbf{k}_L)$.

The minimum variance estimator $\hat{v}_r^{\rm mv}(\mathbf{k}_L)$ has the best possible reconstruction noise power spectrum, but has the drawback that if $\bar{P}_{ge}(k_S, k_{Sr})$ is not known perfectly, then the reconstruction bias is a function $b_v^{\rm mv}(k_{Lr})$. This is in contrast to the undistorted case, where a single bias parameter b_v must be marginalized. The robust estimator $\hat{v}_r^{\rm rob}$ has higher noise, but its velocity bias $b_v^{\rm rob}$ is constant on large scales, under certain assumptions which we will state explicitly.

To construct the minimum variance estimator $\hat{v}_r^{\rm mv}$, we repeat the logic from §2.3.5, allowing power spectra to be anisotropic. We consider a general quadratic estimator of the form:

$$\hat{v}_r^{\rm mv}(\mathbf{k}_L) = \int \frac{d^3\mathbf{k}_S}{(2\pi)^3} \frac{d^2\mathbf{l}}{(2\pi)^2} \, W(\mathbf{k}_S, \mathbf{l}) \, \delta_g^*(\mathbf{k}_S) \, T^*(\mathbf{l}) \, (2\pi)^3 \delta^3\left(\mathbf{k}_L + \mathbf{k}_S + \frac{\mathbf{l}}{\chi_*}\right) \tag{2.98}$$

and solve for the weights $W(\mathbf{k}_S, \mathbf{l})$ which minimize the noise power spectrum

$$N_{v_r}^{\rm mv}(k_L, k_{Lr}) = \int \frac{d^3\mathbf{k}_S}{(2\pi)^3} \frac{d^2\mathbf{l}}{(2\pi)^2} \, |W(\mathbf{k}_S, \mathbf{l})|^2 \bar{P}_{gg}^{\rm tot}(k_S, k_{Sr}) C_l^{TT,{\rm tot}} \, (2\pi)^3 \delta^3\left(\mathbf{k}_L + \mathbf{k}_S + \frac{\mathbf{l}}{\chi_*}\right) \tag{2.99}$$

subject to the constraint $\langle \hat{v}_r^{\rm mv}(\mathbf{k}_L) \rangle = v_r(\mathbf{k}_L)$, which is equivalent to:

$$1 = \frac{K_*}{\chi_*^2} \int \frac{d^3\mathbf{k}_S}{(2\pi)^3} \frac{d^2\mathbf{l}}{(2\pi)^2} \, W(\mathbf{k}_S, \mathbf{l}) \bar{P}_{ge}(k_S, k_{Sr}) \, (2\pi)^3 \delta^3\left(\mathbf{k}_L + \mathbf{k}_S + \frac{\mathbf{l}}{\chi_*}\right) \tag{2.100}$$

This constrained minimization problem can be solved by a short calculation involving Lagrange multipliers. The minimum variance estimator $\hat{v}_r^{\rm mv}(\mathbf{k}_L)$ and its noise power spectrum $N_{v_r}^{\rm mv}(k_L, k_{Lr})$ are found to be:

$$\hat{v}_r^{\rm mv}(\mathbf{k}_L) = \frac{K_*}{\chi_*^2} N_{v_r}^{\rm mv} \int \frac{d^3\mathbf{k}_S}{(2\pi)^3} \frac{d^2\mathbf{l}}{(2\pi)^2} \frac{\bar{P}_{ge}(k_S, k_{Sr})}{\bar{P}_{gg}^{\rm tot}(k_S, k_{Sr}) C_l^{\rm tot}} \delta_g(\mathbf{k}_S)^* T(\mathbf{l})^* \, (2\pi)^3 \delta^3\left(\mathbf{k}_L + \mathbf{k}_S + \frac{\mathbf{l}}{\chi_*}\right) \tag{2.101}$$

$$\begin{aligned}
N^{\rm mv}_{v_r}(k_L,k_{Lr}) &= \frac{\chi_*^4}{K_*^2}\left[\int\frac{d^3\mathbf{k}_S}{(2\pi)^3}\,\frac{d^2\mathbf{l}}{(2\pi)^2}\,\frac{\bar P_{ge}(k_S,k_{Sr})^2}{\bar P^{\rm tot}_{gg}(k_S,k_{Sr})C_l^{TT,\rm tot}}\,(2\pi)^3\delta^3\left(\mathbf{k}_L+\mathbf{k}_S+\frac{\mathbf{l}}{\chi_*}\right)\right]^{-1} \\
&= \frac{\chi_*^2}{K_*^2}\left[\int\frac{k_S\,dk_S}{2\pi}\,\left(\frac{\bar P_{ge}(k_S,k_{Lr})^2}{\bar P^{\rm tot}_{gg}(k_S,k_{Lr})C_l^{TT,\rm tot}}\right)_{l=k_S\chi_*}\right]^{-1} \qquad (2.102)
\end{aligned}$$

The final result is very similar to the quadratic estimator derived previously in the undistorted case in Eq. (2.56) above. Note that the reconstruction noise power spectrum is anisotropic in the presence of photo-z errors. We have written it as $N_{v_r}(k_L,k_{Lr})$, but we note that it only depends on k_{Lr}.

Now we analyze the effect of the optical depth degeneracy, by assuming that the estimator $\hat v_r^{\rm mv}$ is defined using fiducial power spectrum $\bar P^{\rm fid}_{ge}(k_S,k_{Sr})$, which may differ from the true power spectrum $\bar P^{\rm true}_{ge}(k_S,k_{Sr})$. A short calculation shows that $\langle \hat v_r^{\rm mv}(\mathbf{k}_L)\rangle = b_v^{\rm mv}(k_{Lr})v_r(\mathbf{k}_L)$, where the velocity reconstruction bias $b_v^{\rm mv}(k_{Lr})$ is given by:

$$b_v^{\rm mv}(k_{Lr}) = \frac{\int dk_S\,F(k_S,k_{Lr})\bar P^{\rm true}_{ge}(k_S,k_{Lr})}{\int dk_S\,F(k_S,k_{Lr})\bar P^{\rm fid}_{ge}(k_S,k_{Lr})} \qquad (2.103)$$

where

$$F(k_S,k_{Lr}) = \left(\frac{k_S\bar P^{\rm fid}_{ge}(k_S,k_{Lr})}{\bar P^{\rm tot}_{gg}(k_S,k_{Lr})C_l^{TT,\rm tot}}\right)_{l=k_S\chi_*} \qquad (2.104)$$

We see that the velocity bias is not constant on large scales: it depends on the radial component k_{Lr} of the wavenumber $\mathbf{k}_L$. This is a potential problem for cosmological parameter constraints, since it may require introducing many nuisance parameters in order to parameterize the velocity bias $b_v^{\rm mv}(k_{Lr})$.

2.5.5 A quadratic estimator which is robust to photo-z errors

We now construct a "robust" velocity reconstruction estimator $\hat v_r^{\rm rob}$ whose reconstruction bias b_v is constant on large scales, as in the undistorted case. The construction is simple: we define

$$\hat v_r^{\rm rob}(\mathbf{k}_L) = W(k_{Lr})^{-1}\hat v_r^{\rm und}(\mathbf{k}_L) \qquad (2.105)$$

where $\hat v_r^{\rm und}(\mathbf{k}_L)$ is the *undistorted* quadratic estimator, defined by:

$$\hat v_r^{\rm und}(\mathbf{k}_L) = N^{\rm und}_{v_r}\frac{K_*}{\chi_*^2}\int\frac{d^3\mathbf{k}_S}{(2\pi)^3}\,\frac{d^2\mathbf{l}}{(2\pi)^2}\,\frac{\widetilde P_{ge}(k_S)}{\widetilde P^{\rm tot}_{gg}(k_S)C_l^{TT,\rm tot}}\Big(\delta_g^*(\mathbf{k}_S)T^*(\mathbf{l})\Big)(2\pi)^3\delta^3\left(\mathbf{k}_L+\mathbf{k}_S+\frac{\mathbf{l}}{\chi_*}\right) \qquad (2.106)$$

$$N_{v_r}^{\rm und}(k_L) \;=\; \frac{\chi_*^2}{K_*^2} \left[\int \frac{k_S\, dk_S}{2\pi} \left(\frac{\widetilde P_{ge}(k_S)^2}{\widetilde P_{gg}^{\rm tot}(k_S) C_l^{TT,{\rm tot}}} \right)_{l=k_S\chi_*} \right]^{-1} \tag{2.107}$$

This is the same as the previous definition in Eq. (2.56), but we have rewritten it to emphasize that it is defined using undistorted power spectra $\widetilde P_{gg}^{\rm tot}$, $\widetilde P_{ge}$ throughout.

With the prefactor $W(k_{Lr})^{-1}$ in Eq. (2.105), the robust estimator $\hat v_r^{\rm rob}$ is an unbiased reconstruction in the distorted case, i.e. $\langle \hat v_r^{\rm rob}(\mathbf{k}_L)\rangle = v_r(\mathbf{k}_L)$. This statement is not obvious, but follows from a short calculation using Eqs. (2.86), (2.88), (2.100).

Another short calculation shows that the reconstruction noise of the robust estimator is:

$$N_{v_r}^{\rm rob}(k_L, k_{Lr}) = \left(\frac{N_{v_r}^{\rm und}(k_L)}{W(k_{Lr})} \right)^2 \frac{K_*^2}{\chi_*^2} \int \frac{k_S\, dk_S}{2\pi} \left(\frac{\widetilde P_{ge}(k_S)^2 \bar P_{gg}^{\rm tot}(k_S, k_{Lr})}{\widetilde P_{gg}^{\rm tot}(k_S)^2 C_l^{TT,{\rm tot}}} \right)_{l=k_S\chi_*} \tag{2.108}$$

where $N_{v_r}^{\rm und}(k_L)$ is the undistorted reconstruction noise in Eq. (2.107).

Next we compute the reconstruction bias b_v for the robust estimator. Suppose the velocity reconstruction $\hat v_r^{\rm rob}(\mathbf{k}_L)$ is defined using fiducial galaxy-electron power spectrum $\bar P_{ge}^{\rm fid}(k_S, k_{Sr}) = W_{\rm fid}(k_{Sr}) \widetilde P_{ge}^{\rm fid}(k_S)$, and the true power spectrum is given by $\bar P_{ge}^{\rm true}(k_S, k_{Sr}) = W_{\rm true}(k_{Sr}) \widetilde P_{ge}^{\rm true}(k_S)$. Then a short calculation shows that $\langle \hat v_r^{\rm rob}(\mathbf{k}_L)\rangle = b_v^{\rm rob}(k_{Lr}) v_r(\mathbf{k}_L)$, where the velocity reconstruction bias $b_v^{\rm rob}(k_{Lr})$ is given by:

$$b_v^{\rm rob}(k_{Lr}) = \frac{W_{\rm true}(k_{Lr})}{W_{\rm fid}(k_{Lr})}\, b_v^{\rm und} \tag{2.109}$$

where $b_v^{\rm und}$ is the undistorted bias parameter, defined previously in Eq. (2.70) and independent of $\mathbf{k}_L$.

From Eq. (2.109), we see that the velocity reconstruction bias $b_v^{\rm rob}$ is independent of $\mathbf{k}_L$ if the photometric error distribution $W(k_{Lr})$ is well-characterized, so that $W_{\rm fid}(k_{Lr}) = W_{\rm true}(k_{Lr})$ to a good approximation. If $W(k_{Lr})$ is poorly characterized, then more nuisance parameters would be necessary, to model uncertainty in the photometric error distribution.

This situation is qualitatively similar to weak gravitational lensing, where photo-z errors must be well-characterized to avoid introducing extra nuisance parameters. Because weak lensing is of central importance for upcoming large-scale structure surveys, photometric redshift errors are expected to be precisely characterized. Therefore, it seems reasonable to assume that in the kSZ context, photometric redshift errors will also be characterized well enough that the bias $\hat{v}_r^{\mathrm{rob}}$ is constant on large scales. In the context of a real photometric survey such as LSST, this assumption should probably be revisited using detailed survey-specific modeling, but this is outside the scope of this work. Our analysis here is simply to show that there is no "showstopper" problem in doing kSZ tomography using photometric catalogs.

In summary, we have now shown how to modify the minimum-variance velocity reconstruction $\hat{v}_r^{\mathrm{mv}}(\mathbf{k}_L)$, obtaining a "robust" reconstruction $\hat{v}_r^{\mathrm{rob}}(\mathbf{k}_L)$ whose bias b_v^{rob} is constant on large scales. This construction depends on the following assumptions. First, the distorted and undistorted galaxy-electron power spectra must be related by $\bar{P}(k_S, k_{Sr}) = W(k_{Sr})\widetilde{P}(k_S)$. Second, the photometric redshift error distribution $W(k_{Sr})$ must be well-characterized.

In principle, the robust estimator has higher reconstruction noise than the minimum-variance estimator. However, the two are nearly equal in practice. For example, for LSSTY10 × S4, the noise curves are identical at large scales and at most 3% different on small scales. In this work, we have used minimum-variance noise curves in forecasts (since it makes no practical difference), but in real data analysis we recommend using the robust estimator.

Throughout this section, we have constructed reconstruction estimators $\hat{v}_r(\mathbf{k}_L)$ for the radial velocity. As in the undistorted case, a radial velocity reconstruction $\hat{v}_r$ can be converted to either a reconstruction of the full velocity field $\hat{v}(\mathbf{k}_L) = -i\mu^{-1}\hat{v}_r(\mathbf{k}_L)$, or the density field $\hat{\delta}(\mathbf{k}_L) = \mu^{-1}(k_L/faH)\hat{v}_r(\mathbf{k}_L)$, with noise power spectra

$$N_{vv}(\mathbf{k}_L) = \mu^{-2} N_{v_r}(k_L) \qquad\qquad N_{\delta\delta}(\mathbf{k}_L) = \mu^{-2}\left(\frac{k_L}{faH}\right)^2 N_{v_r}(k_L) \tag{2.110}$$

2.6 Discussion

We have shown that several proposed kSZ tomography statistics are "bispectrum estimation in disguise" and mathematically equivalent. Among these statistics, the kSZ-derived radial velocity quadratic estimator $\hat{v}_r$ is particularly convenient, since it naturally generates additional higher-point statistics. For example, an auto correlation of the form $\langle \hat{v}_r(\mathbf{k})^* \hat{v}_r(\mathbf{k}) \rangle$ is a four-point estimator in the underlying CMB and galaxy fields.

This perspective puts kSZ tomography on the same footing as more familiar higher-point estimators in cosmology, making its properties more transparent. For example, the degeneracy breaking mechanism recently proposed in [188] appears "automatically" when

$\hat{v}_r$ is included in a Fisher matrix forecast which also includes a galaxy survey with redshift-space distortions.

There are two kSZ tomography observables. First, kSZ tomography measures the small-scale galaxy-electron power spectrum $P_{ge}(k_S)$ on 1-halo dominated scales. This measurement probes the distribution of electrons in halos and will be interesting to combine with other probes, especially galaxy-galaxy lensing, thermal SZ, and X-ray observations.

Second, kSZ tomography measures 3-d cosmological modes on large scales, with lower noise than can be achieved with galaxy surveys. Thus, even though the kSZ appears on small scales in the CMB, its cosmological constraining power arises from its ability to constrain large-scale physics.

In this work, we have sometimes made simplifications or approximations which could be explored in more detail in future work:

- The simplified "snapshot" geometry from §2.1 neglects evolution along the lightcone, and makes the flat-sky approximation.
- We have assumed that the kSZ anisotropy is sourced by the large-scale velocity field v_r. This is an approximation to a gauge-invariant quantity, namely the CMB dipole in the electron rest frame. On Hubble scales this approximation may become inaccurate.
- We used symmetry arguments to show that the kSZ bispectrum is unbiased by contributions from other CMB secondaries. These symmetry arguments break down in the presence of sky cuts or evolution along the lightcone.
- We have neglected terms which are subleading in the squeezed limit $k_L \ll k_S$, but such terms may become important at high SNR.
- We have not included all non-Gaussian contributions to higher N-point functions. For example, our forecasts assume that the quadratic estimator $\hat{v}_r$ has auto correlations of the form $\langle \hat{v}_r(\mathbf{k})^* \hat{v}_r(\mathbf{k}) \rangle \propto (P_{v_r}(k) + N_{v_r}(k))$. This is an approximation to a four-point function of type $\langle \delta_g \delta_g T T \rangle$. Similar approximations are often made in the context of CMB lens reconstruction. We are in the process of using N-body simulations to study this issue systematically [83].
- Our model for photometric errors assumes that the error distribution is known perfectly, that drastic outliers are negligible, and that every galaxy has an independent photo-z error.

Acknowledgements

Research at Perimeter Institute is supported by the Government of Canada through Industry Canada and by the Province of Ontario through the Ministry of Research & Innovation. MSM is grateful to Perimeter for supporting visits during which this work was carried out. KMS was supported by an NSERC Discovery Grant and an Ontario Early Researcher Award. SF was supported by Miller and BCCP fellowships at the University of California, Berkeley. MCJ is supported by the National Science and Engineering Research Council through a Discovery grant. We thank Nick Battaglia, Neal Dalal, Jo Dunkley, Emmanuel Schaan, Marcel Schmittfull, Urovs Seljak, David Spergel and Martin White for useful discussions and Emanuela Dimastrogiovanni for collaboration during the early stages of this work.

Chapter 3

Exploring kSZ velocity reconstruction

The cosmic microwave background (CMB) has been a gold mine of cosmological information. So far, the constraining power of the CMB has come mainly from "primary" anisotropy from the last scattering surface (which dominates at angular wavenumbers $l \lesssim 2000$) and gravitational lensing (which dominates at $2000 \lesssim l \lesssim 4000$). On even smaller scales ($l \gtrsim 4000$), the CMB temperature is dominated by the kinetic Sunyaev-Zeldovich (kSZ) effect: Doppler shifting of CMB photons by free electrons in the late universe.

The kSZ effect has been detected in cross-correlation with large-scale structure, with the latest measurements approaching 10σ [88, 159, 165, 63, 94, 58, 166], and upcoming experiments such as Simons Observatory [4] should make percent-level measurements in the next few years. In anticipation of these upcoming measurements, it is very interesting to ask how best to constrain cosmological parameters with the kSZ effect, possibly in cross-correlation with large-scale structure.

A variety of kSZ-sensitive statistics have been proposed (e.g. [67, 60, 95, 88, 123, 12, 182, 64, 183] and references therein), but in this work we focus on the velocity reconstruction estimator $\hat{v}_r$ from [64].[1] Velocity reconstruction is a particularly convenient kSZ estimator for cosmological applications, since it is straightforward to include $\hat{v}_r$ in analyses

---

[1] The term "velocity reconstruction" is sometimes used to refer to two different statistics. First, the quadratic estimator $\hat{v}_r$ which reconstructs velocity modes from the kSZ and large-scale structure. Second, a linear operation which reconstructs velocity modes from a galaxy catalog (with no kSZ input, although this

involving multiple large-scale structure fields, or incorporate complications like redshift-space distortions (RSD) [183].

The kSZ velocity reconstruction $\hat{v}_r$ is a quadratic estimator which reconstructs the large-scale radial velocity $\hat{v}_r(\mathbf{k}_L)$ from small-scale modes of a galaxy field $\delta_g(\mathbf{k}_S)$ and CMB temperature $T(\mathbf{l})$. (For the precise definition, see §3.4.) The scales involved are roughly $k_L \sim 10^{-2}$ Mpc^{-1}, $k_S \sim 1$ Mpc^{-1}, and $l_{\rm CMB} \sim 5000$. Thus, the underlying signal for the reconstruction is the velocity field on large scales where it can be modelled very accurately, but the reconstruction noise is hard to model, since the noise is derived from nonlinear scales.

KSZ velocity reconstruction is interesting for cosmology because its noise power spectrum is smaller on large scales than previously known methods, such as galaxy surveys, as we will explain in the next few paragraphs. First, we note that on large scales, linear theory is a good approximation, and radial velocity v_r, velocity v, and matter overdensity δ_m are related in Fourier space by:

$$v_r(\mathbf{k}_L) = \mu v(\mathbf{k}_L) = \mu \frac{faH}{k_L} \delta_m(\mathbf{k}_L) \tag{3.1}$$

Here, $f = \partial \log D / \partial \log a$ is the usual RSD parameter, and $\mu = k_{Lr}/k_L$ is the cosine of the angle between the Fourier mode $\mathbf{k}_L$ and the line of sight. Therefore, by applying appropriate factors of μ and (faH/k), the radial velocity reconstruction $\hat{v}_r$ may be viewed as a reconstruction of v or δ_m. This allows us to compare the noise power spectrum of kSZ velocity reconstruction to other LSS observables, which measure the density field δ_m.

To take a concrete example, consider a galaxy survey, which measures the density field δ_m with a noise power spectrum $N(k) = b_g^{-2} n_g^{-1}$ which is constant on large scales. The noise power spectrum of the kSZ velocity reconstruction $\hat{v}_r(\mathbf{k}_L)$ is more complicated, but for now we just note that $N_{v_r}(k_L)$ is also constant on large scales. (The noise power spectrum N_{v_r} will be discussed in depth in §3.4, §3.5.) To compare the two, we convert the kSZ velocity reconstruction to a reconstruction of δ_m using Eq. (3.1), obtaining noise power spectrum:

$$N_{\delta_m}^{\rm kSZ}(\mathbf{k}_L) = \left(\frac{k_L}{\mu faH} \right)^2 N_{v_r}(\mathbf{k}_L) \tag{3.2}$$

Due to the factor k_L^2 on the RHS, the kSZ-derived reconstruction of the large-scale modes

---

operation is an ingredient in a kSZ stacking analysis [165, 166]). In this chapter, “velocity reconstruction” always refers to the kSZ quadratic estimator $\hat{v}_r$.

has *parametrically lower noise* than the galaxy field.[2] This low-noise large-reconstruction has several potential applications (e.g. [143, 205, 193, 45, 98, 49]), but we will concentrate on the cosmological parameter f_{NL}. In [147, 49], it was shown that adding kSZ data to an analysis of galaxy clustering can significantly improve f_{NL} constraints, relative to the galaxies alone. In this forecast, the f_{NL} sensitivity arises from non-Gaussian bias [56, 181] in the galaxy survey. The field v_r is not directly sensitive to f_{NL}, but including it helps improve the f_{NL} constraint, using the idea of sample variance cancellation [173].

Summarizing, kSZ velocity reconstruction estimator is emerging as an interesting new tool for constraining cosmology, using upcoming kSZ and large-scale structure data. However, there is currently a major caveat. As mentioned above, the reconstruction $\hat{v}_r$ is derived from LSS modes on scales $k_S \sim 1$ Mpc^{-1}, and therefore the reconstruction noise depends on statistics of nonlinear modes which are difficult to model. Forecasting work so far (e.g. [64, 183, 147]) has used simple analytic models which approximate the true statistics of the reconstruction noise. The purpose of this work is to assess the validity of these approximations, by applying kSZ velocity reconstruction to N-body simulations.

In the bullet points below, we separate the issues by dissecting the different approximations which are usually made, and summarize the main results of this chapter.

- In [183] it was argued that the kSZ-derived velocity reconstruction $\hat{v}_r(\mathbf{k})$ is an estimator of the true radial velocity on large scales:

  $$\hat{v}_r(\mathbf{k}) = b_v v_r^{\text{true}}(\mathbf{k}) + (\text{reconstruction noise}) \tag{3.3}$$

  where the reconstruction noise is uncorrelated with v_r^{true}, and the bias b_v is constant on large scales. The value of b_v depends on the mismatch between the true small-scale galaxy-electron power spectrum $P_{ge}(k_S)$ and the fiducial spectrum $P_{ge}^{\text{fid}}(k_S)$ used to construct the quadratic estimator.

  In this chapter, we will confirm all of these "map-level" properties of the velocity reconstruction estimator $\hat{v}_r$ using N-body simulations. We also find that, although b_v is constant on the largest scales, it starts to acquire scale dependence at a surprisingly small value of k (see Figure 3.3).

- Moving from "map level" to power spectra, we next consider the power spectrum of the reconstruction noise. In [183], an analytic model was given for the noise power

---

[2] Loophole: This is only true for modes where $|\mu| = |k_r|/k$ is not too small. For modes with small μ, the factor μ^{-2} in Eq. (3.2) acts as an SNR penalty, and "transverse" modes with $\mu = 0$ cannot be reconstructed at all from the kSZ.

spectrum, which makes the approximation that the small-scale galaxy field $\delta_g(\mathbf{k}_S)$ and the small-scale CMB $T(\mathbf{l})$ are uncorrelated. This is a good approximation if the CMB modes are noise-dominated, but potentially dubious if the CMB is kSZ-dominated. In this chapter, we will denote the reconstruction noise power spectrum computed in this approximation by $N_{v_r}^{(0)}(\mathbf{k}_L)$, and call it the "kSZ $N^{(0)}$-bias". This terminology is intended to emphasize an analogy with CMB lensing which will be explained later in the chapter.

We compare the reconstruction noise power spectrum in our simulations with the kSZ $N^{(0)}$-bias, and find a significant discrepancy, even in the limit $\mathbf{k}_L \to 0$. For the fiducial survey parameters used in this chapter (see §3.2), the $N^{(0)}$-bias underpredicts the true reconstruction noise power spectrum by a factor 2–3. This turns out to have a small effect on the bottom-line constraint on f_{NL}, but this may not be the case for other choices of survey parameters (CMB noise, galaxy density, redshift, etc.) This result shows that the $N^{(0)}$-bias proposed in [183] as a model for reconstruction noise is sometimes incomplete.

- Motivated by this discrepancy between theory and simulation, we revisit the calculation of the kSZ reconstruction noise, and find additional terms. The new terms are analogous to the $N^{(1)}$-bias [109] and $N^{(3/2)}$-bias [40] in CMB lensing, and are obtained from a six-point halo model calculation. We calculate the new terms under some simplifying approximations, and find that they explain the excess noise seen in simulations (see Figure 3.6). The new terms are algebraically simple enough that including them in future forecasts or data analysis should be straightforward (see Eq. (3.82)).

- Moving from the reconstruction noise power spectrum to higher-point statistics, we next study the question of whether reconstruction noise is a Gaussian field. As a simple test for Gaussianity, we compute the correlation matrix between k-bands of the estimated reconstruction noise power spectrum (which would be the identity matrix for a Gaussian field). The bandpower covariance determines statistical errors on parameters derived from power spectra. In particular, the f_{NL} Fisher matrix forecasts from [147] implicitly assume that bandpower correlations are small, and we would like to test this assumption.

  In simulation, we find that bandpower correlations are small on the very large scales which dominate f_{NL} constraints, but increase rapidly with k, and become order-one at $k \sim 0.03$ Mpc^{-1}.

- Putting everything together, we develop an "end-to-end" pipeline which recovers f_{NL}

from a simulated galaxy catalog and kSZ map. The pipeline applies the quadratic estimator $\hat{v}_r$, then performs MCMC exploration of the posterior likelihood for parameters (f_{NL}, b_g, b_v), given realizations of the galaxy field δ_g and velocity reconstruction $\hat{v}_r$. When deriving the posterior likelihood, we assume that the reconstruction noise power spectrum is equal to the $N^{(0)}$-bias, and that the reconstruction noise is a Gaussian field. Based on previous bullet points, these approximations are imperfect, but their impact on parameter constraints should be small, and therefore it seems plausible that the posterior likelihood will produce valid parameter constraints.

We find that kSZ velocity reconstruction works! We run the pipeline on simulations with both zero and nonzero f_{NL}, in a noise regime where sample variance cancellation is important, and demonstrate that it recovers unbiased f_{NL} estimates, with statistical errors consistent with Fisher matrix forecasts.

These results largely serve as zeroth-order validation of the basic kSZ velocity reconstruction framework from [64, 183] and f_{NL} forecasts from [147], with the addition of new terms in the reconstruction noise. This initial exploratory study can be extended in several interesting directions; see §3.7 for systematic discussion.

To test kSZ velocity reconstruction as accurately as possible, we want to use as much simulation volume as we can. For this reason, we use collisionless N-body simulations, which have much lower computational cost per unit volume than hydrodynamical simulations. We approximate the electron overdensity field by the dark matter field ($\delta_e = \delta_m$), and approximate the galaxy catalog by a halo catalog ($\delta_g = \delta_h$). These are crude approximations, and in particular our approximation $\delta_e = \delta_m$ means that we overpredict the galaxy-electron power spectrum $P_{ge}(k_S)$ by an order-one factor. However, in this chapter our goal is to compare theory and simulation, and the level of agreement is unlikely to depend on details of small-scale power spectra, as long as the analysis is self-consistent. Since we use collisionless simulations, we can also leverage the high-resolution Quijote public simulations [199] with a total volume of 100 Gpc^3 and $f_{NL} = 0$. For $f_{NL} \neq 0$, we run `GADGET-2` [187] with a custom initial condition generator.

This chapter builds on several papers which explore the effects of primordial non-Gaussianity in N-body simulations, e.g. [56, 62, 158, 86, 82, 201, 87, 168, 22, 31] and references therein. The new ingredient is the kSZ velocity reconstruction $\hat{v}_r$. To our knowledge, there is only one previous paper which explores kSZ velocity reconstruction in simulations [46]. There, a large correlation was found between the reconstructed radial velocity $\hat{v}_r$ and the true radial velocity $v_r^{\rm true}$, but the reconstruction noise was not compared with theory, and non-Gaussian simulations were not studied.

This chapter is organized as follows. In §3.2, we describe our simulation pipeline for generating large-scale structure and kSZ realizations. In §3.3, we show large-scale structure and CMB power spectra from our simulations. In §3.4, we study the kSZ velocity reconstruction estimator $\hat{v}_r$ in detail, and characterize key properties such as bias, noise, and non-Gaussian bandpower covariance. In §3.5, we calculate kSZ reconstruction noise in the halo model, and find new terms $N^{(1)}$ and $N^{(3/2)}$ which agree with the simulations. We present our MCMC-based f_{NL} pipeline in §3.6, and conclude in §3.7. The code for this work can be accessed at `https://github.com/utkarshgiri/kineticsz`.

3.1 Preliminaries and notation

3.1.1 "Snapshot" geometry

Following [183], we use the following simplified "snapshot" geometry throughout the chapter. We take the universe to be a periodic 3-d box with comoving side length $L = 1\ h^{-1}$ Gpc and volume $V = L^3$, "snapshotted" at redshift $z_* = 2$, corresponding to comoving distance $\chi_* \approx 5200$ Mpc. The notation $(\cdot)_*$ means "evaluated at redshift z_*", e.g. H_* is the Hubble expansion rate at z_*, and χ_* is comoving distance between $z = 0$ and $z = z_*$.

Three-dimensional large-scale structure fields, such as the galaxy overdensity $\delta_g(\mathbf{x})$, are defined on a 3-d periodic box of comoving side length L. Two-dimensional angular fields, such as the CMB $T(\boldsymbol{\theta})$, are defined on a 2-d periodic flat sky with angular side length L/χ_*. We define line-of-sight integration by projecting the 3-d box onto the xy-face of the cube, with a factor $1/\chi_*$ to convert from spatial to angular coordinates. We denote transverse coordinates of the box by (x, y), but denote the radial coordinate by r (not z, to avoid notational confusion with redshift). We denote a unit three-vector in the radial direction by $\hat{\mathbf{r}}$, and denote the transverse part of a three-vector $\mathbf{x}$ by $\mathbf{x}_\perp$. Thus a galaxy at spatial location $\mathbf{x}$ appears at angular sky location $\boldsymbol{\theta} = \mathbf{x}_\perp/\chi_*$.

In the full lightcone geometry, the kSZ temperature anisotropy is given by a line-of-sight integral $T(\boldsymbol{\theta}) = \int dr\, K(r)\, (\hat{\mathbf{r}} \cdot \mathbf{q}_e(\boldsymbol{\theta}, r))$, where $\mathbf{q}_e = (1 + \delta_e)\mathbf{v}_e$ is the dimensionless electron momentum field, and $K(\cdot)$ is the kSZ radial weight function:

$$K(z) = -T_{\rm CMB}\, \sigma_T\, n_{e,0}\, x_e(z)\, e^{-\tau(z)}\, (1 + z)^2 \tag{3.4}$$

In the snapshot geometry, this line-of-sight integral becomes:

$$T_{\rm kSZ}(\boldsymbol{\theta}) = K_* \int_0^L dr\, \Big(\hat{\mathbf{r}} \cdot \mathbf{q}_e(\chi_* \boldsymbol{\theta} + r\hat{\mathbf{r}})\Big) \tag{3.5}$$

3.1.2 Fourier conventions

Our Fourier conventions for a 3-d field $f(\mathbf{x})$ with power spectrum $P(k)$ are:

$$f(\mathbf{k}) = \int d^3\mathbf{x}\, f(\mathbf{x}) e^{-i\mathbf{k}\cdot\mathbf{x}} \qquad \langle f(\mathbf{k}) f(\mathbf{k}')^* \rangle = P(k)(2\pi)^3 \delta^3(\mathbf{k}-\mathbf{k}') \tag{3.6}$$

In a finite pixelized 3-d volume V, we use Fourier conventions:

$$f(\mathbf{k}) = \frac{V}{N_{\rm pix}} \sum_{\mathbf{x}} f(\mathbf{x}) e^{-i\mathbf{k}\cdot\mathbf{x}} \qquad \Big\langle f(\mathbf{k}) f(\mathbf{k}')^* \Big\rangle = V P(k) \delta_{\mathbf{k}\mathbf{k}'} \tag{3.7}$$

With these conventions, the radial velocity $v_r(\mathbf{k})$ and matter overdensity $\delta_m(\mathbf{k})$ are related in linear theory by:

$$v_r(\mathbf{k}) = i k_r \left(\frac{faH}{k^2} \right) \delta_m(\mathbf{k}) \tag{3.8}$$

Here, $f(z) = (\partial \log D(z) / \partial \log a)$, where $D(z)$ is the growth function.

Similarly, our Fourier conventions for a 2-d flat-sky field $f(\boldsymbol{\theta})$ with angular power spectrum C_l are:

$$f(\mathbf{l}) = \int d^2\boldsymbol{\theta}\, f(\boldsymbol{\theta}) e^{-i\mathbf{l}\cdot\boldsymbol{\theta}} \qquad \Big\langle f(\mathbf{l}) f(\mathbf{l}')^* \Big\rangle = C_l (2\pi)^2 \delta^2(\mathbf{l}-\mathbf{l}') \tag{3.9}$$

In finite pixelized 2-d area A this becomes:

$$f(\mathbf{l}) = \frac{A}{N_{\rm pix}} \sum_{\boldsymbol{\theta}} f(\boldsymbol{\theta}) e^{-i\mathbf{l}\cdot\boldsymbol{\theta}} \qquad \Big\langle f(\mathbf{l}) f(\mathbf{l}')^* \Big\rangle = A C_l \delta_{\mathbf{l}\mathbf{l}'} \tag{3.10}$$

In our code, we often represent 2-d fields using dimensionful coordinates $\mathbf{x}_\perp = \chi_* \boldsymbol{\theta}$ and $\mathbf{k}_\perp = \mathbf{l}/\chi_*$, which eliminates factors of χ_* in some equations. For example, the line of sight integral (3.5) becomes $T(\mathbf{x}_\perp) = K_* \int dr\, (\hat{\mathbf{r}} \cdot q_e(\mathbf{x}_\perp + r\hat{\mathbf{r}}))$.

3.1.3 Primordial non-Gaussianity and halo bias

Single-field slow-roll inflation is arguably the simplest model of the early universe. In this model, the initial curvature perturbation ζ is a Gaussian field to an excellent approximation [2, 138]. This is not the case in many alternative models, and searching for primordial non-Gaussianity (deviations from Gaussian initial conditions) is a powerful probe of physics of the early universe. A wide variety of observationally distinguishable non-Gaussian models has been proposed (see e.g. [8] and references therein).

In this chapter, we will concentrate on "local-type" non-Gaussianity, in which the initial curvature perturbation ζ is of the form:

$$\zeta(\mathbf{x}) = \zeta_G(\mathbf{x}) + \frac{3}{5} f_{NL} \big(\zeta_G(\mathbf{x})^2 - \langle \zeta_G^2 \rangle \big) \tag{3.11}$$

where ζ_G is a Gaussian field, and f_{NL} is a cosmological parameter to be constrained from observations. Local-type non-Gaussianity is fairly generic in multifield early universe models, such as curvaton models [125, 134, 133], or modulated reheating models [70, 110]. Conversely, there are theorems [138, 52] which show that $f_{NL} = 0$ in single-field early universe models, i.e. models in which a single field both dominates the stress-energy of the early universe, and determines the initial curvature perturbation.

In a pioneering paper [56], Dalal et al showed that large-scale clustering of dark matter halos depends sensitively on f_{NL}. More precisely, the halo bias b_h is scale dependent on large scales, with functional form:

$$b_h(k) = b_g + f_{NL} \frac{b_{ng}}{\alpha(k,z)} \tag{3.12}$$

where b_g is the Gaussian (scale-independent) bias, and:

$$\alpha(k,z) \equiv \frac{2k^2 T(k) D(z)}{3 \Omega_m H_0^2} \tag{3.13}$$

The quantity $\alpha(k,z)$ relates the matter overdensity $\delta_m(\mathbf{k},z)$ to initial curvature $\zeta(\mathbf{k})$ in linear theory: $\delta_m(\mathbf{k},z) = (3/5)\alpha(k,z)\zeta(\mathbf{k})$. On large scales $k \to 0$, $\alpha(k,z)$ is proportional to k^2, leading to an $f_{NL}k^{-2}$ term in the halo bias. Thanks to this term, even small values of f_{NL} can produce large observable effects on large scales. Although current large-scale structure constraints on f_{NL} [44] are not competitive with CMB constraints [8], future LSS experiments which probe large volumes and high redshifts should be comparable or better than the CMB [43, 59, 66, 10, 73, 167].

The parameter b_{ng} in Eq. (3.12) is given exactly by [181, 21]:

$$b_{ng} = 2 \frac{\partial \log n_h}{\partial \log \sigma_8} \tag{3.14}$$

This exact expression is of limited usefulness, since the derivative on the RHS is not an observable quantity. Treating b_{ng} as a free parameter is not a viable option for data analysis, since it would be degenerate with f_{NL} (only the combination $b_{ng} f_{NL}$ would be observable). However, in spherical collapse models of halo formation, b_{ng} is related to the Gaussian bias as:

$$b_{ng} = 2\delta_c(b_g - 1) \tag{3.15}$$

where δ_c is the collapse threshold, given by $\delta_c = 1.69$ in the Press-Schechter model [163], or $\delta_c = 1.42$ in Sheth-Tormen [177]. Although Eq. (3.15) is an approximation to the exact result (3.14), it is usually accurate at the 10–20% level [62, 158, 86, 82, 201, 87, 168, 22, 31], and is suitable for data analysis, since the parameters (b_g, f_{NL}) can be jointly constrained without degeneracy.

In our N-body simulations, we find that Eq. (3.15) gives a good fit to the non-Gaussian bias observed in our N-body simulations, if the Sheth-Tormen threshold $\delta_c = 1.42$ is used. (See Figure 3.1 below.) This is consistent with previous simulation-based studies [158, 86, 87, 22], which used the parameterization $b_{ng} = 2\sqrt{q}(1.69)(b_g - 1)$, and found a fudge-factor $\sqrt{q}$ around 0.84 for friends-of-friends halos (which we use in our pipeline, see §3.2.2). In the rest of the chapter, we model large-scale halo bias using Eq. (3.12), where b_{ng} is given by Eq. (3.15) with $\delta_c = 1.42$.

3.2 Simulation pipeline

3.2.1 Collisionless approximation

Simulating high-fidelity kSZ maps for velocity reconstruction is very computationally challenging. KSZ anisotropy appears on small angular scales in the CMB, where it is sourced by electron density fluctuations on small scales $k_S \sim 1$ Mpc^{-1}, leading to high resolution requirements in a simulation. Furthermore, on these small scales, collisionless N-body simulations are not really accurate enough to simulate the electron density, and hydrodynamical simulations should be used instead, which are much more expensive. At the same time, the cosmological constraining power of the kSZ comes from the largest scales, so a large simulation volume is required, if the goal is to make a simulation with an interesting f_{NL} constraint. This combination of volume and resolution requirements presents a serious computational challenge, and new simulation methods are probably required to satisfy all requirements strictly.

In this work, our goal is simply to test kSZ velocity reconstruction for biases as precisely as possible, under a self-consistent set of assumptions. For this purpose, perfectly accurate kSZ simulations are not required, and approximations are acceptable, as long as they are self-consistent. We will make the approximation that the electron density perfectly traces the dark matter density ($\delta_e = \delta_m$). This overestimates power spectra such as P_{ge}, P_{ee}, or $C_l^{\rm kSZ}$ by an order-one factor on small scales, since hydrodynamic effects suppress electron fluctuations relative to dark matter [175]. However, the question of whether kSZ velocity reconstruction is biased is unlikely to depend on the details of these small scale power spectra. For our purposes, what is crucial is that the approximation $\delta_e \approx \delta_m$ is applied consistently throughout the simulation and reconstruction pipelines.

The approximation $\delta_e \approx \delta_m$ dramatically decreases computational cost, since we can use collisionless N-body simulations. Similarly, instead of simulating galaxies, we use dark matter halos as a proxy for galaxies, i.e. we make the approximation $\delta_g \approx \delta_h$. In the rest of the chapter, we use "galaxies" synonymously with "halos", and "electrons" synonymously with "dark matter particles".

3.2.2 N-body simulations

We are interested in collisionless N-body simulations for both zero and nonzero f_{NL}. For $f_{NL} = 0$, rather than running our own simulations from scratch, we use the Quijote simulations [199], a large suite of publicly available N-body simulations. We use 100 simulations with 1024^3 particles and volume 1 h^{-3} Gpc^3 each.

For $f_{NL} \neq 0$, we generated a limited number of N-body simulations by running `GADGET-2` [187] with non-Gaussian initial conditions as follows. We simulate the initial curvature ζ, by simulating a Gaussian field ζ_G, and then adding a quadratic term:

$$\zeta(\mathbf{x}) = \zeta_G(\mathbf{x}) + \frac{3}{5} f_{NL}\big(\zeta_G(\mathbf{x})^2 - \langle \zeta_G^2 \rangle\big) \tag{3.16}$$

where the squaring operation is performed in real space. We evolve ζ to the Newtonian potential Φ at redshift $z_{\rm ini} = 127$, using linear transfer functions computed using `CLASS` [117]. We then generate initial conditions for `GADGET-2` at $z_{\rm ini} = 127$ using the Zeldovich approximation [105]:

$$\Psi_i(\mathbf{q}) = -\partial_i \partial^{-2} \delta_m(\mathbf{q}) = -\frac{2}{3a^2 H(a)^2}\Big(\partial_i \Phi(\mathbf{q})\Big) \tag{3.17}$$

$$v_i(\mathbf{q}) = \frac{\partial \Psi_i}{\partial \tau} = -\frac{2}{3aH(a)}\Big(\partial_i \Phi(\mathbf{q})\Big) \tag{3.18}$$

Here, $\mathbf{q}$ is the initial Lagrangian location of particles which in our case occupy center of 3D mesh, $\Psi_i(\mathbf{q})$ is the initial particle displacement, and $v_i(\mathbf{q})$ is the initial velocity. We evolve particles from $z_{\text{ini}} = 127$ to $z_* = 2$ using `GADGET-2` with the same parameters (cosmological parameters, force softening length, etc.) as the Quijote simulations.

3.2.3 Large-scale structure fields: δ_m, δ_h, q_r

The output of an N-body simulation is a catalog of particles with velocities. In this section, we describe our postprocessing of the catalog, to obtain pixelized 3-d maps of the matter overdensity $\delta_m(\mathbf{x})$, halo overdensity $\delta_h(\mathbf{x})$, and radial momentum $q_r(\mathbf{x})$.

To compute $\delta_m(\mathbf{x})$, we grid particle positions on a regular 3D mesh using the cloud-in-cell (CIC) algorithm [96], implemented in the public code `nbodykit` [89]. We use a 3D mesh with 1024^3 pixels, corresponding to pixel size 1 h^{-1} Mpc.

To obtain a halo catalog, we run the `Rockstar` halo-finder [27] on the particle positions. (Note that the Quijote simulations include a halo catalog, but we run our own halo finder instead, so that simulations with zero and nonzero f_{NL} are processed consistently.) Rockstar implements a modified version of the Friends-of-Friends (FOF) algorithm [57]. Under the FOF scheme, a particle f is a friend of particle p if f lies within a radius b (called the linking length) of p. The basic idea of FOF is to link all the particles which are friends of each other and also the particles which are friends of their friends and group them together to define halos in the simulation. The groups with particle counts larger than a threshold are taken to be an instance of a virialized halo. The radius b is called the linking length and is often defined in terms of inter-particle distance. After the halo catalog is produced, it is processed to obtain a halo overdensity map $\delta_h(\mathbf{x})$ by CIC-gridding halo positions.

We use an FOF linking length of 0.28 and require a minimum of 40 particles to classify a structure as a halo. This results in halo bias $b_h \sim 3.24$ and density $n_h^{3d} \approx 2.5 \times 10^{-4}$ Mpc^{-3} for simulations with $f_{NL} = 0$ at redshift $z_* = 2$. Since we are using halos as proxies for galaxies, our effective 2-d galaxy number density is $dn_g^{2d}/dz = (\chi_*^2/H_*)n_h^{3d} = 0.8$ arcmin^{-2}. In comparison, DESI has a combined (ELG+LRG+QSO) number density $dn_g^{2d}/dz = 0.91$ arcmin^{-2} at its peak at $z = 0.75$ [61], while Vera Rubin Observatory "gold" sample will have a number density $dn_g^{2d}/dz = 36$ arcmin^{-2} at its peak at $z = 0.6$ [131].

The radial momentum field deserves some discussion. We are interested in making 3-d maps of the true radial velocity v_r^{true}, in order to compare it to the kSZ velocity reconstruction $\hat{v}_r$ on large scales. However, in an N-body simulation, the definition of v_r^{true} is ambiguous. Here are three possibilities:

1. We can use the radial momentum $q_r = (1+\delta)v_r$. Since momentum is particle-weighted, it can be directly computed from particle positions and velocities.
2. We can use the linear velocity field $v_r^{\rm lin}(\mathbf{k})$, obtained by applying linear transfer functions to the initial conditions.
3. We can choose a smoothing scale, and define the velocity to be the smoothed momentum, divided by the smoothed density (appropriately regulated to avoid dividing by zero in voids).

We actually tried all three possibilities, and found that the first (the radial momentum q_r) has the highest correlation with the kSZ velocity reconstruction $\hat{v}_r$. This makes sense intuitively by considering the case of a "near-void" region whose density is close to zero. In a near-void region, the velocity reconstruction $\hat{v}_r$ is small, since a factor of the small-scale inhomogeneity $\delta_g(\mathbf{k}_S)$ appears in $\hat{v}_r$. Since the momentum q_r is also small in a near-void, but the radial velocity v_r is not, we expect $\hat{v}_r$ to correlate more strongly with q_r than with v_r.

Since q_r has the highest correlation with $\hat{v}_r$, and is also most straightforward to derive from an N-body simulation, we will use q_r throughout the chapter. (In hindsight, it would make sense to rename the quadratic estimator $\hat{v}_r \to \hat{q}_r$, and call it "kSZ momentum reconstruction" instead of "kSZ velocity reconstruction". However, we will use the $\hat{v}_r$ notation and velocity reconstruction terminology, for consistency with previous papers.) With this motivation for introducing the radial momentum, it is straightforward to compute $q_r(\mathbf{x})$ from an N-body simulation. We simply CIC-grid particles as before, weighting each particle by its radial velocity.

A technical point: we use compensated CIC-gridding with 1024^3 pixels throughout our pipeline, even though this suppresses power at wavenumbers close to the Nyquist frequency of the pixelization [96, 169, 89]. The suppression is a 3% at $k = 0.8k_{\rm Nyq}$, and 30% at $k = k_{\rm Nyq}$ [89]. In our kSZ velocity reconstruction pipeline, this does not lead to biases, provided that CIC-gridded fields and power spectra are used self-consistently throughout the pipeline. For example, we find (Figure 3.3 below) that the kSZ velocity reconstruction bias b_v is 1 on large scales, if the quadratic estimator $\hat{v}_r$ is implemented with CIC-gridding, and defined self-consistently using CIC-gridded power spectra $P_{ge}(k_S), P_{gg}(k_S)$ (see Eq. (3.26)).

3.2.4 CMB maps

Given the output from an N-body simulation, we simulate a kSZ map as follows. Let $\mathbf{x}_i$ denote the 3-d position of the i-th particle in the simulation (where $i = 1, \cdots, N_{\rm part}$), let

$\mathbf{v}_i$ denote the velocity, and let $\boldsymbol{\theta}_i = \mathbf{x}_{\perp i}/\chi_*$ denote the projected angular sky location. We approximate the momentum $\mathbf{q}(\mathbf{x})$ as a sum of velocity-weighted delta functions:

$$\mathbf{q}(\mathbf{x}) = \frac{1}{n_p} \sum_i \mathbf{v}_i \delta^3(\mathbf{x} - \mathbf{x}_i) \tag{3.19}$$

where $n_p = N_{\rm part}/L_{\rm box}^3$ is the 3-d particle number density. Plugging into the line-of-sight integral (Eq. (3.5)), the kSZ temperature is:

$$T_{\rm kSZ}(\boldsymbol{\theta}) = \frac{K_*}{\chi_*^2 n_p} \sum_i (\hat{\mathbf{r}} \cdot \mathbf{v}_i) \delta^2(\boldsymbol{\theta} - \boldsymbol{\theta}_i) \tag{3.20}$$

In our pipeline, we discretize CMB maps using $(1024)^2$ pixels, corresponding to angular pixel size $(\Delta\theta) = L_{\rm box}/(1024\chi_*) = 0.96$ arcmin, and Nyquist frequency $l_{\rm Nyq} = \pi/(\Delta\theta) = 11250$. We evaluate the RHS of Eq. (3.20) by gridding each delta function onto the 2-d mesh using the Cloud-in-Cell (CIC) scheme [96].

We add simulations of the lensed primary CMB and instrumental noise to our simulations, treating both contributions as Gaussian fields. We use noise power spectrum:

$$N_l = s_w^2 \exp\left[\frac{l(l+1)\theta_{\rm fwhm}^2}{8\ln 2}\right] \tag{3.21}$$

with white noise level $s_w = 0.5$ μK-arcmin, and beam size $\theta_{\rm fwhm} = 1$ arcmin. Note that we treat the non-kSZ CMB as Gaussian, which neglects possible biases from non-Gaussian secondaries. This is a loose end, although symmetry arguments suggest that biases are probably small. For more discussion, see §3.7.

In the rest of the work, we fix fiducial survey parameters described above ($s_w = 0.5$ μK-arcmin, $\theta_{\rm fwhm} = 1$ arcmin, $b_g = 3.24$, effective $dn_g/dz = 0.8$ arcmin^{-2}). Our galaxy survey parameters are similar to DESI, and our CMB parameters are intentionally futuristic (a bit better than CMB-S4), in order to maximize statistical power of our simulations.

3.3 LSS and CMB power spectra

In this section we present matter, halo, and CMB power spectra from our simulation pipeline. In the next section we will study higher-point statistics and kSZ velocity reconstruction. We start by confirming that the large-scale halo bias is described by the model:

$$b_h(k) = b_g + f_{NL} \frac{2\delta_c(b_g - 1)}{\alpha(k,z)} \qquad (\delta_c = 1.42) \tag{3.22}$$

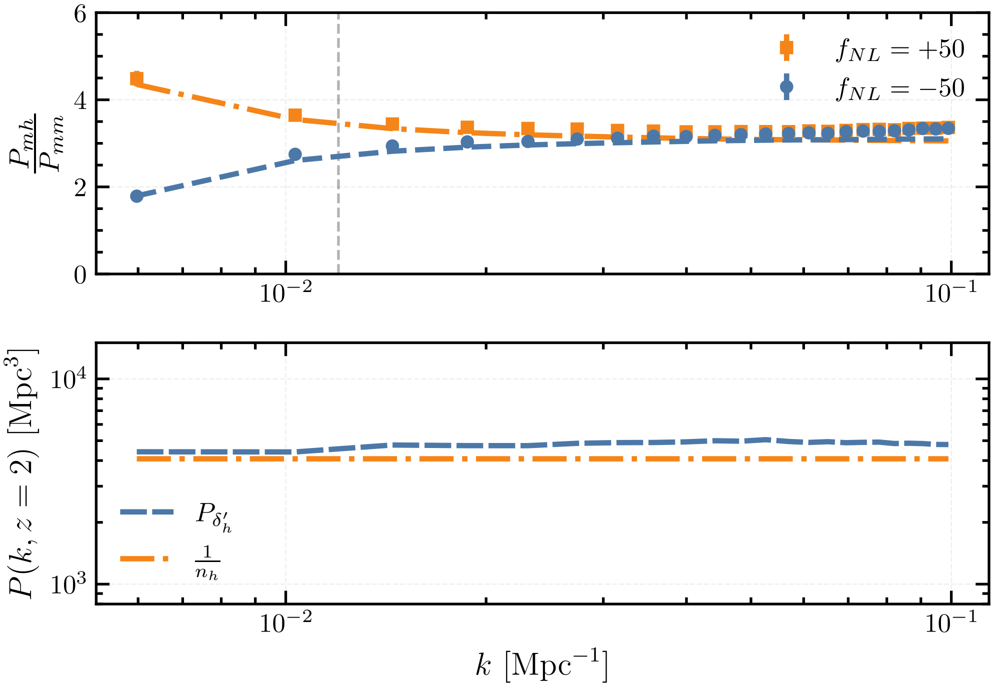

Figure 3.1: *Top panel.* Large-scale halo bias $b_h(k) = P_{mh}(k)/P_{mm}(k)$ from N-body simulations with $f_{NL} = \pm 50$. For comparison, we show the bias model (3.22), with $b_g = 3.01, 3.15$ for $f_{NL} = -50, 50$ respectively. (These values were obtained from the MCMC pipeline to be presented in §3.6.) For each value of f_{NL}, we use four N-body simulations with volume $1\ h^{-3}\ \mathrm{Gpc}^3$ each. *Bottom panel.* Halo shot noise from simulation from the same set of simulations, defined as the power spectrum of the field $\delta'_h(\mathbf{k}) = \delta_m(\mathbf{k}) - b_h(k)\delta_m(\mathbf{k})$, compared to the Poisson prediction $P_{\delta'_h}(k) = 1/n_h$.

in agreement with previous studies [56, 62, 158, 86, 82, 201, 168, 31]. In Figure 3.1 (top), we estimate the halo bias $b_h(k) = P_{mh}(k)/P_{mm}(k)$ directly from the matter-halo and matter-matter power spectra of simulations with $f_{NL} = \pm 50$, and find good agreement with the bias model in Eq. (3.22).

Next we consider the halo-halo power spectrum $P_{hh}(k)$. On large scales, we want to check that linear halo bias plus shot noise is a good description, i.e.

$$P_{hh}(k) = b_h(k)^2 P_{mm}(k) + \frac{1}{n_h} \tag{3.23}$$

A stronger version of this check is to show that the power spectrum of the field $\delta'_h = \delta_h - b_h(k)\delta_m$ is consistent with pure shot noise: $P_{\delta'_h \delta'_h}(k) = 1/n_h$. In Figure 3.1 (bottom), we find good agreement, thus confirming the model (3.23).

Taken together, Eqs. (3.22), (3.23) are a complete model for halo clustering on large scales. Turning next to small scales, we present small-scale power spectra which are relevant for kSZ velocity reconstruction. The definition of the kSZ velocity reconstruction estimator $\hat{v}_r$ (Eq. (3.25) below) involves the small-scale galaxy-electron and galaxy-galaxy power spectra $P_{ge}(k_S), P_{gg}(k_S)$, evaluated at wavenumbers $k_S \sim 1$ Mpc^{-1}. In the collisionless N-body approximation used in this work ($\delta_e \approx \delta_m$, $\delta_g \approx \delta_h$), these power spectra are equal to $P_{mh}(k_S)$ and $P_{hh}(k_S)$, which we show for reference in the top panel of Figure 3.2.

The definition of $\hat{v}_r$ also involves the small-scale CMB power spectrum C_l^{tot}, which is the sum of kSZ, noise, and lensed CMB contributions. These contributions are shown in the bottom panel of Figure 3.2. The kSZ contribution C_l^{kSZ} is estimated directly from the simulations.

As another check on our pipeline, in Figure 3.2 we compare C_l^{kSZ} to the "standard" analytic estimate C_l^{SkSZ}, and find good agreement. The analytic estimate is derived following [104, 175] by approximating the electron momentum as $\mathbf{q}_e = (1+\delta_e)\mathbf{v}$ where the linear velocity $\mathbf{v}$ and nonlinear electron field δ_e are Gaussian. In this approximation, the kSZ power spectrum is:

$$C_l^{SkSZ} = \frac{(faH_*)^2 K_*^2 L}{2} \int \frac{d^3\mathbf{k}'}{(2\pi)^3} P_{mm}^{NL}(|\mathbf{k}-\mathbf{k}'|) P_{mm}(k') \left. \frac{k(k-2k'\mu)(1-\mu^2)}{k'^2(k^2+k'^2-2kk'\mu)} \right|_{\substack{\mathbf{k}=\mathbf{l}/\chi_* \\ \mu=\hat{\mathbf{k}}\cdot\hat{\mathbf{k}}'}} \tag{3.24}$$

where P_{mm} and P_{mm}^{NL} are the linear and non-linear matter power spectrum, and L is the box size.

The kSZ power spectrum in Figure 3.2 underestimates the predicted C_l from hydrodynamical simulations (e.g. [170]) by a factor $\sim$2. This is because our "snapshot" geometry

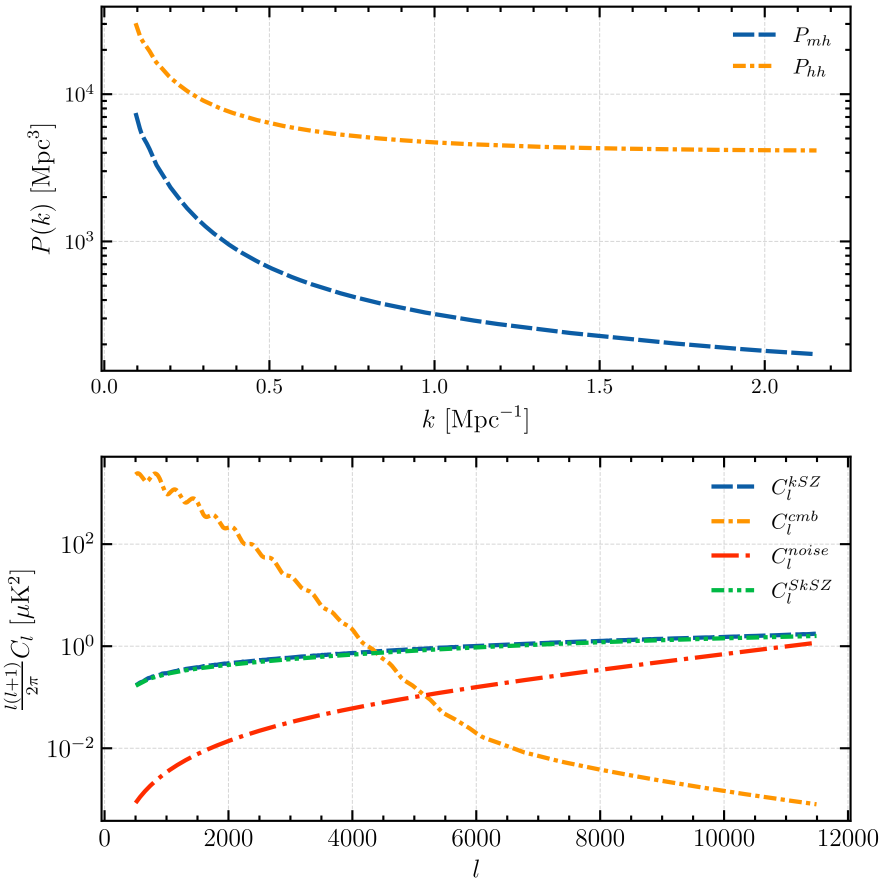

Figure 3.2: *Top.* Small scale halo-halo and matter-halo power spectrum from Quijote N-body simulations. These power spectra are used in the definition of the velocity reconstruction estimator $\hat{v}_r$ (Eq. (3.26) below). *Bottom.* Plot showing various contributions to the CMB power spectrum. The lensed CMB power spectrum is computed using the `CLASS` Boltzmann code [34], and the noise power spectrum is based on Eq. (3.21) with $s_w = 0.5$ μK-arcmin and $\theta_{\rm fwhm} = 1$ arcmin. The kSZ power spectrum $C_l^{\rm kSZ}$ is estimated directly from our simulation pipeline. For comparison, we also show the "standard" analytical estimate C_l^{SkSZ}, based on [175] and computed using Eq. (3.24).

only includes kSZ fluctuations from a redshift slice of thickness $L_{\rm box} = 1\ h^{-1}$ Gpc. (We also make the approximation that electrons trace dark matter, i.e. $P_{ee} \approx P_{mm}$, which has the opposite effect of increasing C_l, but this is a smaller effect.) This is not an issue for purposes of this work, where our goal is to test kSZ velocity reconstruction for biases as precisely as possible, under a self-consistent set of assumptions. We considered making the simulations more realistic, by adding simulated kSZ outside the simulated redshift range, but we expect that this would be nearly equivalent to adding uncorrelated Gaussian noise, and would only serve to decrease the precision of our tests.

3.4 The KSZ quadratic estimator applied to N-body simulations

3.4.1 KSZ quadratic estimator

In this section, we describe our implementation of the kSZ velocity reconstruction estimator $\hat{v}_r$. The inputs to kSZ velocity reconstruction are the 2-d CMB map $T(\mathbf{l})$ and 3-d galaxy overdensity field $\delta_g(\mathbf{k})$. The outputs are the 3-d radial velocity reconstruction $\hat{v}_r(\mathbf{k})$ and noise power spectrum $N_{v_r}^{(0)}(\mathbf{k}_L)$. These are given by [183]:

$$\hat{v}_r(\mathbf{k}_L) = N_{v_r}^{(0)}(\mathbf{k}_L)\frac{K_*}{\chi_*^2}\int \frac{d^3\mathbf{k}_S}{(2\pi)^3}\,\frac{d^2\mathbf{l}}{(2\pi)^2}\,\frac{P_{ge}(k_S)}{P_{gg}(k_S)C_l^{\rm tot}}\delta_g^*(\mathbf{k}_S)T^*(\mathbf{l})\,(2\pi)^3\delta^3\left(\mathbf{k}_L+\mathbf{k}_S+\frac{\mathbf{l}}{\chi_*}\right) \tag{3.25}$$

$$N_{v_r}^{(0)}(\mathbf{k}_L) = \frac{\chi_*^4}{K_*^2}\left[\int \frac{d^3\mathbf{k}_S}{(2\pi)^3}\,\frac{d^2\mathbf{l}}{(2\pi)^2}\,\frac{P_{ge}(k_S)^2}{P_{gg}(k_S)C_l^{\rm tot}}(2\pi)^3\delta^3\left(\mathbf{k}_L+\mathbf{k}_S+\frac{\mathbf{l}}{\chi_*}\right)\right]^{-1} \tag{3.26}$$

The noise power spectrum in the second line (3.26) is obtained by calculating the two-point function $\langle \hat{v}_r(\mathbf{k}_L)\hat{v}_r(\mathbf{k}_L')^*\rangle$, under the approximation that the galaxy catalog and CMB are independent. To emphasize an analogy with CMB lens reconstruction that will be explained in §3.5, we will call the noise power spectrum defined in Eq. (3.26) the "kSZ $N^{(0)}$-bias" throughout the chapter. One of our goals is to compare the kSZ $N^{(0)}$ bias to the reconstruction noise in N-body simulations, to test the accuracy of the approximation leading to Eq. (3.26).

In principle, $N_{v_r}^{(0)}(\mathbf{k}_L)$ is a function of both $k_L = |\mathbf{k}_L|$, and the direction of $\mathbf{k}_L$ relative to the line of sight. However, on the large scales which are relevant for constraining f_{NL}, it approaches a constant:

$$N_{v_r}^{(0)}(\mathbf{k}_L) \to \frac{\chi_*^4}{K_*^2} \left[\int \frac{d^2\mathbf{l}}{(2\pi)^2} \frac{P_{ge}(l/\chi_*)^2}{P_{gg}(l/\chi_*) C_l^{\rm tot}} \right]^{-1} \qquad (\mathbf{k}_L \to 0) \tag{3.27}$$

In Eqs. (3.25), (3.26), we have given Fourier-space expressions for $\hat{v}_r(\mathbf{k}_L)$ and $N_{v_r}^{(0)}(\mathbf{k}_L)$. These expressions are computationally expensive, and in practice alternative expressions are used, which factorize the computation into FFT's as follows. The velocity reconstruction $\hat{v}_r(\mathbf{k}_L)$ is computed as:

$$\hat{v}_r(\mathbf{k}_L) = N_{v_r}^{(0)}(\mathbf{k}_L) \frac{K_*}{\chi_*^2} \int d^3\mathbf{x}\, \tilde{\delta}_g(\mathbf{x})\, \tilde{T}\Big(\frac{\mathbf{x}_\perp}{\chi_*}\Big) e^{-i\mathbf{k}_L\cdot\mathbf{x}} \tag{3.28}$$

where the filtered galaxy field $\tilde{\delta}_g(\mathbf{x})$ and filtered CMB $\tilde{T}(\boldsymbol{\theta})$ are defined by:

$$\tilde{\delta}_g(\mathbf{x}) = \int \frac{d^3\mathbf{k}_S}{(2\pi)^3} \frac{P_{ge}(\mathbf{k}_S)}{P_{gg}(\mathbf{k}_S)} \delta_g(\mathbf{k}_S) e^{i\mathbf{k}_S\cdot\mathbf{x}} \qquad \tilde{T}(\boldsymbol{\theta}) = \int \frac{d^2\mathbf{l}}{(2\pi)^2} \frac{1}{C_l^{\rm tot}} T(\mathbf{l}) e^{i\mathbf{l}\cdot\boldsymbol{\theta}} \tag{3.29}$$

Similarly, the kSZ $N^{(0)}$-bias is computed efficiently as:

$$N_{v_r}^{(0)}(\mathbf{k}_L) = \frac{\chi_*^4}{K_*^2} \left[\int d^3\mathbf{x}\, f_1(\mathbf{x})\, f_2\Big(\frac{\mathbf{x}_\perp}{\chi_*}\Big) e^{-i\mathbf{k}_L\cdot\mathbf{x}} \right]^{-1} \tag{3.30}$$

where the 3-d field f_1 and 2-d field f_2 are defined as:

$$f_1(\mathbf{x}) = \int \frac{d^3\mathbf{k}_S}{(2\pi)^3} \frac{P_{ge}(k_S)^2}{P_{gg}(k_S)} e^{i\mathbf{k}_S\cdot\mathbf{x}} \qquad f_2(\boldsymbol{\theta}) = \int \frac{d^2\mathbf{l}}{(2\pi)^2} \frac{1}{C_l^{\rm tot}} e^{i\mathbf{l}\cdot\boldsymbol{\theta}} \tag{3.31}$$

Eqs. (3.28), (3.30) for $\hat{v}_r$ and $N_{v_r}^{(0)}$ are mathematically equivalent to Eqs. (3.25), (3.26), but have much lower computational cost.

One more detail of our $\hat{v}_r$ implementation. The definitions of $\hat{v}_r$ and $N_{v_r}^{(0)}$ above involve small-scale power spectra $P_{ge}(k_S)$, $P_{gg}(k_S)$, and $C_l^{\rm tot}$. In this work, we do not attempt to model these small-scale spectra (e.g. with the halo model). Instead, we measure them directly from simulation, by estimating each power spectrum in bandpowers, and interpolating to get a smooth function of wavenumber. The estimated power spectra $P_{ge}(k_S)$, $P_{gg}(k_S)$, and $C_l^{\rm tot}$ in our simulations were shown previously in Figure 3.2.

By estimating small-scale power spectra directly from simulation, our pipeline is "cheating", since $P_{ge}(k_S)$ is not observable. (The other two small-scale power spectra $P_{gg}(k_S)$

and $C_l^{\rm tot}$ can be estimated directly from data in a real experiment, and so it is not cheating to measure them from simulations.) In a real experiment, we would need to use a fiducial model $P_{ge}^{\rm fid}(k_S)$, which need not equal the true power spectrum $P_{ge}^{\rm true}(k_S)$. In [183], it is predicted that in this situation, the velocity reconstruction acquires a large-scale linear bias:

$$\hat{v}_r(\mathbf{k}_L) = b_v v_r(\mathbf{k}_L) + (\text{Reconstruction noise}) \tag{3.32}$$

where the velocity reconstruction bias b_v is 1 if $P_{ge}^{\rm fid} = P_{ge}^{\rm true}$, but can differ from 1 if $P_{ge}^{\rm fid} \neq P_{ge}^{\rm true}$. We will test this prediction in the next section.

3.4.2 Noise and bias of velocity reconstruction

In [183] we predicted that the velocity reconstruction estimator $\hat{v}_r(\mathbf{k}_L)$ is an unbiased estimator of the radial momentum $q_r(\mathbf{k}_L)$ on large scales, and that the reconstruction noise is given by the $N^{(0)}$-bias in Eq. (3.26). These statements are "predictions" since they are derived using analytic approximations to the statistics of large-scale structure on nonlinear scales. In this section, we will test these key predictions with N-body simulations.

We start by stating precisely the predictions we would like to test. We define the kSZ velocity reconstruction bias $b_v(\mathbf{k}_L)$ of the simulation by:

$$b_v(\mathbf{k}_L) = \frac{P_{q_r\hat{v}_r}(\mathbf{k}_L)}{P_{q_rq_r}(\mathbf{k}_L)} \tag{3.33}$$

Then we predict that $b_v \to 1$ on large scales, if we assume that the galaxy-electron power spectrum $P_{ge}(k_S)$ is known in advance and used in the quadratic estimator (3.25). If fiducial power spectrum $P_{ge}^{\rm fid}(k_S) \neq P_{ge}^{\rm true}(k_S)$ is used, then we make the weaker prediction that b_v approaches a constant on large scales.

We define the reconstruction noise field $\eta(\mathbf{k}_L) = \hat{v}_r(\mathbf{k}_L) - b_v(\mathbf{k}_L) q_r(\mathbf{k}_L)$, or equivalently:

$$\hat{v}_r(\mathbf{k}_L) = b_v(\mathbf{k}_L) q_r(\mathbf{k}_L) + \eta(\mathbf{k}_L) \qquad \text{where } P_{\eta q_r}(\mathbf{k}_L) = 0 \tag{3.34}$$

Then we predict that the power spectrum $P_\eta(\mathbf{k}_L)$ is equal to the kSZ $N^{(0)}$-bias $N_{v_r}^{(0)}(\mathbf{k}_L)$ given previously in Eq. (3.26).

Note that in the above, we compare $\hat{v}_r$ to the radial momentum q_r, since $\hat{v}_r$ is expected to be more correlated with momentum than with other definitions of the radial velocity, and momentum is also more straightforward to define in simulation (see discussion in §3.2.3).

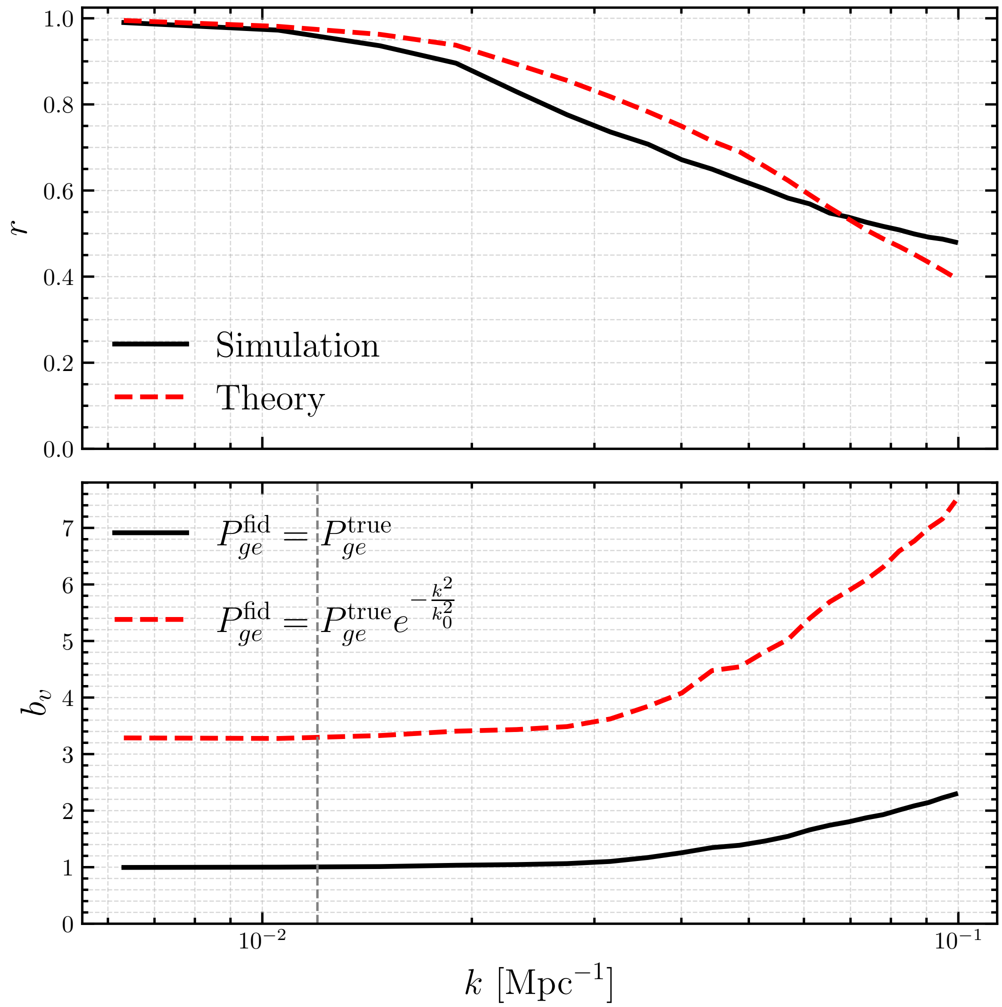

Figure 3.3: *Top panel.* Correlation coefficient r between fields $\hat{v}_r$ and q_r, where $\hat{v}_r$ is the kSZ velocity reconstruction derived from an N-body simulation, and q_r is the true radial momentum of the simulation. We estimate r in k-bins using Eq. (3.35), excluding wavenumbers with $\mu = 0$. The "theory" curve was obtained using Eq. (3.36). *Bottom panel.* KSZ velocity reconstruction bias b_v, estimated in k-bins using Eq. (3.37). The solid line was computed assuming perfect knowledge of the galaxy-electron power spectrum $P_{ge}(k_S)$ in the definition of $\hat{v}_r$. The dashed line was computed using fiducial galaxy-electron power spectrum $P_{ge}^{\mathrm{fid}}(k_S) = P_{ge}^{\mathrm{true}}(k_S)\exp(-k^2/k_0^2)$, where $k_0 = 1$ Mpc^{-1}. The vertical line at $k = 0.012$ Mpc^{-1} is the k_{max} that we use in our MCMC pipeline later (§3.6).

In the rest of this section, we will test the above predictions with simulations. All results in this section use 100 Quijote simulations with $f_{NL} = 0$ and total volume 100 h^{-3} Gpc^3.

Before exploring bias and reconstruction noise, we do a simple intuitive comparison between the radial momentum q_r and the reconstruction $\hat{v}_r$. In Figure 3.3 (top) we show the correlation coefficient between q_r and $\hat{v}_r$. More precisely, we choose a set of k-bins, and for each k-bin b we define a correlation coefficient $r_b^{\rm sim}$ by:

$$r_b^{\rm sim} = \frac{\sum_{\mathbf{k}\in b} \hat{v}_r^*(\mathbf{k}) q_r(\mathbf{k})}{\left(\sum_{\mathbf{k}\in b} |q_r(\mathbf{k})|^2\right)^{1/2} \left(\sum_{\mathbf{k}\in b} |\hat{v}_r(\mathbf{k})|^2\right)^{1/2}} \tag{3.35}$$

It is seen that the kSZ-derived velocity reconstruction $\hat{v}_r(\mathbf{k})$ is nearly 100% correlated to the true momentum on large scales. This is crucial, since we want to use velocity reconstruction to cancel sample variance in the galaxy field and constrain f_{NL}, which requires a high correlation. To quantify this better, we compare to the "theory" prediction for the correlation coefficient:

$$r_b^{\rm theory} = \left(\frac{\sum_{\mathbf{k}\in b} \mu_{\mathbf{k}}^2 P_{vv}(k)}{\sum_{\mathbf{k}\in b} (\mu_{\mathbf{k}}^2 P_{vv}(k) + N_{v_r}(\mathbf{k}))} \right)^{1/2} \tag{3.36}$$

where $\mu_{\mathbf{k}} = (\hat{\mathbf{k}} \cdot \hat{\mathbf{r}})$ as usual. This expression for $r_b^{\rm theory}$ was calculated assuming $b_v = 1$ and $P_\eta = N_{v_r}^{(0)}$.

In Figure 3.3 (top), the correlation coefficient seen in simulation qualitatively agrees with the theory prediction, but we do see some level of mismatch. On large scales, $r_b^{\rm sim}$ is a little smaller than $r_b^{\rm theory}$. This is consistent with a factor 2–3 increase in reconstruction noise that we will describe shortly. Intriguingly, on small scales, $r_b^{\rm sim}$ is a little larger than $r_b^{\rm theory}$. By comparing Figs 3.3 (bottom) and 3.4, this can be interpreted as arising from enhancement of the velocity bias b_v on small scales, with no corresponding enhancement in reconstruction noise.

Next we would like to test the prediction that the velocity reconstruction bias $b_v \to 1$ on large scales. In Figure 3.3 (bottom), we show the bias from N-body simulations, estimated in non-overlapping k-bins by defining:

$$(b_v)_b = \frac{\sum_{\mathbf{k}\in b} q_r(\mathbf{k})^* \, \hat{v}_r(\mathbf{k})}{\sum_{\mathbf{k}\in b} |q_r(\mathbf{k})|^2} \tag{3.37}$$

for each k-bin b. The bias is 1 on large scales as predicted. As k increases, the bias is an increasing function of k, and becomes large for surprisingly small values of k. For example,

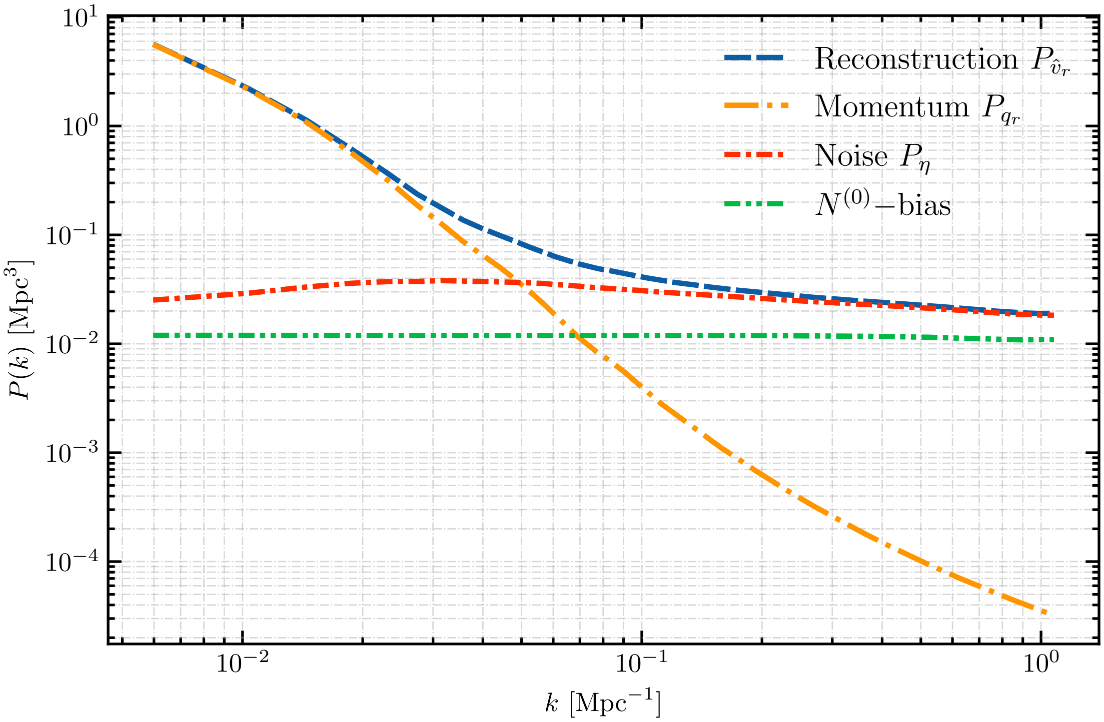

Figure 3.4: Velocity reconstruction signal and noise power spectra from 100 high resolution Quijote simulations. $P_{\hat{v}_r}$ and P_{q_r} are the power spectra of the noisy velocity reconstruction $\hat{v}_r$, and the true radial momentum q_r (both from simulation). P_η is the reconstruction noise from simulation, defined as the power spectrum of the noise field η defined in Eq. (3.34). $N^{(0)}_{v_r}$ is the kSZ $N^{(0)}$-bias in Eq. (3.26).

$b_v \approx 2.4$ at $k = 0.1$ Mpc^{-1}. The level of scale dependence seen in the velocity bias $b_v(k)$ is much higher than the familiar case of halo bias (see Fig. 3.1). However, on the very large scales ($k \lesssim 0.01$) that are important for f_{NL} constraints, b_v is constant to an excellent approximation.

In Figure 3.3 (bottom), we also show the velocity bias b_v if we construct the quadratic estimator $\hat{v}_r$ using fiducial galaxy-electron power spectrum $P^{\rm fid}_{ge}(k_S) \neq P^{\rm true}_{ge}(k_S)$. For illustrative purposes, we have arbitrary chosen $P^{\rm fid}_{ge}(k_S) = P^{\rm true}_{ge}(k_S)\exp(-k^2/k_0^2)$, where $k_0 = 1$ Mpc^{-1}. As predicted, we find that b_v approaches a constant on large scales, but the value is $\neq 1$.

Finally, we come to the main result of this section: comparing the reconstruction noise

P_η in simulation with the kSZ $N^{(0)}$-bias. In Figure 3.4, we show four power spectra:

- The total power spectrum $P_{\hat{v}_r}$ of the kSZ velocity reconstruction (including noise), estimated from simulation.
- The power spectrum P_{q_r} of the radial momentum, estimated from simulation.
- The reconstruction noise power spectrum P_η, estimated from simulation using the definition of η in Eq. (3.34).
- The kSZ $N^{(0)}$-bias $N^{(0)}_{v_r}$, computed using Eq. (3.26).

Contrary to the prediction from [183], the reconstruction noise P_η in simulation exceeds the kSZ $N^{(0)}$-bias by a factor 2–3! This increase in noise can potentially affect f_{NL} constraints, even though the f_{NL} constraints are derived from large scales where the velocity reconstruction is signal-dominated, because sample variance cancellation plays a role in the constraints. We will explore this issue in more detail in §3.5 and §3.6.

As a code check, we also estimated the power spectrum of a "fake" kSZ velocity reconstruction $\hat{v}_r^{\text{fake}}$, constructed by applying the quadratic estimator to a galaxy catalog δ_g and a CMB map T derived from independent N-body simulations. The power spectrum of $\hat{v}_r^{\text{fake}}$ is exactly equal to $N^{(0)}_{v_r}$, since by construction $N^{(0)}_{v_r}$ is the reconstruction noise under the approximation that δ_g and T are independent. In our simulations, we find the expected exact agreement between P_η^{fake} and $N^{(0)}_{v_r}$. This is a strong check on our pipeline, and indicates that the discrepancy between P_η and $N^{(0)}_{v_r}$ is a real effect arising from higher-point correlations in the N-body simulation. In §3.5, we will explain this discrepancy using the halo model.

3.4.3 Bandpower covariance

So far, our comparisons between theory and simulation have focused on mean power spectra: either the cross spectrum $P_{\hat{v}_r q_r}$ which determines the bias $b_v(k)$, or the noise power spectrum $P_{\eta\eta}$. However, for either forecasts or data analysis, the power spectrum *covariance* is also important. If the reconstruction noise η were a Gaussian field, then its power spectrum covariance would be:

$$\text{Cov}(P_\eta(b), P_\eta(b')) = \frac{2}{N_b} P_\eta(b)^2 \delta_{bb'} \tag{3.38}$$

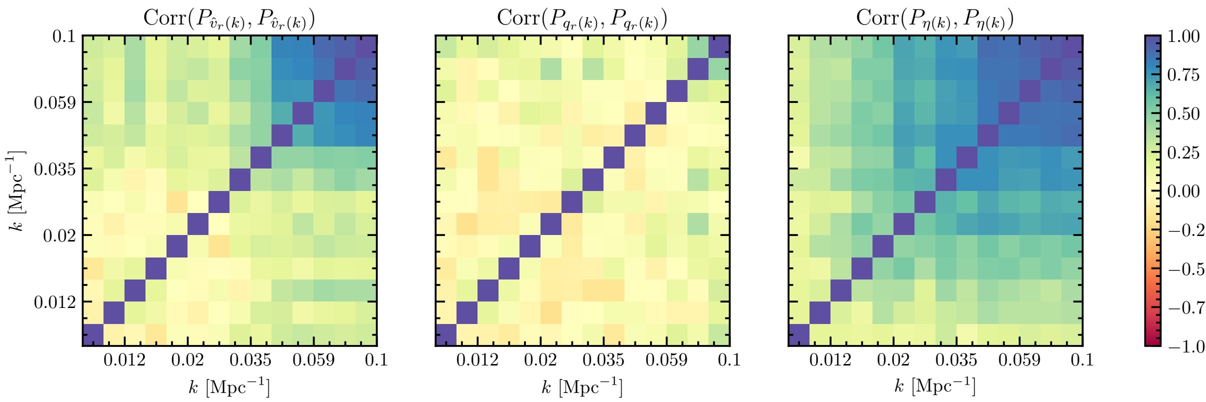

Figure 3.5: Correlation coefficient between bandpowers $P(k)$ of the velocity reconstruction $\hat{v}_r(\mathbf{k})$ (left panel), true momentum $q_r(\mathbf{k})$ (middle panel), and reconstruction noise $\eta(k) = \hat{v}_r(\mathbf{k}) - b_v(\mathbf{k})q_r(\mathbf{k})$ (right panel). Correlation coefficients were estimated from 100 Quijote simulations.

where b, b' denote narrow non-overlapping k-bins, and N_b denotes the number of modes in bin b. The standard Fisher matrix forecasting formalism implicitly assumes that the Gaussian bandpower covariance (3.38) is a good approximation. Our MCMC f_{NL} pipeline in §3.6 will make slightly stronger assumptions, by assuming that the full probability density function of η is well-described by its Gaussian approximation.

As one test of the Gaussian approximation, we estimate the correlation matrix between bandpowers and show the result in Figure 3.5. We find that non-Gaussian bandpower covariance is small at low k, but very significant (correlations of order one) at high k. The transition between the two regimes is fairly sharp and occurs at $k \sim 0.03$ Mpc^{-1}. This suggests that non-Gaussian bandpower covariance is unlikely to be an issue for constraining f_{NL}, where statistical weight comes from the very largest scales. (For example, in the f_{NL} analysis in the next section, we will use $k_{\max} = 0.012$ Mpc^{-1}.) However, the bandpower covariance in Figure 3.5 assumes our fiducial survey parameters, and we have not explored parameter dependence systematically.

3.5 Higher-order biases to kSZ reconstruction noise

In §3.4.2, we found a discrepancy between the reconstruction noise P_η in simulation and the kSZ $N^{(0)}$-bias. In this section, we will elaborate on our previous statements that the

$N^{(0)}$-bias does not include all terms in the reconstruction noise, derive additional terms which arise in the halo model, and numerically compare the new terms to the simulations.

3.5.1 Setup

We will calculate the total power spectrum of the reconstruction $P_{\hat{v}_r\hat{v}_r}(\mathbf{k}_L)$, which will contain all signal and noise terms. First, we set up the calculation using schematic notation which just keeps track of how many terms are present, and how each term factorizes as a product of fields. Since the quadratic estimator has schematic form $\hat{v}_r \sim (\delta_g T)$, its power spectrum has schematic form:

$$P_{\hat{v}_r\hat{v}_r}(k_L) \sim \big\langle (\delta_g T)(\delta_g T) \big\rangle \,. \tag{3.39}$$

Our calculation will make a series of approximations which we will explain as we go along. First, we make the approximations:

- *Approximation 1.* We write the CMB as $T = T_{kSZ} + T_{\rm other}$, and make the approximation that the non-kSZ contribution $T_{\rm other}$ is statistically independent of the galaxy catalog. This neglects possible non-Gaussian effects from CMB secondaries, e.g. CMB lensing.
- *Approximation 2.* The electron radial momentum factorizes as $q_r = (1+v_r)\delta_e$ in the kSZ line-of-sight integral (3.5).

Under these approximations, we can write $P_{\hat{v}_r\hat{v}_r}(\mathbf{k}_L)$ schematically as:

$$P_{\hat{v}_r\hat{v}_r}(\mathbf{k}_L) \sim \big\langle \delta_g\delta_g \big\rangle \big\langle T_{\rm other}T_{\rm other} \big\rangle + \big\langle (\delta_g v_r \delta_e)(\delta_g v_r \delta_e) \big\rangle \tag{3.40}$$

We write the six-point function $\langle (\delta_g v_r \delta_e)(\delta_g v_r \delta_e) \rangle$ appearing on the RHS as a sum over Wick contractions, plus a non-Gaussian part $\langle (\delta_g v_r \delta_e)(\delta_g v_r \delta_e) \rangle_{ng}$. There are 15 Wick contractions, but we make the following approximation, which reduces the number to 3:

- *Approximation 3.* In the Gaussian part of the six-point function $\langle (\delta_g v_r \delta_e)(\delta_g v_r \delta_e) \rangle$, terms where v_r Wick-contracts with either δ_g or δ_e are negligible.

  The rationale for this approximation is as follows. The kSZ velocity reconstruction $\hat{v}_r(\mathbf{k}_L)$ is determined by the galaxy and electron fields $\delta_g(\mathbf{k}), \delta_e(\mathbf{k})$ on "kSZ" scales $k \sim 1$ Mpc^{-1}. On these scales, radial velocity modes $v_r(\mathbf{k})$ are very small, which implies that terms proportional to $P_{gv_r}(k)$ and $P_{ev_r}(k)$ should also be small.

In this approximation, $P_{\hat{v}_r}$ has schematic form:

$$P_{\hat{v}_r}(\mathbf{k}_L) = \underbrace{\left\langle \delta_g \delta_g \right\rangle \left\langle T_{\text{other}} T_{\text{other}} \right\rangle + (\delta_g v_r \delta_e)(\delta_g v_r \delta_e)}_{N^{(0)}} + \underbrace{(\delta_g v_r \delta_e)(\delta_g v_r g \delta_e)}_{P_{vv}} + \underbrace{(\delta_g v_r \delta_e)(\delta_g v_r \delta_e)}_{N^{(1)}} + \underbrace{\left\langle (\delta_g v_r \delta_e)(\delta_g v_r \delta_e) \right\rangle_{ng}}_{N^{(3/2)}} \tag{3.41}$$

(3.42)

where the non-Gaussian n-point function $\langle \cdot \rangle_{ng}$ denotes the expectation value after subtracting all Wick contractions.

Detailed calculation of each term now shows that the first two terms combine to give the $N^{(0)}$-bias, the third term is the "signal" power spectrum $P_{v_r}(\mathbf{k}_L)$, and the fourth and fifth terms are new reconstruction noise terms $N^{(1)}$ and $N^{(3/2)}$:

$$P_{\hat{v}_r \hat{v}_r}(\mathbf{k}_L) = P_{v_r}(\mathbf{k}_L) + N^{(0)}_{v_r}(\mathbf{k}_L) + N^{(1)}(\mathbf{k}_L) + N^{(3/2)}(\mathbf{k}_L) \tag{3.43}$$

where the precise (non-schematic) forms of the new bias terms $N^{(1)}$ and $N^{(3/2)}$ are:

$$N^{(1)}(\mathbf{k}_L) = N^{(0)}_{v_r}(\mathbf{k}_L)^2 \frac{K_*^4}{\chi_*^8} \int \frac{d^2\mathbf{l}}{(2\pi)^2} \frac{d^2\mathbf{l}'}{(2\pi)^2} \left(\frac{P_{ge}(k_S)^2}{P_{gg}(k_S) C_l^{\text{tot}}} \frac{P_{ge}(k_S')^2}{P_{gg}(k_S') C_{l'}^{\text{tot}}} P_{v_r}(\mathbf{q}) \right)_{\substack{\mathbf{k}_S = \mathbf{k}_L + \mathbf{l}/\chi_* \\ \mathbf{k}_S' = \mathbf{k}_L + \mathbf{l}'/\chi_* \\ \mathbf{q} = -\mathbf{k}_L + (\mathbf{l}+\mathbf{l}')/\chi_*}} \tag{3.44}$$

$$\begin{aligned} N^{(3/2)}(\mathbf{k}_L) = N^{(0)}_{v_r}(\mathbf{k}_L)^2 \frac{K_*^4}{\chi_*^8} \int & \frac{d^2\mathbf{l}}{(2\pi)^2} \frac{d^2\mathbf{l}'}{(2\pi)^2} \frac{d^3\mathbf{q}}{(2\pi)^3} \frac{d^3\mathbf{q}'}{(2\pi)^3} \\ & \times \left[\frac{P_{ge}(k_S)}{P_{gg}(k_S) C_l^{\text{tot}}} \frac{P_{ge}(k_S')}{P_{gg}(k_S') C_{l'}^{\text{tot}}} \left\langle \delta_g(\mathbf{k}_S) v_r(\mathbf{q}) \delta_e(\mathbf{p}) \delta_g^*(\mathbf{k}_S') v_r^*(\mathbf{q}') \delta_e^*(\mathbf{p}') \right\rangle'_{ng} \right]_{\substack{\mathbf{k}_S = \mathbf{k}_L - \mathbf{l}/\chi_* \\ \mathbf{k}_S' = \mathbf{k}_L - \mathbf{l}'/\chi* \\ \mathbf{p} = -\mathbf{q} + \mathbf{l}/\chi_* \\ \mathbf{p}' = -\mathbf{q}' + \mathbf{l}'/\chi_*}} \end{aligned} \tag{3.45}$$

Here, a primed N-point function $\langle \prod_{i=1}^N X_i(\mathbf{k}_i) \rangle'$ denotes the expectation value without the delta function $(2\pi)^3 \delta^3(\sum \mathbf{k}_i)$.

We have chosen to call the new terms the kSZ $N^{(1)}$-bias and $N^{(3/2)}$-bias, to emphasize an analogy with CMB lensing. The $N^{(0)}$ and $N^{(1)}$ biases represent the total KSZ reconstruction noise if all LSS fields are Gaussian. The $N^{(1)}$-bias is a Wick contraction which is more difficult to compute, since the integrals cannot be factored into a sequence of convolutions. The $N^{(3/2)}$-bias represents additional noise bias arising from non-Gaussianity of the LSS fields (δ_g and δ_e). All of these statements are also true for the CMB lensing $N^{(1)}$-bias [109] and $N^{(3/2)}$-bias [40]. However, the analogy is not perfect: in the CMB lensing case, there is a systematic expansion in powers of the lensing potential ϕ, and there is no analogous expansion in the kSZ case. On a related note, when we evaluate the kSZ biases numerically, we will find that the $N^{(1)}$-bias is much smaller than $N^{(0)}$, whereas the $N^{(3/2)}$-bias is comparable to $N^{(0)}$.

3.5.2 KSZ $N^{(1)}$-bias

In the limit $k_L \ll k_S$, the $N^{(1)}$-bias in Eq. (3.44) can be simplified a lot. We make the following approximations inside the integral:

$$N_{v_r}^{(0)}(\mathbf{k}_L) \approx N_{v_r}^{(0)}(0) \qquad \mathbf{k}_S = \mathbf{k}_L + \mathbf{l}/\chi_* \approx \mathbf{l}/\chi_* \qquad \mathbf{k}'_S = -\mathbf{q} + \mathbf{l}/\chi_* \approx \mathbf{l}/\chi_* \tag{3.46}$$

where the third approximation is valid since the integrand contains the factor $P_{v_r}(\mathbf{q})$, which peaks for $q \ll k_S$. Making these approximations in Eq. (3.44), and changing variables from $\mathbf{l}'$ to $\mathbf{l}'' = (\mathbf{l} + \mathbf{l}')$, the integral factorizes as:

$$N^{(1)}(\mathbf{k}_L) \approx N_{v_r}^{(0)}(0)^2 \, \frac{K_*^4}{\chi_*^8} \left(\int \frac{d^2\mathbf{l}}{(2\pi)^2} \, \frac{P_{ge}(k_S)^4}{P_{gg}(k_S)^2 (C_l^{\rm tot})^2} \right)_{k_S = l/\chi_*} \left(\int \frac{d^2\mathbf{l}''}{(2\pi)^2} \, P_{v_r}(\mathbf{q}) \right)_{\mathbf{q} = -\mathbf{k}_L + \mathbf{l}''/\chi_*} \tag{3.47}$$

We simplify the second factor as:

$$\begin{aligned} \left(\int \frac{d^2\mathbf{l}''}{(2\pi)^2} \, P_{v_r}(\mathbf{q}) \right)_{\mathbf{q} = -\mathbf{k}_L + \mathbf{l}''/\chi_*} &= k_{Lr}^2 \int \frac{d^2\mathbf{l}''}{(2\pi)^2} \left(\frac{P_v(q)}{q^2} \right)_{\mathbf{q} = -\mathbf{k}_L + \mathbf{l}''/\chi_*} \\ &= \frac{k_{Lr}^2 \chi_*^2}{2\pi} \int_{|k_{Lr}|}^{\infty} dq \frac{P_v(q)}{q} \quad \text{(by change of variables)} \end{aligned} \tag{3.48}$$

where we use ($P_{v_r}(q) = (k_{Lr}/q)^2 P_v(q)$) to simplify the first line. To make the first factor more intuitive, we define the dimensionless quantity:

$$W(l) = N_{v_r}^{(0)}(0) \frac{K_*^2}{\chi_*^4} \left(\frac{P_{ge}(k_S)^2}{P_{gg}(k_S) C_l^{\rm tot}} \right)_{\mathbf{k}_S = \mathbf{l}/\chi_*} \tag{3.49}$$

which satisfies (using Eq. (3.26)):

$$\int \frac{d^2\mathbf{l}}{(2\pi)^2} W(l) = 1\,. \tag{3.50}$$

Plugging into Eq. (3.47) we get:

$$N^{(1)}(\mathbf{k}_L) \approx \frac{k_{Lr}^2 \chi_*^2}{2\pi} \left(\int \frac{d^2\mathbf{l}}{(2\pi)^2} W(l)^2 \right) \left(\int_{|k_{Lr}|}^{\infty} dq \frac{P_v(q)}{q} \right) \qquad (k_L \ll k_S) \tag{3.51}$$

Note that for $k_L \ll k_S$, the $N^{(1)}$-bias only depends on $|k_{Lr}| = |\mu| k_L$. In the limit $k_{Lr} \ll k_{eq}$, where $k_{eq} \sim 0.02$ Mpc^{-1} is the matter-radiation equality scale, $N^{(1)}(k_{Lr})$ is proportional to $|k_{Lr}|$. (In contrast to the $N^{(0)}$-bias, which is constant on large scales.)

It will also be useful to have an expression for the $N^{(1)}$-bias after angle-averaging $\mathbf{k}_L$ (e.g. in Figure 3.6 below). We omit the details of the calculation and quote the final result:

$$N^{(1)}(k_L)_{\text{avg}} \approx \frac{\chi_*^2}{6\pi} \left(\int \frac{d^2\mathbf{l}}{(2\pi)^2} W(l)^2 \right) \left(\frac{1}{k_L} \int_0^{k_L} dq\, q^2 P_v(q) + k_L^2 \int_{k_L}^{\infty} dq\, \frac{P_v(q)}{q} \right) \tag{3.52}$$

where "avg" means "angle-averaged over $\mathbf{k}_L$", and $k_L \ll k_S$ has been assumed.

3.5.3 KSZ $N^{(3/2)}$-bias and halo model evaluation

In the limit $k_L \ll k_S$, the $N^{(3/2)}$-bias in Eq. (3.45) also simplifies. We start by using the halo model to compute the non-Gaussian six-point function:

$$\big\langle \delta_g(\mathbf{k}_1)\delta_e(\mathbf{k}_2)\delta_g(\mathbf{k}_3)\delta_e(\mathbf{k}_4)v_r(\mathbf{k}_5)v_r(\mathbf{k}_6)\big\rangle'_{ng} \tag{3.53}$$

which appears in $N^{(3/2)}$.

We briefly summarize the ingredients of the halo model; for a systematic review see [50]. Let $n(M)$ be the halo mass function, or number of halos per unit volume per unit halo mass. Let $b(M)$ be the large-scale bias of a halo of mass M. Let $n_h = \int_{M_{\min}}^{\infty} dM\, n(M)$ be the mean halo number density, and let ρ_m be the mean matter density. Here, $M_{\min}$ is the minimum halo mass for our catalog (corresponding to 40 particles). Let $u_M(k)$ be the Fourier-transformed mass profile of a halo of mass M, normalized so that $u_M(0) = 1$.

It will be convenient to define:

$$\alpha_n(k_1,\cdots,k_n) = \frac{1}{n_h}\int_{M_{\min}}^{\infty} dM\, n(M) \prod_{i=1}^{n} \frac{M u_M(k_i)}{\rho_m} \tag{3.54}$$

$$\beta_n(k_1,\cdots,k_n) = \frac{1}{n_h}\int_{M_{\min}}^{\infty} dM\, n(M)b(M) \prod_{i=1}^{n} \frac{M u_M(k_i)}{\rho_m} \tag{3.55}$$

$$\beta'_n(k_1,\cdots,k_n) = \frac{1}{n_h}\int_{0}^{\infty} dM\, n(M)b(M) \prod_{i=1}^{n} \frac{M u_M(k_i)}{\rho_m} \tag{3.56}$$

Note that for $n = 0$, we have $\alpha_0 = 1$ and $\beta_0 = b$, where $b = n_h^{-1}\int_{M_{\min}}^{\infty} dM\, n(M)b(M)$ is the halo bias.

Under the assumptions of the halo model, the connected six-point function in Eq. (3.53) can be calculated exactly. In Appendix **??**, we present the details of the calculation, and diagrammatic rules for calculating n-point functions in the halo model, which may be of more general interest. In the next few paragraphs (Eqs. (3.57)–(3.67)), we summarize the result of the calculation.

We assume that the radial velocity modes $v_r(\mathbf{k}_5), v_r(\mathbf{k}_6)$ in the six-point function (3.53) are evaluated on linear scales $\mathbf{k}_5, \mathbf{k}_6$. Then the six-point function factorizes into lower-order correlation functions (i.e. there are no fully connected contributions). More precisely, the six-point function (3.53) is given by:

$$\begin{aligned}
&\Big\langle \delta_g(\mathbf{k}_1)\delta_e(\mathbf{k}_2)\delta_g(\mathbf{k}_3)\delta_e(\mathbf{k}_4)v_r(\mathbf{k}_5)v_r(\mathbf{k}_6)\Big\rangle_{ng} \\
&= \Big[\big(Q^{ge}_{\mathbf{k}_1\mathbf{k}_2\mathbf{k}_5}Q^{ge}_{\mathbf{k}_3\mathbf{k}_4\mathbf{k}_6} + Q^{gg}_{\mathbf{k}_1\mathbf{k}_3\mathbf{k}_5}Q^{ee}_{\mathbf{k}_2\mathbf{k}_4\mathbf{k}_6} + Q^{ge}_{\mathbf{k}_1\mathbf{k}_4\mathbf{k}_5}Q^{ge}_{\mathbf{k}_2\mathbf{k}_3\mathbf{k}_6}\big) + \big(\mathbf{k}_5 \leftrightarrow \mathbf{k}_6\big)\Big] \\
&+\Big[\big(P^{\delta_g v_r}_{\mathbf{k}_1\mathbf{k}_5}R^{ege}_{\mathbf{k}_2\mathbf{k}_3\mathbf{k}_4\mathbf{k}_6} + P^{\delta_e v_r}_{\mathbf{k}_2\mathbf{k}_5}R^{gge}_{\mathbf{k}_1\mathbf{k}_3\mathbf{k}_4\mathbf{k}_6} + P^{\delta_e v_r}_{\mathbf{k}_3\mathbf{k}_5}R^{gee}_{\mathbf{k}_1\mathbf{k}_2\mathbf{k}_4\mathbf{k}_6} + P^{\delta_e v_r}_{\mathbf{k}_4\mathbf{k}_5}R^{geg}_{\mathbf{k}_1\mathbf{k}_2\mathbf{k}_3\mathbf{k}_6}\big) + \big(\mathbf{k}_5 \leftrightarrow \mathbf{k}_6\big)\Big] \\
&+\Big[S_{\mathbf{k}_1\mathbf{k}_2\mathbf{k}_3\mathbf{k}_4}P^{v_r v_r}_{\mathbf{k}_5\mathbf{k}_6}\Big]
\end{aligned} \tag{3.57}$$

where we have introduced the following notation for some 2-, 3-, and 4-point functions:

$$P^{XY}_{\mathbf{k}_1\mathbf{k}_2} = \big\langle X(\mathbf{k}_1)Y(\mathbf{k}_2)\big\rangle \qquad (X, Y \in \{\delta_g, \delta_e, v_r\}) \tag{3.58}$$

$$Q^{XY}_{\mathbf{k}_1\mathbf{k}_2\mathbf{k}_3} = \big\langle \delta_X(\mathbf{k}_1)\delta_Y(\mathbf{k}_2)v_r(\mathbf{k}_3)\big\rangle \qquad (X, Y \in \{g, e\}) \tag{3.59}$$

$$R^{XYZ}_{\mathbf{k}_1\mathbf{k}_2\mathbf{k}_3\mathbf{k}_4} = \big\langle \delta_X(\mathbf{k}_1)\delta_Y(\mathbf{k}_2)\delta_Z(\mathbf{k}_3)v_r(\mathbf{k}_4)\big\rangle_{ng} \qquad (X, Y, Z \in \{g, e\}) \tag{3.60}$$

$$S_{\mathbf{k}_1\mathbf{k}_2\mathbf{k}_3\mathbf{k}_4} = \big\langle \delta_g(\mathbf{k}_1)\delta_e(\mathbf{k}_2)\delta_g(\mathbf{k}_3)\delta_e(\mathbf{k}_4)\big\rangle_{ng} \tag{3.61}$$

The quantities Q, R, S on the RHS of Eq. (3.57) are given explicitly by:

$$Q^{ge}_{\mathbf{k}_1\mathbf{k}_2\mathbf{k}_3} = \beta_1(k_2) \left(\frac{ik_{3r}}{k_3}\right) P_{mv}(k_3)\,(2\pi)^3\delta^3\left(\textstyle\sum \mathbf{k}_i\right) \tag{3.62}$$

$$Q^{gg}_{\mathbf{k}_1\mathbf{k}_2\mathbf{k}_3} = \frac{b}{n_h} \left(\frac{ik_{3r}}{k_3}\right) P_{mv}(k_3)\,(2\pi)^3\delta^3\left(\textstyle\sum \mathbf{k}_i\right) \tag{3.63}$$

$$Q^{ee}_{\mathbf{k}_1\mathbf{k}_2\mathbf{k}_3} = n_h\beta_2'(k_1,k_2) \left(\frac{ik_{3r}}{k_3}\right) P_{mv}(k_3)\,(2\pi)^3\delta^3\left(\textstyle\sum \mathbf{k}_i\right) \tag{3.64}$$

$$R^{gge}_{\mathbf{k}_1\mathbf{k}_2\mathbf{k}_3\mathbf{k}_4} = \frac{\beta_1(k_3)}{n_h} \left(\frac{ik_{4r}}{k_4}\right) P_{mv}(k_4)\,(2\pi)^3\delta^3\left(\textstyle\sum \mathbf{k}_i\right) \tag{3.65}$$

$$R^{gee}_{\mathbf{k}_1\mathbf{k}_2\mathbf{k}_3\mathbf{k}_4} = \beta_2(k_2,k_3) \left(\frac{ik_{4r}}{k_4}\right) P_{mv}(k_4)\,(2\pi)^3\delta^3\left(\textstyle\sum \mathbf{k}_i\right) \tag{3.66}$$

$$\begin{aligned} S_{\mathbf{k}_1\mathbf{k}_2\mathbf{k}_3\mathbf{k}_4} = \Bigg[& \frac{\alpha_2(k_2,k_4)}{n_h} + \beta_1(k_2)\beta_1(k_4)P_{\rm lin}(\mathbf{k}_1+\mathbf{k}_2) + b\beta_2'(k_2,k_4)P_{\rm lin}(\mathbf{k}_1+\mathbf{k}_3) \\ & + \beta_1(k_2)\beta_1(k_4)P_{\rm lin}(\mathbf{k}_1+\mathbf{k}_4) + b\beta_2(k_2,k_4)P_{\rm lin}(k_1) + \beta_1'(k_2)\beta_1(k_4)P_{\rm lin}(k_2) \\ & + b\beta_2(k_2,k_4)P_{\rm lin}(k_3) + \beta_1(k_2)\beta_1'(k_4)P_{\rm lin}(k_4)\Bigg](2\pi)^3\delta^3(\textstyle\sum \mathbf{k}_i) \end{aligned} \tag{3.67}$$

where $P_{mv}(k) = (faH/k)P_{\rm lin}(k)$ is the linear matter-velocity power spectrum.

Taken together, Eqs. (3.57)–(3.67)) are a complete calculation of the six-point function (3.53) in the halo model, in a rather daunting form with 22 terms! However, we will now argue that most of these terms are negligible, when we compute the $N^{(3/2)}$-bias by plugging the six-point function into the integral (3.45).

In the integral (3.45), the six-point function is evaluated at the following configuration of wavenumbers $\mathbf{k}_1, \cdots, \mathbf{k}_6$:

$$\mathbf{k}_1 = \mathbf{k}_L - \frac{\mathbf{l}}{\chi_*} \qquad \mathbf{k}_2 = -\mathbf{q} + \frac{\mathbf{l}}{\chi_*} \qquad \mathbf{k}_3 = -\mathbf{k}_L + \frac{\mathbf{l}'}{\chi_*} \qquad \mathbf{k}_4 = \mathbf{q}' - \frac{\mathbf{l}'}{\chi_*} \qquad \mathbf{k}_5 = \mathbf{q} \qquad \mathbf{k}_6 = -\mathbf{q}' \tag{3.68}$$

To understand which terms are negligible, we classify wavenumbers as either "small-scale" (meaning a typical kSZ scale ∼1 Mpc^{-1}), or "large-scale" (meaning $\ll$ 1 Mpc^{-1}). In the integral (3.45), we formally integrate over all wavenumbers $(\mathbf{l}, \mathbf{l}', \mathbf{q}, \mathbf{q}')$, but we will assume that q, q' are large-scale , and $(l/\chi_*), (l'/\chi_*)$ are small-scale, since these wavenumber configurations dominate the integral. We will also assume that k_L is large-scale, since we are interested in the $N^{(3/2)}$-bias in the limit $k_L \to 0$.

Now we can state our criteria for deciding which terms in the six-point function are negligible:

- *Approximation 4.* In the six-point function (3.53), terms where $P_{\rm lin}$ is evaluated at a small-scale wavenumber give negligible contributions to $N^{(3/2)}$.

  Rationale: On a small scale k, clustering is small compared to halo shot noise, so terms in the reconstruction noise proportional to $P_{\rm lin}(k)$ should be subdominant to other contributions.

- *Approximation 5.* Each term in the "primed" six-point function (3.53) contains a single delta function $\delta^3(\cdots)$. If the delta function argument is a small-scale wavenumber (in the sense defined above), then we assume that the six-point term under consideration gives a negligible contribution to $N^{(3/2)}$. For example, the term $(Q^{gg}_{\mathbf{k}_1\mathbf{k}_3\mathbf{k}_6} Q^{ee}_{\mathbf{k}_2\mathbf{k}_4\mathbf{k}_5})$ containing the delta function $\delta^3(\mathbf{q} + (\mathbf{l} - \mathbf{l}')/\chi_*)$ is negligible, whereas the term $(Q^{gg}_{\mathbf{k}_1\mathbf{k}_2\mathbf{k}_6} Q^{ee}_{\mathbf{k}_2\mathbf{k}_3\mathbf{k}_5})$ containing the delta function $\delta^3(\mathbf{k}_L - \mathbf{q} - \mathbf{q}')$ is non-negligible.

  Rationale: In Eq. (3.45), the $N^{(3/2)}$-bias is computed by by integrating over small-scale wavenumbers $(\mathbf{l}/\chi_*), (\mathbf{l}/\chi_*)$ and large-scale wavenumbers $\mathbf{q}, \mathbf{q}'$. If the six-point function contains a term such as $\delta^3(\mathbf{q} + (\mathbf{l} - \mathbf{l}')/\chi_*)$, this imposes a constraint that $(\mathbf{l} - \mathbf{l}')/\chi_*$ be a large-scale wavenumber, which is only satisfied in a small part of the $(\mathbf{l}, \mathbf{l}')$-plane. Therefore we expect a small contribution to $N^{(3/2)}$.

Most of the six-point terms in Eq. (3.57) are eliminated using these criteria. On the first line of (3.57), all of the QQ-terms are eliminated using Approximation 5, except $(Q^{ge}_{\mathbf{k}_1\mathbf{k}_2\mathbf{k}_6} Q^{ge}_{\mathbf{k}_3\mathbf{k}_4\mathbf{k}_5})$ which is non-negligible, and $(Q^{ge}_{\mathbf{k}_1\mathbf{k}_2\mathbf{k}_5} Q^{ge}_{\mathbf{k}_3\mathbf{k}_4\mathbf{k}_6})$ which is a special case: it contains the delta function $\delta^3(\mathbf{k}_L)$, and we neglect it since we are interested in the $N^{(3/2)}$-bias for nonzero k_L. All eight PR-terms on the second line of Eq. (3.57) are eliminated using Approximation 5. Finally, the last six S-terms (out of eight total S-terms) in Eq. (3.67) are eliminated using Approximation 4. For example, the third term in (3.67) contains $P_{\rm lin}(\mathbf{k}_1 + \mathbf{k}_3) = P_{\rm lin}((\mathbf{l} - \mathbf{l}')/\chi_*)$, and $(\mathbf{l} - \mathbf{l}')/\chi_*$ is small-scale (except in a small part of the $(\mathbf{l}, \mathbf{l}')$-plane).

Summarizing this section so far, we have argued only three terms (out of 22) in the six-point function (3.57) contribute significantly to the $N^{(3/2)}$ bias:

$$\begin{aligned}
&\big\langle \delta_g(\mathbf{k}_1)\delta_e(\mathbf{k}_2)\delta_g(\mathbf{k}_3)\delta_e(\mathbf{k}_4)v_r(\mathbf{k}_5)v_r(\mathbf{k}_6)\big\rangle'_{ng} \\
&\quad \approx -\beta_1(k_2)\beta_1(k_4)\left(\frac{k_{5r}k_{6r}}{k_5 k_6}\right) P_{mv}(k_5) P_{mv}(k_6) (2\pi)^3 \delta^3(\mathbf{k}_1 + \mathbf{k}_2 + \mathbf{k}_6) \\
&\quad + \left(\frac{\alpha_2(k_2, k_4)}{n_h} + \beta_1(k_2)\beta_1(k_4) P_{\rm lin}(\mathbf{k}_1 + \mathbf{k}_2)\right) P_{v_r}(\mathbf{k}_5) (2\pi)^3 \delta^3(\mathbf{k}_5 + \mathbf{k}_6)
\end{aligned} \tag{3.69}$$

Using this expression, we now proceed to compute the $N^{(3/2)}$-bias, by plugging the six-point function (3.69) into our general expression (3.45) for the $N^{(3/2)}$-bias, obtaining:

$$\begin{aligned}
N^{(3/2)}(\mathbf{k}_L) &= N^{(0)}_{v_r}(\mathbf{k}_L)^2 \frac{K_*^4}{\chi_*^8} \int \frac{d^2\mathbf{l}}{(2\pi)^2}\frac{d^2\mathbf{l}'}{(2\pi)^2}\frac{d^3\mathbf{q}}{(2\pi)^3} \\
&\quad \times \left[\frac{P_{ge}(k_S)}{P_{gg}(k_S)C_l^{\rm tot}} \frac{P_{ge}(k'_S)}{P_{gg}(k'_S)C_{l'}^{\rm tot}} \beta_1(p)\beta_1(p') \left(\frac{q_r q'_r}{qq'}\right) P_{mv}(q)P_{mv}(q') \right]_{\substack{\mathbf{k}_S=\mathbf{k}_L-\mathbf{l}/\chi_* \\ \mathbf{k}'_S=\mathbf{k}_L-\mathbf{l}'/\chi_* \\ \mathbf{q}'=\mathbf{k}_L-\mathbf{q} \\ \mathbf{p}=-\mathbf{q}+\mathbf{l}/\chi_* \\ \mathbf{p}'=-\mathbf{q}'+\mathbf{l}'/\chi_*}} \\
&\quad + N^{(0)}_{v_r}(\mathbf{k}_L)^2 \frac{K_*^4}{\chi_*^8} \int \frac{d^2\mathbf{l}}{(2\pi)^2}\frac{d^2\mathbf{l}'}{(2\pi)^2}\frac{d^3\mathbf{q}}{(2\pi)^3} \\
&\quad \times \left[\frac{P_{ge}(k_S)}{P_{gg}(k_S)C_l^{\rm tot}} \frac{P_{ge}(k'_S)}{P_{gg}(k'_S)C_{l'}^{\rm tot}} \left(\frac{\alpha_2(p,p')}{n_h} + \beta_1(p)\beta_1(p')P_{\rm lin}(\mathbf{k}_L-\mathbf{q})\right) P_{v_r}(\mathbf{q}) \right]_{\substack{\mathbf{k}_S=\mathbf{k}_L-\mathbf{l}/\chi_* \\ \mathbf{k}'_S=\mathbf{k}_L-\mathbf{l}'/\chi_* \\ \mathbf{p}=-\mathbf{q}+\mathbf{l}/\chi_* \\ \mathbf{p}'=-\mathbf{q}+\mathbf{l}'/\chi_*}}
\end{aligned} \tag{3.70}$$

We make the following approximations inside the integrals, which are valid for $k_L \ll k_S$:

$$N_{v_r}(\mathbf{k}_L) \approx N_{v_r}(0) \qquad k_S \approx p \approx l/\chi_* \qquad k'_S \approx p' \approx l'/\chi_* \tag{3.71}$$

as in the $N^{(1)}$ case (see discussion near Eq. (3.46)). We also write $P_{\rm lin}(q')P_{v_r}(q) = P_{mv}(q')P_{mv}(q)\, q_r^2/(qq')$, to combine the two terms in (3.70) into a single term:

$$\begin{aligned}
N^{(3/2)}(\mathbf{k}_L) \approx N^{(0)}_{v_r}(0)^2 \frac{K_*^4}{\chi_*^8} \int \frac{d^2\mathbf{l}}{(2\pi)^2}\frac{d^2\mathbf{l}'}{(2\pi)^2}\frac{d^3\mathbf{q}}{(2\pi)^3} \\
\times \left[\frac{P_{ge}(k_S)}{P_{gg}(k_S)C_l^{\rm tot}} \frac{P_{ge}(k'_S)}{P_{gg}(k'_S)C_{l'}^{\rm tot}} \left(\frac{\alpha_2(k_S,k'_S)}{n_h} P_{v_r}(q) \right.\right. \\
\left.\left. + \beta_1(k_S)\beta_1(k'_S)\left(\frac{q_r^2+q_r q'_r}{qq'}\right) P_{mv}(q)P_{mv}(q') \right) \right]_{\substack{k_S=l/\chi_* \\ k'_S=l'/\chi_* \\ \mathbf{q}'=\mathbf{k}_L-\mathbf{q}}}
\end{aligned} \tag{3.72}$$

We symmetrize the integrand by replacing $(q_r^2 + q_r q'_r) \to (q_r + q'_r)^2/2 = k_{Lr}^2/2$, and use the definition of $W(l)$ in Eq. (3.49), obtaining:

$$N^{(3/2)}(\mathbf{k}_L) \approx \int \frac{d^2\mathbf{l}}{(2\pi)^2}\frac{d^2\mathbf{l}'}{(2\pi)^2}\frac{d^3\mathbf{q}}{(2\pi)^3} W(l)W(l') \times \left[\frac{1}{P_{ge}(k_S)P_{ge}(k'_S)} \left(\frac{\alpha_2(k_S,k'_S)}{n_h} P_{v_r}(q) + \beta_1(k_S)\beta_1(k'_S)\left(\frac{k_{Lr}^2}{2qq'}\right) P_{mv}(q)P_{mv}(q') \right]_{\substack{k_S=l/\chi_* \\ k'_S=l'/\chi* \\ \mathbf{q}'=\mathbf{k}_L-\mathbf{q}}} \tag{3.73}$$

So far, our approximations should be very accurate in the limit $k_L \ll k_S$. To simplify further, we make two more approximations that are not as precise, but should suffice for an initial estimate of the size of $N^{(3/2)}$. First, we assume that on kSZ scales, the galaxy-electron power spectrum is dominated by its 1-halo term:

$$P_{ge}(k_S) \sim P_{ge}^{1h}(k_S) = \frac{1}{\rho_m n_h} \int dM\, n(M) M u_M(k_S) \tag{3.74}$$

We then write some of the intermediate quantities which appear in the integral (3.73) as follows:

$$\frac{\alpha_2(k_S,k'_S)}{P_{ge}(k_S)P_{ge}(k'_S)} \sim \frac{\big\langle M^2 u_M(k_S) u_M(k'_S)\big\rangle_M}{\big\langle M u_M(k_S)\big\rangle_M \big\langle M' u_{M'}(k'_S)\big\rangle_{M'}} \tag{3.75}$$

$$\frac{\beta_1(k_S)}{P_{ge}(k_S)} \sim \frac{\big\langle M b(M) u_M(k_S)\big\rangle_M}{\big\langle M u_M(k_S)\big\rangle_M} \tag{3.76}$$

where we have introduced the following notation, to denote an average over halos in the catalog:

$$\big\langle \cdots \big\rangle_M = \frac{1}{n_h} \int_{M_{\rm min}}^\infty n(M)\,(\cdots) \tag{3.77}$$

Our second approximation is that the factors $u_M(k_S)$ approximately cancel on the RHS of (3.75), (3.76), since they appear in both the numerator and denominator. Then the right-hand sides of Eqs. (3.75), (3.76) simplify as:

$$\frac{\alpha_2(k_S,k'_S)}{P_{ge}(k_S)P_{ge}(k'_S)} \sim A \qquad\qquad \frac{\beta_1(k_S)}{P_{ge}(k_S)} \sim B \tag{3.78}$$

where the dimensionless constants A, B are defined by:

$$A = \frac{\langle M^2 \rangle_M}{\langle M \rangle_M^2} \qquad\qquad B = \frac{\langle M b(M) \rangle_M}{\langle M \rangle_M} \tag{3.79}$$

Making the approximations (3.78) in Eq. (3.73), the $N^{(3/2)}$-bias simplifies significantly:

$$\begin{aligned} N^{(3/2)}(\mathbf{k}_L) &\sim \int \frac{d^2\mathbf{l}}{(2\pi)^2} \frac{d^2\mathbf{l}'}{(2\pi)^2} \frac{d^3\mathbf{q}}{(2\pi)^3} W(l) W(l') \left[\frac{A}{n_h} P_{v_r}(q) + \frac{B^2 k_{Lr}^2}{2qq'} P_{mv}(q) P_{mv}(q') \right]_{\mathbf{q}'=\mathbf{k}_L-\mathbf{q}} \\ &= \frac{A}{n_h} \langle v_r^2 \rangle + \frac{B^2 k_{Lr}^2}{2} \int \frac{d^3\mathbf{q}}{(2\pi)^3} \left[\frac{P_{mv}(q) P_{mv}(q')}{qq'} \right]_{\mathbf{q}'=\mathbf{k}_L-\mathbf{q}} \end{aligned} \tag{3.80}$$

where in the second line, we have used $\int d^2\mathbf{l}/(2\pi)^2 \, W(l) = 1$, and $\langle v_r^2 \rangle$ denotes the variance of the radial velocity field:

$$\langle v_r^2 \rangle \equiv \int \frac{d^3\mathbf{k}}{(2\pi)^3} P_{v_r}(k) = \int \frac{k^2 \, dk}{6\pi^2} P_v(k) \tag{3.81}$$

Finally, we note that in the 3-d integral (3.80), one angular integral can be done analytically, reducing to a 2-d integral. We omit the details and quote the final result:

$$N^{(3/2)}(\mathbf{k}_L) \sim \frac{A}{n_h} \langle v_r^2 \rangle + \frac{B^2 k_{Lr}^2}{8\pi^2 k_L} \int_0^\infty dq \int_{|k_L - q|}^{k_L+q} dq' \, P_{mv}(q) P_{mv}(q') \tag{3.82}$$

To angle-average over $\mathbf{k}_L$ (as we will do in Figure 3.6 shortly), we replace $k_{Lr}^2 \to k_L^2/3$ in the second term. The A-term in Eq. (3.82) is constant in k_L, and the B-term goes to zero at both low and high k_L, with a peak at $k_L \sim 0.03$ Mpc^{-1}.

3.5.4 Numerical evaluation and discussion

In the last few sections, we identified several new contributions to the kSZ reconstruction noise, going beyond the $N^{(0)}$-bias from [182]. Can these new contributions explain the excess noise in our simulations, shown previously in Figure 3.4?

In Figure 3.6, we numerically evaluate the $N^{(0)}$, $N^{(1)}$, and $N^{(3/2)}$ biases as follows. All power spectra are angle-averaged over $\mathbf{k}$. We compute the $N^{(0)}$-bias using Eqs. (3.30), (3.31), but to maximize consistency with our simulations, we replace integrals (either $\int d^3\mathbf{x}$, $\int d^3\mathbf{k}$, or $\int d^2\mathbf{l}$) by sums over the discrete set of pixels (or Fourier modes) used in our simulation pipeline.

We compute the angle-averaged $N^{(1)}$-bias using Eq. (3.52), and the $N^{(3/2)}$-bias using Eq. (3.82). Note that (3.52) and (3.82) are approximations which are accurate for $k \to 0$. To evaluate (3.82), we need numerical values for the constants A, B defined in Eq. (3.79). We get $A = 2.3$ using the measured halo mass function from our N-body simulations. We approximate $B \sim b_g$, where $b_g = 3.24$ is the halo bias of our simulations. (This is an approximation since b_g is calculated weighting all halos equally, whereas B is the mass-weighted halo bias.)

Our first result in Figure 3.6 is that the $N^{(1)}$-bias is negligible. As a check on our $N^{(1)}$ calculation, we compared to Gaussian Monte Carlo simulations which are designed to isolate the $N^{(1)}$-bias, and find good agreement. In more detail, each Gaussian simulation consists of 3-d Gaussian fields v_r, δ_g, δ_e with the same auto and cross power spectra as the Quijote simulations. For each triple (i, j, k) of Gaussian simulations, let $\hat{v}_r^{ijk}$ denote the kSZ velocity reconstruction using fields v_r^i, δ_g^j, δ_e^k from simulations i, j, k. Then the cross power spectrum between $\hat{v}_r^{ijk}$ and $\hat{v}_r^{ikj}$ is equal to $N^{(1)}$, with no $N^{(0)}$ or $N^{(3/2)}$ contribution, since $N^{(1)}$ is the only surviving contraction in Eq. (3.41).

Our main result in Figure 3.6 is that the $N^{(3/2)}$-bias agrees well with the excess noise seen in simulations! (Surprisingly, the agreement holds to high k, even though we have freely made approximations which are only valid for $k \to 0$.) Our conclusion is that higher-order biases are real, non-negligible contributions to kSZ reconstruction noise which can be calculated systematically in the halo model.

The preceding results have assumed fiducial survey parameters from §3.2. In this chapter, we will not explore dependence on galaxy density n_g or redshift z, although this should be fairly straightforward using our expressions for $N^{(0)}$ and $N^{(3/2)}$ bias. However, one parameter which is easy to analyze is the CMB noise level. In the approximation (3.82), the $N^{(3/2)}$-bias is independent of the CMB noise. On the other hand, Eq. (3.26) shows that the $N^{(0)}$-bias is proportional to $C_l^{\rm tot} = (C_l + N_l)$ evaluated on kSZ scales $l \sim 5000$. Therefore, as the CMB experiment becomes more sensitive, the $N^{(3/2)}$-bias becomes more important, relative to $N^{(0)}$.

Since our simulations use futuristic CMB noise parameters (0.5 μK-arcmin, $\theta_{\rm fwhm} =$ 1 arcmin), and galaxy survey parameters comparable to DESI, it seems likely that $N^{(3/2)}$ will be small (relative to $N^{(0)}$) for DESI in combination with near-future CMB experiments such as Simons Observatory. However, if DESI is replaced by an experiment with larger galaxy density (e.g. Rubin Observatory), or if the CMB noise is $\lesssim 1$ μK-arcmin, then $N^{(3/2)}$ may be important.

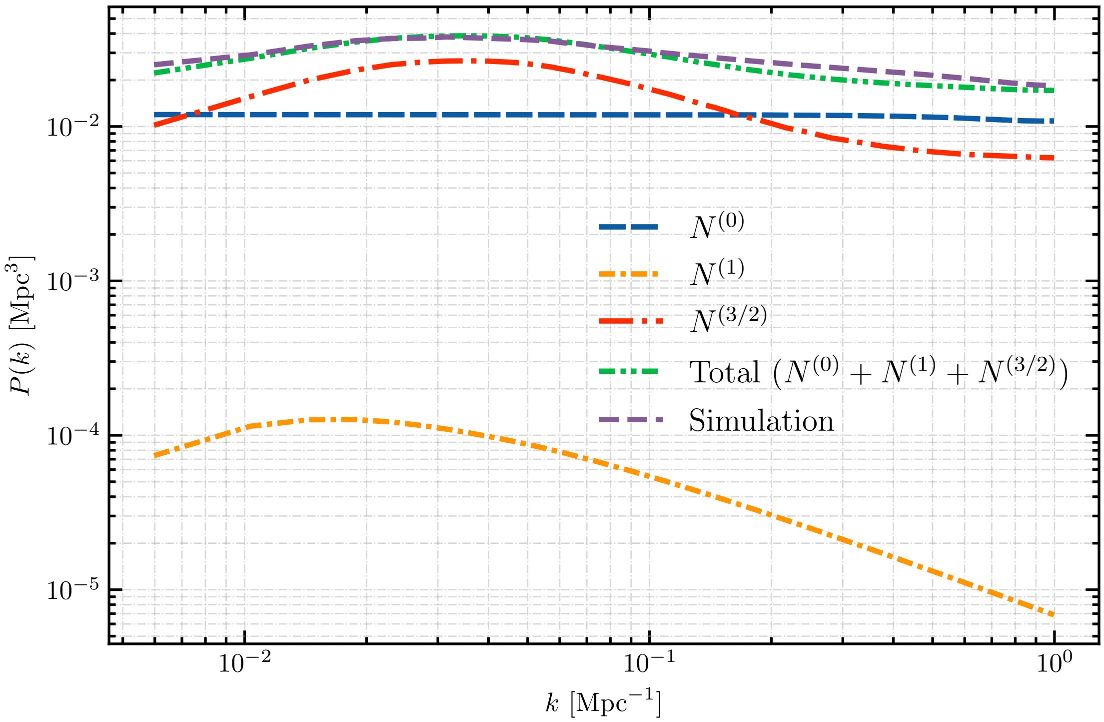

Figure 3.6: Contributions to the KSZ reconstruction noise, computed as described in §3.5.4. The reconstruction noise in simulations agrees well with the sum of analytic contributions $(N^{(0)} + N^{(1)} + N^{(3/2)})$. All noise power spectra have been angle-averaged over $\mathbf{k}$, and $N^{(1)}$ and $N^{(3/2)}$ have been computed using approximations which are valid for $k \to 0$.

3.6 Recovering f_{NL} with an MCMC pipeline

In this section, we develop an MCMC-based analysis pipeline which recovers the value of f_{NL} from a galaxy catalog and CMB map. We demonstrate the ability of our pipeline to recover the correct value of f_{NL}, and validate its statistical errors with Monte Carlo simulations.

In our pipeline, f_{NL} sensitivity arises entirely from f_{NL} dependence of the galaxy bias: $b(k) = b_g + f_{NL} b_{ng}/k^2$. The velocity reconstruction $\hat{v}_r$ is not directly f_{NL}-sensitive. However, $\hat{v}_r$ can be used to cancel sample variance in the galaxy field, thus improving the statistical error on f_{NL} relative to a measurement of δ_g alone. The idea of sample variance cancellation was introduced by Seljak in [173]. Sample variance cancellation is automatically incorporated by our MCMC pipeline, since we write down the full posterior likelihood $\mathcal{L}(f_{NL}|\delta_g, \hat{v}_r)$ (Eq. (3.90) below), which includes sample variance cancellation automatically.

When constructing our posterior likelihood, we assume that the reconstruction noise power spectrum is given by the $N^{(0)}$-bias in Eq. (3.26). This neglects the $N^{(3/2)}$ bias, even though we have shown that $N^{(3/2)}$ is comparable to $N^{(0)}$ for our fiducial survey parameters. In principle, neglecting $N^{(3/2)}$ can produce both biased f_{NL} estimates and underestimated statistical errors (as in the CMB lensing case). However, in this section we will find that within statistical errors of our simulations, our MCMC pipeline recovers unbiased estimates of f_{NL}, with scatter consistent with a Fisher matrix forecast.

In our pipeline, we have perfect knowledge of the galaxy-electron power spectrum $P_{ge}(k_S)$, and therefore we expect the reconstruction bias b_v to equal 1. However, in our MCMC's, we will include b_v as a nuisance parameter and marginalize it, so that our analysis is more representative of real experiments. As a consistency check, we expect the value of b_v recovered from the MCMC's to be consistent with 1.

3.6.1 MCMC pipeline description

The inputs to our pipeline are a realization $\delta_h(\mathbf{k})$ of the 3-d halo field, and the kSZ velocity reconstruction $\hat{v}_r(\mathbf{k})$. We want to constrain the cosmological parameter f_{NL}, and the nuisance parameters b_g, b_v. Here, b_g is the Gaussian halo bias, and b_v is the kSZ velocity reconstruction bias from §3.4.2. For notational compactness, let π denote the three-component parameter vector $\pi = (f_{NL}, b_g, b_v)$.

We start by writing down the two-point statistics of the fields δ_g and $\hat{v}_r$. For each Fourier mode $\mathbf{k}$, let $\theta(\mathbf{k})$ be the two-component vector of fields:

$$\theta(\mathbf{k}) = \begin{pmatrix} \delta_h(\mathbf{k}) \\ \hat{v}_r(\mathbf{k}) \end{pmatrix} \tag{3.83}$$

Let $C(\mathbf{k},\pi)$ be the 2-by-2 Hermitian matrix defined by:

$$\left\langle \theta(\mathbf{k})\, \theta(\mathbf{k}')^\dagger \right\rangle = C(\mathbf{k},\pi)\, (2\pi)^3 \delta^3(\mathbf{k}-\mathbf{k}') \tag{3.84}$$

We model $C(\mathbf{k},\pi)$ on large scales by:

$$\begin{aligned} C_{11}(k,\pi) &= b_h(k,\pi)^2 P_{\rm lin}(k) + \frac{1}{n_h} && (3.85) \\ C_{12}(\mathbf{k},\pi) &= -ik_r \left(\frac{faH}{k^2}\right) b_v\, b_h(k,\pi) P_{\rm lin}(k) && (3.86) \\ C_{22}(\mathbf{k},\pi) &= k_r^2 \left(\frac{faH}{k^2}\right)^2 b_v^2\, P_{\rm lin}(k) + N_{v_r}^{(0)}(\mathbf{k}) && (3.87) \end{aligned}$$

where $b_h(k,\pi)$ is the non-Gaussian halo bias:

$$b_h(k,\pi) = b_g + f_{NL} \frac{2\delta_c(b_g - 1)}{\alpha(k,z)} \qquad (\delta_c = 1.42) \tag{3.88}$$

and $N_{v_r}^{(0)}(\mathbf{k})$ was given in Eq. (3.26). The model for $C(\mathbf{k},\pi)$ in Eqs. (3.85)–(3.87) follows if we assume that δ_h and $\hat{v}_r$ are modeled as:

$$\begin{aligned} \delta_h(\mathbf{k}) &= b_h(k)\, \delta_m(\mathbf{k}) + (\text{Poisson noise}) \\ \hat{v}_r(\mathbf{k}) &= ib_v k_r \frac{faH}{k} \delta_m(\mathbf{k}) + (\text{Reconstruction noise}) \end{aligned} \tag{3.89}$$

In the previous section, we tested these assumptions systematically, thus validating our model (3.85)–(3.87) for the two-point function $C(\mathbf{k},\pi)$.

However, to run an MCMC we need to go beyond the two-point function, by writing down a model for the posterior likelihood $\mathcal{L}(\pi|\theta)$ for parameter vector π, given data realization $\theta(\mathbf{k})$. Here, we simply assume the Gaussian likelihood derived from the two-point function in Eqs. (3.85)–(3.87):

$$\mathcal{L}(\pi|\theta) \propto \prod_{\mathbf{k}} \big(\text{Det}\, C(\mathbf{k},\pi)\big)^{-1/2} \exp\left(-\frac{\theta(\mathbf{k})^\dagger C(\mathbf{k},\pi)^{-1} \theta(\mathbf{k})}{2V} \right) \tag{3.90}$$

where the survey volume V on the RHS arises from our finite-volume Fourier convention in Eq. (3.7). This "field-level" likelihood function makes fewer approximations than a likelihood function based on power spectrum bandpowers. However, we emphasize that the likelihood (3.90) treats δ_g and $\hat{v}_r$ as Gaussian fields, and results from previous sections do not imply its validity. Indeed, the main purpose of this section is to validate the Gaussian likelihood function, by showing that it leads to valid constraints on f_{NL}.

We truncate the likelihood (3.90) at $k_{\max} = 0.012$ Mpc^{-1}. The posterior likelihood is sampled using Goodman-Weare sampling algorithm [85] implemented in the public library `emcee` [78]. We use flat priors over a reasonable range of values for all three model parameters of the model, and run the chain long enough to fulfil recommended convergence criterion based on correlation length.

3.6.2 Unbiased f_{NL} estimates from MCMC

We now present results from running our MCMC pipeline on N-body simulations. First, we check for additive bias in f_{NL}, by confirming that when the MCMC pipeline is run on simulations with $f_{NL} = 0$, there is no bias toward positive or negative f_{NL}.

In Figure 3.7, we jointly analyze all 100 Quijote simulations with $f_{NL} = 0$, by multiplying together their posterior likelihoods. We run three versions of the MCMC pipeline as follows. First, we constrain parameters using the halo field alone (δ_h). Second, we use our standard setup described in the previous section, where we include the halo field and the kSZ velocity reconstruction ($\delta_h + \hat{v}_r$). Third, we use the halo field and a perfect, noise-free realization of the matter overdensity ($\delta_h + \delta_m$). Note that in the second case ($\delta_h + \hat{v}_r$), the MCMC parameters are (f_{NL}, b_g, b_v), whereas in the first and third cases, the parameters are (f_{NL}, b_g). In the second case ($\delta_h + \hat{v}_r$), the likelihoods in Figure 3.7 are marginalized over the additional parameter b_v.

The f_{NL} constraint in Figure 3.7 from ($\delta_h + \hat{v}_r$) is significantly better than the δ_h-only constraint, and slightly worse than the ($\delta_h + \delta_m$)-constraint. This shows that sample variance cancellation between δ_h and $\hat{v}_r$ is happening, and the level of cancellation is comparable to what would be obtained from a perfect measurement of δ_m.

From Figure 3.7, we can also conclude that the f_{NL} estimates from our MCMC pipeline are not additively biased. The combined ($\delta_h + \hat{v}_r$) likelihood is consistent with $f_{NL} = 0$, within the statistical error from 100 simulations. Any additive f_{NL} bias must be smaller than this statistical error (roughly $\Delta f_{NL} = 2$).

Next, we check for multiplicative bias in f_{NL}, by analyzing simulations with $f_{NL} \neq 0$ and confirming that we recover the correct value of f_{NL}. In Figure 3.8, we present results

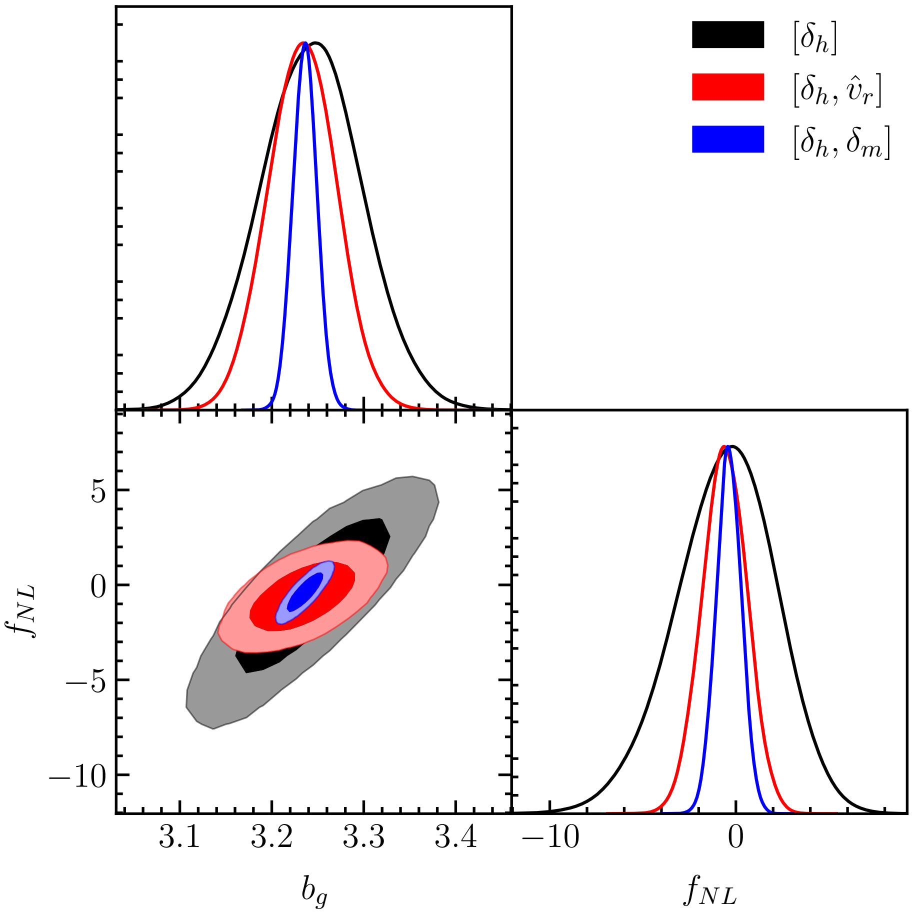

Figure 3.7: MCMC posteriors on (b_g, f_{NL}) from combined analysis of 100 high resolution Quijote simulations with $f_{NL} = 0$. The three likelihoods correspond to MCMC analysis of the halo field alone (δ_h), joint analysis of the halo field and kSZ velocity reconstruction $(\delta_h, \hat{v}_r)$, and joint analysis of the halo field and the noise-free matter field (δ_h, δ_m). In the second case $(\delta_h, \hat{v}_r)$, likelihoods have been marginalized over the additional nuisance parameter b_v.

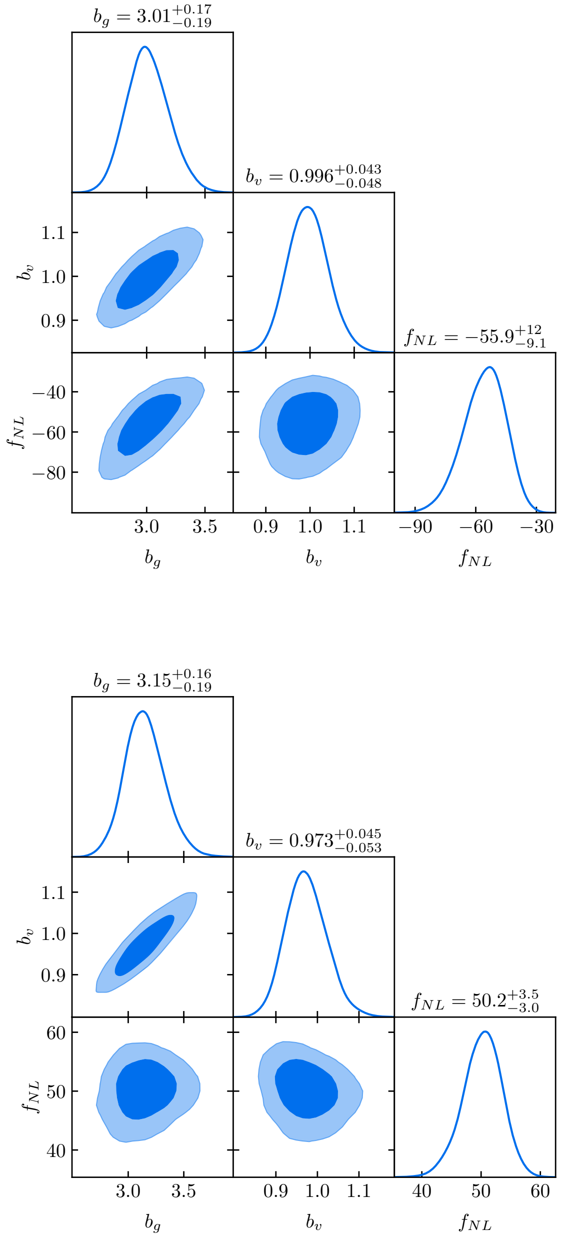

Figure 3.8: MCMC constraints for $f_{NL} = -50$ (top panel) and $f_{NL} = 50$ (bottom). Each panel combines likelihoods from four N-body simulations, each with volume 1 h^{-3} Gpc^3. The recovered f_{NL} values are consistent with the true values, within statistical errors.

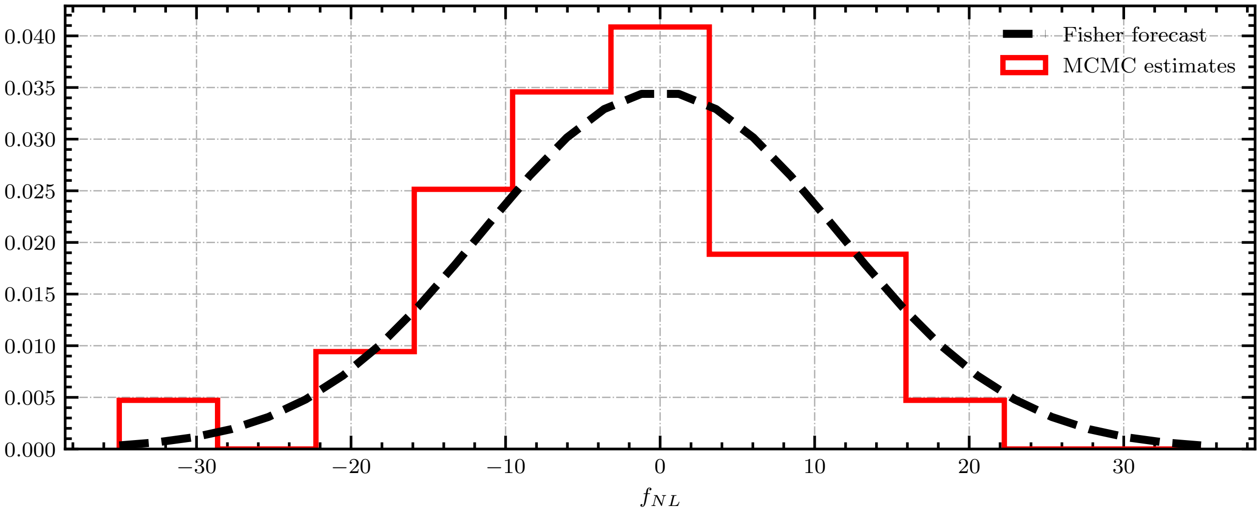

Figure 3.9: A test of the error estimates from our MCMC pipeline. The solid histogram contains one f_{NL} estimate from each of 100 high-res Quijote simulations with $f_{NL} = 0$, obtained by taking the median of the f_{NL} posterior likelihood (after marginalizing over b_g, b_v). The dashed line is a Gaussian whose width is equal to the Fisher forecasted error on f_{NL}. The two distributions have equal widths, within statistical errors from 100 simulations.

from non-Gaussian N-body simulations with $f_{NL} = \pm 50$. It is seen that the MCMC pipeline recovers the correct value of f_{NL} within its reported statistical error (around 10–20%). The total simulation volume is smaller (8 h^{-3} Gpc^3) here than in the $f_{NL} = 0$ case (100 h^{-3} Gpc^3), where Quijote simulations are available. Therefore, we cannot characterize the behavior of the MCMC pipeline as precisely as we can in the $f_{NL} = 0$ case. However, the current observational situation is that f_{NL} has not been detected, and the priority for upcoming experiments will be testing the null hypothesis that $f_{NL} = 0$. In this situation, it should suffice to have a precise characterization of the pipeline on simulations with $f_{NL} = 0$, and a ≈10-20% test for bias on simulations with nonzero f_{NL}.

3.6.3 Consistency between MCMC results and Fisher matrix forecasts

The tests in the previous section show that the MCMC pipeline recovers unbiased estimates of f_{NL}, but do not test statistical errors on f_{NL} inferred from the posteriors. In this section, we will validate f_{NL} errors from the MCMC pipeline.

For the sake of discussion, we briefly describe a completely rigorous, Bayesian procedure for validating f_{NL} errors (even though this is not what we will end up doing!) Suppose we choose a prior $p(f_{NL})$, and generate a large number of simulations with f_{NL} values sampled from the prior. For each simulation s, we use MCMC to compute the posterior likelihood $p(f_{NL}|s)$, and rank the true value of f_{NL} within the posterior likelihood, to obtain a quantile $0 < q < 1$. Then we should find that q is uniform distributed, if the posterior likelihoods have been computed correctly. This is a precise statement that can be proved rigorously. This check validates error estimates from the MCMC pipeline, in the sense that if the MCMC pipeline overestimates its error bars (i.e. returns posterior likelihoods which are too wide), then the distribution of q-values will be narrower than uniform.

The difficulty with this method is that it would require many simulations with $f_{NL} \neq 0$, which would be very expensive. Instead, we will use an alternative method which uses only simulations with $f_{NL} = 0$ (so that we can use the Quijote simulations). For each such simulation, let $f_{NL}^{\rm med}$ be the median of the MCMC posterior likelihood for f_{NL} (marginalized over b_g, b_v). Let $\sigma(f_{NL}^{\rm med})$ be the RMS scatter in $f_{NL}^{\rm med}$ over 100 Quijote simulations. We will compare $\sigma(f_{NL}^{\rm med})$ to the Fisher forecasted statistical error on f_{NL} (which we will denote $\sigma_F(f_{NL})$). Intuitively, we expect that $\sigma(f_{NL}^{\rm med}) \approx \sigma_F(f_{NL})$, but this is not rigorously guaranteed, so this test is not quite as precise as the Bayesian test described above. However, the Cramér-Rao inequality implies $\sigma(f_{NL}^{\rm med}) \geq \sigma_F(f_{NL})$.

We briefly describe the implementation of our Fisher matrix forecast. The 3-by-3 Fisher matrix is given by:

$$F_{ab} = \frac{1}{2} \sum_{\mathbf{k}} \mathrm{Tr} \left[C(\mathbf{k},\pi)^{-1} \frac{\partial C(\mathbf{k},\pi)}{\partial \pi_a} C(\mathbf{k},\pi)^{-1} \frac{\partial C(\mathbf{k},\pi)}{\partial \pi_b} \right] \tag{3.91}$$

where a, b index elements of the parameter vector $(\pi_1, \pi_2, \pi_3) = (f_{NL}, b_g, b_v)$. The 2-by-2 covariance matrix $C(\mathbf{k}, \pi)$ was defined previously in Eqs. (3.85)–(3.87), and parameter derivatives of C are straightforward to compute. The Fisher-forecasted statistical error on f_{NL}, marginalized over (b_g, b_v), is given by $\sigma_F(f_{NL}) = \sqrt{(F^{-1})_{11}}$.

In Figure 3.9, the solid histogram shows values of $f_{NL}^{\rm med}$ for all 100 Quijote simulations. The dashed curve is a Gaussian whose width is equal to the Fisher forecasted error on f_{NL}. We find that $\sigma(f_{NL}^{\rm med}) = 10.54$ and $\sigma_F(f_{NL}) = 11.54$. These values are equal (at 2σ) within statistical errors from 100 Quijote simulations. This agreement was not guaranteed in advance, since the Fisher forecast makes approximations (neglecting $N^{(3/2)}$-bias, treating δ_g and $\hat{v}_r$ as Gaussian fields), whereas $\sigma(f_{NL}^{\rm med})$ is a Monte Carlo error estimate based on N-body simulations. The observed agreement directly valdiates previous Fisher forecasts based on kSZ velocity reconstruction (e.g. [183, 147]).

3.7 Discussion

KSZ velocity reconstruction is a promising method for constraining cosmology. However, almost all work to date (with the notable exception of [46]) has been based on analytic modeling which has not been tested with simulations. In this chapter, we have made a detailed comparison between analytic models and N-body simulations. Overall, we have found good agreement, concluding with an end-to-end pipeline which recovers unbiased estimates of f_{NL} from simulated galaxy and kSZ datasets, with statistical errors which are consistent with a Fisher matrix forecast. This initial study is a starting point for future refinements, and we list some possibilities here:

- We have found a discrepancy between velocity reconstruction noise in our N-body simulations, and the kSZ $N^{(0)}$-bias which is typically used in forecasts. Using the halo model, we revisited the calculation of the reconstruction noise power spectrum, and found new terms: the kSZ $N^{(1)}$ and $N^{(3/2)}$ biases. We computed these terms numerically and found that $N^{(1)}$ is negligible, while $N^{(3/2)}$ matches the excess noise seen in simulations (Figure 3.6). Our final expression for $N^{(3/2)}$ (Eq. (3.82)) is algebraically simple enough that it should be straightforward to include in future forecasts or data analysis.

- Similarly, we have found that the non-Gaussian bandpower covariance of the reconstruction noise can be large (§3.4.3). It would be interesting to model this effect, e.g. using the halo model.

  For our choice of fiducial survey parameters (§3.2), neither the non-Gaussian bandpower covariance nor the $N^{(3/2)}$-bias has much impact on the bottom-line f_{NL} constraint. However, this may not be the case for other choices of survey parameters (CMB noise, galaxy density, redshift, etc.), and systematic exploration of parameter dependence would be valuable.

- We have used collisionless N-body simulations, making the approximations that electrons trace dark matter ($\delta_e = \delta_m$) and galaxies are in one-to-one correspondence with dark matter halos ($\delta_g = \delta_h$). These are crude approximations, and our simulations overpredict the small-scale galaxy-electron power spectrum $P_{ge}(k_S)$ by an order-one factor. We do not think this is an issue for purposes of this work, where our goal is to test agreement between simulations and theory under self-consistent assumptions. However, it would be good to check this by incorporating baryonic physics, for example using the Illustris-TNG simulation [148].

- We have used a snapshot geometry (§3.1.1), which could be generalized to a lightcone geometry with redshift evolution.

- We have not included CMB foregrounds and other non-Gaussian secondaries (e.g. lensing). This issue is not as serious as it sounds, since there are symmetry arguments which show that the velocity reconstruction bias produced by foregrounds and secondaries should be small.

  In the case of CMB lensing, there is a symmetry which reverses the sign of the primary CMB anisotropy $T_{\rm pri} \rightarrow -T_{\rm pri}$ while leaving late-universe LSS unchanged. Strictly speaking, this is an approximate symmetry which assumes that the last scattering surface and the late universe are statistically independent, but this is an excellent approximation on small scales. Under this symmetry, the lensed CMB is odd ($T_{\rm len} \rightarrow -T_{\rm len}$), whereas the kSZ and other secondaries/foregrounds are even ($T \rightarrow T$). This implies that lensing cannot produce a velocity reconstruction bias $\langle \hat{v}_r \rangle$.

  Most non-kSZ secondaries (including CMB lensing, but also e.g. tSZ or CIB) are even under radial reflection symmetry, whereas the kSZ is odd. This implies that there is no velocity reconstruction bias. However, radial reflection is only an approximate symmetry in a lightcone geometry (unlike the snapshot geometry where it is exact), so there will be some residual bias which should be quantified with simulations. Additionally, even if foregrounds/secondaries produce minimal velocity reconstruction bias, their non-Gaussian statistics may produce extra reconstruction noise (relative to a Gaussian field), and it would be useful to quantify this with simulations.

- A natural extension of this work would be to study the effect of redshift space distortions (RSD's) or photometric redshift errors. Ref. [183] makes analytic predictions for the effect of RSD's and photo-z errors on kSZ velocity reconstruction, on large scales and assuming a simplified photo-z model. It would be interesting to compare these predictions to simulations. Additionally, simulations could be used to study small-scale RSD's ("Fingers of God") and catastrophic photo-z errors, where analytic predictions are difficult.

  If RSD's are included in the simulations, then it should be possible to break the kSZ optical depth degeneracy, as first proposed in [188]. More precisely, the $\langle g v_r \rangle$ correlation function contains terms proportional to μ^0 and μ^2, and by comparing the amplitude of these terms, the parameter combination f/b_g can be constrained, with no contribution from b_v. It would be very interesting to test this picture with simulations.

- We have focused on constraining f_{NL}, and it would be interesting to study other applications of kSZ tomography, for example using sample variance cancellation to constrain the RSD parameter $f = \partial \log D / \partial \log a$. Similarly, we could generalize the non-Gaussian model, by introducing scale-dependent f_{NL}, or the "g_{NL} model" with ζ^3-type non-Gaussianity.

Acknowledgements

We thank Niayesh Afshordi, Neal Dalal, Simone Ferraro, Matt Johnson, Mathew Madhavacheril, Moritz Münchmeyer, and Emmanuel Schaan for discussions. KMS was supported by an NSERC Discovery Grant, an Ontario Early Researcher Award, a CIFAR fellowship, and by the Centre for the Universe at Perimeter Institute. Research at Perimeter Institute is supported by the Government of Canada through Industry Canada and by the Province of Ontario through the Ministry of Research & Innovation.

Chapter 4

MCMC analysis pipeline for CHIME/FRB

In this chapter, we present an MCMC pipeline for performing parameter inference on Fast Radio Bursts (FRBs) observed by the CHIME/FRB experiment. CHIME (Canadian Hydrogen Intensity Mapping Experiment) is a modern interferometric telescope in Canada with a dedicated pipeline for detecting these mysterious radio transients. The FRB pulses detected in real-time by CHIME are subsequently fit with a physically motivated FRB model in an offline analysis. Currently, we have a fitting routine in place that fits a model by directly optimizing a likelihood. Using a Bayesian approach with MCMC sampling, we can go beyond this simple approach to better characterize their properties. We discuss the details of the experiment, the model that we fit and the steps taken to make the MCMC sampling process computationally time efficient, so as to make the Bayesian fitting a practical approach for analysing the large number of FRBs that CHIME is detecting.

FRBs are extremely bright pulses of very short ($\sim$millisecond) duration and transient nature that are seen in the radio part of the electromagnetic spectrum. Discovered for the first time in 2007 [127] in the archival data of the Parkes radio telescope in Australia, FRBs have emerged as one of the most exciting phenomena in the field of time-domain astronomy [51, 157]. They show up sporadically in the radio data as solitary pulses and come from random locations in the sky. They are highly coherent with spectral and temporal features reminiscent of pulsars but unlike pulsars, they do not show periodic emission. Seen across a wide range of frequencies between 110 MHz to 8 GHz [79, 162], their sky distribution is quite isotropic [106] and they have been found to be coming from cosmological distances [47, 164, 24]. However, what truly sets them apart is their energy scale, which is orders of magnitude larger than a typical pulse from a pulsar (see Figure 4.3). Explaining their origin has become a central unresolved problem in astronomy, and numerous theories have been proposed to explain the extraordinary emission mechanism that powers them and progenitors that host them [161].

To date, we have detected hundreds of FRBs across several telescopes [127, 196, 174], with a majority of them being one off events where only a single emission from the source was observed. However, a significant number of FRB sources have been seen to repeat *i.e.* the same source emits pulses intermittently [186, 14, 18]. These repeaters have proven very consequential. Not only do they rule out cataclysmic models for their sources, and in turn for at least a sub-population of FRBs, they also allow us to point powerful telescopes in their direction for follow-up studies [47]. These powerful telescopes often use interferometry [139, 195] to combine simultaneous observations of the source using receivers with very long baselines (separation) and localize the source within a galaxy with sub-arcsecond precision. The localizations facilitate characterisation of parent galaxies, shedding light on the environment where their progenitors reside. These localizations have confirmed the long held belief that FRBs are not just extra-galactic but are coming from cosmological distances.

Being a novel, transient phenomenon, FRBs generally remained elusive for a considerable period of time, with less than 20 detections in the decade following their first detection [156]. Traditional telescopes usually have one or more limitations that make them inefficient when it comes to detecting FRBs. Some of the common shortcomings include limited sensitivity, limited sky exposure, narrow bandwidths, small field of view or lack of real-time data processing and analysis tools. As a result, FRB detections remained sporadic even when their rate was estimated to be as high as 1000 per sky per day. All this has changed with the advent of CHIME/FRB [13]. With its large field of view, high sensitivity, broad bandwidth and specifically optimized detection pipeline, it has been extremely prolific in detecting FRBs. So far, CHIME/FRB has detected over 2000 FRBs, thereby increasing the total count by a factor of 15.

The science case for CHIME goes beyond just detecting FRBs. FRBs offer a new window into the Universe and have several potential astrophysical and cosmological applications [126, 160, 137, 75, 136]. By physically modelling an FRB pulse, we can tease out a lot of useful information. Using the intensity data, CHIME/FRB can estimate the arrival time of FRBs with millisecond precision. High precision of time estimates are needed when associating coincident emissions during multi-wavelength observations across

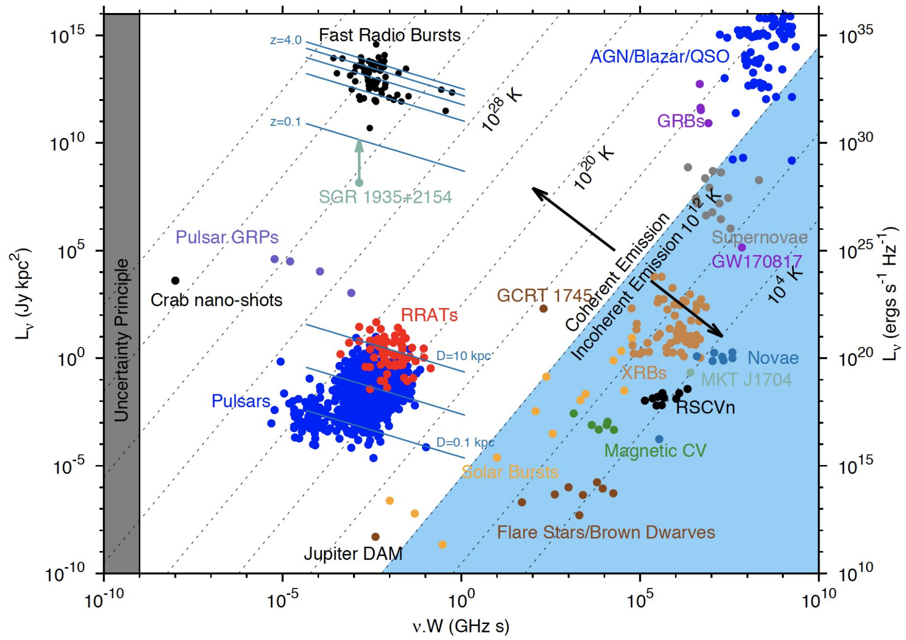

Figure 4.1: A figure showing the unique place FRBs occupy in the luminosity-width plane. The widths of FRBs, which constrain the size of their emission region, are similar to pulsars but their spectral luminosity is several orders of magnitude larger. Their brightness temperature too is exceptionally high. Figure credit: Evan Keane.

telescopes. An example of this is the recent discovery of bursts coming from a galactic magnetar — SGR 1935 2154 that was seen by several telescopes [15, 141, 191, 36]. Precise arrival time estimates are also needed for resolving short time-scale features as well as any short-timescale periodicity, both of which hold clues into the origin of FRBs. The width of a coherent pulse corresponds to the light travel time through the pulse emitting region, and therefore the pulse width of an FRB constrains the size of emission engines, providing us useful hints about the emission mechanism. The spectrum of an FRB is another feature that sheds light on their emission mechanism. Lastly, the coherent pulses undergo dispersion, scattering and scintillation due to propagation effects which modifies their appearance. All these effects can be modelled in the intensity data to learn about the intervening media. The high spectral resolution of CHIME/FRB helps with the precise estimation of frequency dependent features including spectrum, dispersion measure and scattering.

This chapter goes into the details of FRB modelling and presents an end-to-end MCMC pipeline for estimating the model parameters from CHIME/FRB intensity data. The pipeline builds upon the native fitting code `fitburst` to incorporate qualities of Bayesian formulation of statistical inference. It uses the high-performance python library `JAX` for model composition and likelihood evaluation and is capable of running on both CPUs and GPUs. To efficiently sample the posterior, we develop a vectorized and just-in-time compiled implementation of the popular affine-invariant MCMC sampling algorithm [85] that executes each step of iteration in a vectorized fashion. Moving the likelihood evaluation and sampling to GPU accelerates the analysis by leveraging their high through-puts and is particularly well suited for our use case. The GPU version of the code dramatically reduces the wall-time for analysis. This has allowed us to pursue an approach to model fitting where we we fit progressively complex models, starting with a simple model defined on a sub-space of parameters, and eventually converge to the model that best fits the data. With this exploratory workflow, we have found that our MCMC pipeline gives us a much higher rate of success compared to `fitburst` when fitting models to data using an automated pipeline without manual intervention. Given the time taken by the this MCMC pipeline is of the same order as the direct fitting pipeline, we anticipate that more and more events would be analyzed by this pipeline going into the future. The MCMC sampler is made public at `https://github.com/utkarshgiri/jaims`.

4.1 Highlights from CHIME/FRB

- CHIME/FRB became operational in a precommissioning mode in mid 2018 and detected its first FRB on 2018 July 25. Not only was this observation monumental for CHIME/FRB and laid to rest many uncertainties regarding its operation, but it was also the first event to be seen at such a low frequency and provided much needed motivation for continued observation at low frequencies where many prominent telescopes operate. In [16], we reported observations of 13 FRBs, including an event that turned out to be a repeater, the second repeater ever seen. The repeater was analyzed in [14].
- In [18], CHIME/FRB reported a set of 8 repeating FRBs along with their ∼arcminute localizations to aid follow-up studies by the FRB community.
- A major clue towards understanding the origin of FRB was the high-significance observation of a ∼16 day periodic activity in FRB 180916.J0158+65 [15]. The FRB was seen to be active in a period of 5 days with no activity outside it. Both an

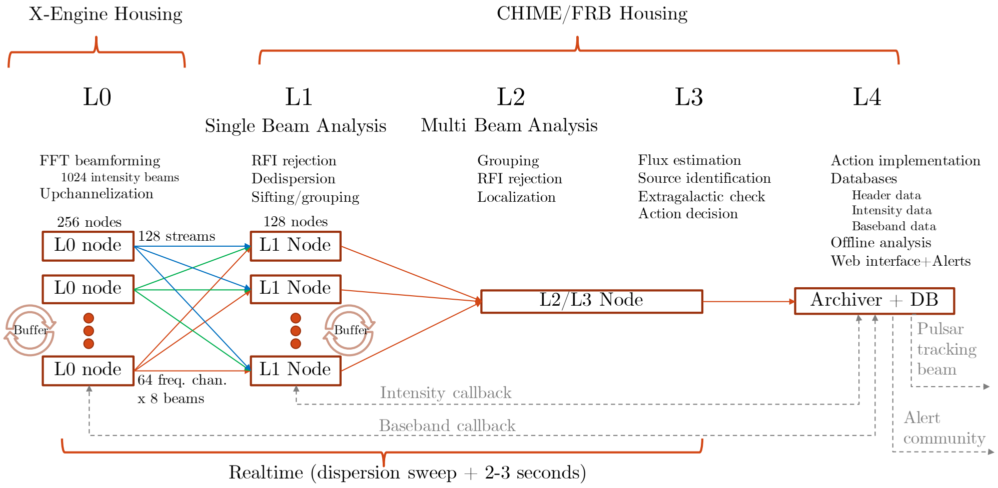

Figure 4.2: Schematic of the CHIME telescope signal path

intrinsic emission modulation as well as external geometrical or physical model could explain the observed periodicity.

- In another milestone paper [19], we reported the detection of two FRB like bursts coming from the direction of galactic magnetar SGR-1935 2154. The bursts were observed during a period of unusually high activity from the SGR, lasting over several days [36]. Remarkably, the bursts were coincident with peaks in X-ray light-curves as seen by several X-ray and Gamma-ray telescopes [141, 191]. This observation has given a strong boost to theories proclaiming magnetars to be the FRB engines.
- CHIME/FRB presented a catalogue of 535 FRBs [17], the first catalogue release of this size and scope observed in a single survey with uniform selection effects. The catalogue paper was accompanied with several science papers that perform population analysis of the events.

4.2 Instrument

The Canadian Hydrogen Intensity Mapping Experiment (CHIME) is a Canadian interferometric telescope at the Dominion Radio Astrophysical Observatory in British Columbia, Canada. Designed primarily with the aim of mapping neutral hydrogen in the universe

[149, 23], it was soon realized that the same instrument would be ideal for detecting transients like FRBs and led to the development of a separate project with a dedicated back end for real-time detection of FRBs — CHIME/FRB .

The CHIME instrument has been described in detail in an overview paper [13]. Here we give a brief summary. The CHIME telescope comprises of four 20m × 100m cylindrical reflectors with no moving parts, aligned in the North-South direction and operating between $400 - 800$ MHz. Each of these reflectors come with 256 dual-polarization antennas installed along its focal plane axis. The analog signal received by the feeds gets digitized to a time-series with a 1 nano-second time-resolution before getting channelized to 1024 frequency channels at a resolution of 2.56 μs using customized integrated circuits called Field-Programmable Gate Arrays (FPGAs). The channelized output from FPGAs is processed by a series of pipelines (see Figure 4.2). First among them is the Level-0 or the L0 pipeline which performs the task of beamforming using Fast-Fourier Transforms [192, 150, 139]. It is built out of 256 GPU nodes that correlate data from all the feeds with appropriate time delays to constructively interfere them to produce beams with increased sensitivity to a particular location in the sky. In total it produces 1024 beams on the sky and further up-channelizes the data-stream by a factor of 16 (total 16384 channels) at a time resolution of 1-ms.

The data then goes to the L1 pipeline which is responsible for detecting FRBs. After filtering out some extreme but mitigable instances of human-made radio frequency interference (RFI), the CPU based L1 pipeline uses a near optimal tree-based algorithm to search for FRBs in real-time. The pipeline utilizes a ring-buffer to store and persist the intensity data and on detecting a candidate event above a nominal signal-to-noise (SNR), it triggers a dump of a few seconds of data around the event for further offline analysis. Finally the pipeline also has a machine-learning based routine for sifting through the candidate events to identify genuine FRBs. The L2 pipeline performs another iteration of RFI removal and groups together instances of an event that are detected in multiple beams. The L3 pipeline is responsible for estimating the flux associated with the pulse as well as possible source identification and association. The last in the series is the L4 pipeline which is responsible for maintaining a database for candidate meta-data.

4.3 Data

Once a detection is triggered by the L1 pipeline, few seconds of intensity data around the event is dumped to disk. The intensity data is a 2D array with the two axes being

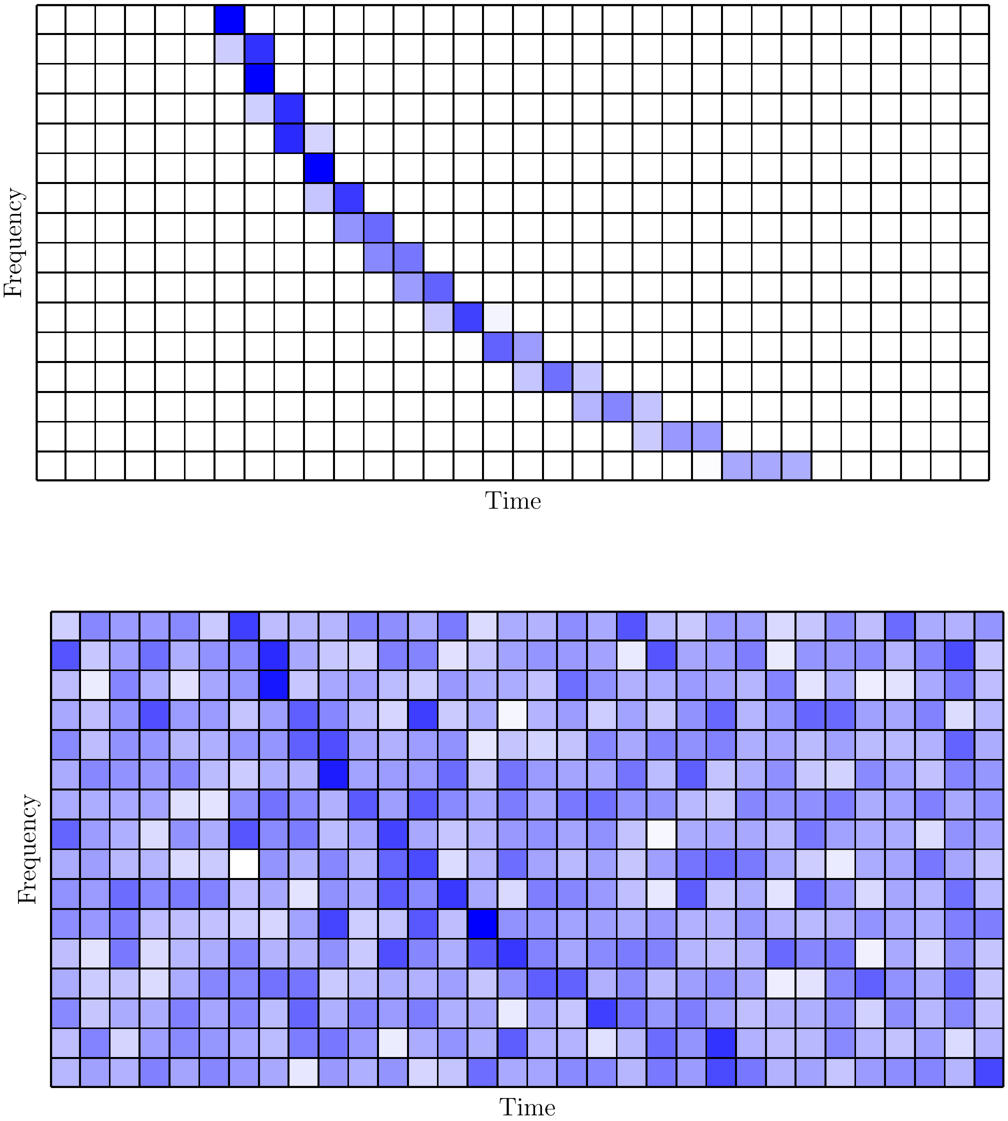

Figure 4.3: *Top panel.* Toy 16-channel example of a dispersed pulse as seen in the intensity data for an arbitrary choice of parameters. The x-axis is time while the y-axis is frequency. *Bottom panel.* The same pulse embedded in Gaussian noise.

.

frequency and time. For CHIME , the data has in total 16384 frequency channels. An FRB arriving in the intensity data is dispersed in time as can be seen in Figure 4.3. This happens due to the fact that propagating electromagnetic waves obey a dispersion relation given by [113]

$$\omega^2 = \omega_e^2 + c^2k^2 \tag{4.1}$$

where ω_e is the electron plasma angular frequency given by

$$\omega_e^2 = \frac{4\pi n_e e^2}{m_e} \tag{4.2}$$

As a result of this dispersion, the group velocity of coherent radio waves passing through electron plasma becomes

$$v_g = \frac{\partial \omega}{\partial k} = c\left(1 - \left[\frac{\omega_e}{\omega}\right]^2\right)^{1/2} \tag{4.3}$$

For purely vacuum media or high-frequency waves ($\omega_e/\omega \to 0$), the group velocity is close to the speed of light c. However, most of the space is filled with free electrons which are cold and tenuous with densities in the range $10^{-4} - 10^4$ cm^{-3} ($0 < \omega_e/\omega \ll 1$) and therefore produces tangible decrease in group velocity and thus the pulse arrival time at a given observing frequency ν is

$$\begin{aligned}
\Delta t(\nu) = t(\nu) - t(\infty) &= \int \frac{dl}{v_g} - \int \frac{dl}{c} \\
&= \int \frac{dl}{c}\left(1 + \frac{\omega_e^2}{2\omega^2} + ...\right) - \int \frac{dl}{c} \\
&\approx \int dl \frac{1}{2c}\frac{4\pi n_e e^2}{m_e}\frac{1}{(2\pi\nu)^2} \\
&= \frac{1}{\nu^2}\left[\frac{e^2}{2\pi m_e c}\right]\int dl\ n_e \\
&= \frac{a}{\nu^2}DM
\end{aligned} \tag{4.4}$$

where the constant $a = [\frac{e^2}{2\pi m_e c}] = 4.148$ GHz^2 cm^3 pc^{-1} ms and $DM = \int n_e dl$. The integral over the electron density n_e counts the number of electrons encountered by the FRB along its path from source to observer and is called the dispersion measure (DM). For each of the 16384 frequency channels in our intensity data, we can use estimate of initial arrival time t_0 and DM from the real-time pipeline to extract a sweep of ~100 ms of data centered on the pulse. Thus the 2D array data that we fit our model to has approximately 16384×100 elements.

4.4 Pulse Model

In this section, we will describe how the intensity $I(\nu, t)$ is modelled in terms of 7 parameters that we will describe one by one. The basic pulse model we fit to an observed FRB accounts for its intrinsic features as well as propagation effects imprinted on the burst [17, 140]. The intrinsic profile of an FRB consists of a Gaussian pulse in time with a frequency-dependent modulation given by its spectrum. The Gaussian profile is a two parameter model given by

$$\frac{1}{\sqrt{2\pi w^2}} \exp\left(- \frac{(t-t_0)^2}{2w^2} \right)$$

where t_0 is the time of arrival of the burst at our telescope at a reference frequency and w is the width of the pulse. We model the spectrum of the burst using a 3 parameter power-law given by

$$A_s \left(\frac{\nu}{\nu_0} \right)^{n_s + \alpha \ln(\frac{\nu}{\nu_0})}$$

where A_s is the amplitude, n_s is the spectral index and α models the running of spectral index as a function of frequency. They combine together to give us the total intrinsic pulse profile

$$I_{intrinsic}(\nu, t) = A_s \left(\frac{\nu}{\nu_0} \right)^{n_s + \alpha \ln(\frac{\nu}{\nu_0})} \left[\frac{1}{\sqrt{2\pi w^2}} \exp\left(- \frac{(t-t_0)^2}{2w^2} \right) \right] \tag{4.5}$$

This intrinsic profile captures features that are likely intrinsic to the FRB generation process. In addition to these intrinsic features, the observed pulse is also modified due to propagation effects. Chief among these are scattering and dispersion.

Scattering, or multi-path propagation of the FRB causes many copies of the pulse to be super-imposed with different delays. This results in a temporal broadening of the pulse which can be modelled under a thin screen approximation where the Gaussian profile gets convolved with a decaying exponential of the form e^{-t/τ_s} where the scattering time is given by

$$\tau_s = \tau \left(\frac{\nu}{\nu_s} \right)^{-SI} \tag{4.6}$$

where τ is called the scattering measure defined at a reference frequency ν_s and parameterizes the spectral broadening. We choose the center of the observing bandwidth as the reference frequency for scattering i.e. $\nu_s = 600$ MHz. The parameter SI is called the scattering index characterizing the frequency dependence of the broadening. The scattering index depends on the nature of plasma inhomogeneities and in particular their power spectrum ($\propto \langle n_e^2 \rangle$). It can be a free parameter in principle but in almost all cases we fix its value to 4.

$$I_{scattered}(\nu, t) = I_{intrinsic}(\nu, t) \otimes \left[\theta(t) \frac{1}{\tau_s} \exp\left(-\frac{t}{\tau_s}\right)\right] \tag{4.7}$$

where $\theta(t)$ is the Heaviside function and $\otimes$ denotes a convolution operation.

Finally, the dispersion leads to a frequency dependent delay in the arrival of the FRB pulse as discussed in §4.3 and leads to a time shift given by

$$I(\nu, t) = I_{scattered}(\nu, t - \Delta t(\nu)) \tag{4.8}$$

where $\Delta t(\nu)$ is given by Eq. (4.4) and is dependent on two new parameters: DM and DI. Eq. (4.8) gives the final model that we use for computing a 2-d data array $I_{ij}(\nu_i, t_j)$ given arbitrary values of the parameters $\boldsymbol{\theta} = (t_0, DM, w, A_s, n_s, \alpha, \tau)$

4.5 MCMC

Given the *forward model* of an FRB as in Eq. (4.8) , the process of parameter estimation is the inverse problem (much like most data analysis problems in astrophysics and cosmology) of inferring the region in parameter space that is most likely to describe the FRB properties.

In order to infer the model parameters, we work under the Bayesian framework which formalizes the inference problem. The Bayesian approach returns a distribution over the parameter space assigning a higher probability to regions in the space which best fit the data. The approach naturally incorporates our previous beliefs or knowledge about the parameter space expressed in the form of a distribution called the *prior*.

Formally, the posterior distribution $\mathcal{P}(\boldsymbol{\theta}|\mathcal{D})$ over parameters $\boldsymbol{\theta} = (t_0, DM, w, A_s, n_s, \alpha, \tau)$, of our fiducial model described in §4.4, for a dataset $\mathcal{D}$ is given by

$$\mathcal{P}(\boldsymbol{\theta}|\mathcal{D}) \propto \mathcal{P}(\mathcal{D}|\boldsymbol{\theta})\mathcal{P}(\boldsymbol{\theta}) = \mathcal{L}_{\boldsymbol{\theta}}(\mathcal{D})\mathcal{P}(\boldsymbol{\theta}) \tag{4.9}$$

where $\mathcal{P}(\boldsymbol{\theta})$ is the prior over the model parameters and $\mathcal{L}_{\boldsymbol{\theta}}(\mathcal{D})$ is the likelihood. In our case, we prefer uninformative priors for our model parameters and use a uniform distribution with broad support. The likelihood is given by

$$\mathcal{L}_{\boldsymbol{\theta}} = \exp(-\chi^2(\boldsymbol{\theta}, \mathcal{D})/2) \tag{4.10}$$

with

$$\chi^2(\boldsymbol{\theta}, \mathcal{D}) = \sum_{t,\nu} \frac{(\mathcal{D}(t,\nu) - I(t,\nu|\boldsymbol{\theta}))^2}{\sigma_\nu^2} \tag{4.11}$$

where σ_ν^2 is the per channel variance of our data that we compute using the entire stretch of data saved to disk. Intuitively, the model parameters can be inferred by performing a dense sampling of the parameter space and rejecting all those samples which do not give a forward model in a close neighbourhood of the observed data after accounting for the noise. However, this naive approach of sampling is inefficient given the complexity of the problem we are tackling.

A much more efficient way of obtaining the posterior distribution is Monte Carlo Markov Chain (MCMC) that refers to a class of algorithms that sample from a given probability distribution p where in the asymptotic limit, the samples generated using the algorithm are indistinguishable from samples generated from p. The sampling relies on the philosophy of Markov processes (where each new sample is a random variable x_{n+1} drawn from a conditional distribution $p(x_{n+1}|x)$ conditioned only on the previous sample x and not on the entire history) to generate a sequence of points in parameter space which eventually converge to the true posterior distribution. There are many algorithms to realize MCMC sampling process, each with their own pros and cons and usually one chooses the algorithm that best suits their needs.

4.6 Affine-invariant sampler

The MCMC algorithm that we use for sampling the posterior is the affine-invariant ensemble sampling algorithm proposed by Goodman and Weare [85]. The affine-invariance property of the algorithm implies that the sampler remains robust to affine transformation *i.e.* scaling and shift operations of the random variable with a given distribution. The algorithm evolves an ensemble of walkers, each of which are assigned a to a random position in the parameter space to begin with, and moves them to the most probable region in the parameter space. The algorithm has excellent auto-correlation property and requires minimal hand-tuning of run-time parameters compared to other traditionally used MCMC algorithms. In [78], a parallel version of this algorithm was developed which is capable of using multiple CPU cores in parallel and a pure python implementation was presented in the form of a public library `emcee` [77]. The improvised algorithm utilized disjoint sets of walkers, where the walkers in one set had their position updated based on the walkers from the other set. In particular, the entire ensemble of K walkers is divided into two sets: a main set S^i and a complimentary set $S^{\sim i}$ each of size K/2. The position of each walker in the main set for the iteration $t+1$ is given by

$$X_k(t+1) = X_j(t) + Z[X_k(t) - X_j(t)] \tag{4.12}$$

where X_k is a walker in the main set and X_j is a randomly selected walker from the complimentary set $S^{\sim i}$. Z here is a random number generated from a distribution given by

$$g(z) \propto \begin{cases} \dfrac{1}{\sqrt{z}} & \text{if } z \in \left[\dfrac{1}{2}, 2\right], \\ 0 & \text{otherwise} \end{cases} \tag{4.13}$$

The chain will satisfy detailed balance if the proposal is accepted with probability

$$q = \min\left(1,\, Z^{N-1}\frac{p(X_k(t+1))}{p(X_k(t))}\right) \quad , \tag{4.14}$$

Once the position of all the walkers in the set S^i is updated, the position of walkers in the set $S^{\sim i}$ is updated similarly using now the set S^i as the complimentary set.

4.6.1 GPU implementation

The likelihood defined in Eq. (4.10) is a numerically intensive function involving a complex model $I(t,\nu)$ with 16k-by-100 elements in a 2D array. Each walker at every step of sampling requires this likelihood to be evaluated. Given the particular nature of our model, the likelihood evaluation can be dramatically accelerated by utilizing the high throughputs provided by Graphical Processing Units (GPUs). GPUs are particularly well suited for performing parallel numerical operations on contiguous block of data. Furthermore, for when sampling with K walkers, the position of half the walkers (K/2) at a given iteration can be updated simultaneously. This way of updating the positions can be done efficiently using a vectorized (batched) implementation of both likelihood evaluation as well as update.

We implement this GPU compatible version of the algorithm using the public library `JAX` [37]. `JAX` is a modern high-performance library for numerical calculations on GPUs implemented primary for machine learning research and application. `JAX` uses XLA (Accelerated Linear Algebra; a domain-specific compiler for linear algebra) to compile and run programs on GPUs and has an API very similar to the popular numerical library NumPy. Compilation happens under the hood by default, with library calls getting just-in-time compiled and executed. But `JAX` also lets us just-in-time compile our own Python functions into XLA-optimized kernels. We make use of just-in-time compilation as well as another useful feature offered by `JAX` called `vmap` (vectorized map) to improve our code.

The pipeline can be run from the command-line on one of the analysis nodes of CHIME/FRB . The program takes the native event ID as an input and begins by reading the entire intensity data for the event stored on hard drives. It then uses the real-time estimate of arrival time t_0 and DM to produce a 16k by 100 size array of data around the pulse This preprocessing is performed using the iautils package developed by the CHIME/FRB collaboration. This constitutes our $\mathcal{D}(t,\nu)$ in Eq. (4.10). The model that we use is similar to the one used in `fitburst` but is rewritten in `JAX` and incorporates several changes that speeds up the original implementation by up to a factor of $\sim$3. We compose the model pulse at an upsampled factor of 4 and 2 in time and frequency which we then boxcar-convolve to get the predicted pulse at our instrumental resolution. This comprises our $I(t,\nu)$. Additionally, we also implement a simpler purely Gaussian model without any scattering that we fit initially to refine our parameters before running the full 7-parameter model.

We now have all the ingredients for our likelihood evaluation. We begin the process by fitting a Gaussian model with parameters $\boldsymbol{\theta} = (t_0, w, A_s, n_s, \alpha)$ where the DM has been kept fixed to the rough value estimated by the real-time detection pipeline which has a sub-percent precision. This initial iteration provides a reasonable estimate of width (w) and the spectral parameters (A_s, n_s, and α) of the model. We impose bounds on the parameters via a uniform prior and depending on the convergence of our samples, decide to relax or keep the bounds. Next, we fit the same Gaussian model, but this time with DM as a free parameter. This step gives the best Gaussian fit to the data. Finally, we fit the full 7-parameter model of Eq. (4.10) with parameters $\boldsymbol{\theta} = (t_0, DM, w, A_s, n_s, \alpha, \tau)$. Figure 4.4 shows this model fit to a significantly scattered event seen by CHIME/FRB. Figure 4.5 shows the resultant triangle plot for the model parameters showing 2-d marginalized posterior distribution of all the parameter pairs as well as 1-d marginalized posterior distribution.

4.7 Future Direction

The MCMC pipeline is currently getting integrated into the CHIME/FRB's analysis pipeline that processes incoming events in an automated fashion. Our development is still

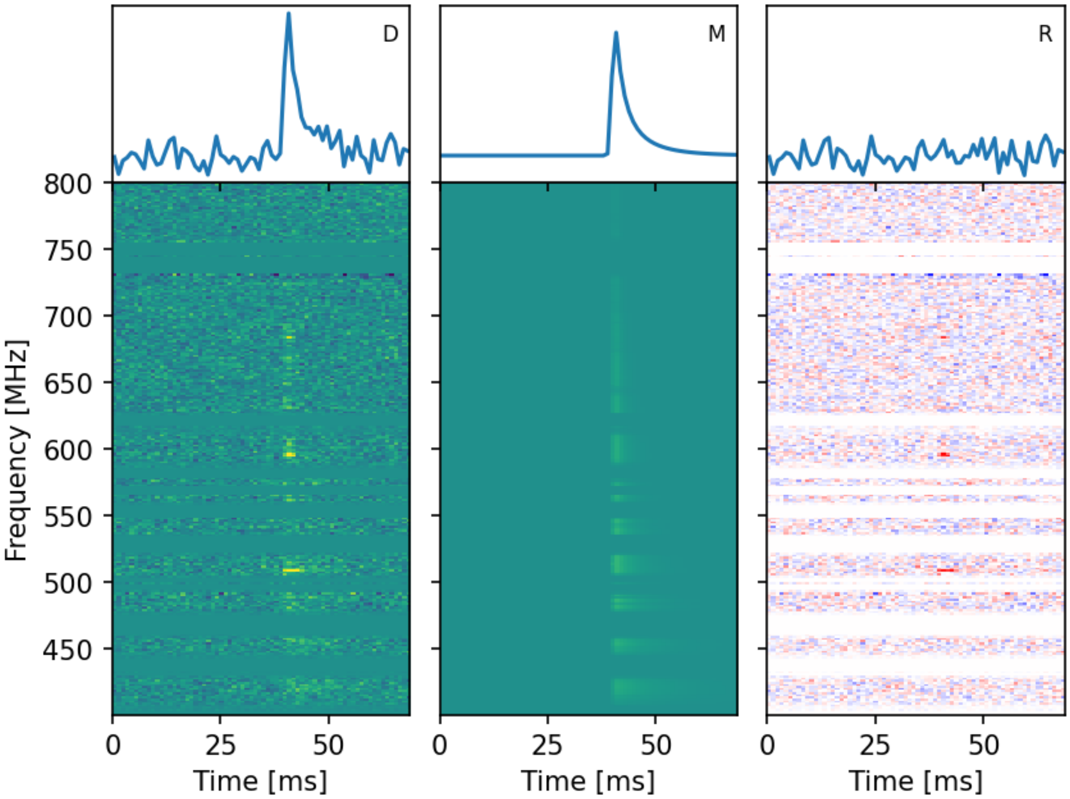

Figure 4.4: Figure showing the result of fitting a model to an FRB candidate. *Left panel.* The result of dedispersing the intensity data using the best fit DM and arrival time t_0. *Centre Panel.* The best fit pulse profile obtained from the pulse fitting process. *Right panel.* The residual left after subtracting the pulse model from dedispersed intensity data. Some frequency channels have been masked out as they are polluted with radio frequency interferences(RFI). The masked channels are most clearly visible in the panel on the right but the same channels have also been masked in the other panels. This plot is produced using a routine developed by Ziggy Pleunis and other members of CHIME/FRB collaboration.

a work in progress where we will continue to explore ideas that improve the workflow. Currently, we see a $> 90\%$ success rate when running the pipeline out-of-the-box on a set of *recently* observed events. These events were detected using a configuration that results in a more precise estimates of t_0 and DM from the real-time pipeline which are used as initial input to the MCMC pipeline. Going forward, the plan is to develop a

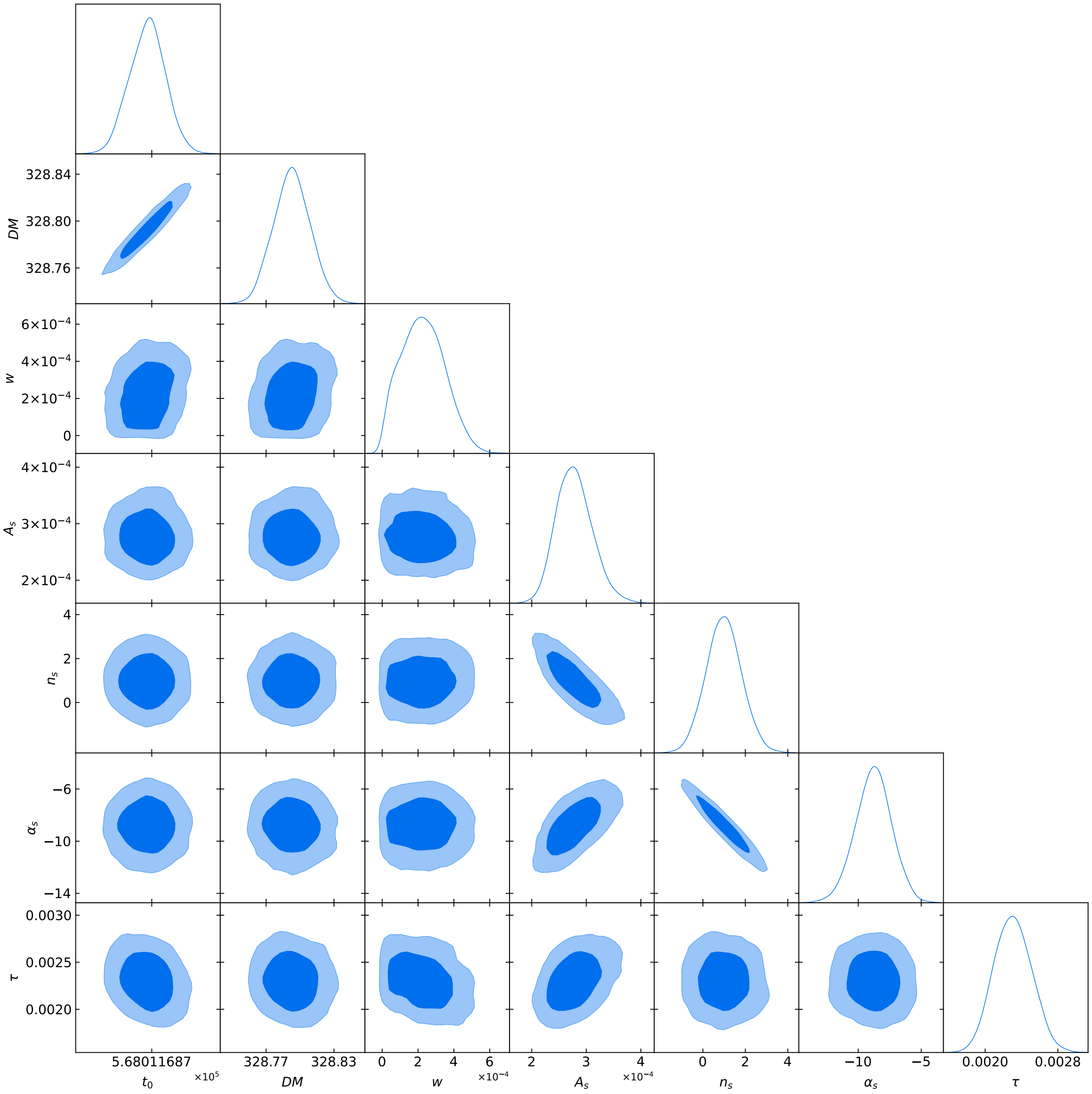

Figure 4.5: A triangle plot showing the covariance between all the parameters pairs as well as marginalized posterior distribution for each of the 7 free parameters of the model. The dispersion index and scattering index have been kept fixed during the fit to −2 and −4, respectively. The plot is produced using `getdist` [120].

more versatile logic that results in an even better success rate. There are other frontiers where more work is needed. The pipeline has not yet been fully tested on multi-component events. Fitting multi-component model out-of-the box might prove a non-trivial challenge. Another shortcoming of the current setup is the lack of a proper beam model. A Bayesian modeling of the beam can be naturally incorporated into this framework where one can easily marginalize over the beam parameters when computing the parameter constraints. Model comparison so far has proven pretty time consuming on CPUs, but now with the likelihood re-written in `JAX` , one can use publicly available nested sampling libraries written in `JAX` [9], which are several orders of magnitude faster than existing CPU implementations, to compute the evidence for model comparison [179]. Having model comparison can help us identify events which are better fit with the basic Gaussian model and hence rule out scattering with significance for these events. Identifying sub-populations with no scattering could be quite illuminating.

4.8 Discussion

Bayesian inference has become the preferred way of estimating model parameters in much of Astronomy and Astrophysics. Experiments like Planck[3, 5], Ligo-Virgo Collaboration [1], EHT [71] all use Bayesian formalism for inference purposes. CHIME/FRB itself used an earlier CPU-only version of this MCMC pipeline for estimating FRB parameters in our very first science paper [14]. We also internally corroborated the results from our direct fitting routine `fitburst` with that from this pipeline for over 200 events that have been presented in the catalogue paper [17]. In the very near future, we plan to use this toolkit to revisit the analysis of events seen from SGR 1935 2154. As mentioned before, CHIME/FRB detected 2 bursts from this source on April 28, 2020 which coincided with peaks in X-ray and Gamma-ray light-curves. However, based on the least-squares direct fit results, the radio bursts appear to be leading their high energy counterparts by a few milliseconds [122, 141]. Its precise time of arrival remains a point of interest for the FRB community since in almost all models, the radio pulse is predicted to arrive after or at the same time as the X-ray pulse. A Bayesian estimate of the time of arrival that marginalizes over all the remaining parameter could resolve any remaining ambiguities.

Given its simple intuitive interpretation and the benefits it offers, it would be very rewarding to develop this work further into a mature pipeline that can run out-of-the-box on majority of the events. The speed-up obtained by promoting the likelihood evaluations as well as the sampling to GPUs offers a time-efficient way of realizing this goal.

Chapter 5

Conclusion

The kSZ effect in the CMB will be detected at percent level within the next few years. Sourced by the Doppler shifting of CMB photons when they scatter of electron clouds with bulk radial velocity, the kSZ effect is a secondary anisotropy in the CMB that is proportional to the product of large-scale velocity at a location and the local electron density. A high significance detection will enable several high impact applications of the effect. On small-scales, it will allow us to probe the baryon distribution in the Universe both within as well as in the outskirts of halos, something which has been notoriously challenging so far. On the cosmological side, kSZ is a unique probe of large-scale velocity.

In chapter 2 of this thesis, we present a bispectrum estimator of type $\langle ggT \rangle$ for estimating the kSZ signal by combining two legs of galaxy density field with a CMB temperature map containing the kSZ signal. The signal-to-noise of the estimator peaks in the squeezed limit where we show that it factorizes as the product of large-scale galaxy velocity power spectrum (P_{gv}) and small scale galaxy electron power spectrum (P_{ge}). Thus measuring the bispectrum in mode bins, gives us a measurement of P_{gv} and P_{ge} as a function of scale, up to a factor that can be exchanged between the two. We show that the bispectrum is related to several existing estimators of kSZ including the pair-sum method and velocity template method, both of which have been used to detect kSZ at a few sigmas with existing CMB experiments and galaxy surveys. The bispectrum estimator is robust to secondary effects like CMB lensing, CIB and tSZ due to the odd parity of kSZ and allows a straightforward way of incorporating issues like redshift-space distortions and photo-z effect. Using the machinery, we forecast $\sim 500\sigma$ detection of kSZ in the near future.

Due to the the coupling between small scale electron density and large-scale radial velocity in the kSZ source term, one can construct a quadratic estimator $\hat{v}_r$ for the radial velocity field which combines a tracer of electron density at small scales – for instance the galaxy density field – with a CMB temperature map at similar scales, to estimate large-scale radial velocity field. Our bispectrum formalism is closely related to $\hat{v}_r$ and we analyzed the behaviour of this estimator analytically in Chapter 2. We found that the leading order noise for the estimator, which we call the N^0 bias, becomes scale independent at the large scales where the reconstruction is of interest. This behaviour of the reconstruction noise implies that modes reconstructed using this approach offer us the best probe of cosmology at the largest scales edging past traditional methods that use galaxy density obtained from galaxy surveys. Although future galaxy surveys will be limited by cosmic variance and not by Poisson noise of galaxy samples, having an additional lower-noise tracer has several interesting applications. One such application is its use in cancelling sample variance when constraining scale-dependent signatures at the largest scales. One primary candidate for sample variance cancellation is in constraining primordial non-gaussianity parameter f_{NL} using the scale dependent bias induced by a non-zero f_{NL}. The Fisher forecasts for this look very promising [147]. However the analysis makes several assumptions. In particular it assumes that the fields involved are all Gaussian even at small-scales. This simple picture breaks down under realistic scenarios and can potentially jeopardize its return.

To explore this in detail, in Chapter 3, we implement kSZ velocity reconstruction in an N-body simulation pipeline and explore its properties. We process a large suite of N-body simulation data producing consistent realizations of CMB temperature maps and halo catalogues which are then fed to an implementation of the quadratic estimator to reconstruct the radial velocity in a 3D volume. In our subsequent analysis, we find that at the map level, our analytic expectations from chapter 2 hold. We obtain a very high correlation reconstruction with a constant bias on large scales. We find that the reconstruction noise can be larger than the analytic prediction which is usually assumed. We revisit the analytic prediction and find additional noise terms which explain the discrepancy. The new terms are analogous to the $N^{(1)}$ and $N^{(3/2)}$ biases in CMB lensing. The $N^{(1)}$ bias, which is a Gaussian contribution to the total noise, turns out to be subdominant in comparison to the leading order $N^{(0)}$ noise term. The $N^{(3/2)}$ bias, which arises due to the non-gaussian nature of the underlying fields, is obtained from a six-point halo model calculation. Finally, we implement an MCMC pipeline which estimates f_{NL} from N-body simulations, using a multi-tracer approach which uses the reconstructed velocity field along with halos in the simulations and improves constraints on f_{NL} by nearly a factor of 2.5 under a fiducial setup similar to a combination of the CMB-S4 experiment and the DESI spectroscopic survey. Overall, these results confirm that kSZ velocity reconstruction will be a powerful probe of cosmology in the near future, but new terms should be included in the noise power spectrum.

Fast Radio Bursts, the other main topic in this thesis, are an exciting new phenomenon in radio astronomy. These millisecond duration transient pulses of extreme energy come from extra-galactic distances and offer a new window on to the universe. Their dispersion measure (DM), an observable quantity proportional to the electron column density from their source to us, makes them a unique probe of the electron (baryon) distribution.

CHIME (Canadian Hydrogen Intensity Mapping Experiment) is a modern interferometric telescope in Canada with a dedicated pipeline for detecting these mysterious radio transients. The CHIME/FRB experiment has propelled research in this field by reporting several interesting results and has produced a large catalogue of more than 500 FRBs in a short duration of operation. The FRB pulses detected in real-time by CHIME are subsequently fit with a physically motivated FRB model in an offline analysis. In chapter 4, we go into the details of FRB modelling and present an end-to-end MCMC pipeline for estimating the model parameters from CHIME/FRB intensity data. The pipeline builds upon the native fitting code fitburst to incorporate qualities of Bayesian formulation of statistical inference. It uses the high-performance python library `JAX` for model composition and likelihood evaluation and is capable of running on both CPUs and GPUs. To efficiently sample the posterior, we develop a vectorized and just-in-time compiled implementation of the popular affine-invariant MCMC sampling algorithm. Moving the likelihood evaluation and sampling to GPUs accelerates the analysis by leveraging their high through-puts and is particularly well suited for our use case. The GPU version of the code dramatically reduces the wall-time for analysis. Since the time taken by the this MCMC pipeline is of the same order as the direct fitting pipeline, we anticipate that more and more events would be analyzed by this pipeline going into the future.

Together, the kSZ effect and FRBs will provide us some key insights into the small-scale baryonic physics in the coming years. The cross-correlation between galaxies and FRB DM map will probe the galaxy-electron power spectrum P_{ge} [137]. For the purposes of kSZ velocity reconstruction, a large sample of FRBs with known redshifts will help mitigate the problem of bias in kSZ velocity reconstruction arising due to uncertainty in small-scale P_{ge}. Our lack of knowledge of the baryon distribution severely limits the potential returns of future galaxy lensing surveys. Both kSZ and FRBs can help alleviate us this issue.

References

[1] B P Abbott, R Abbott, T D Abbott, S Abraham, F Acernese, K Ackley, C Adams, V B Adya, C Affeldt, M Agathos, and et al. A guide to ligo–virgo detector noise and extraction of transient gravitational-wave signals. *Classical and Quantum Gravity*, 37(5):055002, Feb 2020.

[2] Viviana Acquaviva, Nicola Bartolo, Sabino Matarrese, and Antonio Riotto. Second order cosmological perturbations from inflation. *Nucl. Phys. B*, 667:119–148, 2003.

[3] P. A. R. Ade, N. Aghanim, M. Arnaud, M. Ashdown, J. Aumont, C. Baccigalupi, A. J. Banday, R. B. Barreiro, J. G. Bartlett, and et al. Planck2015 results. *Astronomy Astrophysics*, 594:A13, Sep 2016.

[4] Peter Ade, James Aguirre, Zeeshan Ahmed, Simone Aiola, Aamir Ali, David Alonso, Marcelo A. Alvarez, Kam Arnold, Peter Ashton, Jason Austermann, and et al. The simons observatory: science goals and forecasts. *Journal of Cosmology and Astroparticle Physics*, 2019(02):056–056, Feb 2019.

[5] N. Aghanim, Y. Akrami, M. Ashdown, J. Aumont, C. Baccigalupi, M. Ballardini, A. J. Banday, R. B. Barreiro, N. Bartolo, and et al. Planck 2018 results. *Astronomy Astrophysics*, 641:A6, Sep 2020.

[6] N. Aghanim et al. Planck 2018 results. I. Overview and the cosmological legacy of Planck. *Astron. Astrophys.*, 641:A1, 2020.

[7] N. Aghanim et al. Planck 2018 results. VI. Cosmological parameters. *Astron. Astrophys.*, 641:A6, 2020.

[8] Y. Akrami et al. Planck 2018 results. IX. Constraints on primordial non-Gaussianity. 5 2019.

[9] Joshua G. Albert. Jaxns: a high-performance nested sampling package based on jax, 2020.

[10] David Alonso and Pedro G. Ferreira. Constraining ultralarge-scale cosmology with multiple tracers in optical and radio surveys. *Phys. Rev. D*, 92(6):063525, 2015.

[11] David Alonso, Pedro G. Ferreira, Matt J. Jarvis, and Kavilan Moodley. Calibrating photometric redshifts with intensity mapping observations. *Phys. Rev.*, D96(4):043515, 2017.

[12] David Alonso, Thibaut Louis, Philip Bull, and Pedro G. Ferreira. Reconstructing cosmic growth with kinetic Sunyaev-Zel'dovich observations in the era of stage IV experiments. *Phys. Rev.*, D94(4):043522, 2016.

[13] M. Amiri, K. Bandura, P. Berger, M. Bhardwaj, M. M. Boyce, P. J. Boyle, C. Brar, M. Burhanpurkar, P. Chawla, and et al. The chime fast radio burst project: System overview. *The Astrophysical Journal*, 863(1):48, Aug 2018.

[14] M. Amiri et al. A Second Source of Repeating Fast Radio Bursts. *Nature*, 566(7743):235–238, 2019.

[15] M. Amiri et al. Periodic activity from a fast radio burst source. 1 2020.

[16] Mandana Amiri et al. Observations of fast radio bursts at frequencies down to 400 megahertz. *Nature*, 566(7743):230–234, 2019.

[17] Mandana Amiri et al. The First CHIME/FRB Fast Radio Burst Catalog. 6 2021.

[18] B. C. Andersen et al. CHIME/FRB Discovery of Eight New Repeating Fast Radio Burst Sources. *Astrophys. J. Lett.*, 885(1):L24, 2019.

[19] B. C. Andersen et al. A bright millisecond-duration radio burst from a Galactic magnetar. *Nature*, 587(7832):54–58, 2020.

[20] Tobias Baldauf. Field theory in cosmology.

[21] Tobias Baldauf, Uros Seljak, Leonardo Senatore, and Matias Zaldarriaga. Galaxy Bias and non-Linear Structure Formation in General Relativity. *JCAP*, 10:031, 2011.

[22] Tobias Baldauf, Urovs Seljak, Leonardo Senatore, and Matias Zaldarriaga. Linear response to long wavelength fluctuations using curvature simulations. *JCAP*, 09:007, 2016.

[23] Kevin Bandura, Graeme E. Addison, Mandana Amiri, J. Richard Bond, Duncan Campbell-Wilson, Liam Connor, Jean-François Cliche, Greg Davis, Meiling Deng, Nolan Denman, and et al. Canadian hydrogen intensity mapping experiment (chime) pathfinder. *Ground-based and Airborne Telescopes V*, Jul 2014.

[24] K. W. Bannister, A. T. Deller, C. Phillips, J.-P. Macquart, J. X. Prochaska, N. Tejos, S. D. Ryder, E. M. Sadler, R. M. Shannon, S. Simha, and et al. A single fast radio burst localized to a massive galaxy at cosmological distance. *Science*, 365(6453):565–570, Jun 2019.

[25] Nicholas Battaglia. The Tau of Galaxy Clusters. *JCAP*, 1608(08):058, 2016.

[26] Peter S. Behroozi, Charlie Conroy, and Risa H. Wechsler. A Comprehensive Analysis of Uncertainties Affecting the Stellar Mass-Halo Mass Relation for 0 ¡ z ¡ 4. *Astrophys. J.*, 717:379–403, 2010.

[27] Peter S. Behroozi, Risa H. Wechsler, and Hao-Yi Wu. The Rockstar Phase-Space Temporal Halo Finder and the Velocity Offsets of Cluster Cores. *Astrophys. J.*, 762:109, 2013.

[28] Andreas A. Berlind and David H. Weinberg. The Halo occupation distribution: Towards an empirical determination of the relation between galaxies and mass. *Astrophys. J.*, 575:587–616, 2002.

[29] F. Bernardeau, S. Colombi, E. Gaztanaga, and R. Scoccimarro. Large scale structure of the universe and cosmological perturbation theory. *Phys. Rept.*, 367:1–248, 2002.

[30] Suman Bhattacharya and Arthur Kosowsky. Dark Energy Constraints from Galaxy Cluster Peculiar Velocities. *Phys. Rev.*, D77:083004, 2008.

[31] Matteo Biagetti, Titouan Lazeyras, Tobias Baldauf, Vincent Desjacques, and Fabian Schmidt. Verifying the consistency relation for the scale-dependent bias from local primordial non-Gaussianity. *Mon. Not. Roy. Astron. Soc.*, 468(3):3277–3288, 2017.

[32] Federico Bianchini and Alessandra Silvestri. Kinetic Sunyaev-Zel'dovich effect in modified gravity. *Phys. Rev.*, D93(6):064026, 2016.

[33] Mark Birkinshaw. The Sunyaev-Zel'dovich effect. *Phys. Rept.*, 310:97–195, 1999.

[34] Diego Blas, Julien Lesgourgues, and Thomas Tram. The cosmic linear anisotropy solving system (class). part ii: Approximation schemes. *Journal of Cosmology and Astroparticle Physics*, 2011(07):034–034, Jul 2011.

[35] Christopher D. Bochenek, Vikram Ravi, Konstantin V. Belov, Gregg Hallinan, Jonathon Kocz, Shri R. Kulkarni, and Dan L. McKenna. A fast radio burst associated with a Galactic magnetar. *Nature*, 587(7832):59–62, 2020.

[36] A. Borghese, F. Coti Zelati, N. Rea, P. Esposito, G. L. Israel, S. Mereghetti, and A. Tiengo. The X-ray reactivation of the radio bursting magnetar SGR 1935+2154. *Astrophys. J. Lett.*, 902(1):L2, 2020.

[37] James Bradbury, Roy Frostig, Peter Hawkins, Matthew James Johnson, Chris Leary, Dougal Maclaurin, George Necula, Adam Paszke, Jake VanderPlas, Skye Wanderman-Milne, and Qiao Zhang. JAX: composable transformations of Python+NumPy programs, 2018.

[38] Joel N. Bregman. The Search for the Missing Baryons at Low Redshift. *Ann. Rev. Astron. Astrophys.*, 45:221–259, 2007.

[39] Philip Bull, Timothy Clifton, and Pedro G. Ferreira. The kSZ effect as a test of general radial inhomogeneity in LTB cosmology. *Phys. Rev.*, D85:024002, 2012.

[40] Vanessa Böhm, Marcel Schmittfull, and Blake D. Sherwin. Bias to CMB lensing measurements from the bispectrum of large-scale structure. *Phys. Rev. D*, 94(4):043519, 2016.

[41] Victoria Calafut, Rachel Bean, and Byeonghee Yu. Cluster mislocation in kinematic Sunyaev-Zel'dovich effect extraction. *Phys. Rev.*, D96(12):123529, 2017.

[42] R. R. Caldwell and A. Stebbins. A Test of the Copernican Principle. *Phys. Rev. Lett.*, 100:191302, 2008.

[43] Carmelita Carbone, Olga Mena, and Licia Verde. Cosmological Parameters Degeneracies and Non-Gaussian Halo Bias. *JCAP*, 07:020, 2010.

[44] Emanuele Castorina et al. Redshift-weighted constraints on primordial non-Gaussianity from the clustering of the eBOSS DR14 quasars in Fourier space. *JCAP*, 09:010, 2019.

[45] Juan I. Cayuso and Matthew C. Johnson. Towards testing CMB anomalies using the kinetic and polarized Sunyaev-Zel'dovich effects. *Phys. Rev. D*, 101(12):123508, 2020.

[46] Juan I. Cayuso, Matthew C. Johnson, and James B. Mertens. Simulated reconstruction of the remote dipole field using the kinetic sunyaev zel'dovich effect. *Physical Review D*, 98(6), Sep 2018.

[47] S. Chatterjee, C. J. Law, R. S. Wharton, S. Burke-Spolaor, J. W. T. Hessels, G. C. Bower, J. M. Cordes, S. P. Tendulkar, C. G. Bassa, P. Demorest, and et al. A direct localization of a fast radio burst and its host. *Nature*, 541(7635):58–61, Jan 2017.

[48] Timothy Clifton, Chris Clarkson, and Philip Bull. The isotropic blackbody CMB as evidence for a homogeneous universe. *Phys. Rev. Lett.*, 109:051303, 2012.

[49] Dagoberto Contreras, Matthew C. Johnson, and James B. Mertens. Towards detection of relativistic effects in galaxy number counts using kSZ Tomography. *JCAP*, 10:024, 2019.

[50] Asantha Cooray and Ravi K. Sheth. Halo models of large scale structure. *Phys. Rept.*, 372:1–129, 2002.

[51] James M. Cordes and Shami Chatterjee. Fast radio bursts: An extragalactic enigma. *Annual Review of Astronomy and Astrophysics*, 57(1):417–465, 2019.

[52] Paolo Creminelli and Matias Zaldarriaga. Single field consistency relation for the 3-point function. *JCAP*, 10:006, 2004.

[53] M. Crocce, S. Pueblas, and R. Scoccimarro. Transients from Initial Conditions in Cosmological Simulations. *Mon. Not. Roy. Astron. Soc.*, 373:369–381, 2006.

[54] A. J. Cuesta, M. Vargas-Magaña, F. Beutler, A. S. Bolton, J. R. Brownstein, D. J. Eisenstein, H. Gil-Marín, S. Ho, C. K. McBride, C. Maraston, N. Padmanabhan, W. J. Percival, B. A. Reid, A. J. Ross, N. P. Ross, A. G. Sánchez, D. J. Schlegel, D. P. Schneider, D. Thomas, J. Tinker, R. Tojeiro, L. Verde, and M. White. The clustering of galaxies in the SDSS-III Baryon Oscillation Spectroscopic Survey: baryon acoustic oscillations in the correlation function of LOWZ and CMASS galaxies in Data Release 12. *MNRAS*, 457:1770–1785, April 2016.

[55] Steven Cunnington, Ian Harrison, Alkistis Pourtsidou, and David Bacon. HI Intensity Mapping for Clustering-Based Redshift Estimation. 2018.

[56] Neal Dalal, Olivier Dore, Dragan Huterer, and Alexander Shirokov. The imprints of primordial non-gaussianities on large-scale structure: scale dependent bias and abundance of virialized objects. *Phys. Rev. D*, 77:123514, 2008.

[57] Marc Davis, George Efstathiou, Carlos S. Frenk, and Simon D.M. White. The Evolution of Large Scale Structure in a Universe Dominated by Cold Dark Matter. *Astrophys. J.*, 292:371–394, 1985.

[58] F. De Bernardis et al. Detection of the pairwise kinematic Sunyaev-Zel'dovich effect with BOSS DR11 and the Atacama Cosmology Telescope. *JCAP*, 1703(03):008, 2017.

[59] Roland de Putter and Olivier Doré. Designing an Inflation Galaxy Survey: how to measure $\sigma(f_{\rm NL}) \sim 1$ using scale-dependent galaxy bias. *Phys. Rev. D*, 95(12):123513, 2017.

[60] Simon DeDeo, David N. Spergel, and Hy Trac. The kinetic sunyaev-zel'dovitch effect as a dark energy probe. 2005.

[61] DESI Collaboration, A. Aghamousa, J. Aguilar, S. Ahlen, S. Alam, L. E. Allen, C. Allende Prieto, J. Annis, S. Bailey, C. Balland, and et al. The DESI Experiment Part I: Science,Targeting, and Survey Design. *ArXiv e-prints*, October 2016.

[62] Vincent Desjacques, Uro**v**s Seljak, and Ilian T. Iliev. Scale-dependent bias induced by local non-gaussianity: a comparison to n-body simulations. *Monthly Notices of the Royal Astronomical Society*, 396(1):85–96, Jun 2009.

[63] DES/SPT Collaboration et al. Detection of the kinematic Sunyaev–Zel'dovich effect with DES Year 1 and SPT. *Mon. Not. Roy. Astron. Soc.*, 461(3):3172–3193, 2016.

[64] Anne-Sylvie Deutsch, Emanuela Dimastrogiovanni, Matthew C. Johnson, Moritz Munchmeyer, and Alexandra Terrana. Reconstruction of the remote dipole and quadrupole fields from the kinetic Sunyaev Zel'dovich and polarized Sunyaev Zel'dovich effects. 2017.

[65] R. H. Dicke, P. J. E. Peebles, P. G. Roll, and D. T. Wilkinson. Cosmic Black-Body Radiation. , 142:414–419, July 1965.

[66] Olivier Doré et al. Cosmology with the SPHEREX All-Sky Spectral Survey. 12 2014.

[67] Olivier Doré, Joseph F. Hennawi, and David N. Spergel. Beyond the damping tail: Cross - correlating the kinetic Sunyaev - Zel'dovich effect with cosmic shear. *Astrophys. J.*, 606:46–57, 2004.

[68] Alan R. Duffy, Joop Schaye, Scott T. Kay, and Claudio Dalla Vecchia. Dark matter halo concentrations in the Wilkinson Microwave Anisotropy Probe year 5 cosmology.

Mon. Not. Roy. Astron. Soc., 390:L64, 2008. [Erratum: Mon. Not. Roy. Astron. Soc.415,L85(2011)].

[69] J. Dunkley, R. Hlozek, J. Sievers, V. Acquaviva, P. A. R. Ade, P. Aguirre, M. Amiri, J. W. Appel, L. F. Barrientos, E. S. Battistelli, and et al. The atacama cosmology telescope: Cosmological parameters from the 2008 power spectrum. *The Astrophysical Journal*, 739(1):52, Sep 2011.

[70] Gia Dvali, Andrei Gruzinov, and Matias Zaldarriaga. A new mechanism for generating density perturbations from inflation. *Phys. Rev. D*, 69:023505, 2004.

[71] A. Broderick et al. Themis: A parameter estimation framework for the event horizon telescope. *The Astrophysical Journal*, 897(2):id. 139, 2020.

[72] Simone Ferraro, J. Colin Hill, Nick Battaglia, Jia Liu, and David N. Spergel. Kinematic Sunyaev-Zel'dovich effect with projected fields. II. Prospects, challenges, and comparison with simulations. *Phys. Rev.*, D94(12):123526, 2016.

[73] Simone Ferraro and Kendrick M. Smith. Using large scale structure to measure f_{NL}, g_{NL} and τ_{NL}. *Phys. Rev. D*, 91(4):043506, 2015.

[74] Simone Ferraro and Kendrick M. Smith. Characterizing the Epoch of Reionization with the small-scale CMB: constraints on the optical depth and physical parameters. 2018.

[75] Anastasia Fialkov and Abraham Loeb. Constraining the CMB Optical Depth Through the Dispersion Measure of Cosmological Radio Transients. *JCAP*, 05:004, 2016.

[76] Samuel Flender, Daisuke Nagai, and Michael McDonald. Constraints on the optical depth of galaxy groups and clusters. *Astrophys. J.*, 837(2):124, 2017.

[77] Daniel Foreman-Mackey, Will Farr, Manodeep Sinha, Anne Archibald, David Hogg, Jeremy Sanders, Joe Zuntz, Peter Williams, Andrew Nelson, Miguel de Val-Borro, and et al. emcee v3: A python ensemble sampling toolkit for affine-invariant mcmc. *Journal of Open Source Software*, 4(43):1864, Nov 2019.

[78] Daniel Foreman-Mackey, David W. Hogg, Dustin Lang, and Jonathan Goodman. emcee: The mcmc hammer. *Publications of the Astronomical Society of the Pacific*, 125(925):306–312, Mar 2013.

[79] V. Gajjar et al. Highest Frequency Detection of FRB 121102 at 4–8 GHz Using the Breakthrough Listen Digital Backend at the Green Bank Telescope. *Astrophys. J.*, 863(1):2, 2018.

[80] Juan Garcia-Bellido and Troels Haugboelle. Looking the void in the eyes - the kSZ effect in LTB models. *JCAP*, 0809:016, 2008.

[81] Andrew Gelman, Aki Vehtari, Daniel Simpson, Charles C. Margossian, Bob Carpenter, Yuling Yao, Lauren Kennedy, Jonah Gabry, Paul-Christian Bürkner, and Martin Modrák. Bayesian workflow, 2020.

[82] Tommaso Giannantonio and Cristiano Porciani. Structure formation from non-Gaussian initial conditions: multivariate biasing, statistics, and comparison with N-body simulations. *Phys. Rev. D*, 81:063530, 2010.

[83] Utkarsh Giri et al. *To appear.*

[84] Utkarsh Giri and Kendrick M. Smith. Exploring KSZ velocity reconstruction with N-body simulations and the halo model. 10 2020.

[85] Jonathan Goodman and Jonathan Weare. Ensemble samplers with affine invariance. *Commun. Appl. Math. Comput. Sci.*, 5(1):65–80, 2010.

[86] M. Grossi, L. Verde, C. Carbone, K. Dolag, E. Branchini, F. Iannuzzi, S. Matarrese, and L. Moscardini. Large-scale non-Gaussian mass function and halo bias: tests on N-body simulations. *Mon. Not. Roy. Astron. Soc.*, 398:321–332, 2009.

[87] Nico Hamaus, Uro**v**s Seljak, and Vincent Desjacques. Optimal constraints on local primordial non-gaussianity from the two-point statistics of large-scale structure. *Physical Review D*, 84(8), Oct 2011.

[88] Nick Hand et al. Evidence of Galaxy Cluster Motions with the Kinematic Sunyaev-Zel'dovich Effect. *Phys. Rev. Lett.*, 109:041101, 2012.

[89] Nick Hand, Yu Feng, Florian Beutler, Yin Li, Chirag Modi, Uros Seljak, and Zachary Slepian. nbodykit: an open-source, massively parallel toolkit for large-scale structure. *Astron. J.*, 156(4):160, 2018.

[90] Duncan Hanson, Anthony Challinor, and Antony Lewis. Weak lensing of the cmb. *General Relativity and Gravitation*, 42(9):2197–2218, Jun 2010.

[91] Andrew P. Hearin, Andrew R. Zentner, Frank C. van den Bosch, Duncan Campbell, and Erik Tollerud. Introducing decorated HODs: modelling assembly bias in the galaxy–halo connection. *Mon. Not. Roy. Astron. Soc.*, 460(3):2552–2570, 2016.

[92] Carlos Hernandez-Monteagudo and Rashid A. Sunyaev. Missing baryons, bulk flows and the E-mode polarization of the Cosmic Microwave Background. *Astron. Astrophys.*, 490:25, 2008.

[93] Carlos Hernandez-Monteagudo, Licia Verde, Raul Jimenez, and David N. Spergel. Correlation properties of the kinematic sunyaev-zel'dovich effect and implications for dark energy. *Astrophys. J.*, 643:598–615, 2006.

[94] J. Colin Hill, Simone Ferraro, Nick Battaglia, Jia Liu, and David N. Spergel. Kinematic Sunyaev-Zel'dovich Effect with Projected Fields: A Novel Probe of the Baryon Distribution with Planck, WMAP, and WISE Data. *Phys. Rev. Lett.*, 117(5):051301, 2016.

[95] Shirley Ho, Simon Dedeo, and David Spergel. Finding the Missing Baryons Using CMB as a Backlight. 2009.

[96] R. W. Hockney and J. W. Eastwood. *Computer Simulation Using Particles.* 1981.

[97] David W. Hogg and Daniel Foreman-Mackey. Data analysis recipes: Using Markov Chain Monte Carlo. *Astrophys. J. Suppl.*, 236(1):11, 2018.

[98] Selim C. Hotinli, James B. Mertens, Matthew C. Johnson, and Marc Kamionkowski. Probing correlated compensated isocurvature perturbations using scale-dependent galaxy bias. *Phys. Rev. D*, 100(10):103528, 2019.

[99] Wayne Hu. Reionization revisited: secondary cmb anisotropies and polarization. *Astrophys. J.*, 529:12, 2000.

[100] Wayne Hu. Mapping the dark matter through the cmb damping tail. *Astrophys. J.*, 557:L79–L83, 2001.

[101] Wayne Hu. Covariant linear perturbation formalism. *ICTP Lect. Notes Ser.*, 14:145–185, 2003.

[102] Wayne Hu and Scott Dodelson. Cosmic microwave background anisotropies. *Annual Review of Astronomy and Astrophysics*, 40(1):171–216, Sep 2002.

[103] Wayne Hu and Takemi Okamoto. Mass reconstruction with cmb polarization. *Astrophys. J.*, 574:566–574, 2002.

[104] Andrew H. Jaffe and Marc Kamionkowski. Calculation of the ostriker-vishniac effect in cold dark matter models. *Phys. Rev. D*, 58:043001, Jul 1998.

[105] Donghui Jeong. *Cosmology with high (z¿1) redshift galaxy surveys.* PhD thesis, University of Texas at Austin, August 2010.

[106] A. Josephy et al. No Evidence for Galactic Latitude Dependence of the Fast Radio Burst Sky Distribution. 6 2021.

[107] A. Kashlinsky, R.G. Arendt, F. Atrio-Barandela, N. Cappelluti, A. Ferrara, and G. Hasinger. Looking at cosmic near-infrared background radiation anisotropies. *Reviews of Modern Physics*, 90(2), Jun 2018.

[108] Ryan Keisler and Fabian Schmidt. Prospects for measuring the relative velocities of galaxy clusters in photometric surveys using the kinetic Sunyaev-Zel'dovich Effect. *Astrophys. J.*, 765:L32, 2013.

[109] Michael H. Kesden, Asantha Cooray, and Marc Kamionkowski. Lensing reconstruction with CMB temperature and polarization. *Phys. Rev. D*, 67:123507, 2003.

[110] Lev Kofman. Probing string theory with modulated cosmological fluctuations. 3 2003.

[111] Eiichiro Komatsu and Uros Seljak. Universal gas density and temperature profile. *Mon. Not. Roy. Astron. Soc.*, 327:1353–1366, 2001.

[112] Ely D. Kovetz, Alvise Raccanelli, and Mubdi Rahman. Cosmological Constraints with Clustering-Based Redshifts. *Mon. Not. Roy. Astron. Soc.*, 468(3):3650–3656, 2017.

[113] S. R. Kulkarni. Dispersion measure: Confusion, constants clarity, 2020.

[114] A. Leauthaud, J. Tinker, P. S. Behroozi, M. T. Busha, and R. Wechsler. A theoretical framework for combining techniques that probe the link between galaxies and dark matter. *Astrophys. J.*, 738:45, 2011.

[115] A. Leauthaud, J. Tinker, K. Bundy, P. S. Behroozi, R. Massey, J. Rhodes, M. R. George, J.-P. Kneib, A. Benson, R. H. Wechsler, M. T. Busha, P. Capak, M. Cortês, O. Ilbert, A. M. Koekemoer, O. Le Fèvre, S. Lilly, H. J. McCracken, M. Salvato,

T. Schrabback, N. Scoville, T. Smith, and J. E. Taylor. New Constraints on the Evolution of the Stellar-to-dark Matter Connection: A Combined Analysis of Galaxy-Galaxy Lensing, Clustering, and Stellar Mass Functions from z = 0.2 to z =1. , 744:159, January 2012.

[116] Julien Lesgourgues. The cosmic linear anisotropy solving system (class) i: Overview, 2011.

[117] Julien Lesgourgues. The Cosmic Linear Anisotropy Solving System (CLASS) I: Overview. 4 2011.

[118] A LEWIS and A CHALLINOR. Weak gravitational lensing of the cmb. *Physics Reports*, 429(1):1–65, Jun 2006.

[119] Antony Lewis. Lensed CMB simulation and parameter estimation. *Phys. Rev. D*, 71:083008, 2005.

[120] Antony Lewis. Getdist: a python package for analysing monte carlo samples, 2019.

[121] Antony Lewis, Anthony Challinor, and Anthony Lasenby. Efficient computation of CMB anisotropies in closed FRW models. *Astrophys. J.*, 538:473–476, 2000.

[122] C. K. Li, L. Lin, S. L. Xiong, M. Y. Ge, X. B. Li, T. P. Li, F. J. Lu, S. N. Zhang, Y. L. Tuo, Y. Nang, and et al. Hxmt identification of a non-thermal x-ray burst from sgr j1935+2154 and with frb 200428. *Nature Astronomy*, 5(4):378–384, Feb 2021.

[123] Ming Li, Raul E. Angulo, Simon D. M. White, and Jens Jasche. Matched filter optimization of kSZ measurements with a reconstructed cosmological flow field. *Mon.Not.Roy.Astron.Soc.*, 443(3):2311–2326, 2014.

[124] D. Nelson Limber. The Analysis of Counts of the Extragalactic Nebulae in Terms of a Fluctuating Density Field. , 117:134, January 1953.

[125] Andrei D. Linde and Viatcheslav F. Mukhanov. Nongaussian isocurvature perturbations from inflation. *Phys. Rev. D*, 56:535–539, 1997.

[126] Eric V. Linder. Detecting helium reionization with fast radio bursts. , 101(10):103019, May 2020.

[127] D. R. Lorimer, M. Bailes, M. A. McLaughlin, D. J. Narkevic, and F. Crawford. A Bright Millisecond Radio Burst of Extragalactic Origin. *Science*, 318(5851):777, November 2007.

[128] Thibaut Louis, Emory F. Bunn, Benjamin Wandelt, and Joseph Silk. Measuring Polarized Emission in Clusters in the CMB S4 Era. *Phys. Rev.*, D96(12):123509, 2017.

[129] Marilena LoVerde and Niayesh Afshordi. Extended limber approximation. *Physical Review D*, 78(12), Dec 2008.

[130] LSST Dark Energy Science Collaboration, R. Mandelbaum, T. Eifler, R. Hlo**v**zek, T. Collett, E. Gawiser, D. Scolnic, D. Alonso, H. Awan, R. Biswas, J. Blazek, P. Burchat, N. E. Chisari, I. Dell'Antonio, S. Digel, J. Frieman, D. A. Goldstein, I. Hook, **v**Z. Ivezić, S. M. Kahn, S. Kamath, D. Kirkby, T. Kitching, E. Krause, P.-F. Leget, P. J. Marshall, J. Meyers, H. Miyatake, J. A. Newman, R. Nichol, E. Rykoff, F. J. Sanchez, A. Slosar, M. Sullivan, and M. A. Troxel. The LSST Dark Energy Science Collaboration (DESC) Science Requirements Document. *ArXiv e-prints*, September 2018.

[131] LSST Science Collaboration. LSST Science Book, Version 2.0. *arXiv e-prints*, page arXiv:0912.0201, December 2009.

[132] LSST Science Collaboration, P. A. Abell, J. Allison, S. F. Anderson, J. R. Andrew, J. R. P. Angel, L. Armus, D. Arnett, S. J. Asztalos, T. S. Axelrod, and et al. LSST Science Book, Version 2.0. *ArXiv e-prints*, December 2009.

[133] David H. Lyth, Carlo Ungarelli, and David Wands. The Primordial density perturbation in the curvaton scenario. *Phys. Rev. D*, 67:023503, 2003.

[134] David H. Lyth and David Wands. Generating the curvature perturbation without an inflaton. *Phys. Lett. B*, 524:5–14, 2002.

[135] Roy Maartens. Is the Universe homogeneous? *Philosophical Transactions of the Royal Society A: Mathematical, Physical and Engineering Sciences*, 369(1957):5115–5137, dec 2011.

[136] J.-P. Macquart, J. X. Prochaska, M. McQuinn, K. W. Bannister, S. Bhandari, C. K. Day, A. T. Deller, R. D. Ekers, C. W. James, L. Marnoch, and et al. A census of baryons in the universe from localized fast radio bursts. *Nature*, 581(7809):391–395, May 2020.

[137] Mathew S. Madhavacheril, Nicholas Battaglia, Kendrick M. Smith, and Jonathan L. Sievers. Cosmology with the kinematic Sunyaev-Zeldovich effect: Breaking the optical depth degeneracy with fast radio bursts. *Phys. Rev. D*, 100(10):103532, 2019.

[138] Juan Martin Maldacena. Non-Gaussian features of primordial fluctuations in single field inflationary models. *JHEP*, 05:013, 2003.

[139] Kiyoshi W. Masui, J. Richard Shaw, Cherry Ng, Kendrick M. Smith, Keith Vanderlinde, and Adiv Paradise. Algorithms for fft beamforming radio interferometers, 2019.

[140] M. M. McKinnon. The analytical solution to the temporal broadening of a gaussian-shaped radio pulse by multipath scattering from a thin screen in the interstellar medium. *Publications of the Astronomical Society of the Pacific*, 126(939):476–481, May 2014.

[141] S. Mereghetti, V. Savchenko, C. Ferrigno, D. Götz, M. Rigoselli, A. Tiengo, A. Bazzano, E. Bozzo, A. Coleiro, T. J.-L. Courvoisier, and et al. Integral discovery of a burst with associated radio emission from the magnetar sgr 1935+2154. *The Astrophysical Journal*, 898(2):L29, Jul 2020.

[142] Tony Mroczkowski et al. Astrophysics with the Spatially and Spectrally Resolved Sunyaev-Zeldovich Effects: A Millimetre/Submillimetre Probe of the Warm and Hot Universe. *Space Sci. Rev.*, 215(1):17, 2019.

[143] Eva-Maria Mueller, Francesco de Bernardis, Rachel Bean, and Michael D. Niemack. Constraints on gravity and dark energy from the pairwise kinematic sunyaev–zel'dovich effect. *The Astrophysical Journal*, 808(1):47, Jul 2015.

[144] Eva-Maria Mueller, Francesco de Bernardis, Rachel Bean, and Michael D. Niemack. Constraints on gravity and dark energy from the pairwise kinematic Sunyaev-Zeldovich effect. *Astrophys. J.*, 808(1):47, 2015.

[145] Eva-Maria Mueller, Francesco de Bernardis, Rachel Bean, and Michael D. Niemack. Constraints on massive neutrinos from the pairwise kinematic Sunyaev-Zel'dovich effect. *Phys. Rev.*, D92(6):063501, 2015.

[146] Moritz Münchmeyer, Mathew S. Madhavacheril, Simone Ferraro, Matthew C. Johnson, and Kendrick M. Smith. Constraining local non-gaussianities with ksz tomography. *To appear*.

[147] Moritz Münchmeyer, Mathew S. Madhavacheril, Simone Ferraro, Matthew C. Johnson, and Kendrick M. Smith. Constraining local non-Gaussianities with kinetic Sunyaev-Zel'dovich tomography. *Phys. Rev.*, D100(8):083508, 2019.

[148] Dylan Nelson et al. The IllustrisTNG Simulations: Public Data Release. 12 2018.

[149] Laura B. Newburgh, Graeme E. Addison, Mandana Amiri, Kevin Bandura, J. Richard Bond, Liam Connor, Jean-François Cliche, Greg Davis, Meiling Deng, Nolan Denman, and et al. Calibrating chime: a new radio interferometer to probe dark energy. *Ground-based and Airborne Telescopes V*, Jul 2014.

[150] Cherry Ng, Keith Vanderlinde, Adiv Paradise, Peter Klages, Kiyoshi Masui, Kendrick Smith, Kevin Bandura, Patrick Joseph Boyle, Matt Dobbs, Victoria Kaspi, and et al. Chime frb: An application of fft beamforming for a radio telescope. *2017 XXXIInd General Assembly and Scientific Symposium of the International Union of Radio Science (URSI GASS)*, Aug 2017.

[151] Takemi Okamoto and Wayne Hu. CMB lensing reconstruction on the full sky. *Phys. Rev.*, D67:083002, 2003.

[152] Hyunbae Park, Marcelo A. Alvarez, and J. Richard Bond. The Impact of baryonic physics on the kinetic Sunyaev-Zel'dovich Effect. 2017.

[153] Hyunbae Park, Eiichiro Komatsu, Paul R. Shapiro, Jun Koda, and Yi Mao. The Impact of Nonlinear Structure Formation on the Power Spectrum of Transverse Momentum Fluctuations and the Kinetic Sunyaev–Zel'dovich Effect. *Astrophys. J.*, 818(1):37, 2016.

[154] Hyunbae Park, Paul R. Shapiro, Eiichiro Komatsu, Ilian T. Iliev, Kyungjin Ahn, and Garrelt Mellema. The Kinetic Sunyaev-Zel'dovich effect as a probe of the physics of cosmic reionization: the effect of self-regulated reionization. *Astrophys. J.*, 769:93, 2013.

[155] A. A. Penzias and R. W. Wilson. A Measurement of Excess Antenna Temperature at 4080 Mc/s. , 142:419–421, July 1965.

[156] E. Petroff, E. D. Barr, A. Jameson, E. F. Keane, M. Bailes, M. Kramer, V. Morello, D. Tabbara, and W. van Straten. FRBCAT: The Fast Radio Burst Catalogue. *Publ. Astron. Soc. Austral.*, 33:e045, 2016.

[157] E. Petroff, J. W. T. Hessels, and D. R. Lorimer. Fast Radio Bursts. *Astron. Astrophys. Rev.*, 27(1):4, 2019.

[158] Annalisa Pillepich, Cristiano Porciani, and Oliver Hahn. Universal halo mass function and scale-dependent bias from N-body simulations with non-Gaussian initial conditions. *Mon. Not. Roy. Astron. Soc.*, 402:191–206, 2010.

[159] Planck Collaboration et al. Planck intermediate results. XXXVII. Evidence of unbound gas from the kinetic Sunyaev-Zeldovich effect. *Astron. Astrophys.*, 586:A140, 2016.

[160] E. Platts, J. Xavier Prochaska, and Casey J. Law. A Data-driven Technique Using Millisecond Transients to Measure the Milky Way Halo. , 895(2):L49, June 2020.

[161] E. Platts, A. Weltman, A. Walters, S. P. Tendulkar, J. E. B. Gordin, and S. Kandhai. A Living Theory Catalogue for Fast Radio Bursts. *Phys. Rept.*, 821:1–27, 2019.

[162] Z. Pleunis et al. LOFAR Detection of 110–188 MHz Emission and Frequency-dependent Activity from FRB 20180916B. *Astrophys. J. Lett.*, 911(1):L3, 2021.

[163] William H. Press and Paul Schechter. Formation of galaxies and clusters of galaxies by selfsimilar gravitational condensation. *Astrophys. J.*, 187:425–438, 1974.

[164] V. Ravi, M. Catha, L. D'Addario, S. G. Djorgovski, G. Hallinan, R. Hobbs, J. Kocz, S. R. Kulkarni, J. Shi, H. K. Vedantham, and et al. A fast radio burst localized to a massive galaxy. *Nature*, 572(7769):352–354, Jul 2019.

[165] Emmanuel Schaan et al. Evidence for the kinematic Sunyaev-Zel'dovich effect with the Atacama Cosmology Telescope and velocity reconstruction from the Baryon Oscillation Spectroscopic Survey. *Phys. Rev.*, D93(8):082002, 2016.

[166] Emmanuel Schaan et al. The Atacama Cosmology Telescope: Combined kinematic and thermal Sunyaev-Zel'dovich measurements from BOSS CMASS and LOWZ halos. 9 2020.

[167] Marcel Schmittfull and Uros Seljak. Parameter constraints from cross-correlation of CMB lensing with galaxy clustering. *Phys. Rev. D*, 97(12):123540, 2018.

[168] Roman Scoccimarro, Lam Hui, Marc Manera, and Kwan Chuen Chan. Large-scale Bias and Efficient Generation of Initial Conditions for Non-Local Primordial Non-Gaussianity. *Phys. Rev. D*, 85:083002, 2012.

[169] Emiliano Sefusatti, Martin Crocce, Roman Scoccimarro, and Hugh Couchman. Accurate Estimators of Correlation Functions in Fourier Space. *Mon. Not. Roy. Astron. Soc.*, 460(4):3624–3636, 2016.

[170] Neelima Sehgal, Paul Bode, Sudeep Das, Carlos Hernandez-Monteagudo, Kevin Huffenberger, Yen-Ting Lin, Jeremiah P. Ostriker, and Hy Trac. Simulations of the microwave sky. *The Astrophysical Journal*, 709(2):920–936, Jan 2010.

[171] U. Seljak and M. Zaldarriaga. CMBFAST: A microwave anisotropy code, September 1999.

[172] Uros Seljak. Extracting primordial non-gaussianity without cosmic variance. *Phys. Rev. Lett.*, 102:021302, 2009.

[173] Urovs Seljak. Extracting primordial non-gaussianity without cosmic variance. *Physical Review Letters*, 102(2), Jan 2009.

[174] RM Shannon, J-P Macquart, KW Bannister, RD Ekers, CW James, S Oslowski, H Qiu, M Sammons, AW Hotan, MA Voronkov, RJ Beresford, M Brothers, AJ Brown, JD Bunton, AP Chippendale, C Haskins, M Leach, M Marquarding, D McConnell, MA Pilawa, EM Sadler, ER Troup, J Tuthill, MT Whiting, JR Allison, CS Anderson, ME Bell, JD Collier, G Gürkan, G Heald, and CJ Riseley. The dispersion-brightness relation for fast radio bursts from a wide-field survey. *Nature*, 562(7727):386—390, October 2018.

[175] L. D. Shaw, D. H. Rudd, and D. Nagai. Deconstructing the Kinetic SZ Power Spectrum. , 756:15, September 2012.

[176] Ravi K. Sheth, H. J. Mo, and Giuseppe Tormen. Ellipsoidal collapse and an improved model for the number and spatial distribution of dark matter haloes. *Mon. Not. Roy. Astron. Soc.*, 323:1, 2001.

[177] Ravi K. Sheth and Giuseppe Tormen. An Excursion Set Model of Hierarchical Clustering : Ellipsoidal Collapse and the Moving Barrier. *Mon. Not. Roy. Astron. Soc.*, 329:61, 2002.

[178] Simons Observatory Collaboration et al. The Simons Observatory: Science goals and forecasts. 2018.

[179] John Skilling. Nested sampling for general Bayesian computation. *Bayesian Analysis*, 1(4):833 – 859, 2006.

[180] Samuel W. Skillman, Michael S. Warren, Matthew J. Turk, Risa H. Wechsler, Daniel E. Holz, and P. M. Sutter. Dark Sky Simulations: Early Data Release. 2014.

[181] Anze Slosar, Christopher Hirata, Uros Seljak, Shirley Ho, and Nikhil Padmanabhan. Constraints on local primordial non-Gaussianity from large scale structure. *JCAP*, 08:031, 2008.

[182] Kendrick M. Smith and Simone Ferraro. Detecting Patchy Reionization in the Cosmic Microwave Background. *Phys. Rev. Lett.*, 119(2):021301, 2017.

[183] Kendrick M. Smith, Mathew S. Madhavacheril, Moritz Münchmeyer, Simone Ferraro, Utkarsh Giri, and Matthew C. Johnson. KSZ tomography and the bispectrum. 2018.

[184] R. E. Smith, J. A. Peacock, A. Jenkins, S. D. M. White, C. S. Frenk, F. R. Pearce, P. A. Thomas, G. Efstathiou, and H. M. P. Couchmann. Stable clustering, the halo model and nonlinear cosmological power spectra. *Mon. Not. Roy. Astron. Soc.*, 341:1311, 2003.

[185] Bjoern Soergel, Alexandro Saro, Tommaso Giannantonio, George Efstathiou, and Klaus Dolag. Cosmology with the pairwise kinematic SZ effect: calibration and validation using hydrodynamical simulations. *Mon. Not. Roy. Astron. Soc.*, 478(4):5320–5335, 2018.

[186] L. G. Spitler, P. Scholz, J. W. T. Hessels, S. Bogdanov, A. Brazier, F. Camilo, S. Chatterjee, J. M. Cordes, F. Crawford, J. Deneva, and et al. A repeating fast radio burst. *Nature*, 531(7593):202–205, Mar 2016.

[187] Volker Springel. The Cosmological simulation code GADGET-2. *Mon. Not. Roy. Astron. Soc.*, 364:1105–1134, 2005.

[188] Naonori S. Sugiyama, Teppei Okumura, and David N. Spergel. Will Kinematic Sunyaev-Zel'dovich Measurements Enhance the Science Return from Galaxy Redshift Surveys? 2016.

[189] R. A. Sunyaev and I. B. Zeldovich. The velocity of clusters of galaxies relative to the microwave background - The possibility of its measurement. *MNRAS*, 190:413–420, February 1980.

[190] Ryuichi Takahashi, Masanori Sato, Takahiro Nishimichi, Atsushi Taruya, and Masamune Oguri. Revising the Halofit Model for the Nonlinear Matter Power Spectrum. *Astrophys. J.*, 761:152, 2012.

[191] M. Tavani et al. An X-ray burst from a magnetar enlightening the mechanism of fast radio bursts. *Nature Astron.*, 5(4):401–407.

[192] Max Tegmark and Matias Zaldarriaga. Fast fourier transform telescope. *Physical Review D*, 79(8), Apr 2009.

[193] Alexandra Terrana, Mary-Jean Harris, and Matthew C. Johnson. Analyzing the cosmic variance limit of remote dipole measurements of the cosmic microwave background using the large-scale kinetic Sunyaev Zel'dovich effect. *Journal of Cosmology and Astroparticle Physics*, 2017(02):040–040, feb 2017.

[194] Alexandra Terrana, Mary-Jean Harris, and Matthew C. Johnson. Analyzing the cosmic variance limit of remote dipole measurements of the cosmic microwave background using the large-scale kinetic sunyaev zel'dovich effect. *Journal of Cosmology and Astroparticle Physics*, 2017(02):040–040, Feb 2017.

[195] A. Richard Thompson, James M. Moran, and Jr. Swenson, George W. *Interferometry and Synthesis in Radio Astronomy, 3rd Edition*. 2017.

[196] D. Thornton et al. A Population of Fast Radio Bursts at Cosmological Distances. *Science*, 341(6141):53–56, 2013.

[197] Patrick Valageas and Takahiro Nishimichi. Combining perturbation theories with halo models for the matter bispectrum. *Astron. Astrophys.*, 532:A4, 2011.

[198] L. Verde. Statistical methods in cosmology. *Lecture Notes in Physics*, page 147–177, 2010.

[199] Francisco Villaescusa-Navarro et al. The Quijote simulations. 9 2019.

[200] Ethan T. Vishniac. Reionization and small-scale fluctuations in the microwave background. *Astrophys. J.*, 322:597–604, 1987.

[201] Christian Wagner and Licia Verde. N-body simulations with generic non-Gaussian initial conditions II: Halo bias. *JCAP*, 03:002, 2012.

[202] Chul-Moon Yoo, Ken-ichi Nakao, and Misao Sasaki. CMB observations in LTB universes: Part II – the kSZ effect in an LTB universe. *JCAP*, 1010:011, 2010.

[203] P. Zhang. The dark flow induced small-scale kinetic Sunyaev-Zel'dovich effect. *MNRAS*, 407:L36–L40, September 2010.

[204] P. Zhang and A. Stebbins. Confirmation of the Copernican Principle at Gpc Radial Scale and above from the Kinetic Sunyaev-Zel'dovich Effect Power Spectrum. *Physical Review Letters*, 107(4):041301, July 2011.

[205] Pengjie Zhang and Matthew C. Johnson. Testing eternal inflation with the kinetic Sunyaev Zel'dovich effect. *JCAP*, 1506(06):046, 2015.

[206] J. P. Zibin and A. Moss. Linear kinetic Sunyaev-Zel'dovich effect and void models for acceleration. *Classical and Quantum Gravity*, 28(16):164005, August 2011.

Appendix A

Some useful results and derivations

A.1 Quadratic Estimator for radial velocity

The kSZ signal in the Fourier space is a convolution given by:

$$T(\mathbf{l}) = \frac{K_*}{\chi^2} \int \frac{d\mathbf{q}^3}{(2\pi)^3} \frac{d\mathbf{q}'3}{(2\pi)^3} \delta_e(\mathbf{q}) v_r(\mathbf{q}') (2\pi)^3 \delta^3 \left(\mathbf{q} + \mathbf{q\prime} + \frac{\mathbf{l}}{\chi_*} \right) \tag{A.1}$$

For large multipoles l where kSZ dominates, the above expression couples large-scale velocity modes with small scale electron-density field. Due to this very nature of kSZ, one can combine the CMB temperature map with a tracer of large-scale electron field and sum over small scale modes and multipoles to get an estimate of the large scale radial field.

Therefore we can write a quadratic estimator which has the general form

$$\hat{v}_r(\mathbf{k}_L) = \int \frac{d^3\mathbf{k}_S}{(2\pi)^3} \frac{d^2\mathbf{l}}{(2\pi)^2} W(\mathbf{k}_S, \mathbf{l}) \delta_g^*(\mathbf{k}_S) T^*(\mathbf{l}) \, (2\pi)^3 \delta^3 \left(\mathbf{k}_L + \mathbf{k}_S + \frac{\mathbf{l}}{\chi_*} \right) \tag{A.2}$$

with ensemble average given by

$$\begin{aligned} \langle \hat{v}_r(\mathbf{k}_L) \rangle &= \int \frac{d^3\mathbf{k}_S}{(2\pi)^3} \frac{d^2\mathbf{l}}{(2\pi)^2} W(\mathbf{k}_S, \mathbf{l}) \langle \delta_g^*(\mathbf{k}_S) T^*(\mathbf{l}) \rangle \, (2\pi)^3 \delta^3 \left(\mathbf{k}_L + \mathbf{k}_S + \frac{\mathbf{l}}{\chi_*} \right) & \text{(A.3)} \\ &= \left[\frac{K_*}{\chi_*^2} \int \frac{d^3\mathbf{k}_S}{(2\pi)^3} \frac{d^2\mathbf{l}}{(2\pi)^2} W(\mathbf{k}_S, \mathbf{l}) P_{ge}(\mathbf{k}_S) \, (2\pi)^3 \delta^3 \left(\mathbf{k}_L + \mathbf{k}_S + \frac{\mathbf{l}}{\chi_*} \right) \right] v_r(\mathbf{k}_L) & \text{(A.4)} \end{aligned}$$

with the *leading-order* [1] variance given by

$$Var(\hat{v}_r(\mathbf{k}_L)) = \int \frac{d^3\mathbf{k}_S}{(2\pi)^3}\frac{d^2\mathbf{l}}{(2\pi)^2}|W(\mathbf{k}_S,\mathbf{l})|^2 P_{gg}(\mathbf{k}_S) C_l\,(2\pi)^3\delta^3\left(\mathbf{k}_L + \mathbf{k}_S + \frac{\mathbf{l}}{\chi_*}\right) \tag{A.5}$$

The optimal quadratic estimator can be derived from Eq. (A.5) by minimizing its variance while keeping it unbiased i.e. $\hat{v}_r(\mathbf{k}_L) = \langle \hat{v}_r(\mathbf{k}_L)\rangle$. The constraint for unbiased estimator reduces to the condition that the term in square brackets in Eq. (A.4) is 1:

$$N = \left[\frac{K_*}{\chi_*^2}\int \frac{d^3\mathbf{k}_S}{(2\pi)^3}\frac{d^2\mathbf{l}}{(2\pi)^2} W(\mathbf{k}_S,\mathbf{l}) P_{ge}(\mathbf{k}_S)\,(2\pi)^3\delta^3\left(\mathbf{k}_L + \mathbf{k}_S + \frac{\mathbf{l}}{\chi_*}\right)\right] = 1 \tag{A.6}$$

We can perform this constrained optimization by using the method of lagrange multipliers. The Lagrangian function for our case will be given by

$$Var(\hat{v}_r(\mathbf{k}_L)) - \lambda N = 0 \tag{A.7}$$

on maximizing this with respect to the weight, we get

$$W^*(\mathbf{k}_S,\mathbf{l}) = W(\mathbf{k}_S,\mathbf{l}) = \lambda\frac{K_*}{\chi_*^2}\frac{P_{ge}(\mathbf{k}_S)}{P_{gg}(\mathbf{k}_S)C_l^{tot}} \tag{A.8}$$

to get λ we substitute this back in N

$$N = \left[\lambda\frac{K_*}{\chi_*^2}\int \frac{d^3\mathbf{k}_S}{(2\pi)^3}\frac{d^2\mathbf{l}}{(2\pi)^2}\frac{P_{ge}(\mathbf{k}_S)^2}{P_{gg}(\mathbf{k}_S)C_l\chi_*^2}\,(2\pi)^3\delta^3\left(\mathbf{k}_L + \mathbf{k}_S + \frac{\mathbf{l}}{\chi_*}\right)\right] = 1 \tag{A.9}$$

which gives

$$\lambda = \frac{\chi_*^4}{K_*}\left[\int \frac{d^3\mathbf{k}_S}{(2\pi)^3}\frac{d^2\mathbf{l}}{(2\pi)^2}\frac{P_{ge}(\mathbf{k}_S)^2}{P_{gg}(\mathbf{k}_S)C_l^{tot}}\,(2\pi)^3\delta^3\left(\mathbf{k}_L + \mathbf{k}_S + \frac{\mathbf{l}}{\chi_*}\right)\right]^{-1} \tag{A.10}$$

and so finally we have an expression for the optimal expression

$$\hat{v}_r(\mathbf{k}_L) = \lambda\frac{K_*}{\chi_*^2}\int \frac{d^3\mathbf{k}_S}{(2\pi)^3}\frac{d^2\mathbf{l}}{(2\pi)^2}\frac{P_{ge}(k_S)}{P_{gg}(k_S)C_l^{\rm tot}}\delta_g^*(\mathbf{k}_S)T^*(\mathbf{l})\,(2\pi)^3\delta^3\left(\mathbf{k}_L + \mathbf{k}_S + \frac{\mathbf{l}}{\chi_*}\right) \tag{A.11}$$

---

[1] One of the major results in this work is the derivation of higher-order contribution to this variance. This is done in the next chapter.

A.2 Mode-counting integral

The purpose of this appendix is to derive Eq. (2.18) for the Fisher matrix $F_{BB'}$ as an integral over scalar wavenumbers. We start from the definition of $F_{BB'}$:

$$F_{BB'} = \frac{V}{2} \int \frac{d^3\mathbf{k}}{(2\pi)^3} \frac{d^3\mathbf{k}'}{(2\pi)^3} \frac{d^2\mathbf{l}}{(2\pi)^2} \frac{B(k,k',l,k_r)^*\, B'(k,k',l,k_r)}{P_{gg}^{\rm tot}(k)\, P_{gg}^{\rm tot}(k')\, C_l^{TT,{\rm tot}}} (2\pi)^3 \delta^3\left(\mathbf{k} + \mathbf{k}' + \frac{\mathbf{l}}{\chi_*}\right) \tag{A.12}$$

and insert the following expression in the integrand on the RHS:

$$1 = \int dK\, dK'\, dL\, d\kappa \left(\delta(|\mathbf{k}| - K)\, \delta(|\mathbf{k}'| - K')\, \delta(|\mathbf{l}| - L)\, \delta(k_r - \kappa) \right) \tag{A.13}$$

to write $F_{BB'}$ in the form

$$F_{BB'} = \frac{V}{2} \int dK\, dK'\, dL\, d\kappa\, I(K,K',L,\kappa) \frac{B(K,K',L,\kappa)^*\, B'(K,K',L,\kappa)}{P_{gg}^{\rm tot}(K)\, P_{gg}^{\rm tot}(K')\, C_L^{TT,{\rm tot}}} \tag{A.14}$$

where $I(K,K',L,\kappa)$ is the "mode-counting integral"

$$I(K,K',L,\kappa) = \int_{\mathbf{k}+\mathbf{k}'+\frac{\mathbf{l}}{\chi_*}=0} \delta(k-K)\delta(k'-K')\delta(l-L')\delta(k_r-\kappa) \tag{A.15}$$

which counts the number of closed triangles $\mathbf{k} + \mathbf{k}' + (\mathbf{l}/\chi_*) = 0$ with lengths (K, K', L) and radial wavenumber κ.

It remains to calculate I explicitly. First note that by rotational symmetry, the quantity

$$J(K,K',\kappa,\mathbf{l}) = \int \frac{d^3\mathbf{k}}{(2\pi)^3} \frac{d^3\mathbf{k}'}{(2\pi)^3} (2\pi)^3 \delta^3\left(\mathbf{k} + \mathbf{k}' + \frac{\mathbf{l}}{\chi_*}\right) \delta(k-K)\delta(k'-K')\delta(k_3-\kappa) \tag{A.16}$$

only depends on $\mathbf{l}$ through its length $l = |\mathbf{l}|$. Therefore I and J are related by:

$$I = \int \frac{d^2\mathbf{l}}{(2\pi)^2} J(\mathbf{l})\delta(l-L) = \frac{L}{2\pi} J(L) \tag{A.17}$$

To compute J, we assume $\mathbf{l}$ points in the x-direction, and use the 3D delta function to eliminate the $d^3\mathbf{k}'$ integral, obtaining:

$$J = \int \frac{d^3\mathbf{k}}{(2\pi)^3} \delta(k-K)\delta(k'-K')\delta(k_3-\kappa) \tag{A.18}$$

where k' is defined in the integrand by $k'^2 = (k_1 - l/\chi_*)^2 + k_2^2 + k_3^2$. Since this a 3D integral with three delta functions, it is given by the inverse Jacobian

$$J = 2\frac{1}{(2\pi)^3}\left(\frac{\partial\{k, k', k_3\}}{\partial\{k_1, k_2, k_3\}}\right)^{-1} \tag{A.19}$$

where the prefactor 2 is because the delta function constraints have two solutions. A short calculation now gives the Jacobian:

$$\frac{\partial\{k, k', k_3\}}{\partial\{k_1, k_2, k_3\}} = \frac{l}{kk'\chi_*}\left[\Gamma\left(k, k', \frac{l}{\chi_*}\right)^2 - k_3^2\right]^{1/2} \tag{A.20}$$

where we have defined

$$\Gamma(k, k', k'') = \frac{\sqrt{(k + k' + k'')(k + k' - k'')(k + k'' - k')(k' + k'' - k)}}{2k''} \tag{A.21}$$

Note that all factors under the square root are positive if the wavenumbers k, k', k'' satisfy the inequalities needed for k, k', k'' to form a closed triangle. By Heron's formula, $\Gamma(k, k', k'')$ can be interpreted as the component of k (or k') perpendicular to k'', in a closed triangle $\mathbf{k} + \mathbf{k}' + \mathbf{k}'' = 0$. Thus the inequality that κ must satisfy to ensure that the delta function constraints have solutions is simply $|\kappa| \le \Gamma(k, k', l/\chi)$.

Putting Eqs. (A.17), (A.19), (A.20) together, we get our bottom-line formula for I:

$$I(K, K', L, \kappa) = \frac{KK'\chi_*}{8\pi^4}\left[\Gamma\left(K, K', \frac{L}{\chi_*}\right)^2 - \kappa^2\right]^{-1/2} \tag{A.22}$$

where the formula is understood to apply when $K, K', (L/\chi_*)$ form a closed triangle, and $|\kappa| \le \Gamma(K, K', L/\chi_*)$. Otherwise, $I = 0$.

A.3 Halo model

Throughout this chapter, we use the halo model to compute nonlinear power spectra involving dark matter, electron, and galaxy fields. In this appendix, we describe the details.

In the halo model, one makes the fundamental assumption that all the dark and baryonic matter is bound up in halos with varying mass and density profiles. The correlation function for density fluctuations then receives two contributions: a “two halo term” which arises from the clustering properties of distinct halos, and a “one halo term” which arises from the correlation in density between two points in the same halo. A review of the halo model can be found in Ref. [50].

Dark matter

In Fourier space, the dark matter power spectrum is given by

$$\begin{aligned} P_{mm}(k,z) &= P^{1h}_{mm}(k,z) + P^{2h}_{mm}(k,z) && \text{(A.23)} \\ P^{1h}_{mm}(k,z) &= \int_{-\infty}^{\infty} d\ln m \; mn(m,z)\left(\frac{m}{\rho_m}\right)^2 |u(k|m,z)|^2 && \text{(A.24)} \\ P^{2h}_{mm}(k,z) &= P^{\rm lin}(k,z)\left[\int_{-\infty}^{\infty} d\ln m \; mn(m,z)\left(\frac{m}{\rho_m}\right) b_h(m,z)u(k|m,z)\right]^2 && \text{(A.25)} \end{aligned}$$

In these expressions, m is the halo mass, ρ_m is the present day cosmological matter density, $n(m,z)$ is the halo mass function (e.g. the differential number density of halos with respect to mass), $u(k|m,z)$ is the normalized Fourier transform of the halo profile, $P^{\rm lin}(k)$ is the linear matter power spectrum, and $b_h(m,z)$ is the linear halo bias.

The halo mass function is defined by

$$n(m,z) = \frac{\rho_m}{m^2} f(\sigma,z)\frac{d\ln\sigma(m,z)}{d\ln m}, \tag{A.26}$$

where $\sigma^2(m,z)$ is the rms variance of mass within a sphere of radius R that contains mass $m = 4\pi\rho_m R^3/3$, defined as

$$\sigma^2(m,z) = \frac{1}{2\pi^2}\int_0^{\infty} dk \; k^2 P^{\rm lin}(k,z) W^2(kR) \tag{A.27}$$

Here, $R = R(m)$ and the window function in Fourier space is

$$W(kR) = \frac{3\left[\sin(kR) - kR\cos(kR)\right]}{(kR)^3} \tag{A.28}$$

We assume the Sheth-Tormen collapse fraction [176]:

$$f(\sigma,z) = A\sqrt{\frac{2a}{\pi}}\left[1 + \left(\frac{\sigma^2}{a\delta_c^2}\right)^p\right]\frac{\delta_c}{\sigma}\exp\left[-\frac{a\delta_c^2}{2\sigma^2}\right] \tag{A.29}$$

with $A = 0.3222$, $a = 0.75$, $p = 0.3$, and $\delta_c = 1.686$. The linear halo bias $b_h(m,z)$ accounts for the biasing of halos in the presence of variations in the density field, and is given by the response of the number density to variations in the collapse threshold δ_c. We use the

Sheth-Tormen bias:

$$\begin{aligned} b_h(m,z) &= 1+\frac{1}{\delta_c}\frac{d\log f}{d\log\sigma} \\ &= 1+\frac{1}{\delta_c}\left(a\frac{\delta_c^2}{\sigma^2}-1\right)+\frac{2p}{\delta_c}\left(1+\left(a\frac{\delta_c^2}{\sigma^2}\right)^p\right)^{-1} \end{aligned} \tag{A.30}$$

Note that the halo bias satisfies a consistency relation:

$$\int_{-\infty}^{\infty} d\ln m\; mn(m,z)\left(\frac{m}{\rho_m(z)}\right)b_h(m,z)=1. \tag{A.31}$$

Finally, we need $u(k|m,z)$, the Fourier transform of the dark matter halo density profile, which for spherically symmetric profiles is defined as

$$u(k|m,z)=\int_0^{r_{\rm vir}} dr\; 4\pi r^2\frac{\sin(kr)}{kr}\frac{\rho(r|m,z)}{m}. \tag{A.32}$$

We assume that halos are truncated at the virial radius, and have mass

$$m=\int_0^{r_{\rm vir}} dr\; 4\pi r^2\rho(r|m,z) \tag{A.33}$$

Note that with this definition of mass, $u(k|m,z)\to 1$ as $k\to 0$. Returning to the two-halo term and using the consistency relation in Eq. (A.31), this property of $u(k|m,z)$ ensures that $P_{mm}^{2h}(k,z)\simeq P^{\rm lin}(k,z)$ in the limit where $k\to 0$, as it should.

We assume that dark matter halos follow an NFW profile:

$$\rho(r|m,z)=\frac{\rho_s}{(r/r_s)(1+r/r_s)^2} \tag{A.34}$$

and relate the scale radius r_s to the virial radius $r_{\rm vir}$ by the concentration parameter $c=r_{\rm vir}/r_s$. We model the concentration by the median power law fit of [68], neglecting stochasticity:

$$c(m,z)=A\left(\frac{m}{2\times 10^{12}h^{-1}M_\odot}\right)^{\alpha}(1+z)^{\beta} \tag{A.35}$$

with $A=7.85$, $\alpha=-0.081$, and $\beta=-0.71$.

Including halos in the range $10^4M_\odot < m < 10^{17}M_\odot$, our model reproduces the non-linear matter power spectrum using the commonly used 'halofit' model of Ref. [184] at the $< 10\%$ level over the range 10^{-5} Mpc$^{-1} < k < 20$ Mpc^{-1}.

Electrons

The electron distribution in the halo model is modelled by assuming gas is bound within dark matter halos, having density profiles $\rho_{\rm gas}(m,z)$ which we assume to be a function of the host halo mass and redshift only. The gas power spectrum is given by Eq. A.23 with $u(k|m,z)$ calculated through Eq. A.32 by replacing $\rho(m,z)$ with $\rho_{\rm gas}(m,z)$ and computing a grid of templates. To estimate the systematic uncertainty associated with the distribution of free electrons within halos, we employ three models for the electron profile: the universal gas profile of Ref. [111] and two fitting functions from Ref. [25] based on simulations with two different sub-grid feedback models ("AGN" and "SH"). Throughout we assume that electrons trace gas, and neglect the deficit in large scale power caused by collapse of gas into stars within halos [2].

The universal gas profile of Ref. [111] is obtained by assuming that the gas has a polytropic equation of state $P \propto \rho^\gamma$ with unknown γ and demanding hydrostatic equilibrium within the gravitational potential well of the dark matter halo (assumed NFW, as above). The two unknown parameters, γ and an integration constant from the equation for hydrostatic equilibrium, are fixed by demanding that the slope of the gas profile matches that of the dark matter at twice the virial radius. Therefore, within this model, we explicitly require that gas traces dark matter on the largest scales.

The fitting function for the AGN and SH models of Ref. [25] is given by [3]

$$\rho_{\rm gas} = \frac{\Omega_b}{\Omega_m}\rho_c(z)\bar{\rho}_0(m,z)\left(\frac{r}{2R_{200}(m,z)}\right)^\gamma \left[1+\left(\frac{r}{2R_{200}(m,z)}\right)^{\alpha(m,z)}\right]^{-(\beta(m,z)+\gamma)/\alpha(m,z)} \tag{A.36}$$

where $\gamma = -0.2$, $R_{200}(m,z)$ is radius at which the dark matter halo reaches a density $200\rho_c(z)$, and the parameters $\bar{\rho}_0(m,z)$, $\alpha(m,z)$, and $\beta(m,z)$ are fitted with a power law in halo mass and redshift:

$$A = A_0^x\left(\frac{M_{200}}{10^{14}M_\odot}\right)^{\alpha_m^x}(1+z)^{\alpha_z^x} \tag{A.37}$$

with parameters in the AGN and SH model given from Table 2 of Ref. [25]. For the AGN model, we have $\{A_0^{\rho_0},\alpha_m^{\rho_0},\alpha_z^{\rho_0}\} = \{4000, 0.29, -0.66\}$, $\{A_0^{\alpha},\alpha_m^{\alpha},\alpha_z^{\alpha}\} = \{0.88, -0.03, 0.19\}$, and $\{A_0^{\beta},\alpha_m^{\beta},\alpha_z^{\beta}\} = \{3.83, 0.04, -0.025\}$. For the SH model, we have $\{A_0^{\rho_0},\alpha_m^{\rho_0},\alpha_z^{\rho_0}\} = \{19000, 0.09, -0.95\}$, $\{A_0^{\alpha},\alpha_m^{\alpha},\alpha_z^{\alpha}\} = \{0.70, -0.017, 0.27\}$, $\{A_0^{\beta},\alpha_m^{\beta},\alpha_z^{\beta}\} = \{4.43, 0.005, 0.037\}$.

---

[2] This can cause a $\sim 30-50\%$ decrease in power on large scales [175]

[3] To be consistent with a universal NFW profile, where β is the power law index at large r, one must correct Eq. A1 of Ref. [25] as we have done here.

In Fig. A.1 we compare the 1-halo terms in the power spectrum for the three gas models to the 1-halo term for dark matter for halos in the range $10^{10}M_\odot < m < 10^{17}M_\odot$. The one halo term is the dominant contribution to the power spectrum over the plotted range. On scales $k.5$ Mpc^{-1}, one can approximate the gas power spectrum by the dark matter power spectrum. At higher k, the difference between the gas profiles and dark matter and among the various gas models becomes apparent, with the three models giving different predictions at the $\sim 50\%$ level. This is indicative of the 'theory' error bar on the electron power spectrum, which depends in detail on how the various feedback processes are modelled.

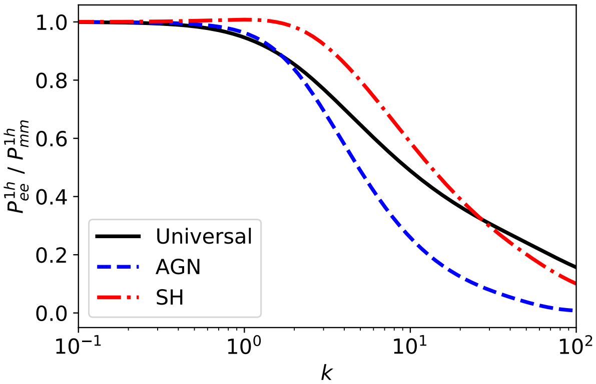

Figure A.1: The ratio of the one halo gas power spectrum P^{1h}_{ee} and the one halo dark matter power spectrum P^{1h}_{mm} for three models of the gas profile.

Galaxies

We model the distribution of galaxies within dark matter halos by the Halo Occupation Distribution (HOD) model [28] of Refs. [114, 115]. This model has been calibrated using measurements of the galaxy-galaxy power spectrum, galaxy-galaxy weak lensing, and the stellar mass function [115] to a redshift of $z = 1$. We extrapolate the applicable redshift range to $z \sim 4$ using fits for the stellar mass-halo mass relation in Ref. [26]. This is the 'baseline HOD model' of Ref. [91].

Briefly, the ingredients going into the HOD model are as follows. First, we assume separate distributions for central and satellite galaxies. The number of central galaxies in a halo is always 0 or 1, and centrals are at exact halo centers. The mean number of centrals

$\bar{N}_c(m)$ in a halo of mass m is fixed by the amount of stellar mass in each dark matter halo and given by:

$$\bar{N}_c(m) = \frac{1}{2} - \frac{1}{2}\mathrm{erf}\left(\frac{\log_{10}(m_*^{\mathrm{thresh}}) - \log_{10}\left[m_*(m)\right]}{\sqrt{2}\sigma_{\log m_*}}\right) \tag{A.38}$$

where $m_*(m)$ is the stellar mass in a halo of mass m. We specify the galaxy sample by imposing a threshold m_*^{thresh} in stellar mass of observable galaxies, and we assume a log-normal distribution for the stellar mass at fixed halo mass with constant redshift-independent scatter $\sigma_{\log m_*} = 0.2$ (consistent with [115]). We employ the model developed in Ref. [26] for $m_*(m)$, which we refer the reader to for more details. A fiducial threshold is $m_*^{\mathrm{thresh}} = 10^{10.5}\ M_\odot$, which corresponds to a halo mass of $m \simeq 10^{12}\ M_\odot$ at $z = 0$. In the body of the text, we match the number densities for various surveys by adjusting m_*^{thresh}.

For the satellite galaxies, we assume that the spatial profile is NFW, and the mean number of satellites $\bar{N}_s(m)$ in a halo of mass m is given by:

$$\bar{N}_s(m) = \bar{N}_c(m)\left(\frac{m}{m_{\mathrm{sat}}}\right)^{\alpha_{\mathrm{sat}}} e^{-m_{\mathrm{cut}}/m} \tag{A.39}$$

We choose values for the free parameters m_{sat}, α_{sat}, and m_{cut} (which depend on the choice of m_*^{thresh}) consistent with the 'SIG_MOD1' model of Ref. [115] (from the median redshift bin). We show $\bar{N}_c$ and $\bar{N}_s$ at $z = 0$ for our choice of parameters in Fig. A.2.

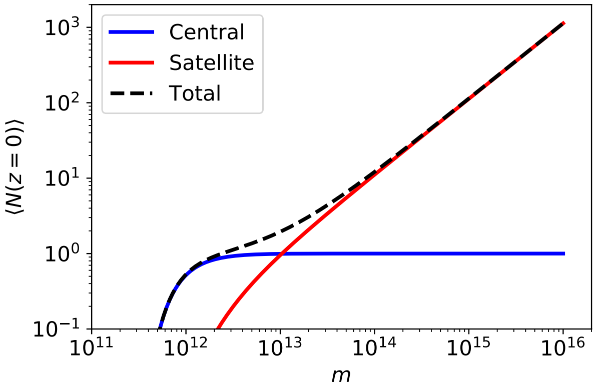

Figure A.2: The number of central and satellite galaxies as a function of halo mass using the assumed HOD at $z = 0$.

We define the one and two halo contributions to the galaxy-galaxy power spectrum as (see e.g. [28]):

$$P_{gg}(k,z) = P_{gg}^{1h}(k,z) + P_{gg}^{2h}(k,z) \tag{A.40}$$

$$P_{gg}^{1h}(k,z) = \int_{-\infty}^{\infty} d\ln m\, \frac{mn(m,z)}{n_g^2}\Big(2\big\langle N_c(m)N_s(m)\big\rangle u_c(k)u_s(k|m,z) + \big\langle N_s(m)(N_s(m)-1)\big\rangle u_s(k|m,z)^2\Big) \tag{A.41}$$

$$P_{gg}^{2h}(k,z) = P^{\mathrm{lin}}(k,z)\left[\int_{-\infty}^{\infty} d\ln m\; mn(m,z)b_h(m,z) \times\left(\frac{\bar{N}_c(m)u_c(k) + \bar{N}_s(m)u_s(k|m,z)}{n_g}^2\right)\right.$$

$$\tag{A.43}$$

Here, n_g is the mean number of galaxies as a function of halo mass and redshift:

$$n_g = \int_{-\infty}^{\infty} d\ln m\; mn(m,z)\left(\bar{N}_c(m) + \bar{N}_s(m)\right). \tag{A.44}$$

and $u_c(k), u_s(k|m,z)$ denote the Fourier-space profiles of the centrals and satellites. Since we are assuming that centrals are at exact halo centers, and satellites are NFW-distributed, we have $u_c(k) = 1$, and $u_s(k|m,z)$ is given by the Fourier-space NFW profile.[4]

The expectation values $\langle N_s(m)(N_s(m)-1)\rangle$ and $\langle N_c N_s\rangle$ appearing in Eq. (A.41) depend on the assumed correlation between centrals and satellites. We consider two extremes: (1) centrals and satellites are totally uncorrelated, and (2) a central is required for a satellite, and therefore centrals and satellites are maximally correlated. In these cases, and assuming that the number of satellites is Poisson distributed, a short calculation shows:

$$\langle N_s(m)(N_s(m)-1)\rangle = \begin{cases} \bar{N}_s(m)^2 & \text{if centrals and satellites are uncorrelated} \\ \bar{N}_s(m)^2/\bar{N}_c(m) & \text{if centrals and satellites are correlated} \end{cases} \tag{A.45}$$

$$\langle N_c(m)N_s(m)\rangle = \begin{cases} \bar{N}_c(m)\bar{N}_s(m) & \text{if centrals and satellites are uncorrelated} \\ \bar{N}_s(m) & \text{if centrals and satellites are correlated} \end{cases} \tag{A.46}$$

---

[4] In Eqs. (A.41), (A.42), we have denoted the profile $u_c(k)$ explicitly, rather than setting it to 1. This is to clarify a technical point which arises in §2.5 when modeling photometric redshift errors. As explained there, photo-z errors modify galaxy profiles as $u(k) \to W(k_r)u(k)$, where $W(k_r)$ is the Fourier-space photo-z error distribution. This convolution is applied to both profiles $u_c(k), u_s(k)$. By Eqs. (A.41), (A.42) it follows that both $P_{gg}^{1h}(k)$ and $P_{gg}^{2h}(k)$ are multiplied by factors of $W(k_r)^2$, as claimed in the body of the chapter (Eq. (2.80)).

When deriving this, note that in the maximally-correlated model, the number of satellites in a halo which contains a central (i.e. the conditional PDF $P(N_s|N_c = 1)$) is a Poisson random variable with mean $\bar{N}_s(m)/\bar{N}_c(m)$ (not mean $\bar{N}_s(m)$).

As our fiducial choice in the following we use the maximally-correlated model. At the level of the galaxy galaxy power spectrum, the difference between these two models is minimal (at the $\sim 5\%$ level for $k < 10^2$ Mpc^{-1}).

Examining the two-halo term, and using the property that $u_g(k|m,z) \to 1$ as $k \to 0$, we see that the linear galaxy bias is given by

$$b_g(z) = \int_{-\infty}^{\infty} d\ln m \; mn(m,z) b_h(m,z) \frac{\langle N_c(m)\rangle + \langle N_s(m)\rangle}{n_g} \tag{A.47}$$

yielding $P_{gg}^{2h}(k,z) \simeq b_g(z)^2 P^{\text{lin}}(k,z)$ on large scales.

Cross-power

The one and two halo contributions to the cross-power between galaxies and gas (or matter) is given by (see e.g. [28])

$$\begin{aligned}
P_{ge}(k,z) &= P_{ge}^{1h}(k,z) + P_{ge}^{2h}(k,z) && \text{(A.48)}\\
P_{ge}^{1h}(k,z) &= \int_{-\infty}^{\infty} d\ln m \; mn(m,z) \frac{m}{\rho_m} u_e(k|m,z) \frac{\langle N_c(m)\rangle u_c(k) + \langle N_s(m)\rangle u_s(k|m,z)}{n_g} && \text{(A.49)}\\
P_{ge}^{2h}(k,z) &= P^{\text{lin}}(k) \left[\int_{-\infty}^{\infty} d\ln m \; mn(m,z) b_h(m,z) \frac{\langle N_c(m)\rangle u_c(k) + \langle N_s(m)\rangle u_s(k|m,z)}{n_g}\right] \\
&\quad \times \left[\int_{-\infty}^{\infty} d\ln m \; mn(m,z) \left(\frac{m}{\rho_m}\right) b_h(m,z) u_e(k|m,z)\right] && \text{(A.50)}
\end{aligned}$$

where notation has been introduced above.

In Fig. A.3, we compare the auto and cross power for galaxies at redshifts $z = 0$ and $z = 1$ including halo masses in the range $10^{10} M_\odot < m < 10^{17} M_\odot$ assuming the 'AGN' model for the gas profile.

kSZ from the halo model

We will also need a model for the kSZ contribution to the CMB power spectrum C_l^{TT}. We model this as the sum of two terms, from late times (i.e. after reionization) and reionization.

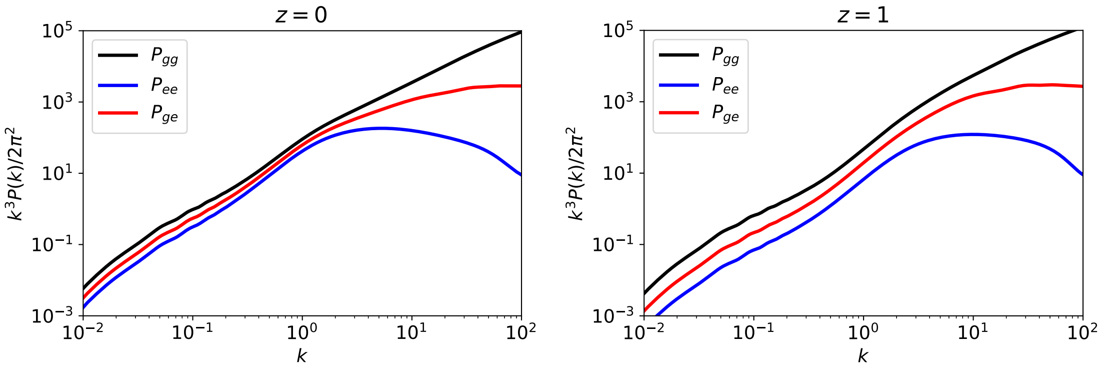

Figure A.3: Auto and cross power spectra in our halo model assuming the 'AGN' model for the gas profile at $z = 0$ (left) and $z = 1$ (right) including halo masses in the range $10^{10}M_\odot < m < 10^{17}M_\odot$.

We use the model from [154] for the reionization contribution to C_l^{TT}. We calculate the late-time kSZ contribution in the well known non-linear approximation from [99]. The kSZ angular power spectrum at large multipoles is dominated by the power spectrum of the transverse momentum field, $P_{q_\perp}(k)$, and is given by [200]

$$C_\ell = \frac{1}{2}\left(\frac{\sigma_T \bar{n}_{e,0}}{c}\right)^2 \int \frac{d\chi}{\chi^2 a^4} e^{-2\tau} P_{q_\perp}\left(k = \frac{l}{\chi}, \chi\right). \tag{A.51}$$

The power spectrum of the transverse momentum field can be approximated as [99]

$$P^{\mathrm{S}}_{q_\perp}(k,z) \;=\; \dot{a}^2 f^2 \int \frac{d^3k'}{(2\pi)^3} P^{nl}_{ee}(|\mathbf{k}-\mathbf{k}'|, z) P^{lin}_{\delta\delta}(k', z) \frac{k(k-2k'\mu')(1-\mu'^2)}{k'^2(k^2+k'^2-2kk'\mu')}$$

where P^{nl}_{ee} is the non-linear power spectrum of the electron distribution, which we calculated in the halo model. We show the resulting kSZ power spectra for different halo profiles in Fig. A.4. The differences between these profiles at the ℓ-range of interest in this work is only of the order of 10%. However the true uncertainty on the kSZ signal size is likely larger than that (compare for example the simulations in [175]). Nevertheless we are using consistent assumptions in this work by calculating P_{gg}, P_{ge} and P_{ee} from the same model.

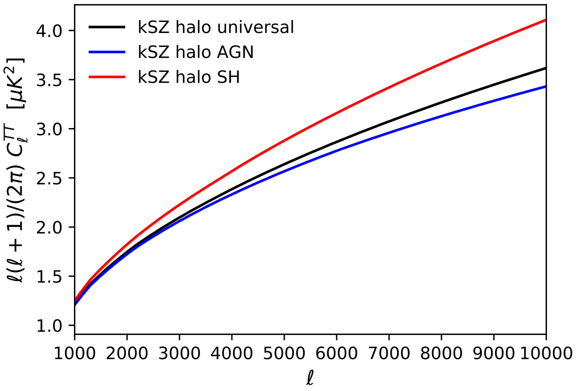

Figure A.4: CMB power spectrum from kSZ from redshifts $0 < z < 6$ calculated in the halo model using different electron distribution profiles.

Appendix B

Diagrammatic rules for the halo model

The main purpose of this appendix is to derive Eqs. (3.57)–(3.67) for the non-Gaussian six-point function

$$\Big\langle \delta_g(\mathbf{k}_1)\delta_e(\mathbf{k}_2)\delta_g(\mathbf{k}_3)\delta_e(\mathbf{k}_4)v_r(\mathbf{k}_5)v_r(\mathbf{k}_6)\Big\rangle_{ng} \tag{B.1}$$

in the halo model. In general, n-point correlation functions in the halo model consist of many combinatorial terms. A second purpose of this appendix is to show that these terms can be enumerated using diagrammatic rules, similar to Feynman rules in QFT.

We consider the simplest version of the halo model, in which halos are linearly biased tracers of a Gaussian field $\delta_{\rm lin}$ (the linear density field). In this model, the expected number of halos per volume per unit halo mass is:

$$s(M,\mathbf{x}) = n(M)\big(1 + b(M)\delta_{\rm lin}(\mathbf{x})\big) \tag{B.2}$$

where $n(M)$ is the halo mass function and $b(M)$ is the linear bias. We will call $s(M,\mathbf{x})$ the *halo source field*, and distingiush it from the halo density field $\delta_h(\mathbf{x})$, which is a sum of delta functions. By assumption in the halo model, the halo density field is given by Poisson-sampling the halo source field.

We consider fields δ_X which are sums over halos:

$$\delta_X(\mathbf{k}) = \sum_j W_X(M_j,k)e^{-i\mathbf{k}\cdot\mathbf{x}_j} \tag{B.3}$$

where the j-th halo has mass M_j and position $\mathbf{x}_j$. In particular, in our collisionless approximation (§3.2.1), the electron field δ_e and galaxy field δ_g are of the form (B.3), with weight functions $W_X(M,z)$ given by:

$$W_e(M,k) = \frac{M}{\rho_m} u_M(k) \qquad\qquad W_g(M,k) = \begin{cases} 1/n_h & \text{if } M \geq M_{\text{min}} \\ 0 & \text{if } M < M_{\text{min}} \end{cases} \tag{B.4}$$

where $u_M(k)$ is the Fourier-transformed density profile of a halo of mass M, normalized so that $u_M(0) = 1$.

B.1 Expectation values in a fixed realization of the halo source field

Expectation values in the halo model can be calculated in two steps. First, we take an "inner" average over Poisson-sampled halos, in a fixed realization of the source field $s(M,\mathbf{x})$. Second, we take an "outer" average over realizations of $s(M,\mathbf{x})$, or equivalently realizations of $\delta_{\text{lin}}(\mathbf{x})$ via Eq. (B.2). In this section, we will analyze the inner average. We consider an n-point expectation value $\langle \delta_{X_1}(\mathbf{k}_1) \cdots \delta_{X_n}(\mathbf{k}_n) \rangle_s$, where the suffix $\langle \cdot \rangle_s$ means that the expectation value is taken over Poisson placements of halos, in a fixed realization of $s(M,\mathbf{x})$.

We plug in the definition (B.3) of δ_X, to write the expectation value as a sum over n-tuples of halos:

$$\big\langle \delta_{X_1}(\mathbf{k}_1) \cdots \delta_{X_n}(\mathbf{k}_n) \big\rangle_s = \left\langle \sum_{j_1,\cdots,j_n} \left(\prod_{i=1}^n W_{X_i}(M_{j_i}, k_i) e^{-i\mathbf{k}_i \cdot \mathbf{x}_{j_i}} \right) \right\rangle_s \tag{B.5}$$

Then, as usual in the halo model, we split the sum into combinatorial terms, based on which elements of the n-tuple $(j_1, \cdots, j_n)$ are equal to each other. For example, consider the four-point function

$$\big\langle \delta_g(\mathbf{k}_1) \delta_e(\mathbf{k}_2) \delta_g(\mathbf{k}_3) \delta_e(\mathbf{k}_4) \big\rangle \tag{B.6}$$

which is a subset of the six-point function (B.1). Writing the four-point function as a sum over halo quadruples, we could keep terms (j_1, j_2, j_3, j_4) such that

$$j_1 = j_4 = j \quad \text{and} \quad j_2 = j_3 = j' \quad \text{with } j \neq j' \tag{B.7}$$

obtaining a contribution which we will denote by T:

$$T = \left\langle \sum_{j\neq j'} \Big(W_g(M_j,k_1)W_e(M_j,k_4)e^{-i(\mathbf{k}_1+\mathbf{k}_4)\cdot\mathbf{x}_j}\Big)\Big(W_e(M_{j'},k_2)W_g(M_{j'},k_3)e^{-i(\mathbf{k}_2+\mathbf{k}_3)\cdot\mathbf{x}_{j'}}\Big)\right\rangle_s \tag{B.8}$$

This term T is one of 7 "two-halo" terms which contribute to the four-point function (B.6), out of 15 total terms. Physically, T corresponds to summing over all quadruples (g_1, e_2, g_3, e_4) such that galaxy g_1 and electron e_4 are in one halo, and galaxy g_2 and electron e_3 are in a different halo. To compute T, we replace each sum $\sum_j$ by an integral $\int d^3\mathbf{x}\, dM\, s(M,\mathbf{x})$, obtaining:

$$\begin{aligned} T &= \left(\int d^3\mathbf{x}\, dM\, W_g(M,k_1)W_e(M,k_4)s(M,\mathbf{x})e^{-i(\mathbf{k}_1+\mathbf{k}_4)\cdot\mathbf{x}}\right) \\ &\quad\times \left(\int d^3\mathbf{x}'\, dM'\, W_e(M',k_2)W_g(M',k_3)s(M',\mathbf{x}')e^{-i(\mathbf{k}_2+\mathbf{k}_3)\cdot\mathbf{x}'}\right) \\ &= \left(\int dM\, W_g(M,k_1)W_e(M,k_4)s(M,\mathbf{k}_1+\mathbf{k}_4)\right)\left(\int dM'\, W_e(M',k_2)W_g(M',k_3)s(M,\mathbf{k}_2+\mathbf{k}_3)\right) \end{aligned} \tag{B.9}$$

We now introduce diagrammatic notation, representing this equation by the diagram:

$$T =$$

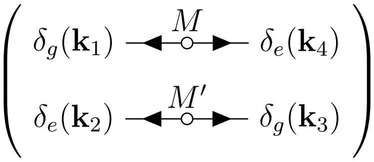

(B.10)

where diagrams are translated to equations using the rules:

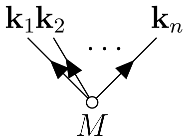

$$= \int dM\, s(M, \textstyle\sum \mathbf{k}_i)$$

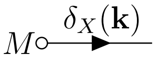

$$= W_X(M,k) \tag{B.11}$$

In general, an n-point correlation function $\langle\delta_{X_i}(\mathbf{k}_i)\cdots\delta_{X_n}(\mathbf{k}_n)\rangle_s$ is the sum over all diagrams obtained using these rules. External lines in the diagrams correspond to fields being correlated, and vertices correspond to halos.

B.2 Fully averaged expectation values

The diagrammatic rules just derived in Eq. (B.11) correspond to an expectation value $\langle\cdot\rangle_s$ over Poisson placements of halos, in a fixed realization of the halo source field $s(M,\mathbf{x})$. In this section, we take the "outer" expectation value over s. We also consider n-point functions which contain factors of the linear density field $\delta_{\rm lin}(\mathbf{k})$, or the radial velocity $v_r(\mathbf{k})$, so that our machinery will be general enough to calculate the six-point function (B.1).

In general, the source function $s(M,\mathbf{x})$ will depend on the halo bias model. We will consider the simplest possibility, namely the linear bias model $s(M,\mathbf{x}) = n(M)(1 + b(M)\delta_{\rm lin}(\mathbf{x}))$, or equivalently in Fourier space:

$$s(M,\mathbf{k}) = n(M)\Big[(2\pi)^3\delta^3(\mathbf{k}) + b(M)\delta_{\rm lin}(\mathbf{k})\Big] \tag{B.12}$$

Now consider a quantity which depends on the halo source field $s(M,\mathbf{k})$, such as the term T from the previous section:

$$T = \int dM\,dM'\,W_g(M,k_1)W_e(M,k_4)W_e(M',k_2)W_g(M',k_3)\Big[s(M,\mathbf{k}_1+\mathbf{k}_4)s(M,\mathbf{k}_2+\mathbf{k}_3)\Big] \tag{B.13}$$

To average over s, we replace all factors of s by the RHS of Eq. (B.12), and take the expectation value over $\delta_{\rm lin}$ using Wick's theorem. This gives:

$$\begin{aligned}\langle T\rangle = \int dM\,dM'\,&W_g(M,k_1)W_e(M,k_4)W_e(M',k_2)W_g(M',k_3)n(M)n(M')\\ &\times\Big[(2\pi)^6\delta^3(\mathbf{k}_1+\mathbf{k}_2)\delta^3(\mathbf{k}_3+\mathbf{k}_4) + b(M)b(M')(2\pi)^3\delta^3(\textstyle\sum\mathbf{k}_i)\Big]\end{aligned} \tag{B.14}$$

Diagramatically, we represent this procedure for averaging over s as follows. We start with the diagram (B.10) representing T, in which each hollow circle contains one factor of $s(M,\mathbf{k})$. We sum over all ways of either pairing vertices with wavy lines (representing a Wick contraction proportional to $P_{\rm lin}$), or leaving vertices unpaired. In the case of T, there are two possibilities:

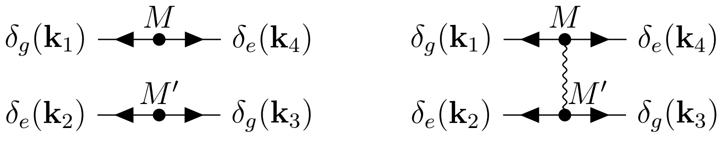

(B.15)

where the diagrams are interpreted using the following diagrammatic rules:

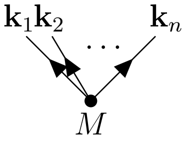

$$= \int dM\, n(M)\, (2\pi)^3 \delta^3\Big(\sum \mathbf{k}_i\Big)$$

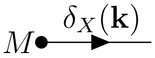

$$= W_X(M, k)$$

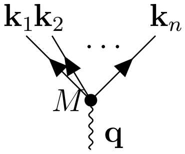

$$= \int dM\, n(M) b(M)\, (2\pi)^3 \delta^3\Big(\mathbf{q} + \sum \mathbf{k}_i\Big)$$

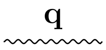

$$= \int \frac{d^3\mathbf{q}}{(2\pi)^3} P_{\rm lin}(q) \tag{B.16}$$

Note that we use hollow vertices in diagrams where s is not averaged (Eq. (B.11)), and solid vertices in diagrams where s is averaged (Eq. (B.16)).

A n-point expectation value of the form $\langle \delta_{X_i}(\mathbf{k}_1) \cdots \delta_{X_n}(\mathbf{k}_n) \rangle$ may be computed by enumerating all diagrams, using the preceding diagrammatic rules. An n-point function which also contains factors of $\delta_{\rm lin}(\mathbf{k})$ or $v_r(\mathbf{k})$, such as the six-point function (B.1), can be represented diagrammatically by adding the following external lines:

$$= P_{\rm lin}(k)$$

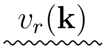

$$= \frac{ik_r}{k} P_{mv}(k) \tag{B.17}$$

where we have assumed that $v_r(\mathbf{k})$ is evaluated on a linear scale, so that $v_r(\mathbf{k}) = (ik_r/k)v(\mathbf{k}) = (ik_r/k)(faH/k)\delta_{\rm lin}(\mathbf{k})$.

B.3 The six-point function $\langle \delta_g^2 \delta_e^2 v_r^2 \rangle$

We calculate the non-Gaussian six-point function (B.1) using the diagrammatic rules in Eqs. (B.16), (B.17). Up to permutations of external legs, there are five possible diagrams:

$D_1 =$

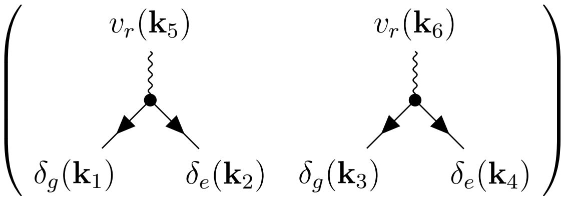

$D_2 =$

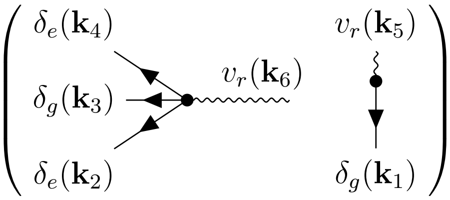

$D_3 =$

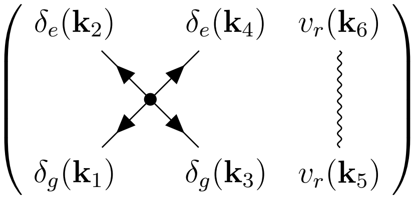

$D_4 =$

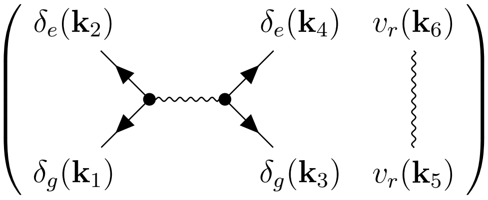

$D_5 =$

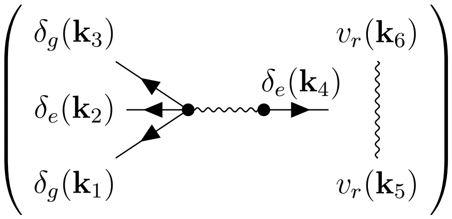

(B.18)

In particular, there are no fully connected diagrams, as claimed in the main text (§3.5.3). We evaluate these diagrams as follows (denoting $\mathbf{k}_{i_1\cdots i_n} = (\mathbf{k}_{i_1} + \cdots + \mathbf{k}_{i_n})$):

$$\begin{aligned}
D_1 &= \left(\int dM\, n(M) b(M) W_g(M, k_1) W_e(M, k_2) \frac{ik_{5r}}{k_5} P_{mv}(k_5)\, (2\pi)^3 \delta^3(\mathbf{k}_{125}) \right) \\
&\qquad \times \left(\int dM'\, n(M') b(M') W_g(M', k_3) W_e(M', k_4) \frac{ik_{6r}}{k_6} P_{mv}(k_6)\, (2\pi)^3 \delta^3(\mathbf{k}_{346}) \right) \\
&= -\beta_1(k_2)\beta_1(k_4) \frac{k_{5r}k_{6r}}{k_5 k_6} P_{mv}(k_5) P_{mv}(k_6)\, (2\pi)^6 \delta^3(\mathbf{k}_{125}) \delta^3(\mathbf{k}_{346}) \qquad \text{(B.19)} \\
D_2 &= \left(\int dM\, n(M) b(M) W_e(M, k_2) W_g(M, k_3) W_e(M, k_4) \frac{ik_{6r}}{k_6} P_{mv}(k_6) (2\pi)^3 \delta^3(\mathbf{k}_{2346}) \right) \\
&\qquad \times \left(\int dM'\, n(M') b(M') W_g(M', k_1) \frac{ik_{5r}}{k_5} P_{mv}(k_5) (2\pi)^3 \delta^3(\mathbf{k}_{15}) \right) \\
&= -b\beta_2(k_2, k_4) \frac{k_{5r}k_{6r}}{k_5 k_6} P_{mv}(k_5) P_{mv}(k_6)\, (2\pi)^6 \delta^3(\mathbf{k}_{2346}) \delta^3(\mathbf{k}_{15}) \qquad \text{(B.20)} \\
D_3 &= \int dM\, n(M) W_g(M, k_1) W_e(M, k_2) W_g(M, k_3) W_e(M, k_4) P_{v_r}(\mathbf{k}_5)\, (2\pi)^6 \delta^3(\mathbf{k}_{1234}) \delta^3(\mathbf{k}_{56}) \\
&= \frac{\alpha_2(k_2, k_4)}{n_h} P_{v_r}(\mathbf{k}_5)\, (2\pi)^6 \delta^3(\mathbf{k}_{1234}) \delta^3(\mathbf{k}_{56}) \qquad \text{(B.21)} \\
D_4 &= \int dM\, dM'\, n(M) n(M') W_g(M, k_1) W_e(M, k_2) W_g(M', k_3) W_e(M', k_4) \\
&\qquad \times b(M) b(M') P_{\text{lin}}(\mathbf{k}_1 + \mathbf{k}_2) P_{v_r}(\mathbf{k}_5)\, (2\pi)^6 \delta^3(\mathbf{k}_{1234}) \delta^3(\mathbf{k}_{56}) \\
&= \beta_1(k_2)\beta_1(k_4) P_{\text{lin}}(\mathbf{k}_1 + \mathbf{k}_2) P_{v_r}(\mathbf{k}_5)\, (2\pi)^6 \delta^3(\mathbf{k}_{1234}) \delta^3(\mathbf{k}_{56}) \qquad \text{(B.22)} \\
D_5 &= \int dM\, dM'\, n(M) n(M') W_g(M, k_1) W_e(M, k_2) W_g(M, k_3) W_e(M', k_4) \\
&\qquad \times b(M) b(M') P_{\text{lin}}(k_4) P_{v_r}(\mathbf{k}_5)\, (2\pi)^6 \delta^3(\mathbf{k}_{1234}) \delta^3(\mathbf{k}_{56}) \\
&= \beta_1(k_2)\beta_1(k_4) P_{\text{lin}}(k_4) P_{v_r}(\mathbf{k}_5)\, (2\pi)^6 \delta^3(\mathbf{k}_{1234}) \delta^3(\mathbf{k}_{56}) \qquad \text{(B.23)}
\end{aligned}$$

where for each diagram, the first line on the RHS gives the result of applying the diagrammatic rules straightforwardly, and the second line uses the α, β notation from Eqs. (3.54)–(3.56).

Comparing with the expression for the six-point function in the main text (Eqs. (3.57)–(3.67)), the diagram D_1 is the term $(Q_{\mathbf{k}_1\mathbf{k}_2\mathbf{k}_5} Q_{\mathbf{k}_3\mathbf{k}_4\mathbf{k}_6})$ on the first line of Eq. (3.57). One can check that the other five QQ-terms in (3.57) are obtained by permuting external legs of D_1.

There is a similar story for the other diagrams. The diagram D_2 is the first PR-term on the second line of Eq. (3.57), and the other seven PR-terms are obtained by permuting external legs of D_2. The diagram D_3 corresponds to the first S-term in Eq. (3.57). The next three S-terms in (3.57) correspond to the diagram D_4, and diagrams obtained from D_4 by permuting external legs. Finally, the last four S-terms in (3.57) correspond to D_5, and diagrams obtained from D_5 by permuting external legs. Putting all 22 diagrams together gives the six-point function shown in the main text (Eqs. (3.57)–(3.67)). Deriving this result was the main goal of this appendix.

B.4 Discussion and generalizations

Diagrammatic rules make some properties of the halo model more transparent. For example, a *connected* n-point function $\langle \delta_{X_1}(\mathbf{k}_1) \cdots \delta_{X_n}(\mathbf{k}_n) \rangle_c$ consists of a one-halo term, plus $(2^{n-1}-1)$ two-halo terms containing one power of $P_{\rm lin}$, with no terms with ≥ 3 halos. This is easy to see from the diagrammatic rules, but not so obvious otherwise.

We have only considered the simplest version of the halo model: linearly biased tracers of a Gaussian field. The diagrammatic rules can be extended to generalizations of this model as well. We sketch a few examples, without attempting to be exhaustive.

Our assumption of linear halo bias can be generalized, for example by a higher-order bias model of the form $\delta_h = b\delta_{\rm lin} + b_2\delta_{\rm lin}^2 + \cdots$. This can be incorporated by adding new vertices to the diagrammatic rules in Eq. (B.16), such as:

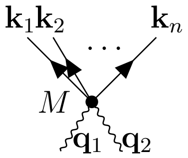

$$= \int dM\, n(M) b_2(M)\, (2\pi)^3 \delta^3(\mathbf{q}_1 + \mathbf{q}_2 + \textstyle\sum \mathbf{k}_i) \tag{B.24}$$

This would give rise to loop diagrams and renormalization, whereas linear bias (as assumed in the main paper) only produces tree diagrams.

As another extension of the halo model, suppose that galaxies are derived from halos using an additional level of Poisson sampling. More precisely, assume that in a halo of mass M, the number of galaxies is a Poisson random variable with mean $N_g(M)$, and the spatial location of each galaxy is a random variable with profile $u_g(M,k)$. We introduce square vertices for galaxies (continuing to denote halos by circular vertices), which are endpoints for external legs of the form $\delta_g(\mathbf{k})$. For example, the following diagram represents a one-halo, two-galaxy term in the three-point function $\langle \delta_g(\mathbf{k}_1)\delta_g(\mathbf{k}_2)\delta_g(\mathbf{k}_3)\rangle$:

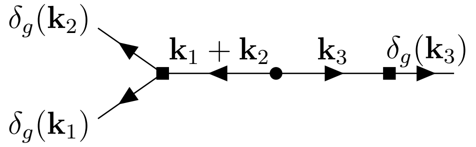

$$= \frac{1}{n_g^3} \int dM\, n(M) N_g(M)^2 u_g(M, \mathbf{k}_1 + \mathbf{k}_2) u_g(M, \mathbf{k}_3) \tag{B.25}$$

Multiple galaxy populations (e.g. centrals and satellites) can be handled by introducing multiple galaxy vertex types.

Finally, the halo model is sometimes generalized by including nonlinear evolution of the density field, rather than assuming s is proportional to δ_{lin}. Nonlinear evolution can be incorporated by adding interaction vertices which couple three or more wavy lines ($\sim\sim\sim$), in a way which is familiar from standard cosmological perturbation theory (for a review see [29]). Indeed, diagrammatic rules are frequently used for perturbative calculations involving *continuous* LSS fields. In this appendix, we have shown how to extend these rules to include discrete fields derived by Poisson sampling, such as halos and galaxies. This way of enumerating combinatorial terms in the halo model is convenient, especially for higher-n correlation functions, where the number of terms is large.